REPORT DOCUMENTATION PAGE	Form Approved OMB No. 0704-0188

Public reporting burden for this collection of information is estimated to average 1 hour per response, including the time for reviewing instructions, searching existing data sources, gathering and maintaining the data needed, and completing and reviewing the collection of information. Send comments regarding this burden estimate or any other aspect of this collection of information, including suggestions for reducing this burden, to Washington Headquarters Services, Directorate for Information Operations and Reports, 1215 Jefferson Davis Highway, Suite 1204, Arlington, VA 22202-4302, and to the Office of Management and Budget, Paperwork Reduction Project (0704-0188), Washington, DC 20503.

1. AGENCY USE ONLY (Leave blank)	2. REPORT DATE 2-5-95 2 Feb 95	3. REPORT TYPE AND DATES COVERED

4. TITLE AND SUBTITLE
Characterization of Solid State Laser and Nonlinear Optical Materials

5. FUNDING NUMBERS

6. AUTHOR(S)
Jin-Joo Song

19951129 121

7. PERFORMING ORGANIZATION NAME(S) AND ADDRESS(ES)
Center for Laser Research
413 Noble Research Center
Oklahoma State University
Stillwater, OK 74078

8. PERFORMING ORGANIZATION REPORT NUMBER

9. SPONSORING / MONITORING AGENCY NAME(S) AND ADDRESS(ES)
U.S. Army Research Office
P.O. Box 12211
Research Triangle Park, NC 27709-2211

DTIC SELECTED
DEC 0 4 1995
F

10. SPONSORING / MONITORING AGENCY REPORT NUMBER

11. SUPPLEMENTARY NOTES
The views, opinions and/or findings contained in this report are those of the author(s) and should not be construed as an official Department of the Army position, policy, or decision, unless so designated by other documentation.

12a. DISTRIBUTION / AVAILABILITY STATEMENT
Approved for public release; distribution unlimited.

12b. DISTRIBUTION CODE

13. ABSTRACT (Maximum 200 words)

Optical properties of materials having applications in solid state laser systems were investigated. The work was divided into two areas based on the materials useful in the different methods for obtaining frequency agility: narrow line emitters with multiple lasing channels and nonlinear optical materials. In the first category the spectral dynamics and lasing properties of a variety of materials such as fluoride and oxide crystals and glasses codoped with two or more rare-earth ions were studied and computers models developed to explain their spectral dynamics. The nonlinear optical materials investigated included rare-earth doped glasses, photorefractive crystals, and semiconductors. Laser spectroscopy techniques used to characterize these materials included four-wave mixing, two photon absorption and fluorescence line narrowing. The results were related to laser device parameters in order to determine the basic physical processes in the operational device parameters.

DTIC QUALITY INSPECTED 5

14. SUBJECT TERMS
Solid state lasers, nonlinear optics, spectroscopy, four-wave-mixing

15. NUMBER OF PAGES
275

16. PRICE CODE

17. SECURITY CLASSIFICATION OF REPORT	18. SECURITY CLASSIFICATION OF THIS PAGE	19. SECURITY CLASSIFICATION OF ABSTRACT	20. LIMITATION OF ABSTRACT
UNCLASSIFIED	UNCLASSIFIED	UNCLASSIFIED	UL

NSN 7540-01-280-5500

Standard Form 298 (Rev. 2-89)
Prescribed by ANSI Std. Z39-18
298-102

CHARACTERIZATION OF SOLID STATE LASER AND NONLINEAR OPTICAL MATERIALS

Final Report

Accesion For	
NTIS CRA&I	☑
DTIC TAB	☐
Unannounced	☐
Justification	

By	
Distribution /	

Availability Codes	
Dist	Avail and / or Special
A-1	

By:
J. J. SONG

February 2, 1995

U.S. ARMY RESEARCH OFFICE
GRANT NUMBER: DAAL03-91-G-0099

CENTER FOR LASER RESEARCH
OKLAHOMA STATE UNIVERSITY
Stillwater, OK 74078

APPROVED FOR PUBLIC RELEASE;
DISTRIBUTION UNLIMITED

TABLE OF CONTENTS

Page

PART C: PUBLICATIONS

LIST OF FIGURES

LIST OF TABLES

GOALS AND SUMMARY OF RESEARCH

On May 30, 1994 we completed our efforts on contract number DAAL03-91-G-0099. The goal of the research was characterization of materials having application in solid state laser systems. The work was divided into (i) spectroscopic and lasing properties of rare-earth doped crystals and glasses, and (ii) nonlinear optical properties of rare-earth doped glasses, photorefractive crystals, and semiconductors.

Problems relevant to three different rare-earth ion based laser materials were investigated. In the first materials, Tm,Ho:YAG, the energy transfer mechanism leading to 2.1 μm laser emission after diode laser pumping were investigated. Two of the transfer processes, the Tm$\rightarrow$Tm cross relaxation process and the Tm$\rightarrow$Ho energy transfer process, were characterized. Enhancement of the Tm$\rightarrow$Tm cross relaxation process by migration in the $^3H_4$ multiplet was observed. The rate parameter for the overall process was established. Rate Parameters describing the Tm$\rightarrow$Ho energy transfer were determined. These parameters were then used in a numerical solution to of a rate equation model of the laser system. Since the parameters were determined spectroscopically, there were no adjustable parameters in the simulation. This model accurately predicted the previously observed delay between the pump laser pulse and the emission at 2.1 μm and the relaxation oscillation. Additionally, a new loss mechanism involving excited state absorption of the pump photons was identified and found to contribute significantly to the observed green emission.

Three Nd^{3+} based laser materials were also investigated. In each material, an excited state absorption mechanism leading to blue emission was identified. For the crystalline systems studied, the $^2P_{3/2}$ multiplet was a resonant state absorption process originating on the $^4F_{3/2}$ and $^2H_{9/2}$ multiplets. A Judd-Ofelt analysis performed showed that this transition had a larger oscillator strength than the transition originating on either the pump or metastable levels. Although the situation involved in the fluoride glass was found to be much more complex, the same

transitions and processes were identified as contributing to the emission observed in this material. The overall effect of this excited state absorption process on the laser efficiency was also considered. A rate equation model was used to identify the important parameters controlling the effects on the energy stored in the metastable state. The relative sizes of the non-radiative decay rates and the rate of the excited state absorption were found to be very important. Excited state absorption was found to be more important in materials with slower non-radiative relaxation rates, such as fluoride glasses, than in materials with fast non-radiative decay, such as garnets. Evidence from laser efficiency measurements indicate a wavelength dependent pump efficiency in Nd:ZBAN fluoride glass laser, possibly an effect of this excited state absorption.

The nonlinear optical properties of three classes of materials were investigated using pump-probe and four wave mixing techniques. For the first class, diluted magnetic semiconductors were chosen since their band gap can be controlled by the Mn concentration. Pump-probe and degenerate four wave mixing experiments were performed on several CdMnSe and CdMnTe samples using below band gap excitation from a mode-locked, Q-switched, Nd:YAG laser. The main contribution to nonlinear optical effects were due to free carriers. Therefore, the coefficients for free carrier absorption, free carrier nonlinear refraction, and two photon absorption by the bound electrons were determined as a function of Mn concentration. While the two photon absorption and nonlinear refraction were primarily band gap dependent, the free carrier absorption was found to be host dependent. In particular, the free carrier absorption coefficient in CdMnSe remained constant where as in CdMnTe there was a strong dependence on the Mn concentration. Lifetime of carriers were studied using degenerate four wave mixing. It was found that carrier lifetime increases with an increase in the band gap and decreases with an increase in number of defects.

The second class of materials studied were photorefractive crystals. Two photon absorption and photorefraction was studied for several BiTeO, SBN and BGO crystals using picosecond and subpicosecond pulses from frequency doubled

Nd:YAG lasers. Use of short pulse lasers allowed large carrier generations via two photon absorption. The large carrier concentrations generated led to high FWM scattering efficiencies in all the materials studied. It was found that while the photorefractive effect was the dominant mechanism for the FWM signal, other mechanisms such as induced absorption in SBN could not be ignored. The response of the signal was found to vary with material and dopants. For example, addition of Fe to SBN resulted in an increase in diffusivity and a decrease in the rise time of the photorefractive signal. Therefore, further study of these materials need to be conducted to determine the optimum dopants.

The last class studied were Eu doped glasses. Permanent index changes in these materials had been observed previously under resonant excitation of the Eu dopants. These permanent changes were thought to be due to local configurational changes of the Eu ions. Experiments were performed on a number of different glasses containing various glass former and modifier ions. The results were analyzed in terms of the strength of the chemical bonds, Charge-to-radius-squared (Q/r^2), mass of the modifiers, and the structure of the former ions. For maximum index changes, optimum modifier ions were found to have a large Q/r^2, a small mass, and a small attraction for the oxygen ions. Best suited former ions had a small attraction for the oxygen and a small Q/r^2. Furthermore, glasses with the greatest degrees of freedom, such as silicates, resulted in the largest index changes. These finding could be used to identify best suited glasses for maximum permanent index changes in Eu doped glasses and fibers.

The following sections expand on the observations oultined above for each material studided.

PART A

SOLID STATE LASER MATERIALS

SECTION I

THEORETICAL BACKGROUND

The optical properties of materials that contain rare-earth ions have long been studied. Excellent reviews of the optical properties of rare-earths can be found in Ref. [5–8]. Early workers, especially J. Becquerel, observed that at low temperatures the optical absorption spectra of rare-earth salts consisted of numerous sharp lines. Understanding of the origin of these sharp radiative transitions was furthered by the development of crystal field theory, by H. Bethe and H. A. Kramers for example, and by J. H. Van Vleck, who suggested that the transitions were due to a forced electric dipole mechanism and occurred between states in the $4f^n$ electronic configuration.(see the extensive discussions of this early work in Ref. [6] and [8]) For a free ion radiative transitions within a configuration were known to be forbidden since the initial and final states have the same parity. Van Vleck proposed that such a transition becomes allowed when the ion is placed in a host material because of an interaction with the local electric field produced by the surrounding ligand ions.

Detailed analysis of the spectra and relaxation mechanisms in rare-earth doped materials followed this early work. The energy levels and transitions observed in the absorption and emission spectra of rare-earth materials were identified and characterized (see for example Ref. [6,7]) and a phenomenological model describing the radiative transitions was developed.[9,10] Various non-radiative relaxation mechanisms, including multiphonon relaxation [8,11–13] and non-radiative interactions between two or more ions (see reviews in Refs. [14–17]), were also identified and studied. A brief summary of some of the important results will be given here.

5

Energy Levels

As mentioned previously, the sharp line structure that appears in the absorption and emission spectra of rare-earth materials is produced by transitions which occur between electronic states arising from the optically active 4f electrons. The electronic configuration for atoms in the lanthanide series is $[1s^2 2s^2 2p^6 3s^2 3p^6 3d^{10} 4s^2 4p^6 4d^{10} 5s^2 5p^6 6s^2] + 4f^N$ where N varies from 2 for Ce to 14 for Yb. In the trivalent ion form, RE^{3+}, the two 6s electrons and one of the 4f electrons are ionized, leaving the lowest energy electronic configuration as $[1s^2 2s^2 2p^6 3s^2 3p^6 3d^{10} 4s^2 4p^6 4d^{10} 5s^2 5p^6] + 4f^n$. Interactions between the optically active $4f^n$ electrons, through Coulombic repulsion and spin-orbit coupling, and interaction with the host material, through the static crystal field, lead to a complex set of electronic states with differing energies. By applying the tensor operator methods developed by Racah and Judd[18], the energy level structure of the trivalent rare-earths can be quantitatively understood in terms of these interactions.[6,7] A brief summary of the approach and its results are given here.

The energy level structure involved arises primarily from three interactions: the Coulombic repulsion between electrons, spin-orbit coupling and the electric field due to surrounding hosts ligands. The Hamiltonian for the optically active 4f electrons is written as

$$H = H_o + H_{Coul} + H_{SO} + H_{SCF}. \tag{1}$$

H_o contains the kinetic energy and nuclear potential term for each of the 4f electrons,

$$H_o = \sum_{i=1}^{n} -\frac{p_i^2}{2m_i} - \frac{Z_{eff} e^2}{r_i} \tag{2}$$

where e is the electronic charge, Z_{eff} is the effective potential due to the nucleus and core electrons, i indexes the optically active 4f electrons, p_i, r_i and m_i are the momentum operator, the position operator and the mass of the ith 4f electron. The summation is over all the optically active 4f electrons. The Coulombic repulsion

energy is given by

$$H_{Coul} = \sum_{i<j}^{n} \frac{e^2}{r_{ij}} \tag{3}$$

where r_{ij} is the position operator between the ith and j^{th} electrons. The spin-orbit interaction is

$$H_{SO} = \sum_{i=1}^{n} \xi(r_i) s_i \cdot l_i \tag{4}$$

where $\xi(r_i)$ is the spin-orbit coupling strength and s_i and l_i are the spin and orbital angular momentum operators, respectively, for the ith electron. Finally, the interaction with the surrounding host (the static crystal field) is

$$H_{SCF} = \sum_{q,k,i} B_q^k \left[C_q^k \right]_i \tag{5}$$

where the B_q^k are crystal field parameters, the C_q^k are spherical tensor operators and once again the sum is over the optically active 4f electrons. The exact form of the crystal field, which C_q^k operators are present and the values of the B_q^k's, is determined by the symmetry of the rare-earth site in the lattice and the strength of the interaction with the surrounding ligands. For rare-earth ions in the materials considered here $H_{SCF} < H_{SO} < H_{Coul}$ with energies of ≈ 100 cm^{-1}, ≈ 1000 cm^{-1} and ≈ 10000 cm^{-1}, respectively. A diagram showing the effects of these interactions is shown in Figure 1. Note that this approach ignores any configuration mixing, many body effects or relativistic effects.

The diagonalization of the Hamiltonian to produce the appropriate eigenvalues and eigenstates is usually approached in three steps. First, the central field approximation is made, combining H_o and H_{Coul} into a single central effective potential treating the Coulombic repulsion as a small perturbation. This yields states characterized by the quantum numbers S, L, M_S and M_L where the energy of the state is dependent only upon L. Using spectroscopic notation these states are labeled as the ^{2S+1}L terms.

Application of the next interaction, the spin-orbit coupling, to these states has two important results. First, part of the degeneracy of the various ^{2S+1}L terms is lifted yielding states that are $2J+1$ degenerate. These states are labeled
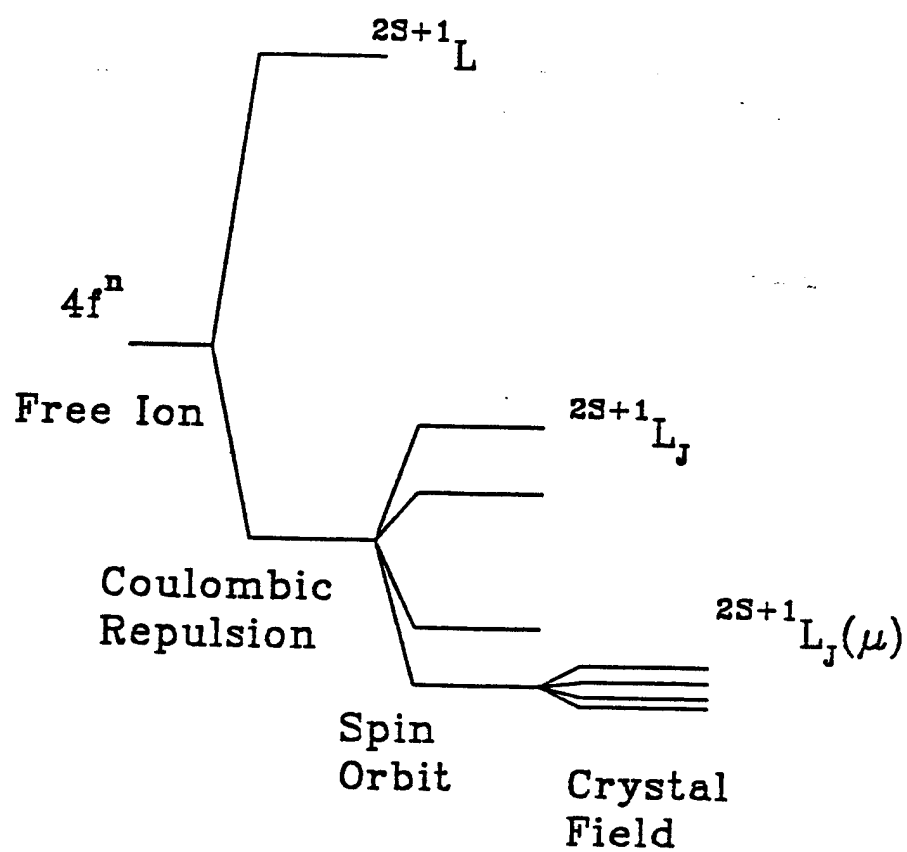
Figure 1. Rare-Earth Ion Energy Level Splittings.

as the $^{2S+1}L_J$ multiplets (the energies are independent of the quantum number J_z). These are the familiar LS coupled or Russell-Saunders states. The second result of applying the spin-orbit interaction is that it mixes states with different values of S and L but having the same value of J. The result of this J-mixing is that S and L are no longer "good" quantum numbers. The spin-orbit coupled states are linear combinations of the Russel-Saunders states:

$$| \gamma 4f^n[S,L]J >= \sum_{\gamma SL} C(\gamma SL) | \gamma 4f^n SLJ > \qquad (6)$$

where γ represents any other quantum numbers needed to identify the state and the $C(\gamma SL)$ are coefficients dependent upon the strengths of the spin-orbit and Coulombic interactions. This is called the intermediate coupling scheme since the resulting wavefunctions are neither pure LS coupled states nor pure jj coupled states. The $[S,L]$ notation on the left hand side is used as a reminder that although S and L are still used to denote the states, they are no longer good quantum numbers and instead only represent the dominant ^{2S+1}L term in the linear combination.

The interaction with the static crystal field is considered next and like the case of spin-orbit coupling two effects are observed. First, the static crystal field removes part of the $2J+1$ degeneracy of the $^{2S+1}L_J$ multiplets producing crystal field states, also called Stark levels, which are often labeled as $^{2S+1}L_J(\mu)$ where μ is a quantum number associated with the crystal field symmetry (for example, an irreducible representation). The second effect of the static crystal field is that it causes mixing of states with the same value of μ but having different J values. Thus J is no longer a good quantum number and the final result are states of the form

$$| \gamma 4f^n[S,L,J]\mu >= \sum_{\gamma SL} C(\gamma SLJJ_z) | \gamma 4f^n SLJJ_z > . \qquad (7)$$

where the $C(\gamma SLJJ_z)$ are dependent on the strength of the crystal field in addition to the strengths of the other interactions. Although S, L and J are still used to label the states, it is understood that only μ is a good quantum number and the

other quantum numbers on the left hand side of the equation (S, L and J) simply represent the dominant multiplet in the linear combination.

The procedure outlined above is carried out in practice by comparison to experiment since at present *ab initio* calculations of the energy levels are complicated by difficulties in calculating the actual crystal field strengths and radial wavefunctions. Furthermore, the calculations can only be done for host materials where the symmetry of the rare-earth site is well defined. In glass materials, for example, the site to site variations in the static crystal field strength and symmetry causes inhomogeneous broadening and a detailed analysis of the Stark level structure is not generally possible. In materials where the calculations are possible, the strengths of the interactions outlined above, and in some cases interactions accounting for additional relativistic and three-body effects, are parameterized and determined by a best fit to experimental data, yielding the eigenvalues (the state energies) and eigenvectors (the electronic wavefunctions) of the system.

Transition Mechanisms

Transitions between the states responsible for the optical spectra in a rare-earth ion/host system occur through a variety of mechanisms. The three dominant mechanisms in rare-earth doped materials are forced electric dipole transitions, multiphonon transitions and non-radiative energy transfer. These mechanisms are often separated into two categories: radiative and non-radiative processes. The former involve absorption or emission of a photon for energy conservation and produce the observed absorption and emission spectra while the latter involve either exchange of energy with the host lattice or energy transfer to other ions in the system.

Radiative Transitions

First consider electric dipole radiative transitions between a pair of electronic states. The transition probability rate for such a transition is governed by Fermi's

rule and involves the matrix element containing the electric dipole operator. The electric dipole matrix element is written as

$$M_{ed} = <\Psi_F \mid \mathbf{P} \mid \Psi_I>$$ (8)

where $\mid \Psi_F>$ is the wavefunction of the final state, $\mathbf{P}$ is the electric dipole operator and $\mid \Psi_I>$ is the wavefunction of the initial state. The electric dipole operator connects states with opposite parity. In the case of transitions between the states derived in the previous section, the matrix element in Equation (8) is zero and the transition is said to be forbidden since both states arise from the $4f^n$ configuration and therefore have the same parity.

As mentioned previously, Van Vleck suggested that the optical transitions observed in rare-earth materials were due to forced electric dipole transitions. He noted that odd symmetry components of the crystal field mixed states of opposite parity into the $4f^n$ states (configuration mixing). This mixing, ignored in the previous calculation of the energy levels and wavefunctions, provided the initial and final states with some components of opposite parity causing the transition rate to be non-zero. In 1962, B. R. Judd[9] and G. S. Ofelt[10] independently developed similar phenomenological models to explain and quantify this interaction. Detailed descriptions of the Judd-Ofelt theory can be found in [5,8,16,19] and only an outline is given here.

The approach taken by the Judd-Ofelt theory is a straightforward application of perturbation theory. Odd order terms in the crystal field Hamiltonian (designated by $\mathbf{V_{CF}}$) are used as a perturbation causing admixing of states with opposite parity to the initial $4f^n$ states. Using 1st order perturbation theory the new state is given by

$$\mid \Psi_A> = \mid \Phi_A> - \sum_B \frac{<\Phi_B \mid \mathbf{V_{CF}} \mid \Phi_A>}{E_A - E_B} \mid \Phi_B>$$ (9)

where $\mid \Phi_B>$ and E_B are the wavefunction and energy of a state arising from a higher lying configuration, $\mid \Phi_A>$ and E_A are the wavefunction and energy of a state arising from the $4f^n$ configuration and the summation is over all states from configurations having parity opposite that of the $4f^n$ configuration.

The electric dipole matrix element can be written using states described as in Equation (9) with $| \Psi_I >$ as the initial state where $| \Phi_A > \rightarrow | \Phi_I >$ and $| \Psi_F >$ as the final state where $| \Phi_A > \rightarrow | \Phi_F >$. Writing the electric dipole matrix element using these states yields

$$< \Psi_F | P | \Psi_I > = < \Phi_F | P | \Phi_I > - \sum_B \frac{<\Phi_F|V_{CF}|\Phi_B><\Phi_B|P|\Phi_I>}{E_F - E_B}$$
$$- \sum_B \frac{<\Phi_F|P|\Phi_B><\Phi_B|V_{CF}|\Phi_I>}{E_I - E_B} \qquad (10)$$
$$+ \sum_B \frac{<\Phi_B|V_{CF}|\Phi_I>}{E_I - E_B} \sum_B \frac{<\Phi_F|V_{CF}|\Phi_B>}{E_F - E_B} < \Phi_B | P | \Phi_B >$$

This can be simplified to

$$< \Psi_F | P | \Psi_I > = - \sum_B \frac{<\Phi_F|V_{CF}|\Phi_B><\Phi_B|P|\Phi_I>}{E_F - E_B}$$
$$- \sum_B \frac{<\Phi_F|P|\Phi_B><\Phi_B|V_{CF}|\Phi_I>}{E_I - E_B} \qquad (11)$$

where the matrix elements formed between states of the same parity have been set equal to zero. The major contribution of Judd and Ofelt involves the simplification of this expression.

The major assumptions involved are as follows: the states arising from the opposite parity configurations are degenerate, $E_1 = E_2 = E_B$, and the energy differences between the states arising from the higher energy configurations and the states arising from the $4f^n$ configuration are nearly equal: $E_I - E_B \approx E_F - E_B$. The first of these assumptions allows the use of closure the simplify the summation over B while the second assumption allows the two terms in Equation (11) to be combined into a single term. The resulting equation can be further simplified by summing over the Stark levels of the upper and lower multiplets. The result is usually written in terms of the electric dipole linestrength for multiplet to multiplet transitions, S_{ed}, which is proportional to the square of the matrix element and written as

$$S_{ed}[| [S, L]J >, | [S', L']J' >] = e^2 \sum_{t=2,4,6} \Omega_t \left| < [S, L]J \| U^t \| [S', L']J' > \right|^2. \qquad (12)$$

The doubly reduced tensor operators $< [S, L]J \| U^t \| [S', L']J' >$ are usually considered to be host invariant and have been calculated and tabulated by Carnall,

Crosswhite and Crosswhite. [20] All of the constants, radial integrals and other factors have been absorbed into the Judd-Ofelt parameters, the Ω_t's.

The probability rate for an electric dipole transition from the $|~[S,L]J>$ multiplet to the $|~[S',L']J'>$ multiplet is related to the linestrength and can be written as

$$A[|~[S,L]J>,|~[S',L']J'>] = \frac{64\pi^4}{3h(2J+1)\lambda_p^3}\chi_{ed}S_{ed}[|~[S,L]J>,|~[S',L']J'>] \quad (13)$$

where n is the index of refraction, e is the electron charge, λ_p the wavelength of the transition, and χ_{ed} is the local field correction for the rare-earth in the initial manifold given by

$$\chi_{ed} = \frac{n(n^2+2)^2}{9}. \quad (14)$$

The radiative lifetime of an $|~[S,L]J>$ multiplet, τ_{rad}, is related to the radiative decay rate through

$$\frac{1}{\tau_{rad}} = \sum_{[S',L']J'} A[|~[S,L]J>,|~[S',L']J'>] \quad (15)$$

where the summation is over all lower energy multiplets. A branching ratio for an electric dipole transition from the $|~[S,L]J>$ multiplet to the $|~[S',L']J'>$ multiplet can also be defined as

$$\beta[|~[S,L]J>,|~[S',L']J'>] = A[|~[S,L]J>,|~[S',L']J'>]\tau_{rad}. \quad (16)$$

The branching ratio for a transition is a measure of the relative intensity of a transition to the total intensity of all the transitions originating on a given multiplet. Another important quantity, the oscillator strength of a transition, can be written as

$$f[|~[S,L]J>,|~[S',L']J'>] = \frac{8\pi m\nu}{3h(2J+1)e^2n^2}\chi_{ed}S_{ed}[|~[S,L]J>,|~[S',L']J'>] \quad (17)$$

where m is the electron mass, and ν is the frequency of the transition.

The Judd-Ofelt parameters for a given rare-earth ion/host combination are determined by fitting experimentally calculated oscillator strengths for transitions from the ground state multiplet to the excited state multiplets to those found by Equation (17). The oscillator strength of a multiplet to multiplet transition is found from the absorption spectra using

$$f[| [S, L]J >, | [S', L']J' >] = \frac{mc}{\pi e^2 N} \int \alpha(\nu) d\nu \qquad (18)$$

where N is the concentration of rare-earth ions in the sample, $\alpha(\nu)$ is the absorption coefficient at frequency ν and the integral is over frequency range of the transition. Once the Judd-Ofelt parameters are determined from the fitting procedure, the radiative lifetimes of excited states and oscillator strengths for transitions between excited states can be calculated.

Non-Radiative Transitions: Multiphonon Decay

A second mechanism for transitions in rare-earth ion/host systems involves an interaction between the rare-earth ion and the lattice through the exchange of one or more phonons. Very fast transitions involving a small number of lattice phonons occur between the crystal field split Stark levels within a multiplet. These transitions lead to a Boltzman distribution of excited ions within a multiplet and can account for the experimentally measured linewidths of the optical transitions. In addition to these processes, however, there are multiphonon processes that occur on the same time scale as radiative transitions. These processes involve a large number of high energy phonons to provide energy conservation for a transition between a pair of Stark levels from two different multiplets.

Although multiphonon decay in rare-earth materials has been extensively studied,[6,8,12,13,16,21,22] a complete theory describing multiphonon relaxation has not been fully developed. A general theoretical approach and a phenomenological model have been established however.(see for example [8,16]) Multiphonon decay is possible through an interaction between the electronic-vibrational states

of the rare-earth ion/lattice system. These states are written as

$$| \Psi_{a,i,j,k...} \rangle = | \Psi_a \rangle | n_i n_j n_k... \rangle \qquad (19)$$

where $| \Psi_a \rangle$ is the electronic wavefunction, $| n_i n_j n_k... \rangle$ is the wavefunction describing the lattice and the n_i's are the occupation numbers of the phonon modes of the lattice. The interaction mechanism is the dynamic crystal field which can described by a Hamiltonian of the form

$$H_{DCF} = \sum_i Q_i V_i + \frac{1}{2} \sum_{i,j} Q_i Q_j V_{ij} + ... \qquad (20)$$

where the Q_i's are the normal mode coordinates and the $V_{i...}$'s are electron-phonon coupling strengths. Typical theoretical approaches involve the use of nth order perturbation theory using the first order term in the crystal field expansion or use 1st order perturbation theory with the nth order term in the crystal field expansion. In either case since the exact coupling between the rare earth ion and the lattice is not well known, *ab initio* calculations are difficult.

Empirically, multiphonon relaxation rates are found to depend on the temperature of the sample and the energy separation between multiplets.[8,12,22] A multiphonon decay rate is found by comparing the measured fluorescence lifetime, τ_{meas}, with the radiative rate predicted by the Judd-Ofelt theory described previously, τ_{rad}. In the absence of any other interactions the measured and predicted radiative lifetimes are related by

$$\frac{1}{\tau_{meas}} = \frac{1}{\tau_{rad}} + W_{mp} \qquad (21)$$

where W_{mp} is the multiphonon decay rate. Mutiphonon decay rates for different transitions in a given host are found to depend exponentially on the energy gap separating the upper and lower multiplets. This relation is known as the energy gap law and is given by

$$W_{mp} = C \exp(-\alpha \Delta E) \qquad (22)$$

where C and α are host material dependent and ΔE is the energy gap between the upper and lower multiplets involved in the transition.

Phenomenologically, the energy gap law can be understood using a single frequency phonon model. An energy gap ΔE can be bridged by n high energy phonons of frequency ω so $n = \Delta E / \hbar\omega$. For an nth order perturbation approach to be valid, the nth order term must be smaller than the $(n-1)^{th}$ order term:

$$\frac{W_n}{W_{n-1}} = \epsilon \ll 1 \qquad (23)$$

If the ratio between W_n and W_{n-1} is nearly constant for all n then

$$W_n = C\epsilon^n \qquad (24)$$

which can be rewritten as

$$W_n = C\exp(-\alpha\Delta E) \qquad (25)$$

Once C and α are known for a given host, the energy gap law can be used to determine the rate for multiphonon transitions in the material. One important factor to note, however, is that the energy gap law has been found to be valid only for cases where large numbers of phonons are involved. For small energy gaps, where only one or two high energy phonons are needed, the energy gap law no longer holds and can significantly underestimate the decay rates. Investigation of non-radiative relaxation rates between closely spaced multiplets is still an important area of research in rare-earth materials.[23–27]

Non-Radiative Decay: Ion-Ion Energy Transfer

A third mechanism responsible for multiplet to multiplet transitions in rare-earth ions is non-radiative energy transfer.(see Refs. [8,14–17]) In this type of process an ion in an excited state transfers some or all of its energy to another nearby ion which is originally in either its ground state or an excited state without involving either emission or absorption of a photon. Three examples of energy transfer processes are shown in Figure 2. Figure 2(a) shows an example of energy transfer from an ion of type s, a sensitizer, to an ion of type a, an activator. The sensitizer relaxes to its ground state promoting the activator to its excited state. In situations where this process occurs, the fluorescence emission intensity and

measured fluorescence lifetime of the sensitizer are both reduced (or quenched) in the presence of activators. If the activators luminesce, this type of process is referred to as sensitized luminescence since emission is seen from a type of ion that does not directly absorb the pump energy. Early work in this field can be found in Refs. [28–30]. Figure 2(b) shows a second energy transfer process in which one excited sensitizer ion relaxes to the ground state transferring its energy to another sensitizer ion that was initially in the ground state. This process does not lead to luminescence quenching but it can be responsible for spatial energy migration in which energy is transferred from one location in the crystal to another. Long range energy transfer of this type can be studied using laser induced grating spectroscopy.[31–33] The third type of process shown (Figure 2(c)) is an example of an energy transfer upconversion process in which two ions in excited states interact, one ion relaxing to the ground state and the other being promoted to a higher lying level. This type of process can, for example, convert infrared excitation into visible emission and is one process often present in upconversion laser systems.[34,35] The processes represented in Figure 2(a) and Figure 2(c) are examples of spectral energy transfer processes since their effects can be detected by monitoring changes in the spectral content of the emission.

The study of energy transfer has been an extremely important part of the understanding of the optical properties of rare-earth doped materials.(see for example Ref. [8,14,15,17] Two somewhat different mathematical approaches for studying energy transfer have been developed and used: a macroscopic rate equation approach and a microscopic ion-ion interaction approach. The microscopic approach, in which interactions between pairs of ions are considered, is discussed below while the rate equation approach, which is formally the same as the rate equation approach used to describe laser systems, will be described in the next section. The relationship between these two approaches and the limitations of each approach are discussed in detail in Ref. [36].

A starting point for any discussion of the microscopic approach to non-radiative energy transfer must be the pioneering work of Forster [28] and the
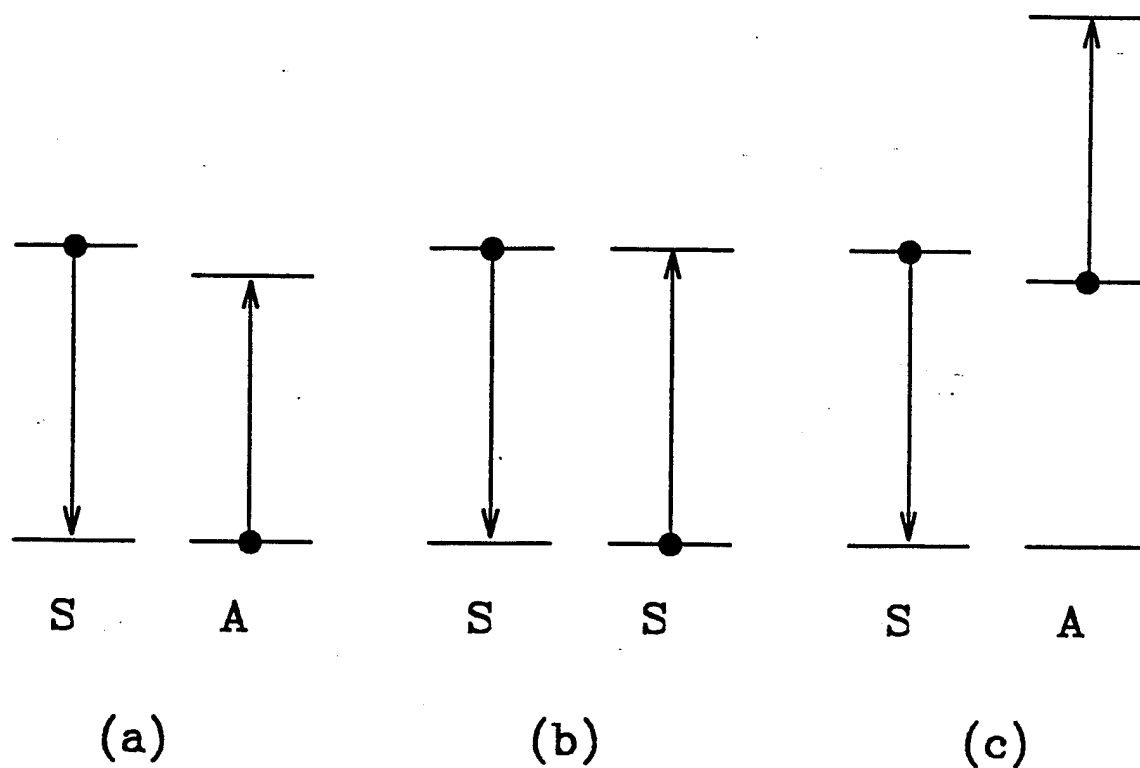
Figure 2. Examples of Energy Transfer Processes. (a) Sensitizer to Activator Energy Transfer (b) Senesitizer to Sensitizer Energy Transfer (c) Upconversion Energy Tranfer.

continuation of this work by Dexter [29]. Forster-Dexter theory provides a simple method of calculating the energy transfer rate from a sensitizer ion to an activator ion with a given spatial separation using the observed emission and absorption spectra of the ions involved. Extensions to this basic theory provide a formalism to understand to more complex systems with many sensitizer and activator ions distributed in the host media [28,30,37] (Reviews in Refs.[8,14,15,17]). The brief review of the Forster-Dexter theory given here parallels the development by Dexter in [29].

A probability rate for energy transfer between two ions as shown in Figure2(a) can be written as follows

$$P_{sa} = \frac{2\pi}{\hbar} |< \Psi_i \mid H_{ij} \mid \Psi_f >|^2 g_e. \tag{26}$$

where $\mid \Psi_i >$ is the wavefunction of the initial state given by

$$\mid \Psi_i >= \mid \Psi(\mathbf{r_s}, E_{se}), \Psi(\mathbf{r_a}, E_{ag}) > \tag{27}$$

where the sensitizer ion at $\mathbf{r_s}$ in the excited state (energy$=E_{se}$) is described by the wavefunction $\Psi(\mathbf{r_s}, E_{se})$ and the activator ion at $\mathbf{r_a}$ in the ground state (energy$=E_{ag}$) is described by the wavefunction $\Psi(\mathbf{r_a}, E_{ag})$. The wavefunction of the final state is

$$\mid \Psi_f >= \mid \Psi(\mathbf{r_s}, E_{sg}), \Psi(\mathbf{r_a}, E_{ae}) > \tag{28}$$

where the sensitizer ion at $\mathbf{r_s}$ in the ground state (energy$=E_{sg}$) is described by the wavefunction $\Psi(\mathbf{r_s}, E_{sg})$ and the activator ion at $\mathbf{r_a}$ in the excited state (energy$=E_{ae}$) is described by the wavefunction $\Psi(\mathbf{r_a}, E_{ae})$. g_e is the density of states of the final state and H_{ij} is the Hamiltonian describing the interaction between the ith and j^{th} ions.

The form of H_{ij} depends upon the type of interaction considered, electric dipole-dipole, electric dipole-quadrupole, exchange, etc. For simplicity, consider only the electric dipole-dipole interaction so

$$H_{ij} = \left[\mathbf{r_s} \cdot \mathbf{r_a} - \frac{3(\mathbf{r_s} \cdot \mathbf{R_{sa}})(\mathbf{r_a} \cdot \mathbf{R_{sa}})}{\mathbf{R_{sa}}^2} \right] \frac{e^2}{R_{sa}^3} \tag{29}$$

where $\mathbf{R_{sa}}$ is the vector connecting the two ions. The matrix element involving this interaction can be evaluated and, using the Einstein A and B coefficients, related to the observed absorption and emission spectra. This yields

$$P_{sa}^{dd} = \frac{3\hbar^4 c^4}{4\pi n^4} \frac{Q_a}{\tau_s R_{sa}^6} \left(\frac{\mathcal{E}}{\sqrt{\epsilon}\mathcal{E}_c} \right)^4 \int \frac{f_s(E)F_a(E)dE}{E^4} \qquad (30)$$

where Q_a is the absorption strength given by $Q_a = \int \sigma(E)dE$ where $\sigma(E)$ is the absorption cross section of the activator at energy E, f_s is the normalized emission spectrum of the sensitizer, $F_a(E)$ is the normalized absorption spectrum of the activator, τ_s is the radiative lifetime of the excited state of the sensitizer (in the absence of the activator), $\mathcal{E}/\mathcal{E}_c$ is the ratio of the applied electric field intensity to that in the crystal, and ϵ is the dielectric constant. This is often written in terms of a critical interaction distance, R_o, as

$$P_{sa}^{dd} = \frac{1}{\tau_s} \left(\frac{R_o}{R_{sa}} \right)^6 \qquad (31)$$

with

$$R_o \equiv \left(\frac{3\hbar^4 c^4}{4\pi n^4} Q_a \left(\frac{\mathcal{E}}{\sqrt{\epsilon}\mathcal{E}_c} \right)^4 \int \frac{f_s(E)F_a(E)dE}{E^4} \right)^{1/6}. \qquad (32)$$

The critical interaction distance is the separation between a sensitizer and an activator that produces an energy transfer rate equivalent to the intrinsic radiative decay rate of the sensitizer. More importantly, the critical interaction distance can be determined from experimentally measured spectra: the absorption spectrum of the activator and the emission spectrum of the sensitizer.

As mentioned previously, the formalism above describes the energy transfer rate between a pair of ions. The extension to a somewhat more realistic material system, in which there are a large number of sensitizer and activator ions can be found in the work of Forster [28] and of Inoukuti and Hirayama [30]. In this approach, each activator ion in the system contributes to the decay of the sensitizer. The observed decay time, in the absence of other decay processes, is given by

$$\rho_s(t) = \exp \left[-\frac{t}{\tau_s} - \frac{t}{\tau_s} \sum_{i=1}^N \left(\frac{R_o}{R_i} \right)^6 \right] \qquad (33)$$

where R_i is the distance to the ith activator and N is the number of activators. To determine the average decay rate of all the sensitizers in the system the rate is averaged over a random distribution of activators, $\rho_a(R_i)$, giving

$$\overline{\rho}_s(t) = \exp\left[-\frac{t}{\tau_s} - \frac{t}{\tau_s}\prod_{i=1}^{N}\int_V \left(\frac{R_o}{R_i}\right)^6 \rho_a(R_i)dV\right] \qquad (34)$$

This can be evaluated in the limit as $N \& V \to \infty$ such that $N/V \to N_a$, the concentration of activators. The average decay in this limit is then given by

$$\overline{\rho}_s(t) = \exp\left[-\frac{t}{\tau_s} - \frac{N_a}{N_o}\Gamma(1/2)\sqrt{\frac{t}{\tau_s}}\right]. \qquad (35)$$

where N_o is the critical concentration given by $N_o = \frac{4\pi}{3}(R_o)^3$. This type of decay is known as static or Forster decay.

One of the assumptions in the derivation of the static decay is that no interaction between sensitizer ions occurs, that is, there is no sensitizer to sensitizer energy transfer. Although developed above for two different types of ions, Forster-Dexter theory can be applied even if the ions are of the same type. In this case one "sensitizer" ion transfers its energy to another "sensitizer" ion. In many systems the concentration of sensitizers is large enough for sensitizer-sensitizer interaction to be significant. R_{ss}, the distance between two sensitizers which will replace R_{sa} in Equation (31), becomes small so the interaction rate for the process in Figure 2(b) is large. This may lead to spatial migration of energy in the excited state of the sensitizer. A wide variety of methods for describing sensitizer to sensitizer energy migration have been developed, including formalisms based on solving the diffusion equation [38], random walk approaches [37,39] and a generalized master equation approach [40].

To treat the most general case in which both energy migration and sensitizer-activator energy transfer occurs, different formalisms have been developed.(see for example Refs. [37,41] and the reviews) Often, these approaches yields results in which each of the energy migration steps (sensitizer to sensitizer energy transfer steps) is treated using Equation (31). Each of the approaches, however, is faced with limitations on its applicability due to the assumptions that must be made,

especially assumptions related to the distribution of ions in the host and the possibility of energy transfer from "activators" to "sensitizers", called back transfer. To avoid these problems, numerical approaches using Monte Carlo simulations have been carried out.[42] Overall the problem of energy transfer in rare-earth doped materials is an extremely complex one and the brief discussion of some of the single-step energy transfer processes above introduces the concepts and terminology used in the discussions of the systems considered later in this work.

Rate Equation Modeling

In the previous sections the various mechanisms for transitions between the levels of rare-earths have been discussed. These rates describe the decay of and excitation of ions from one state to another. A common approach for describing population dynamics in multi-level systems, often used to describe laser systems and energy transfer, involves the use of semiclassical rate equations. Formally, the semiclassical rate equation approach is related to the population density matrix formalism used in quantum mechanics in the limit that the dephasing time (or dipole decay time) is short compared to the time scale on which the populations of the levels evolve. Discussions of rate equations and their use in the study of laser systems and energy transfer can be found in [5,14,15,36,43,44]

Using the rate equation approximation, the time evolution of the population density of the ith level of a multi-level system is written as

$$\frac{dn_i}{dt} = \sum_E W_E(n_i, n_j, \Phi_k, t...) - \sum_R W_R(n_i, n_j, \Phi_k, t, ...) \qquad (36)$$

where $W_E(n_i, n_j, \Phi_k, t, ...)$ is the rate of the Eth process that excites ions to the level (a "pump" process) and $W_R(n_i, n_j, \Phi_k, t, ...)$ is the rate of the Rth relaxation process that depopulates the level. The sums are carried out over all possible excitation and relaxation processes. In general the rates may depend explicitly on the population of the ith level (n_i), the populations of other levels (the n_j's), the intensities of any fields present (the Φ_k's), and the time, t. The exact forms and proportionality constants involved depend on type of process involved in each

rate. The usefulness of the rate equations for describing a given system depends on determining the important mechanisms in the system and the knowledge of the rate parameters (the proportionality constants) describing each process.

Figure 3 shows a simple system described by the following set of rate equations:

$$\dot{n}_1 = -R_{13} + R_{31} + A_{31}n_3 - k_{52}n_5n_1 + k_{25}n_2n_4 + A_{21}n_2 \qquad (37)$$

$$\dot{n}_2 = +A_{32}n_3 + W_{32}n_3 - W_{23}n_2 - A_{21}n_2 - k_{25}n_2n_4 - k_{52}n_5n_1 \qquad (38)$$

$$\dot{n}_3 = -\tau_3^{-1}n_3 - W_{32}n_3 + W_{23}n_2 - R_{31} + R_{13} \qquad (39)$$

$$\dot{n}_4 = -k_{52}n_5n_1 + k_{25}n_2n_4 + A_{54}n_5 - R_{45} + R_{54} \qquad (40)$$

$$\dot{n}_5 = +k_{52}n_5n_1 - k_{25}n_2n_4 - A_{54}n_5 - R_{54} + R_{45} \qquad (41)$$

$$\dot{\Phi}_1 = +R_{54} - R_{45} + \omega_{el}n_5 - \gamma\Phi_l \qquad (42)$$

The terms in these equations describe the various pump, energy transfer, relaxation and emission processes shown in Figure 3. The definitions of the symbols used are as follows:

n_i: population density of the ith level

R_{ij}: stimulated radiative transition term

W_{ij}: non-radiative multiphonon decay rate for a transition between levels i and j

τ_i: radiative lifetime of the ith level

A_{ij}: radiative decay rate for a transition between levels i and j
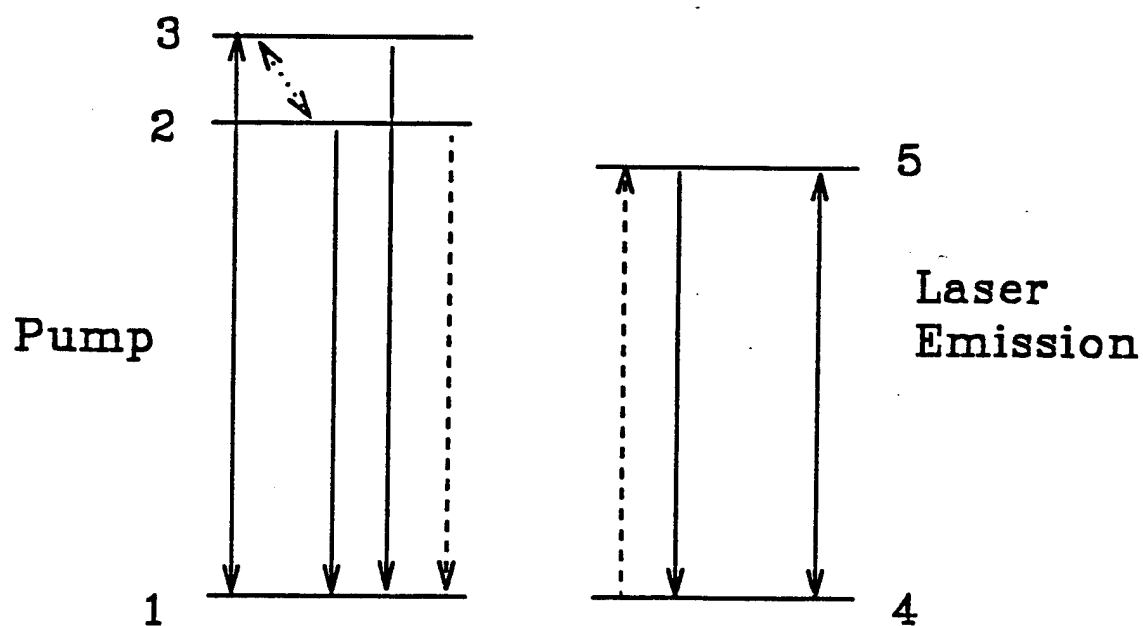
Figure 3. Example of Multi-level System. Solid Lines Represent Radiative Transitions, Dotted Line Represents Multiphonon Relaxation, and Dashed Lines Represent Energy Transfer.

k_{ij}: rate constant for a cross relaxation process in which energy is transferred from level i to level j

γ: cavity decay rate at the output wavelength of the laser

ω: factor describing spontaneous decay into the cavity at the laser wavelength

Φ_l: flux at the laser wavelength.

Each of the terms in the rate equations consists of a rate multiplying a population density or rate parameters multiplying population densities. For spontaneous radiative decay, the term consists of the decay rate, the Einstein A coefficient for the transition (the A_{ij}) or τ_i^{-1} the total radiative decay rate, and the population density of the upper level. Non-radiative multiphonon transitions are treated similarly, using the non-radiative decay rate and the population density of the level in which the transition originates. Note that these equations allow for upward non-radiative transitions along with non-radiative decay. The relation between these rates is given by the Boltzman equation

$$W_{ji} = W_{ij} \exp\left(-\frac{\Delta E_g}{kT}\right). \tag{43}$$

The terms describing the non-radiative ion-ion energy transfer processes depend on two population densities, those of the initial levels in which the two ions are found, and on a rate parameter, k_{lm}, giving the strength of the interaction. The l and the m designate one of the original levels and one of the final levels, respectively. Terms describing the stimulated radiative transitions, R_{ij}, can be written in many different forms. One common form is $R_{ij} = \Phi_r \sigma_{ij} n_i$ where Φ_r is the flux at the resonant wavelength and σ_{ij} is the cross section for the transition. Further discussion of stimulated transitions will be considered in Chapter III.

Often, the rate parameters can be determined from spectroscopic measurements. Absorption and emission spectra can be used to determine the cross sections for stimulated radiative transitions. The total radiative lifetime can be directly found experimentally or can be predicted by a Judd-Ofelt analysis of the absorption spectra, which also gives the radiative decay rates for individual transitions.

Multiphonon rates can be found using the energy gap law or from the difference between the predicted and experimentally measured lifetimes. The rate parameters for the ion-ion energy transfer processes, although in general more difficult to determine, can be found for specific cases from spectroscopic measurements. One of the major difficulties in determining these parameters is that the connection between the microscopic energy transfer models and the rate parameters in the rate equation models is not well understood. The random nature of the distribution of ions in the host material makes the calculation of transfer parameters from microscopic parameters impossible in the general case. If the energy transfer parameters and the other parameters used in the above rate equation model are known, however, the equations can be solved and the population and laser dynamics can be determined. Determining the important processes in the system and finding the parameters describing them is an important step in understanding rare-earth ion based laser systems.

SECTION II

SPECTROSCOPIC AND LASING PROPERTIES
OF Tm,Ho:YAG

Introduction

In a recent publication [45] the lasing properties of $Y_3Al_5O_{12}$:Tm,Ho excited by an alexandrite laser were reported. Several interesting effects were observed. First, a notable (60- 200 μs) time delay was observed between the end of the pump pulse and the onset of laser emission. This delay was found to shorten as the pump intensity was increased. In addition, under these excitation conditions, fluorescence emission in the 530-565 nm spectral region was observed. The intensity of this emission was found to be dependent upon the excitation wavelength. Since this emission occurs at an energy higher than that of the pump photons it was concluded that it arose from either a sequential multiple photon absorption process or an ion-ion interaction process.

Although a significant amount of research has been done on this crystalline laser system [46–50], there are still many important questions about its optical and lasing properties that remain unanswered. Figure 4 shows the general processes involved in the optical pumping of Tm-Ho lasers. Specific values have not yet been determined for all of the physical parameters governing the optical pumping dynamics of the system. Many of the values reported for the spectral parameters have been determined using flashlamp pumping in crystals containing additional dopants such as Cr^{3+} ions.[49,51,52] Significant discrepancies exist in the literature for values of the lifetimes and rise times of various spectral features.[49–57] Computer modeling of laser operation has been accomplished only by using rough

estimates of the values of the rate parameters or by treating them as fitting parameters.[54,58]

The purpose of the work described here is to determine the values of the fundamental physical parameters necessary for a computer simulation of a Tm-Ho laser system that can accurately predict the temporal properties of the laser emission. To accomplish this, results of a spectroscopic study of the dynamics of optically pumped Tm,Ho:YAG are presented. A rate equation model of this system is used to establish values for the rate parameters governing two of the important ion-ion interaction processes. These parameters are then used in a computer model simulating an alexandrite laser pumped Tm,Ho:YAG laser system. Since the rate parameters are established from the spectroscopic data, the computer simulation has no adjustable parameters. The results of this simulation are shown to be consistent with the experimental results found previously for this system.[45]

Model

In order to understand and explain the optical dynamics of Tm-Ho doped laser materials, a model must be developed that includes several types of radiative and nonradiative transitions among the various energy levels of the two trivalent rare earth ions. Figure 4 shows the model generally used to describe diode laser pumped operation of these systems[48,49] and Figure 5 shows more complete energy level diagrams for the Tm^{3+} and Ho^{3+} ions. In a diode laser pumped Tm,Ho:YAG laser the pump laser directly excites the $^3H_4$ multiplet of Tm^{3+}. After this excitation, a number of different processes occur eventually resulting in energy being stored in the $^5I_7$ state of Ho^{3+}. These processes are as follows. The energy difference between the excited states of Tm^{3+} is such that an energy resonance occurs between the $^3H_4 \rightarrow ^3F_4$ and $^3H_6 \rightarrow ^3F_4$ transitions. Thus a cross relaxation process involving these transitions can occur producing two Tm^{3+} ions in the $^3F_4$ metastable state for every ion initially excited by the pump laser. Alternately, energy migration may occur in the $^3H_4$ state followed by this cross relaxation process. After the $^3F_4$ level is populated, fast energy migration among Tm^{3+} ions in
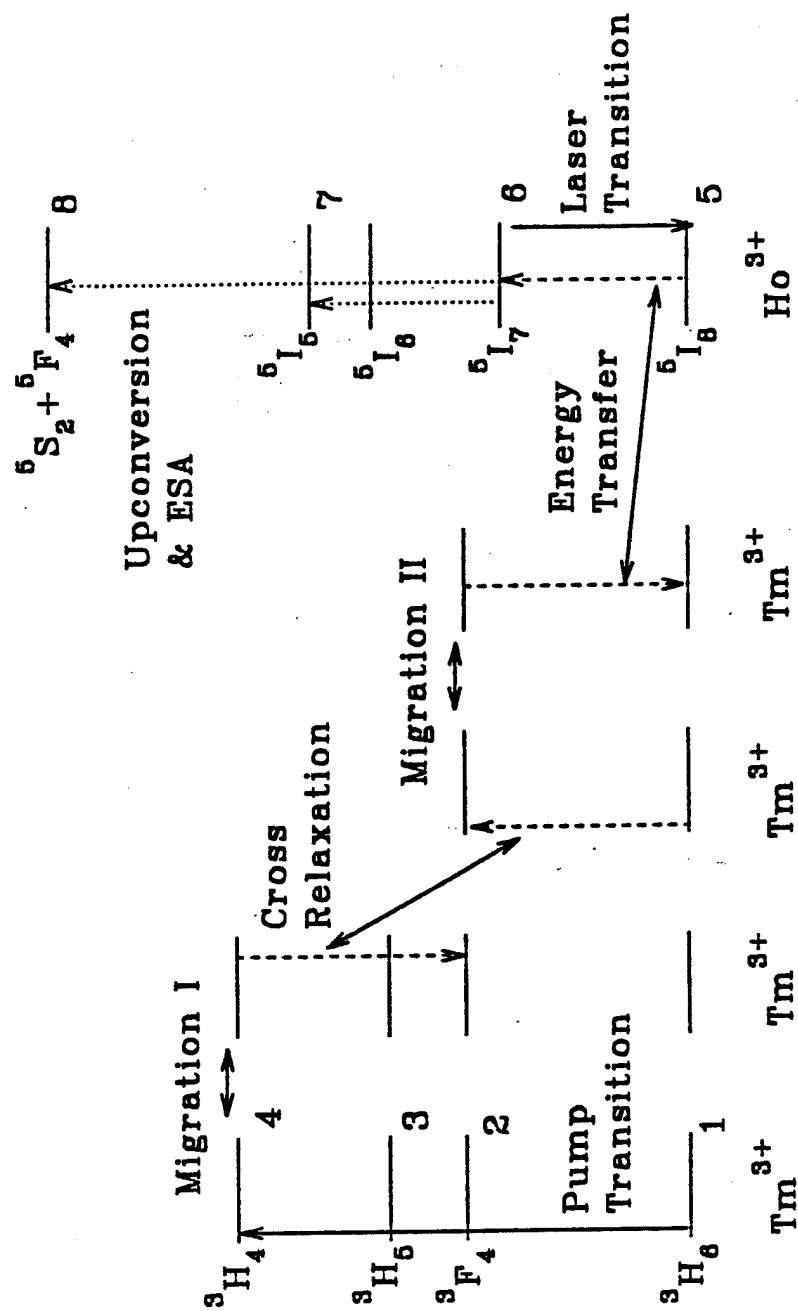
Figure 4. Energy Level Model of Diode Laser Pumped Tm,Ho:YAG Laser Systems.

the metastable state can occur. The details of this process have been described recently.[59,60] Whether energy migration among Tm^{3+} ions occurs both before and after cross relaxation is presently unclear and will be investigated here. Eventually the energy is transferred to a Ho^{3+} ion via a $^3F_4 \rightarrow ^3H_6$, $^5I_8 \rightarrow ^5I_7$ cross relaxation process. The $^5I_7$ multiplet is the Ho^{3+} metastable state and the initial laser level for the 2.09 μm emission seen in these systems.

Additional levels involved in transitions resulting in various loss mechanisms are also shown in Figure 4. One of these, involving the $^5F_4$ and $^5S_2$ multiplets, is often cited to explain the origin of the green emission that is often observed. In this case, an additional cross relaxation process involving the terminal level of the pumping transition and the Ho^{3+} metastable state is considered.[50] A second process that may populate the $^5F_4$ and $^5S_2$ multiplets to produce the green emission is absorption of pump photons by ions in the Ho^{3+} metastable state. The $^5I_5$ and $^5I_6$ multiplets of Ho^{3+} are involved in another possible loss mechanism. This is an upconversion process involving the metastable states of both the Tm^{3+} and Ho^{3+} ions which populates the $^5I_5$ level of Ho^{3+}. Ions excited to the $^5I_5$ multiplet relax rapidly to the $^5I_6$ multiplet followed by energy transfer to the $^3H_5$ multiplet of Tm^{3+}. This transfer process is considered to be instantaneous in the model described below and further discussion of this assumption is given later. In the equations describing the transitions involved in this model, the levels are numbered as follows: i=1 is $^3H_6$, i=2 is $^3F_4$, i=3 is $^3H_5$, i=4 is $^3H_4$, i=5 is $^5I_8$, i=6 is $^5I_7$, i=7 is $^5I_5$, and i=8 is $^5S_2$ and $^5F_5$.

The model outlined above can be mathematically described by a series of rate equations. These equations are:

$$\dot{n}_1 = -R_{14} + R_{41} - k_{42}n_4n_1 - k_{62}n_6n_1 + k_{26}n_5n_2$$
$$+ k_{48}n_4n_6 + k_{27}n_2n_6 - n_7\tau_7^{-1} + n_2\tau_2^{-1} + A_{41}n_4 - A_{31}n_3 \tag{44}$$

$$\dot{n}_2 = 2k_{42}n_4n_1 + k_{62}n_6n_1 - k_{26}n_5n_2 - k_{27}n_2n_6$$
$$- n_2\tau_2^{-1} + A_{42}n_4 + A_{32}n_3 + W_{32}n_3 \tag{45}$$
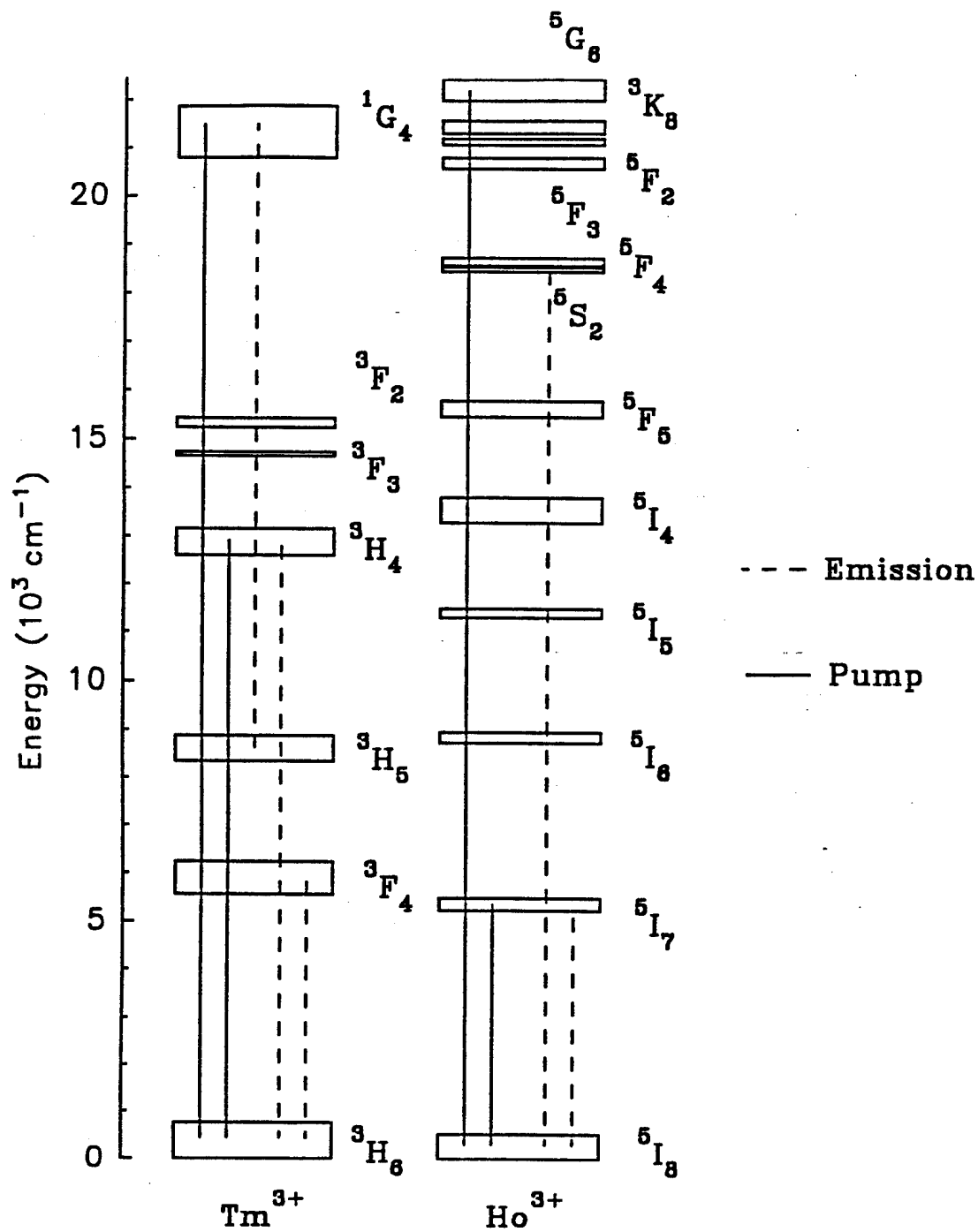
Figure 5. Energy Level Diagram of Tm^{3+} and Ho^{3+} in YAG. Pump Transitions are Designated by Solid Lines and Important Emission Transitions are Designated by Dashed Lines.

$$\dot{n}_3 = +n_7\tau_7^{-1} - n_3\tau_3^{-1} + A_{43}n_4 + W_{43}n_4 - W_{32}n_3 \tag{46}$$

$$\dot{n}_4 = +R_{14} - R_{41} + k_{42}n_4n_1 - k_{48}n_4n_6 - n_4\tau_4^{-1} - W_{43}n_4 \tag{47}$$

$$\dot{n}_5 = +R_{65} - R_{56} + k_{62}n_6n_1 - k_{26}n_5n_2 + n_6\tau_6^{-1} + n_7\tau_7^{-1} + n_8\tau_8^{-1} \tag{48}$$

$$\dot{n}_6 = -R_{65} + R_{56} + R_{86} - R_{68} - k_{62}n_6n_1 + k_{26}n_5n_2$$
$$-k_{48}n_4n_6 - k_{27}n_2n_6 - n_6\tau_6^{-1} \tag{49}$$

$$\dot{n}_7 = +k_{27}n_2n_6 - n_7\tau_7^{-1} \tag{50}$$

$$\dot{n}_8 = +k_{48}n_4n_6 - n_8\tau_8^{-1} \tag{51}$$

$$\dot{n}_p = +R_{65} - R_{56} - n_p\tau_c^{-1} + n_6\omega_{el} \tag{52}$$

The terms in these equations describe the various pump, energy transfer, relaxation, and emission processes shown in Figure 4. The definitions of the symbols used are the same as those defined in Chapter I. The density of lasing photons, n_p, is used rather than the flux at the laser wavelength and τ_c is the cavity lifetime. Additionally, ω_{el} is given by

$$\omega_{el} = \sigma_{65}c\frac{l}{l_c}. \tag{53}$$

Here σ_{65} is the stimulated emission cross section for the laser transition, c is the speed of light, l is the sample length, and l_c is the cavity length. This factor describes the stimulated emission due to one photon/cm^3 and is used to seed the cavity equation.

The terms involving stimulated emission and absorption must be examined in more detail to obtain the required expressions for the transition rates and cross

sections. Optical transitions of rare earth ions in crystals occur between the crystal field split Stark components of different multiplets. In many cases there are several transitions between different combinations of Stark levels that are within the frequency resolution of the experiment and thus can not be resolved spectroscopically. Therefore the experimentally measured spectral properties are the result of the sum of all of the possible transitions at the particular frequency of interest weighted by population and degeneracy factors. The population density rate of change due to absorption involving one of these transitions between a specific pair of Stark levels can be written as

$$R_{lu} = \Phi(\nu)\sigma_{lu}(\nu)n_l d_u \tag{54}$$

where $\Phi(\nu)$ is the photon flux at frequency ν, $\sigma_{lu}(\nu)$ is the absorption cross section for the transition between the two Stark components, n_l is the population in the lth Stark component of the lower multiplet, and d_u is the degeneracy of the upper state. The total population density rate of change at a given frequency is the sum over all Stark component transitions at that frequency

$$R_a(\nu) = \sum_{lu} \Phi(\nu)\sigma_{lu}(\nu)n_l d_u. \tag{55}$$

Note that the lineshape for the transition is contained within the cross sections for the transitions between the individual Stark components. Although the sum is carried out over all the Stark components of both the upper and lower multiplets, only those transitions with $\sigma_{lu}(\nu) \neq 0$ make an effective contribution.

The absorption cross section at frequency ν is given by[61]

$$\sigma_{abs}(\nu) = (1/Z_l) \sum_{lu} d_l \exp\left(-E_l/k_B T\right) \sigma_{lu}(\nu) d_u \tag{56}$$

where E_l is the energy of the lth Stark component (measured with respect to the lowest Stark component in the multiplet), k is the Boltzmann constant, T is temperature, d_l is the degeneracy of the lth Stark component, and Z_l is the

partition function for the lower multiplet. The partition function for a multiplet is given by

$$Z = \sum_m d_m \exp\left(-E_m/k_B T\right) \tag{57}$$

where the individual Stark components are indexed by m and the energy is measured with respect to the lowest Stark component of the multiplet. The absorption cross section can be written in terms of the Boltzmann factor, $f_l = d_l exp(-E_l/k_B T)/Z_l$, as

$$\sigma_{abs}(\nu) = \sum_{lu} f_l \sigma_{lu}(\nu) d_u. \tag{58}$$

Using $n_l = f_l n_{tl}$ where n_{tl} is the total population of the lower multiplet, Equation (55) can be written as

$$R_a(\nu) = \Phi(\nu)\sigma_{abs}(\nu)n_{tl}. \tag{59}$$

The population density rate of change for stimulated emission can be written as

$$R_e(\nu) = \Phi(\nu)\sigma_{emi}(\nu)n_{tu} \tag{60}$$

where n_{tu} is the total upper multiplet population. The relationship between $\sigma_{abs}(\nu)$ and $\sigma_{emi}(\nu)$ is

$$\sigma_{emi}(\nu) = \frac{Z_l}{Z_u}\exp\left(\frac{E_{ZL}-h\nu}{k_B T}\right)\sigma_{abs}(\nu) \tag{61}$$

where Z_u is the partition function of the upper multiplet defined as in Equation (57), E_{ZL} is the separation between the lowest Stark components of the upper and lower multiplets, and h is Planck's constant.

In situations where the transitions between different pairs of Stark components are well separated the summation in Equation (55) reduce to a single term. The cross section for the transition is then found by dividing the absorption coefficient by the population in the lower Stark component. For this situation Equation (54) is used to describe the effects of optically stimulated transitions in the rate

equations. However, for Tm,Ho:YAG, there are numerous closely spaced Stark components for the transitions of interest [62,63] and the more complicated expressions for R_{ij} and $\sigma(\nu)$ must be used.(Equation (59),(60), and (61))

Using spectroscopic data and the expressions derived above, quantitative values can be determined for the stimulated radiative transition rates appearing in the rate equations. Specifically, for the 1→4 and 4→1 transitions of Tm^{3+} in YAG as shown in Figure 4, there are a number of transitions occurring at nearly the same (or in fact identical) frequencies. The individual Stark component to Stark component transition cross sections cannot be determined and the terms appearing in the rate equations for R_{14} and R_{41} are given by Equations (59) and (60). The absorption cross section used in determining values for these rates is found by dividing the absorption coefficient by the total ground state population of Tm^{3+} ions. This cross section is a weighted sum of the individual Stark component transition cross sections (the σ_{lu}'s) and the weighting factors are the Boltzmann factors. The stimulated emission cross section can be found from Equation (60) using the measured absorption coefficient with Z_l and Z_u determined from the data in Refs. [62] and [63] and Equation (57).

Similarly, it is possible to determine values for the stimulated radiative transitions between levels 5 and 6 of Ho^{3+}. Since this is the laser transition the photon density at the laser frequency $n_p(\nu_L)$, rather than photon flux at the frequency of the transition $\Phi_L(\nu_L)$ is used. These two quantities are related through the expression

$$n_p = \Phi_L(\nu_L)/c \tag{62}$$

The parameters R_{56} and R_{65} are given by

$$R_{56} = n_p\omega_{el}Bn_5 \tag{63}$$

and

$$R_{65} = n_p\omega_{el}n_6 \tag{64}$$

where B is a factor given by $B = \sigma_{56}/\sigma_{65}$. Since there are numerous Stark level to Stark level transitions in this spectral range Equation (61) must be used to determine the emission cross section from the measured absorption cross section.

Table I lists the cross sections determined from the procedures outlined above and other cavity parameters used in the rate equations for the computer simulations described later. Other known parameters needed for the rate equation model such as relaxation times and transition branching ratios for this system are listed in Table II. The major unknown parameters required for solving the rate equations (excluding the loss mechanisms) are the ion-ion interaction rates describing the Tm-Tm and Tm-Ho cross relaxation process. These parameters are determined from analysis of the visible and near infra-red spectral properties as described below.

Experiment

A nitrogen laser pumped dye laser was used to excite the samples either via the Ho^{3+} absorption line at 453.8 nm or the Tm^{3+} absorption lines at 459.1 and 780.0 nm. The pump beam had less than a 10 ns pulse duration and less than a 0.1 nm spectral bandwidth. This source was used for most of the spectral dynamics studies. An alexandrite laser tunable from 700-800 nm with a 60 μs pulse train consisting of numerous 300 ns long pulses was used for laser pumping and for some spectra measurements. Since this source directly excited the $^3H_4$ multiplet of Tm^{3+}, comparison of the resulting emission spectra to that obtained from the higher energy dye laser excitation was useful in determining whether additional emission lines in the regions of interest were produced by the higher energy excitation. A third excitation source, a Cr,Tm,Ho:YAG laser was used in conjunction with the alexandrite laser to study the origin of the green emission previously reported.

Three different samples were used in this study. The first sample, Tm(6.0%), Ho(0.5%):YAG, was cut from the same boule as the sample used for the investigation of laser properties in Ref.[45]. A second sample, Tm(10.0%):YAG, was used

TABLE I

PARAMETERS USED IN RATE EQUATION MODEL
FOR Tm,Ho:YAG LASER SIMULATIONS

Pump Cross Sections

$$\sigma_{14} = 5.2 \times 10^{-21} cm^2$$

$$\sigma_{41} = 2.8 \times 10^{-21} cm^2$$

Cavity Parameters

$$\tau_c = 33ns$$

$$\omega_{el} = 9.06 \times 10^{-12} cm^3/s$$

Laser Emission Cross Section

$$\sigma_{65} = 1.4 \times 10^{-20} cm^2$$

$$B = 0.159$$

TABLE II

PARAMETERS USED IN Tm,Ho:YAG RATE EQUATION MODEL

Radiative Decay Rates

$$A_{41} = 578s^{-1} \text{ [a]}$$
$$A_{42} = 80s^{-1} \text{ [a]}$$
$$A_{43} = 31s^{-1} \text{ [a]}$$
$$A_{31} = 299s^{-1} \text{ [a]}$$
$$A_{32} = 5s^{-1} \text{ [a]}$$
$$A_{21} = 110s^{-1} \text{ [a]}$$
$$A_{65} = 150s^{-1} \text{ [b]}$$

Non-Radiative Decay Rates

$$W_{43} = 580s^{-1} \text{ [a]}$$
$$W_{32} = 7.7 \times 10^4 s^{-1} \text{ [a]}$$
$$W_{21} = 5.9s^{-1} \text{ [a]}$$

Effective Decay Times

$$\tau_8 = 4.7\mu s \text{ [c]}$$
$$\tau_7 = 16.1\mu s \text{ [d]}$$

a Ref. [64].
b Ref. [52].
c Ref. [65].
d Calculated From data in Refs. [63,64].

to determine spectral properties of Tm^{3+} ions in YAG. Similarly the third sample, Ho(0.5%):YAG, was used to determine spectral properties of the Ho^{3+} ions and to investigate the origin of the green emission observed with alexandrite laser pumping.

Emission from the samples was focused into one of two spectrometers and monitored with various detectors depending on the emission wavelength. For obtaining much of the visible emission spectra, a Spex 0.85 m double spectrometer coupled to a Hammamatsu R943-02 photomultiplier tube was used. A Spex 0.22 m spectrometer with a 500 nm blazed grating and a Hammamatsu R446 photomultiplier were used for detecting some of the visible spectra. This spectrometer with a 2.0 μm blazed grating and an InSb detector were used for monitoring all of the near infra-red spectra.

For all spectral measurements, the signal from the detector was averaged using an EG&G series 4400 boxcar averager. The gate delay of the boxcar was varied to observe emission spectra at different times after the excitation pulse. The output was digitized and stored on the spectrometer control computer. For the fluorescence rise time and decay time measurements the signals were either averaged using the boxcar averager or were averaged using a Tektronix 2440 digital oscilloscope. In all cases the data were down-loaded for analysis on an IBM-compatible personal computer.

Results

The first problem is to correlate important spectral features with specific transitions of the Tm^{3+} and Ho^{3+} ions. Figures 6(a) and 6(b) show the emission spectra in the 725-850 nm region for Tm,Ho:YAG after Tm^{3+} (459.1 nm) and Ho^{3+} (453.8 nm) excitation, respectively. The presence of only weak Ho^{3+} emission in the 740-775 nm region under Tm^{3+} excitation indicates little energy transfer occurs between the upper states of the ions. The emission in the 780-850 nm region is due only to Tm^{3+}.
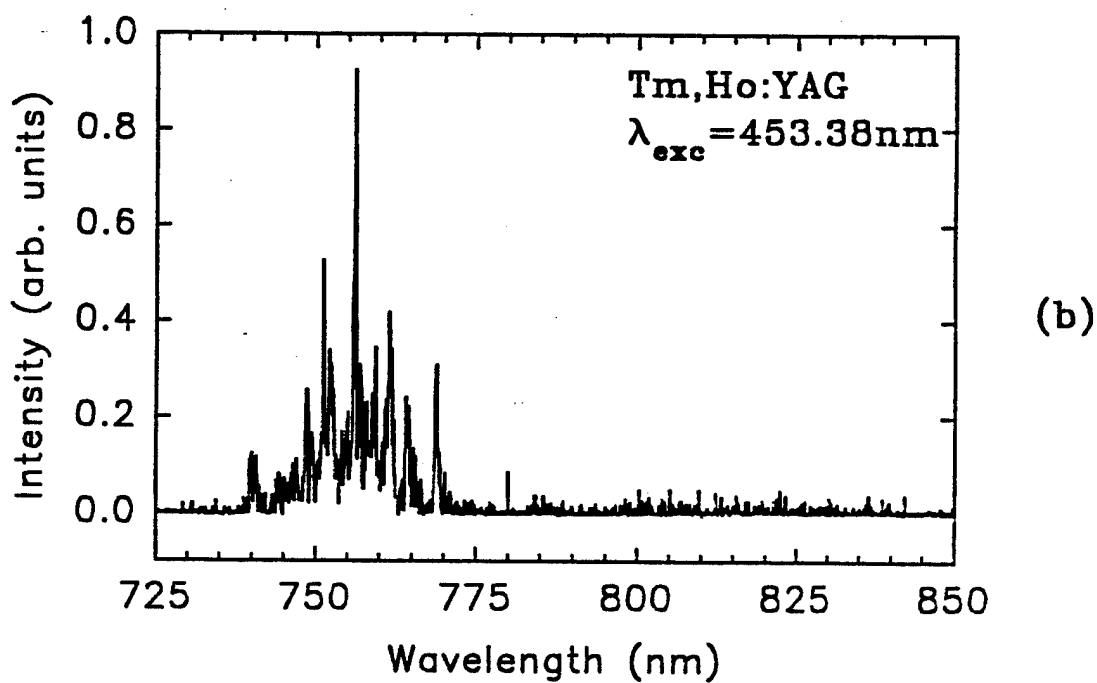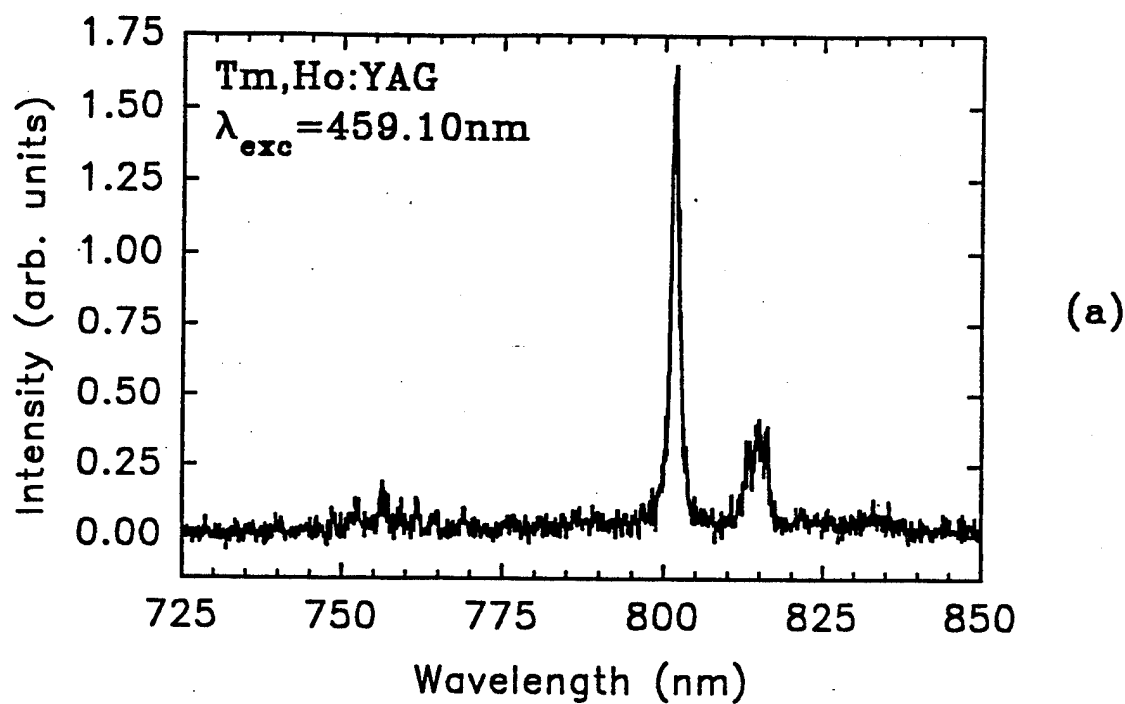
Figure 6. Emission Spectra of Tm,Ho:YAG 725-850 nm. Excitation at (a) 459.10 nm and (b) 453.38 nm.

The observed differences between the emission spectra under different excitation conditions are used to establish the Tm^{3+} transitions responsible for the emission in the 770-850 nm spectral range. Figures 7(a) and 7(b) show these spectra. Figure 7(a) shows Tm,Ho:YAG emission spectrum after 765 nm excitation using the alexandrite laser while Figure 7(b) shows the Tm:YAG spectrum under 459.1 nm excitation. Since there is no significant Ho^{3+} emission in this region (Figure 6(b)), the emission present in Figure 6(a) and not present in Figure 7(a) must be due to transitions in Tm^{3+} originating from levels higher in energy than $^3H_4$, such as the $^1G_4$ level which is the terminal state of the 459.1 nm absorption transition. Thus the strong lines observed at 801.7 nm and between 810-815 nm, visible under 459.1 nm excitation but not observed under 765 nm excitation, are not due to emission from the $^3H_4$ multiplet.

Although the concentration dependence of the $^3H_4$ fluorescence lifetime has been studied previously [55], discrepancies in literature values and differences in sample concentration require the direct measurement of this lifetime in our sample.[50,52,54] The results of fluorescence lifetime measurements in the 800 nm spectral region are consistent with the conclusions stated above. The measured fluorescence lifetimes in this region are as follows: at 801.7 nm a double exponential decay is observed with time constants of 1.6 and 11.5 μs. The lifetime at 822 nm, that of the $^3H_4$ multiplet of Tm^{3+}, is found to be 11.5 μs. The shorter 1.6 μs lifetime measured at 801.7 nm is attributed to a transition originating on the $^1G_4$ multiplet that happens to overlap the $^3H_4$ emission. The lifetime of the $^3H_4$ multiplet is a measure of the $^3H_4 \rightarrow ^3F_4$, $^3H_6 \rightarrow ^3F_4$ cross relaxation rate. Figure 8 shows the concentration dependence of the fluorescence quantum efficiency of the $^3H_4$ multiplet. The fluorescence quantum efficiency of emission from $^3H_4$ can be determined from

$$\eta = A_r/A_m \qquad (65)$$

where A_r is the predicted radiative relaxation rate and A_m is the measured radiative rate. The predicted radiative lifetime is 790 μs [64] giving a predicted rate of 1270 s^{-1} . The data represent a combination of the results obtained here and those
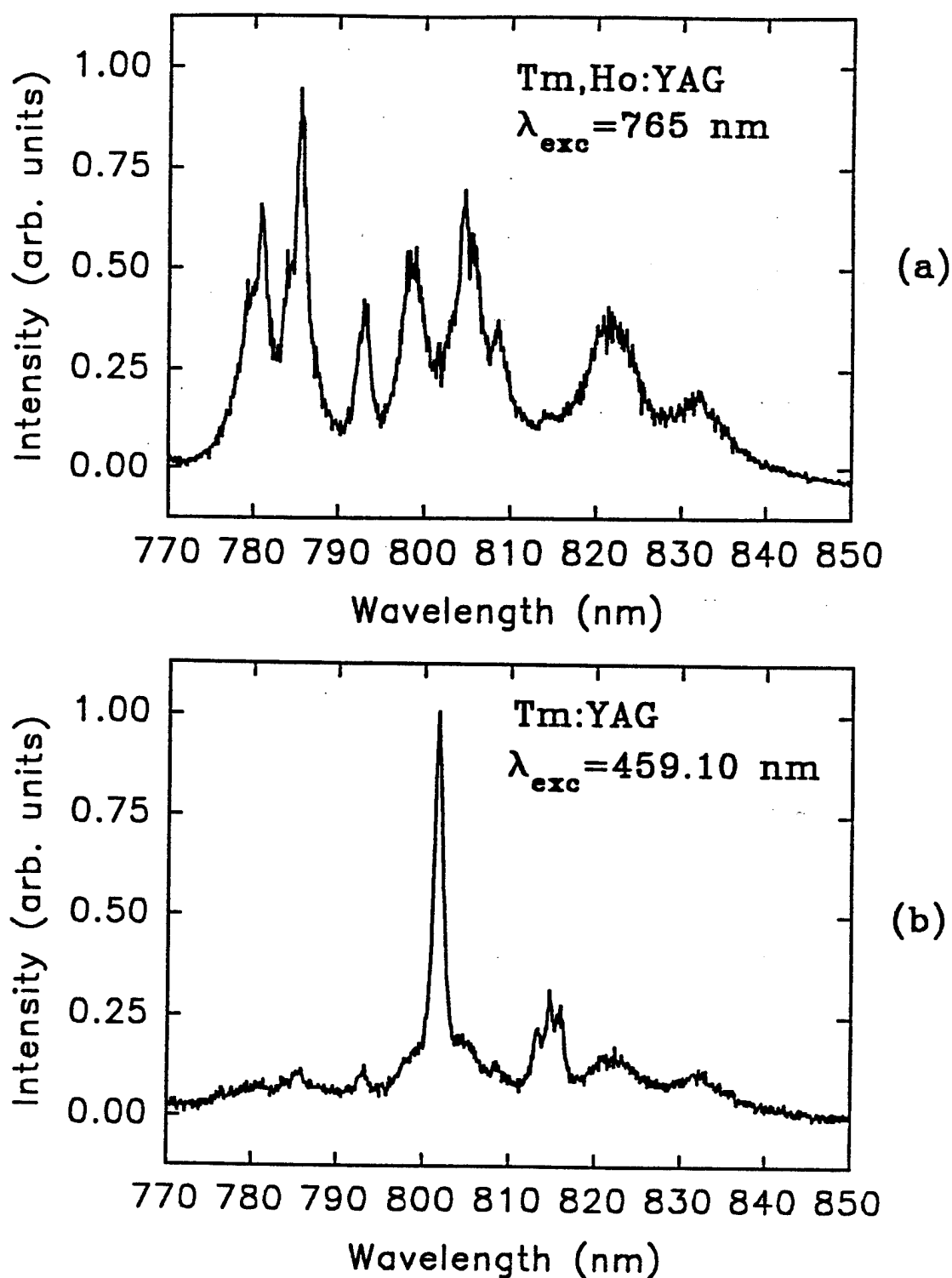
Figure 7. Emission Spectra of Tm,Ho:YAG and Tm:YAG 770-850 nm. (a) Tm,Ho:YAG with excitation at 765 nm and (b) Tm:YAG with excitation at 459.1 nm.

of several other research groups. [55,57] The solid and broken lines represent the theoretical predictions described in the following section.

The time evolution of the fluorescence emission in the 1.6-2.2 μm spectral region is needed to determine the interaction rate between the Tm^{3+} and Ho^{3+} ions in their metastable states. Figure 9 shows the emission from Tm,Ho:YAG in the 1.6-2.2 μm region under excitation at 765 nm. The numerous emission bands in this region correspond to emission from the Tm^{3+} $^3F_4$ and Ho^{3+} $^5I_7$ multiplets. Measurement of the fluorescence decays of the peaks at 1.78 μm and 2.09 μm give the values of the fluorescence lifetimes of the $^3F_4$ and $^5I_7$ levels to be 5±1 ms and 7±1 ms, respectively.

The different dynamic behavior of the various emission bands in this region is clearly shown by the results of the time resolved spectroscopic measurements. Figure 10 shows a series of spectra from a Tm,Ho:YAG sample in the 1.5-2.2 μm spectral region taken at various time delays after excitation at 459.1 nm. At short times after the excitation, the emission spectrum is broad and relatively featureless. At successively longer delays, the emission spectrum changes significantly and additional lines at 1.88, 1.93, 2.02 and 2.09 μm become significant. The broad band of peaks between 1.6-1.9 μm remains essentially unchanged or decays slowly. At very long times (5 and 10 ms) the emission in the whole spectral range shows signs of significant decay.

To identify the origin of each of the bands seen in this region, the emission spectrum of Tm:YAG is needed. Figures 11a and 11b show spectra taken at the same delay time, 300 μs, in Tm:YAG and Tm,Ho:YAG, respectively. The additional peaks at the longer delay times in Figure10 must be associated with Ho^{3+} transitions since they are not present in the Tm:YAG spectrum.

Analysis

Although the concentration dependence of the fluorescence lifetime of the $^3H_4$ multiplet of Tm^{3+} has been studied previously [55,57] further investigation of can help is necessary to determine if energy migration occurs in the $^3H_4$ multiplet.
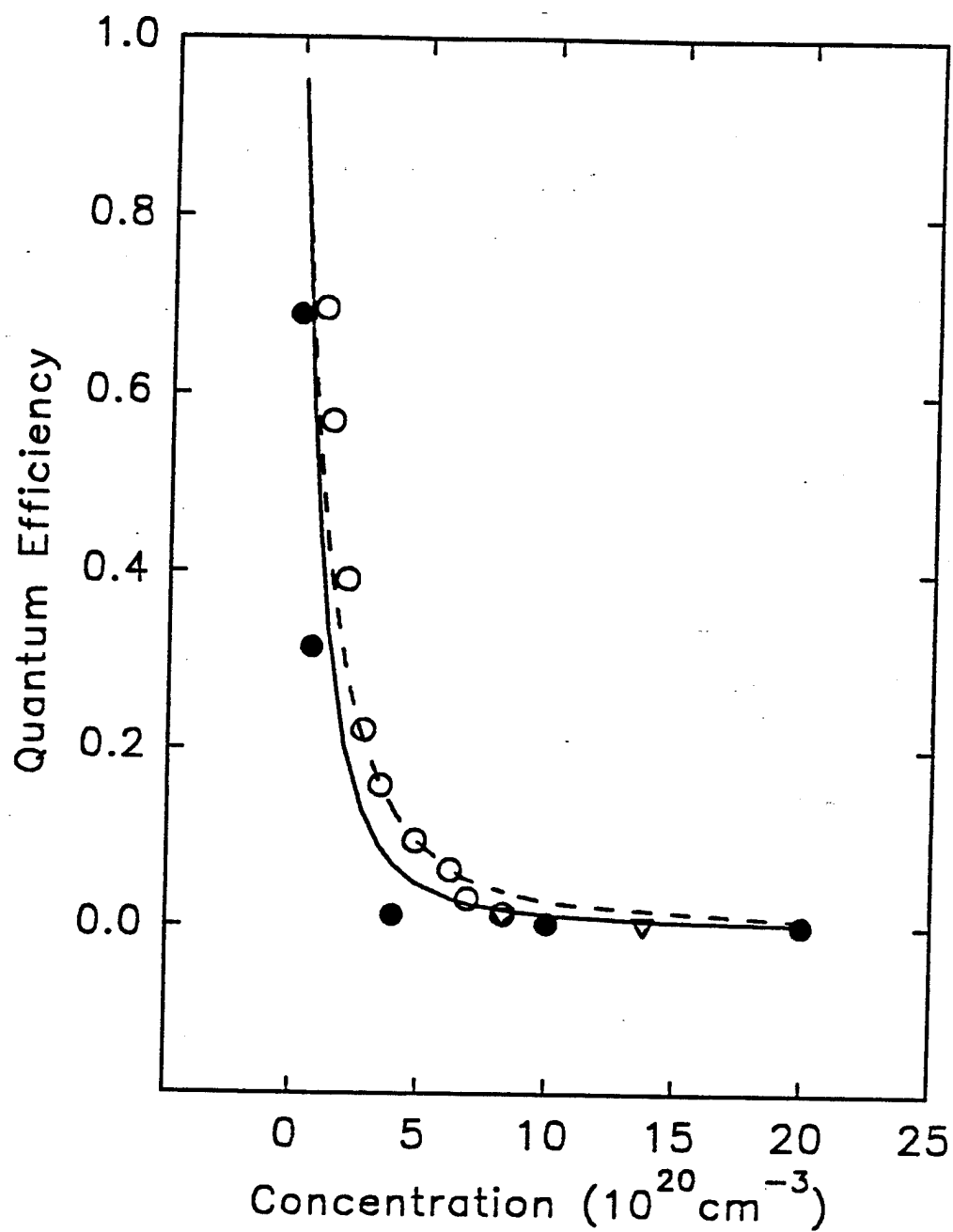
Figure 8. Quantum Efficiency of $^3H_4$ Emission vs Tm^{3+} Concentration.
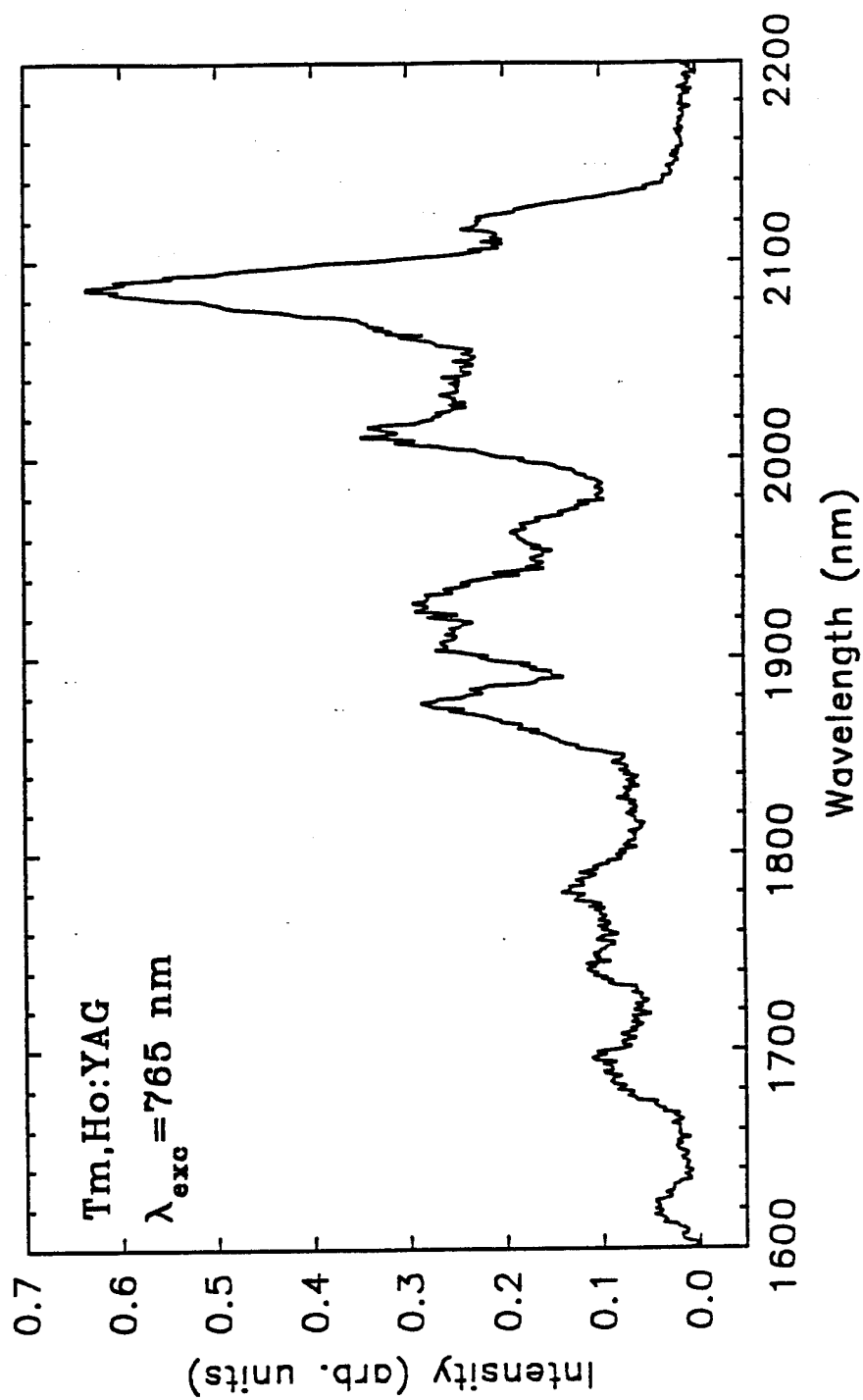
Figure 9. Emission spectrum of Tm,Ho:YAG 1600-2200 nm with excitation at 765 nm.

λ_{exc}=459.10 nm
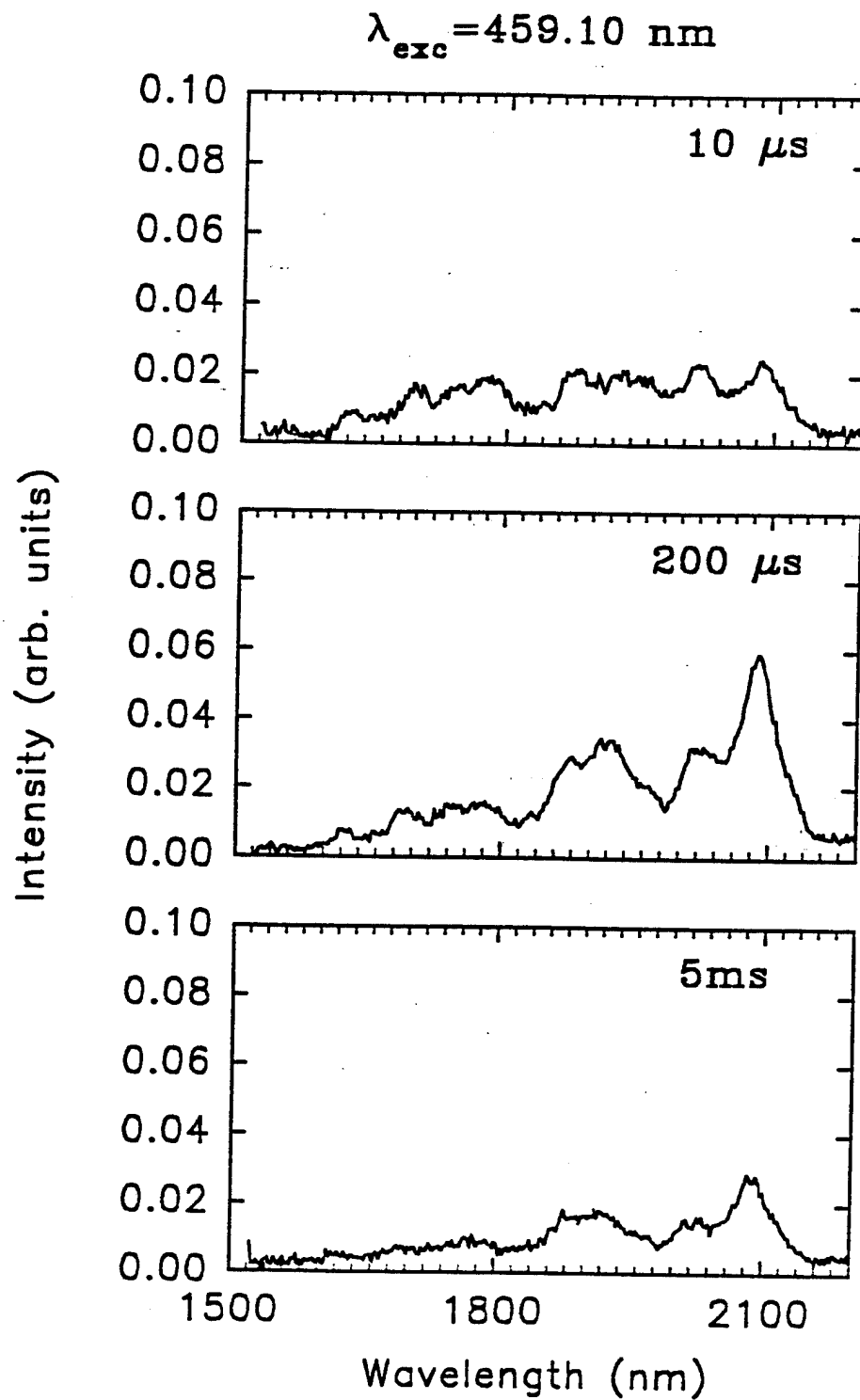
Figure 10. Series of Time-Resolved Spectra of Tm,Ho:YAG.
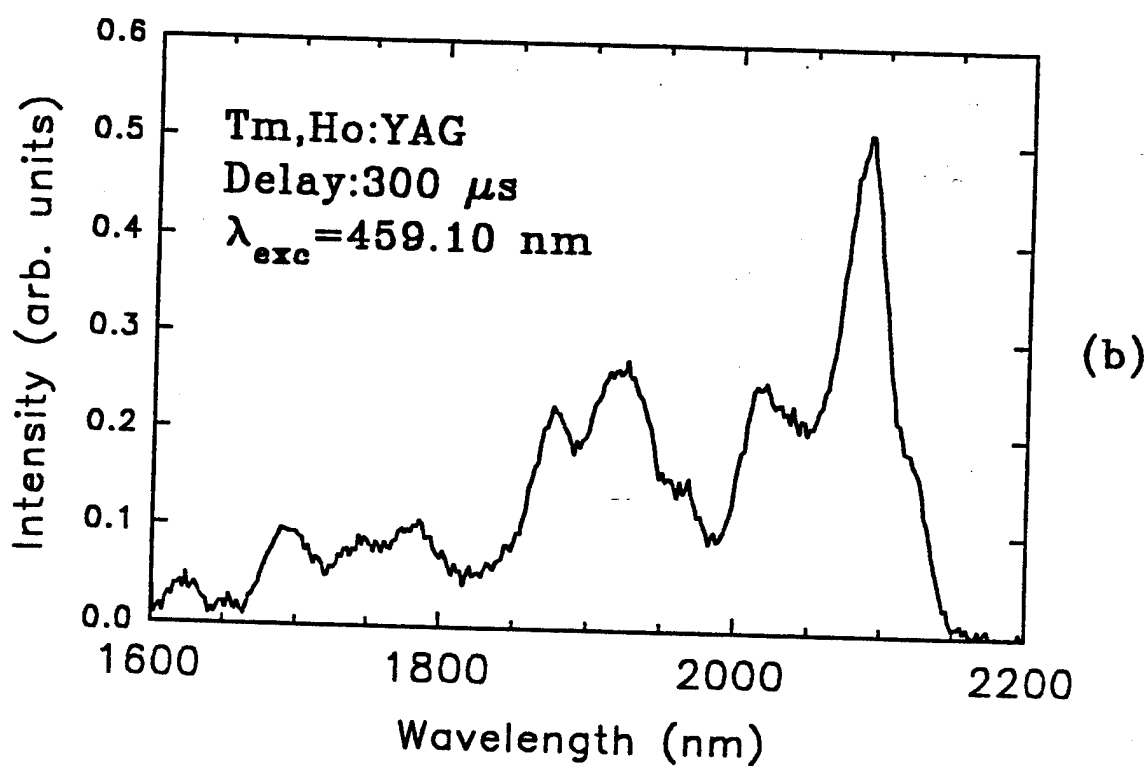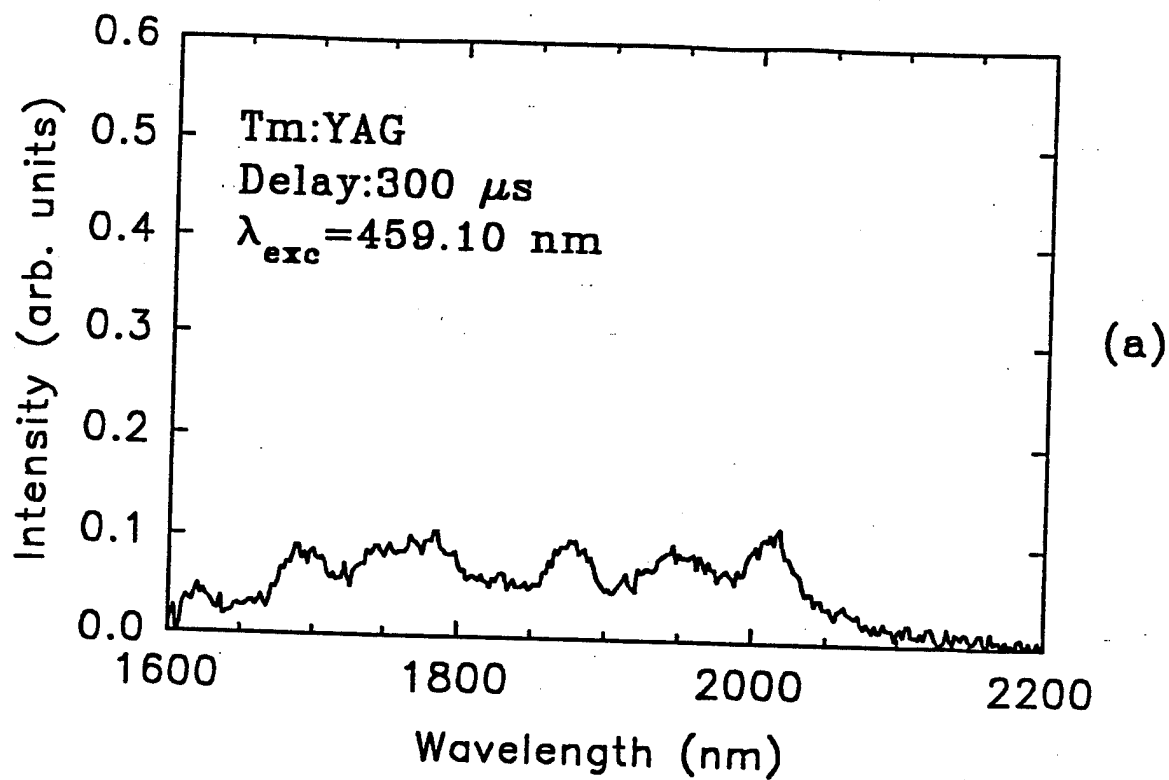
Figure 11. Emission Spectra of Tm:YAG and Tm,Ho:YAG 1600-2200 nm Taken
300 μs After Excitation. (a) Tm:YAG and (b) Tm,Ho:YAG.

The observed concentration quenching is generally attributed to a cross relaxation process in which a Tm^{3+} ion initially in the $^3H_4$ state interacts with a neighboring Tm^{3+} ion initially in the ground state leaving both ions in the $^3F_4$ metastable state. However, a possible additional process for concentration quenching is migration enhanced quenching with energy migration occurring within the $^3H_4$ level and eventual energy loss at a quenching site. The effect of each of these processes is considered here.

Two possible types of ion-ion interactions leading to the quenching of fluorescence from $^3H_4$ are cross relaxation and migration enhanced cross-relaxation mechanisms. The time evolution of the intensity of fluorescence emission from $^3H_4$ can be written as [66]

$$I(t) = I(0)exp[-(A_r t + \gamma t^{1/2} + Wt)] \qquad (66)$$

where $I(0)$ is the initial intensity, γ is a parameter describing the ion-ion cross-relaxation without migration and W is a migration assisted enhancement to the cross-relaxation rate. The parameter γ is of the form described by the Forster-Dexter theory for static disordered decay [28,29]

$$\gamma = (4/3)(\pi)^{3/2} n_{Tm} R_{cr}^3 A_r^{1/2}. \qquad (67)$$

Here R_{cr} is the critical interaction distance between two Tm^{3+} ions for cross-relaxation and n_{Tm} is the concentration of Tm^{3+} ions. The migration enhanced cross-relaxation rate is of the form determined by Burshtein [37]

$$W = \pi(2\pi/3)^{5/2} R_{cr}^3 R_{mig}^3 n_{Tm}^2 A_r \qquad (68)$$

where R_{mig} is the critical interaction distance between Tm^{3+} ions for energy migration. Again it is assumed that electric dipole-dipole interaction is responsible for both the migration and the final cross relaxation quenching step. Equations (67) and (68) above reflect the fact that, for the case of interest here, both the sensitizers and activators are Tm ions.

Following the development in Ref. [66] Equation (66) can be used to obtain an expression for the fluorescence quantum efficiency

$$\eta = [A_r/(A_r + W)][1 - \pi^{1/2}x \exp(x^2)(1 - erf(x)) \tag{69}$$

where

$$x = \gamma/[2(A_r + W)^{1/2}] \tag{70}$$

The only unknown quantities in Equations (67,69) are the critical interaction distances. These critical interaction distances can be determined from spectral overlap data and Equation (32). Figure 12 shows the normalized emission and absorption lineshapes of the $^3H_6 \rightarrow {}^3H_4$ and $^3H_4 \rightarrow {}^3H_6$ transitions. These are the spectra needed to determine a migration rate for the $^3H_4$ migration process. Using the spectra in Figure 12 and Equation (32), R_{mig} is found to be 10.3 Å. The critical interaction distance for cross-relaxation can be found from Ref. [57], adjusted to correspond to our Equation (32), giving $R_{cr} = 6$ Å. Using these values in Equation (69) gives the predicted values for the fluorescence quantum efficiency shown as the solid line in Figure 8. The broken line in Figure 8 is obtained from Equation (69) with $W = 0$ and represents the theoretical prediction for η if the static cross-relaxation process is considered to be the only process responsible for the quenching of the $^3H_4$ level. Both the theoretical curves are obtained with no adjustable parameters.

The differences in the experimental points from different research groups and from the prediction are partly associated with how accurately the Tm^{3+} concentrations in the samples are known. It is not clear from references [55] and [57] how these concentrations are measured. If the results from all the research groups are treated equally the solid line in Figure 8 best agrees with the data. If the quoted concentrations are those in the initial melt used for crystal growth instead of the values measured in the actual sample, they provide a high estimate of the concentration of Tm in the crystal. If this is the case then the solid line will be in much better agreement than the broken line. In either case it appears that some energy migration is taking place in the $^3H_4$ level of Tm^{3+} and this migration enhances the
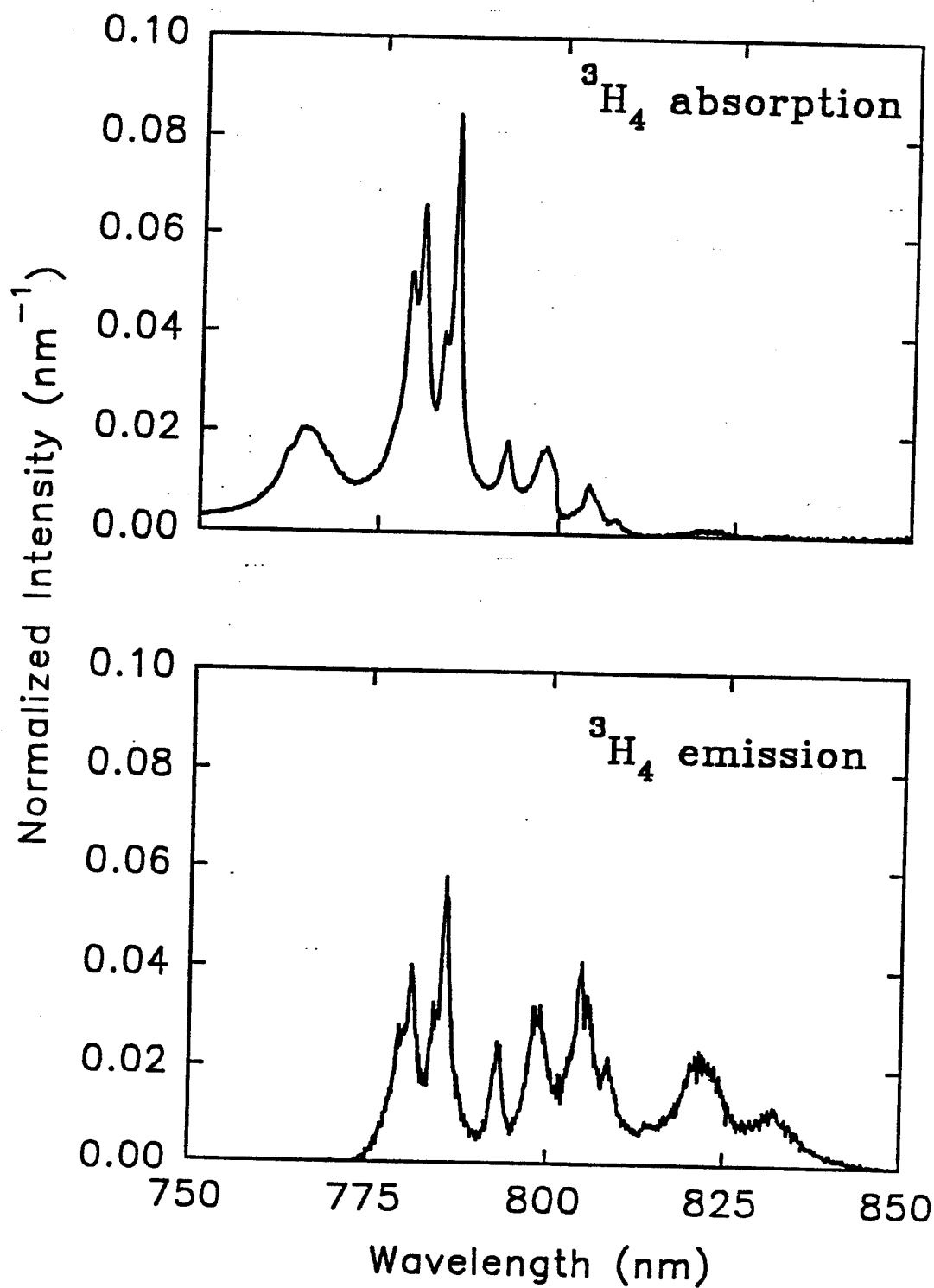
Figure 12. Normalized Absorption and Emission Spectra $^3H_4, ^3H_6$ Transition.

cross-relaxation quenching of the luminescence from this level, especially at high Tm ion concentrations.

The decay dynamics of the fluorescence emission at 822 nm can be used to determine the effective cross relaxation rate parameter for the $^3H_4 \rightarrow {}^3F_4$, $^3H_6 \rightarrow {}^3F_4$ process in the Tm^{3+} ions, k_{42}. At long times after the excitation, the rate equation for the $^3H_4$ multiplet becomes (ignoring the loss mechanisms)

$$\dot{n}_4 = -k_{42}n_4 n_1 - n_4 \tau_4^{-1} - n_4 W_{43}. \tag{71}$$

Solving for $n_4(t)$ yields

$$n_4(t) = \exp(-t/\tau_m) \tag{72}$$

where τ_m is the measured lifetime. In the limit of low excitation intensity then most of the Tm^{3+} population remains in the ground state, i.e. $n_1 \approx N_{Tm}$ and

$$\tau_m^{-1} = k_{42}N_{Tm} + \tau_4^{-1} + W_{43}. \tag{73}$$

The $^3H_4$ multiplet has a predicted lifetime (including radiative and multiphonon decay),[62] of 790 μs. Using this value, our measured lifetime of 11.5 μs and N_{Tm} = 8.3×10^{20} cm^{-3} yields a value for the rate constant k_{42} of 1.0×10^{-16} cm^3/s.

Information about a second energy transfer process, the Tm^{3+} to Ho^{3+} process is obtained from the dynamics of the fluorescence emission in the near infrared spectral region. A relationship between the rate constants describing the forward and reverse energy transfer processes between the $^3F_4(Tm^{3+})$ and $^5I_7(Ho^{3+})$ multiplets can be found. At some time t_{max}, the excited state population $n_6(t)$ reaches a maximum and begins to decay. At this time (ignoring stimulated emission and the loss mechanisms)

$$\dot{n}_6 = -k_{62}n_6 n_1 + k_{26}n_5 n_2 - n_6 \tau_6^{-1} = 0. \tag{74}$$

Solving for k_{26} and using

$$n_1 = N_{Tm} - n_2 - n_4 \tag{75}$$

$$n_5 = N_{Ho} - n_6 \tag{76}$$

yields

$$k_{26} = \frac{n_6}{n_2} \frac{1}{N_{Ho}} \frac{\tau_6^{-1}}{\left(1 - \frac{n_6}{N_{Ho}}\right)} \left[1 + k_{62} N_{Tm} \tau_6 \left(1 - \frac{n_2 + n_4}{N_{Tm}}\right)\right]. \tag{77}$$

At low levels of excitation, $n_6/N_{Ho} = 0$ and $(n_2 + n_4)/N_{Tm} = 0$ so

$$k_{26} = \frac{n_6}{n_2} \frac{\tau_6^{-1}}{N_{Ho}} \left(1 + k_{62} N_{Tm} \tau_6\right). \tag{78}$$

By determining the ratio of the population of n_6 to n_2 at t_{max}, it is possible to relate the two unknown rate constants. Figure 13 shows the 2.09 μm emission peaks $\approx$300 μs after the excitation pulse. Using the spectra taken at 300 μs (Figure11), correcting for detector and grating response, integrating to find the total emission intensity and multiplying by the upper state lifetimes, the relative populations of the two multiplets can be determined. Substituting this value into Equation (78) gives the relationship between the rate constants for forward and backward energy transfer,

$$k_{62} = 0.128 k_{26} - 1.4 \times 10^{-19} cm^3/s. \tag{79}$$

To establish values for the rate constants k_{26} and k_{62} the following rate equations are solved with k_{26} treated as an adjustable parameter and the results fit to the observed spectroscopic data.

$$\dot{n}_1 = -R_{14} + R_{41} - k_{42} n_4 n_1 - k_{62} n_6 n_1 + k_{26} n_5 n_2 \\ + n_2 \tau_2^{-1} + A_{41} n_4 - A_{31} n_3 \tag{80}$$

$$\dot{n}_2 = 2 k_{42} n_4 n_1 + k_{62} n_6 n_1 - k_{26} n_5 n_2 \\ - n_2 \tau_2^{-1} + A_{42} n_4 + A_{32} n_3 + W_{32} n_3 \tag{81}$$
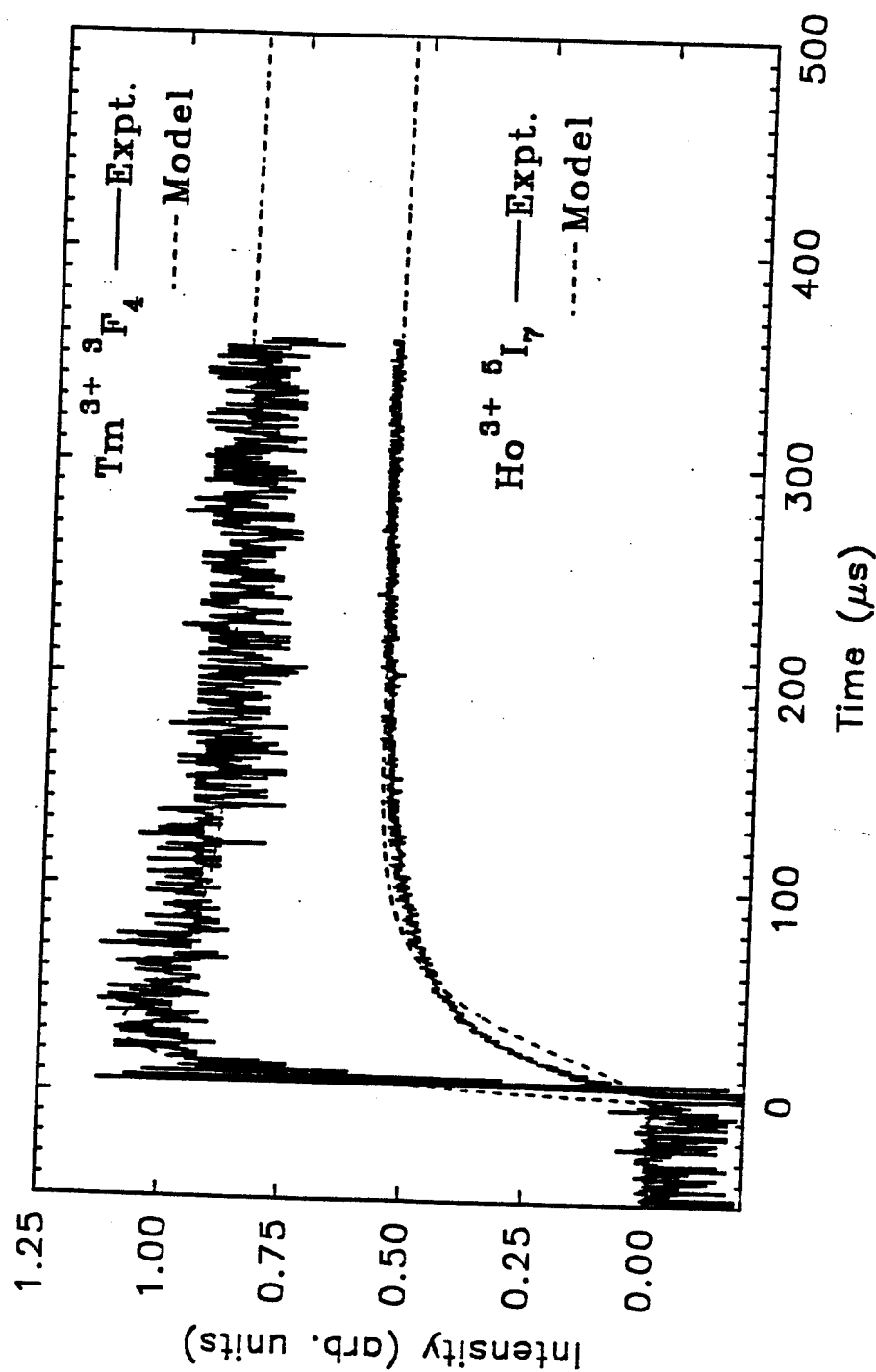
Figure 13. Growth and Decay of Emission in Near Infrared Spectral Region. The Signals are due to Transitions from the Tm^{3+} $^3F_4$ (n_2) and Ho^{3+} $^5I_7(n_5)$ Multiplets. The Solid and Dashed Lines are Numerical Fits Using the Rate Equations Given in the Text.

$$\dot{n}_3 = -n_3\tau_3^{-1} + A_{43}n_4 + W_{43}n_4 - W_{32}n_3 \tag{82}$$

$$\dot{n}_4 = +R_{14} - R_{41} - k_{42}n_4n_1 - n_4\tau_4^{-1} - W_{43}n_4 \tag{83}$$

$$\dot{n}_5 = +k_{62}n_6n_1 - k_{26}n_5n_2 + n_6\tau_6^{-1} \tag{84}$$

$$\dot{n}_6 = -k_{62}n_6n_1 + k_{26}n_5n_2 - n_6\tau_6^{-1} \tag{85}$$

The solutions to the rate equations are obtained numerically using a fourth order adaptive step-size Runge-Kutta routine. The values of the parameters used in the equations are listed in Tables II and III. Since no cavity was used in the spectroscopic measurements, $n_p = 0$ for all times. All loss mechanisms are ignored and optically stimulated transitions between $^5I_7$ and $^5I_8$ are ignored. The results of these calculations are compared with the observed rise times of emission from the Tm^{3+} $^3H_4$ and Ho^{3+} $^5I_7$ multiplets. Figure 13 shows the time evolution of the Tm^{3+} metastable state population calculated numerically overlaid on the oscilloscope trace for the 1.77 μm emission. Figure 13 also shows the time evolution of the Ho^{3+} metastable state population determined numerically overlaid on the trace for the 2.09 μm emission. The experimental results are those obtained for excitation at 780.0 nm. The pump flux is 1.53×10^{24} photons/(cm² s) corresponding to a pulse energy of 1 μJ with a 10 ns duration and a 290 μm beam radius. The numerical predictions closely approximate the experimental results when $k_{26} = 2.0\times10^{-16}$ cm³/s.

Modeling of Laser Operation

Now that the rate constants for this system are known, the rate equation model can be used to qualitatively simulate laser operation. Table I lists the additional parameters used in the laser simulation. The relaxation rates, branching

TABLE III

PARAMETERS USED IN RATE EQUATION MODEL
FOR DETERMINING k_{26} AND k_{62}

Pump Cross Sections

$$\sigma_{14} = 5.8 \times 10^{-21} cm^2$$

$$\sigma_{41} = 1.36 \times 10^{-22} cm^2$$

Energy Transfer Parameters

$$k_{42} = 1.0 \times 10^{-16} cm^3 s_{-1}$$

$$k_{26} = 2.0 \times 10^{-16} cm^3 s_{-1}$$

$$k_{62} = 2.6 \times 10^{-17} cm^3 s_{-1}$$

---

ratios and energy transfer parameters are the same as those in Tables II and III. The cavity lifetime is determined by considering only output coupler losses. The emission cross sections are calculated from the absorption cross sections using Equation (61). The alexandrite laser pump pulse at 785 nm is modeled using a 60 μs pulse train consisting of a series of 300 ns pulses 1 μs apart.

The rate equations describe a macroscopic model dealing only with the populations of the relevant states and the overall system dynamics. A uniform distribution of excitation within the excited volume of the sample is assumed with this model. The model does not analyze the mode structure of the laser or treat the detailed spatial distribution of excitation in the active medium. In addition, only the emission at ≈ 2.097 μm is modeled. The additional laser emission bands observed at higher pump energies are not considered. Despite these simplifications, the model is a suitable description of the physical processes involved in this laser system and is useful in elucidating how these processes affect some of the properties of laser operation.

Figure 14 shows the numerical predictions for the temporal characteristics of the laser output for different pump energies and Figure 15 shows the experimental results for the observed laser emission reported previously in Ref. [45]. The details of the laser experiments are given in Ref. [45]. The similarities are striking. The time delay between the pump pulse and the laser output at ≈ 2.097 μm is modeled quite accurately. The delay between the pump pulse and the laser emission is observed to decrease with increased pump intensity. Additionally, the relaxation oscillations present in the experimental results are also predicted by the numerical model and the overall pulse shape is similar to that observed.

There are, however, some differences between the modeling and the experimental results. The threshold energy predicted by the numerical simulation is significantly lower than that found experimentally and the decay of the laser output in the simulation is somewhat longer than that observed experimentally. These effects may be attributed to additional loss mechanisms not included in the simplified model, such as the mechanism leading to the green fluorescence from the
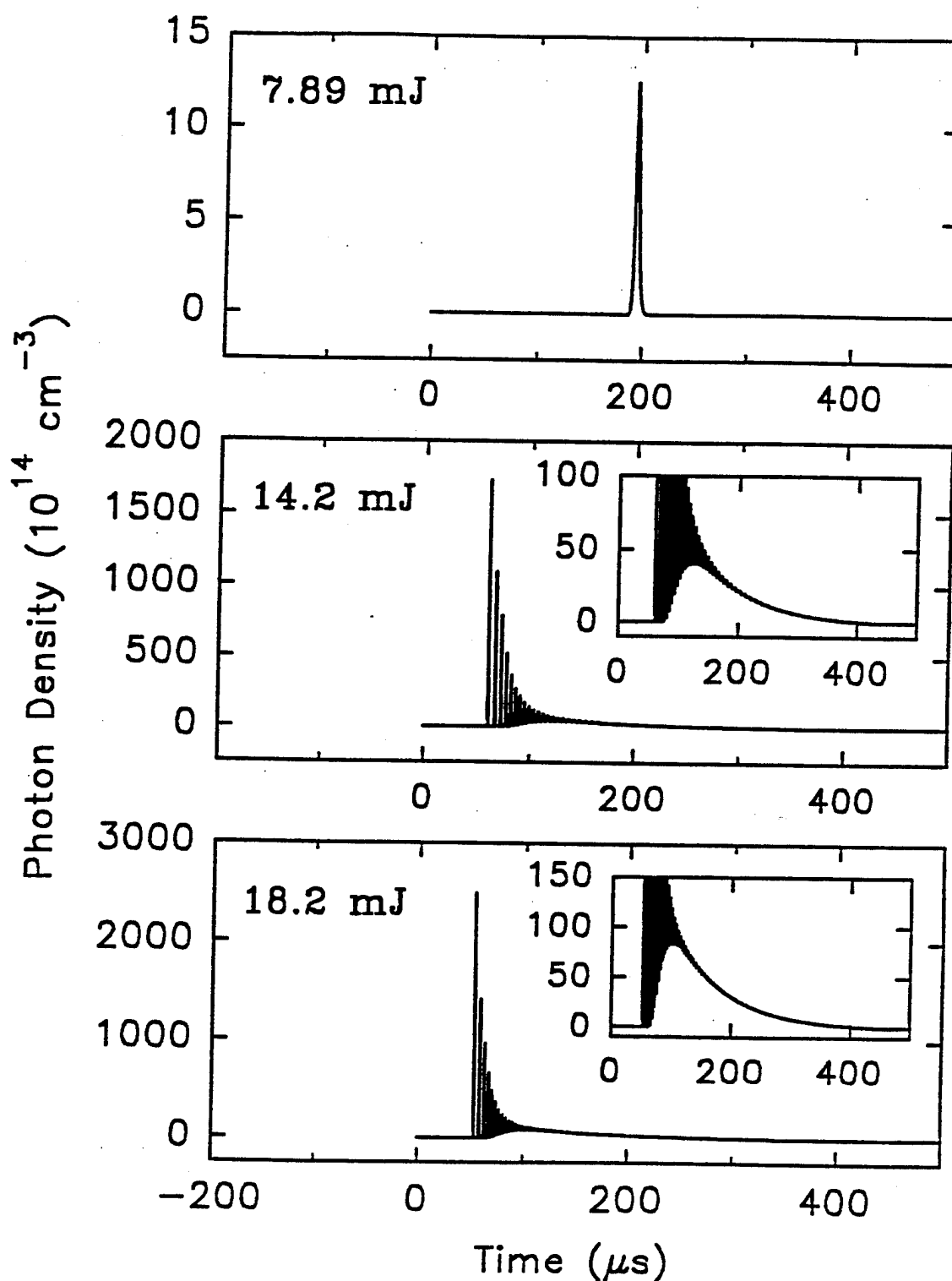
Figure 14. Numerical Modeling Results for a Tm,Ho:YAG Alexandrite Laser Pumped Laser. The insets show the details of the emission.
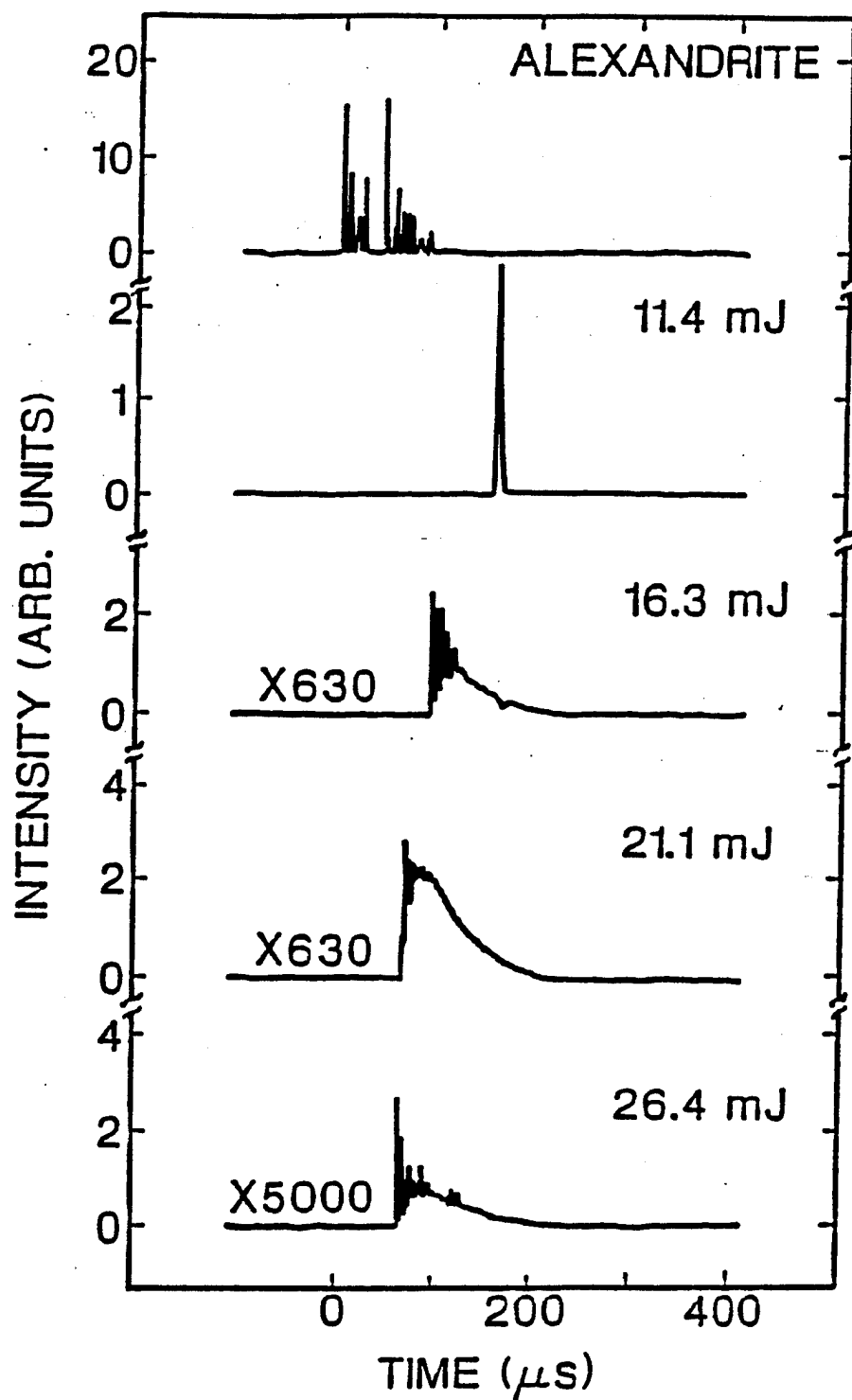
Figure 15. Experimental Results for a Tm,Ho:YAG Alexandrite Laser Pumped Laser. Taken from Ref. [45].

Ho^{3+} $^5S_2$ and $^5F_2$ multiplets to the ground state and the Tm^{3+} $^3F_4$ $\rightarrow$ $^3H_6$ Ho^{3+} $^5I_7$ $\rightarrow$ $^5I_5$ cross relaxation process often considered in CW systems.[52,54,67] Some of these loss mechanisms are discussed further in the following section. Additionally, thermal effects and cavity losses due to scattering and absorption processes not included in the model may affect the results.

Loss Mechanisms

The effects of three processes not considered above that can produce losses in laser operation of Tm,Ho:YAG are investigated here. The first mechanism considered is the energy transfer process involving the interaction of Tm^{3+} and Ho^{3+} ions that are both in their metastable states. This cross relaxation upconversion process populates the $^5I_5$ multiplet of Ho^{3+}. However, since no emission has been reported from the $^5I_5$ or $^5I_6$ [52] multiplets of Ho^{3+} in YAG, any ion excited to the $^5I_5$ multiplet must rapidly relax to the $^5I_6$ multiplet and then transfer its energy to the $^3H_5$ level of Tm^{3+}. Emission from $^5I_6$ must be very efficiently quenched by this energy transfer to Tm^{3+} since if the process was slow, then emission from $^5I_6$ would be detected. The mechanism is treated in the model as an infinitely fast energy transfer process to simulate this very efficient quenching.

The value of the rate parameter describing the interaction of Tm^{3+} and Ho^{3+} ions in their metastable states has been found either by measuring the temperature dependence of the gain of the $^5I_7$ $\rightarrow$ $^5I_8$ transition [51,68] or by measuring the pump power dependence of the emission intensity from the $^5I_7$ [49,67,69] level. Values for k_{26} in the range $2.4\text{-}14\times10^{-17}\text{cm}^3/\text{s}$ have been found. Note that nearly all of these measurements have been in flashlamp pumped systems and that the analysis used ignored other loss mechanisms mentioned earlier.

When the loss mechanism involving the metastable state interaction is included in laser simulation model described above, the predicted laser threshold increases by $\approx$5-25%. The temporal dynamics of the simulated laser emission do not change significantly.

The loss mechanisms leading to green emission seen during laser operation are not yet included in the model. There are at least two competing processes that can produce this emission: a cross relaxation process involving a $^3H_4 \rightarrow {}^3H_6$ transition of a Tm^{3+} coupled with a $^5I_7 \rightarrow {}^5F_2, {}^5S_2$ transition of a Ho^{3+} ion [50], and the absorption of a pump photon by a Ho^{3+} ion in the metastable state (see Figure 4). The second of these processes is investigated here to determine what excitation conditions will lead to excited state absorption of pump photons.

The excitation spectrum found by observing the 538 nm emission at various alexandrite laser wavelengths is shown in Figure 16. Although the resolution is limited to 2 nm, the essential feature is clearly present. Little or no green emission is observed for alexandrite laser wavelengths greater than 770 nm. To supplement the results of this excitation spectrum, fluorescence emission spectra in the green region obtained for simultaneous excitation at 2.1 μm and each of the three alexandrite laser pump wavelengths used in Ref. [45] (765 nm, 780 nm and 785 nm) are shown in Figure 17. The pump pulse energy is the same for each spectrum. Significant green emission is present only with a 765 nm pump wavelength. If either of the excitation beams is blocked during these measurements, the green emission vanishes completely. Thus for these excitation conditions, the green emission is not due to a complex Ho^{3+} ion-ion upconversion process. Instead the green emission is due to the absorption of an alexandrite laser pump photon by a Ho^{3+} ion previously excited to the metastable state.

This experiment establishes the excited state absorption (ESA) of pump photons by Ho^{3+} ions in the metastable state as one process leading to the green emission often reported for Tm,Ho co-doped materials. However, the lack of green emission for the 780 and 785 nm pump wavelengths in the Ho:YAG sample investigated in this experiment, combined with the observation of green emission in Tm,Ho:YAG at identical pump wavelengths [45], indicates that an additional process involving Tm-Ho ion-ion cross relaxation occurs in Tm,Ho:YAG.
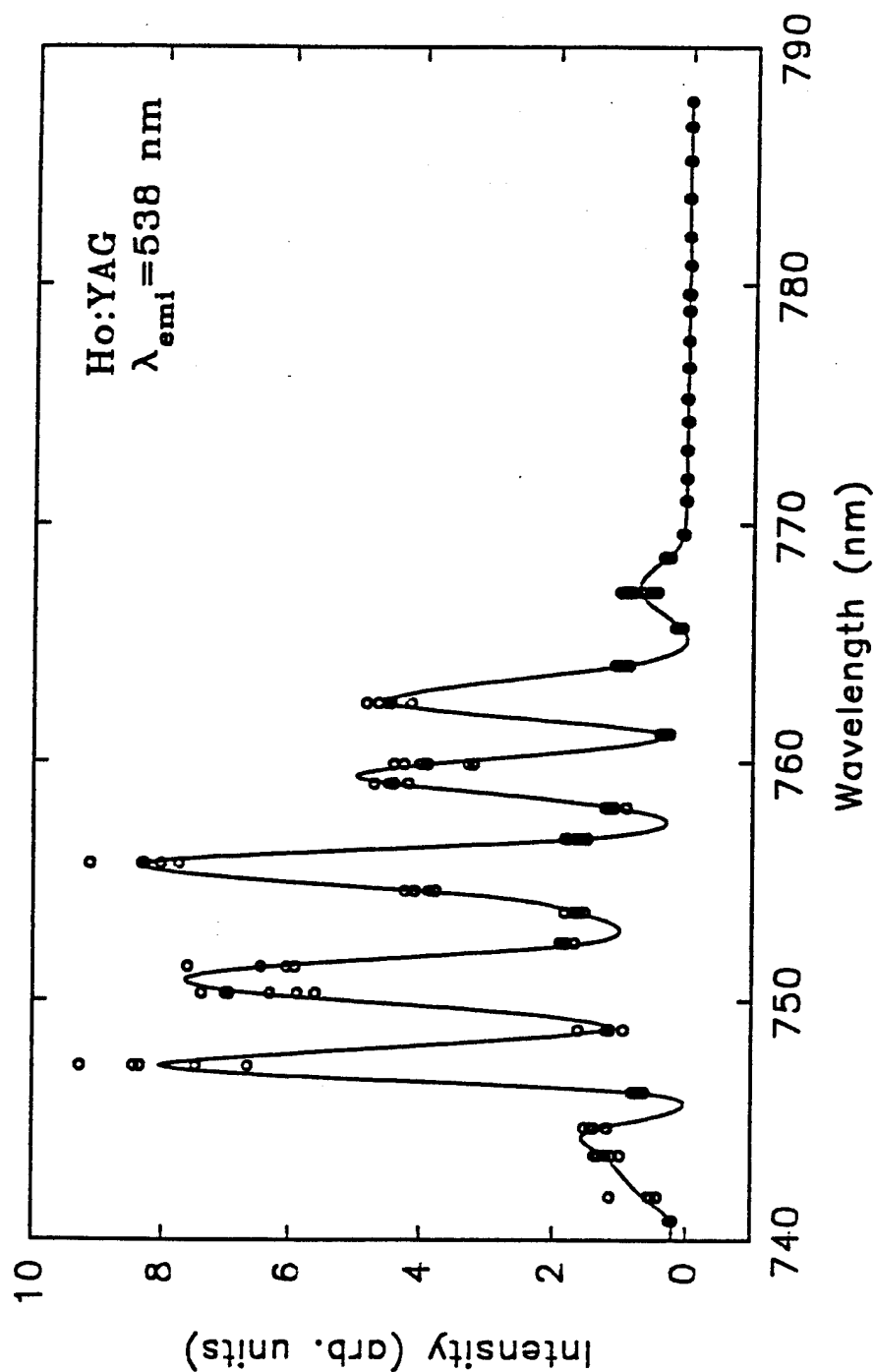
Figure 16. Excitation Spectrum of Ho:YAG. Primary Excitation is at 2.1 μm with a Secondary Excitation Tunable from 700-800 nm. The Open Circles are the Data and the Solid Line is a Spline Fit Drawn Through the Average Value at Each Wavelength
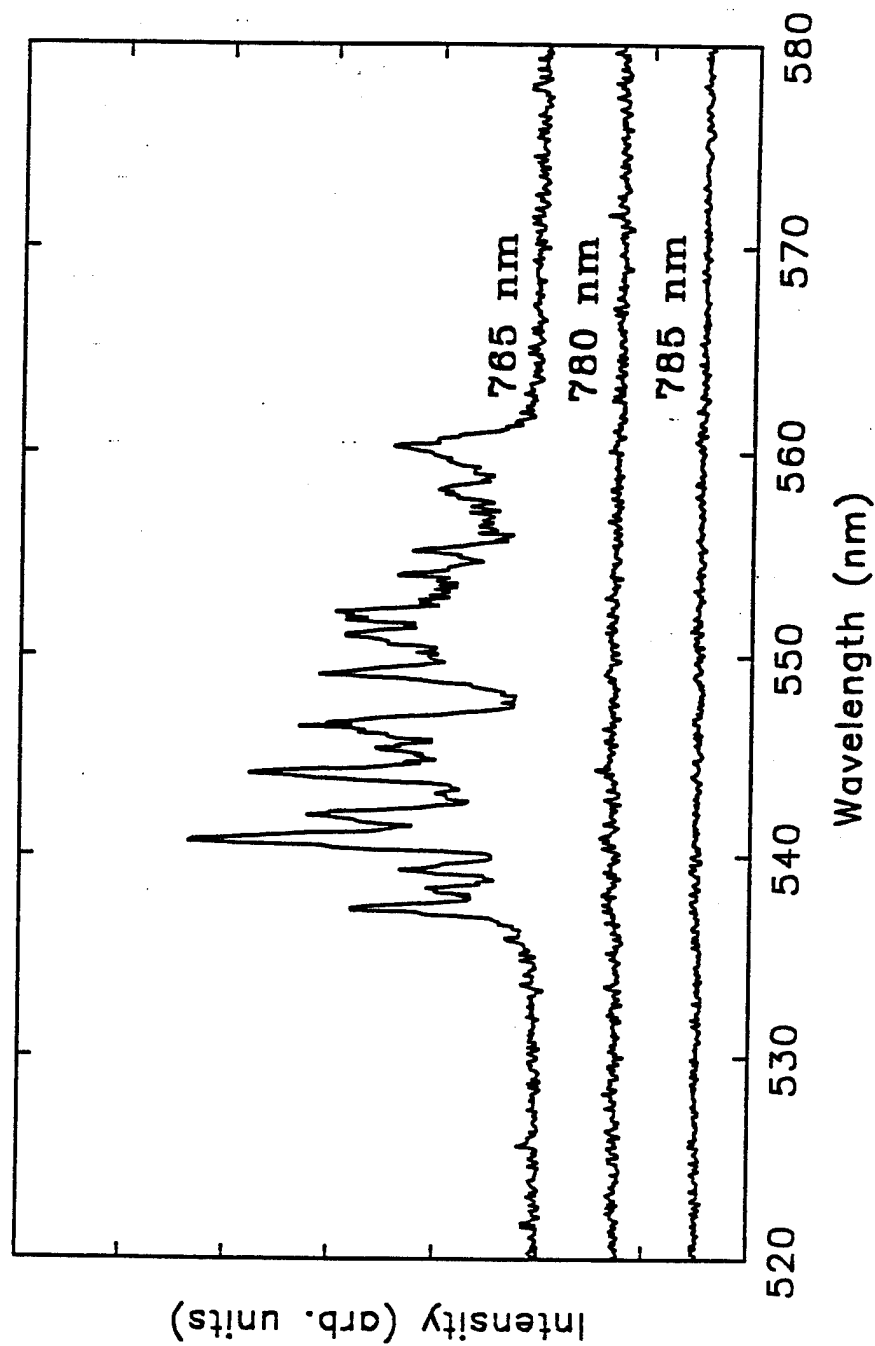
Figure 17. Emission Spectra of Ho:YAG 520-580 nm. Spectra taken at three Different Alexandrite Pump Wavelengths are Shown. The Excitation Pulse Energy is the Same for Each Wavelength.

The effects of both of these mechanisms on the solutions to the rate equations discussed in the previous section need to be considered. Since the rate parameters governing these mechanisms are unknown, order of magnitude estimates are used. Typical values of $\sigma_{68}=1\times10^{-20}$ cm^2 and $k_{48}=3\times10^{-17}$ cm^3/s are considered. No significant change in the laser threshold predicted by the computer simulation is caused by either the ESA or the ion-ion upconversion mechanisms. In addition, the overall laser output dynamics predicted by the model are not significantly changed. The maximum population of level 8 (Figure 4), the origin of the green emission, is predicted by the computer simulation to be only ≈0.1 and 1% of the metastable state populations for the excitation mechanisms of ion-ion interaction and pump photon ESA, respectively. Thus it appears that both of these mechanisms contribute to the observed green fluorescence of the Tm,Ho:YAG laser under the pumping conditions used in [45], but neither significantly effects the overall behavior of the system.

None of the mechanisms described above significantly changed the dynamics of the system predicted by the computer simulation. Specifically, these mechanisms do not explain the large difference in the magnitude of the relaxation oscillations predicted by the numerical model and those observed experimentally. One of the possible causes of this discrepancy may be the spatial distribution of the excitation energy. One of the assumptions in the rate equation model is that of uniform pumping.

Experimentally, nearly 63% of the incident energy was absorbed by the sample, so the pump beam intensity was reduced significantly as it passed through the sample. [45] Thus the sample was not uniformly excited and regions not pumped above threshold act as a loss for the laser emission. These losses have not been accounted for in the model.

Another possible effect of non-uniform pumping is that the upconversion processes may be underestimated. Since these processes involve interactions between two ions in excited states, or an ion an excited state and a pump photon, their effects scale as $(\Phi_p)^2$. Thus regions more strongly excited than the average

value used in the rate equations will have much larger upconversion losses. These effects could be the cause of the differences in the magnitudes of the relaxation oscillations.

Summary and Conclusions

The results of this work are three-fold. First, the values for the energy transfer rate constants in the Tm,Ho:YAG are established from a spectroscopic study of the spectral dynamics of the system. The value of the rate parameter k_{26} determined here, combined with previous experimental work [59,60], gives a more complete understanding of the overall energy migration and energy transfer processes in Tm,Ho-doped materials. The Tm-Ho transfer time using the value for k_{26} is similar to that found by the simple Forster-Dexter[28,29] model of energy transfer, utilizing spectral overlap integrals.[60] This result along with those of a four-wave mixing study [59,60] of energy migration in Tm^{3+}:YAG show conclusively that the overall process consists of two parts, a fast energy migration among Tm^{3+} ions followed by a process of energy transfer from Tm^{3+} to Ho^{3+}. The concentration dependence of the quantum efficiency of the $^3H_4$ emission indicates that this migration occurs in both the initial pump level (the $^3H_4$ multiplet) and in the metastable state (the $^3F_4$ multiplet). A second rate parameter, the rate parameter describing the Tm^{3+} $^3H_4 \rightarrow ^3F_4$ and $^3H_6 \rightarrow ^3F_4$ cross relaxation process, is also found from the data presented here. Note, however, that the rate parameters are determined only for the Tm^{3+} and Ho^{3+} concentration used in this work, which is similar to the optimum concentrations determined for Cr,Tm,Ho:YAG flashlamp pumped lasers.[48]

The second result of this work is the development and use of a rate equation model for a computer simulation of Tm,Ho:YAG laser operation. Since the usefulness of such a simulation depends entirely on the accuracy of the parameters used, all the parameters needed in the model are determined independently through analysis of the spectroscopic results and no fitting parameters are used in the simulation. The simulation accurately predicts temporal delays in the laser

output and reproduces the relaxation oscillations seen in this system. Additional effects due to various loss mechanisms in some cases change the predicted threshold for lasing, but do not affect the overall dynamics of the laser output.

Finally, the existence of a second process leading to the green emission reported in Tm,Ho:YAG (and in other hosts) is firmly established. For laser pumped lasers, this process, identified as the excited state absorption of pump photons by Ho^{3+} ions in the metastable state, can be as important as the ion-ion cross relaxation process usually cited. This mechanism is needed to explain the green emission dependence on pump wavelength while the ion-ion cross relaxation process explains the existence of green emission even when no excited state absorption of pump photons is present.

SECTION III

SPECTROSCOPIC AND LASING PROPERTIES
OF Nd:YAG AND Nd:GSGG

Introduction

For many years Nd^{3+} doped materials have played an important role in the field of solid state lasers and recently much work has concentrated on diode pumped laser operation [70–73] and simulating diode pumped laser operation with tunable solid state lasers [74–78]. Interest in potential new laser host materials and detailed examination of the dynamics involved in the pump process have spurred many studies. Additionally, studies of upconversion and excited state absorption processes leading to fluorescence [79–84] and laser operation from upper states [34,35] have been undertaken.

Results of a study of the absorption and emission characteristics of two different host materials, yttrium aluminum garnet and gadolinium scandium gallium garnet are presented here in an attempt to further understand the dynamics involved in monochromatically pumped systems. Absorption, fluorescence emission and excitation spectra are used to determine the origin and dynamics involved in the emission of photons in the blue and green spectral regions. Analysis of absorption data using the Judd-Ofelt theory [9,10] is performed and used to predict radiative lifetimes of excited states, branching ratios for radiative decay, and oscillator strengths for excited state absorption transitions. Mechanisms leading to the blue emission often reported in these and similar materials are identified.

Experimental Method

Absorption spectra and fluorescence spectra were obtained for two different Nd^{3+} doped oxide crystals. The following samples were used in the study: yttrium aluminum garnet doped with 1.0 % Nd^{3+} (Nd:YAG) and gadolinium scandium gallium garnet doped with 1.0% Nd^{3+} (Nd:GSGG). A Cary 2400 UV-VIS-NIR spectrophotometer was used to find the absorption spectra. Data was acquired, stored, and analyzed using an IBM-compatible personal computer.

Fluorescence spectra were obtained using a variety of excitation sources and spectrometers. A 0.25 m spectrometer was used for the GSGG sample and some preliminary work on the YAG sample. Additionally a 0.85 double spectrometer was also used for the YAG sample. Various photomultiplier tubes, depending on the spectral range of interest, were used. In all cases a PAR Model 162 boxcar averager was used for signal processing. Output from the averager was then converted to a digital signal and recorded on a computer data acquisition system. An alexandrite laser, tunable from 720 nm-800 nm with a pulse train consisting of 20-40 300 ns pulses, was used as the excitation source.

In addition to absorption and fluorescence spectra described above, excitation spectra were recorded for the GSGG sample. A 0.25 m spectrometer was used to select one of the emission lines. The alexandrite laser was then scanned over the range from 730-780 nm. A photomultiplier tube was used to detect the resulting emission in the visible region and a PbS cell was used to detect the emission for the near infrared emission. Again a PAR Model 162 boxcar averager was used for signal processing and data was stored on a computer. The energy of the alexandrite laser was monitored with a Laser Precision Model 7600 energy meter.

Results and Analysis

The absorption spectra and positions of some important multiplets are shown for the region from 10000-30000 cm^{-1} for Nd:YAG (Figure 18) and Nd:GSGG (Figure 19). Assignment of the term values to the various absorption regions is

based upon the crystal field analysis for Nd:YAG in Refs. [85,86] and for Nd:GSGG in Ref. [87]. Absorption spectra for transitions to the $^2P_{3/2}$ multiplet are shown in Figure 20(a) (Nd:YAG) and Figure 20(b) (Nd:GSGG). The positions of the Stark components of this multiplet may be important in determining the origin of emission seen in this work and previous work, [74,76–79] so the identification of their positions is extremely important. The extremely weak oscillator strength of transitions to this multiplet makes assignment of spectral lines difficult and the positions of both of the Stark components have been previously reported at low temperatures only. [85–87] Here these positions of the Stark components are identified from the splitting of the absorption spectrum as 26042 cm^{-1} and 25997 cm^{-1} for Nd:GSGG. For Nd:YAG, although the peaks are not very well resolved, the positions are identified as 25993 cm^{-1} and 25934 cm^{-1}. The other spectral features are due to transitions from the Stark split components of the ground state to the $^2P_{3/2}$ Stark levels.

The oscillator strengths for transitions originating in the ground state multiplet, those experimentally determined (Equation (18)) and those found from the Judd-Ofelt analysis (Equation (17)), are shown in Table IV for both samples. The Judd-Ofelt parameters determined here and those found by others [88–90] are listed in Table V. In both tables there are two entries for this work, corresponding to different integration limits on Equation (18). Two different groupings of certain multiplets are used for each sample and the results are compared.

The Judd-Ofelt parameters can be used to determine transition probabilities and oscillator strengths for excited state to excited state transitions using Equation (13) and (17). This can be done for all those transitions for which the transition matrix elements are available. For Nd^{3+} [20] gives matrix elements for 21 multiplets yielding 441 transitions. A portion of these results are shown in Tables VI, VII, and VIII.

Fluorescence spectra under excitation at 748.6 nm for Nd:YAG and 734.9 nm for Nd:GSGG in the 375-475 nm region are shown in Figures 21(a) and 21(b) and that in the 475-575 nm region is shown in Figures 22(a) and 22(b). The
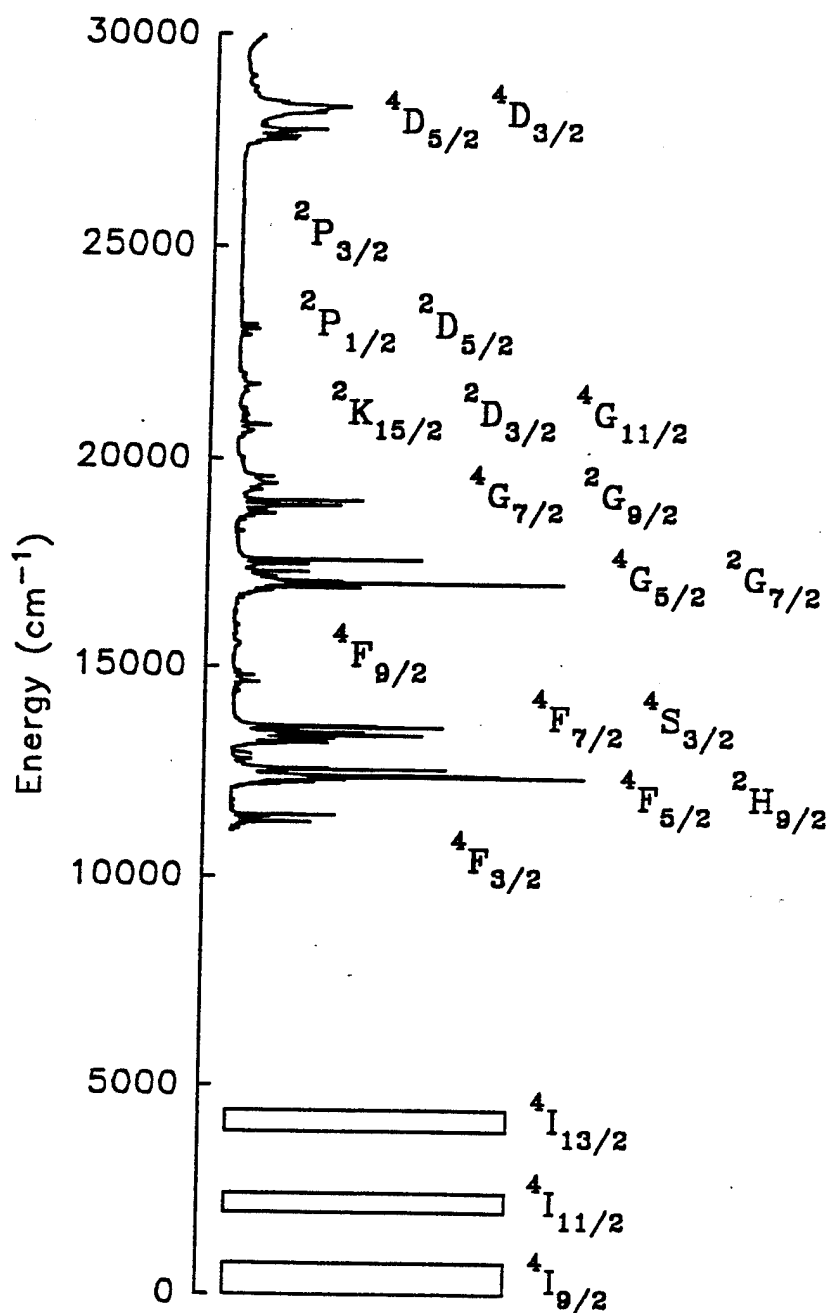
Figure 18. Absorption Spectrum of Nd:YAG. Positions of Lower Levels Taken from Ref. [85].
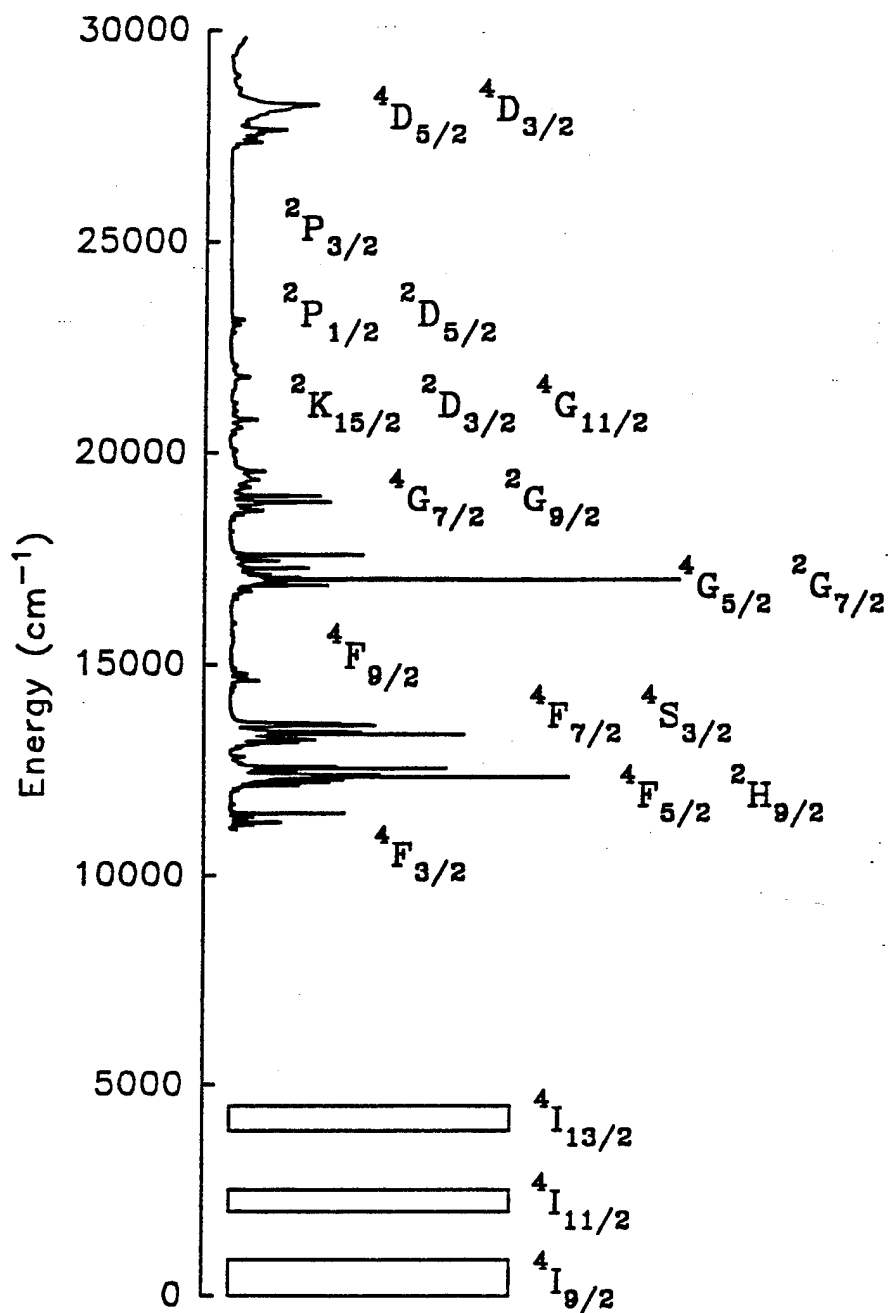
Figure 19. Absorption Spectrum of Nd:GSGG. Positions of Lower Levels Taken from Ref. [86].
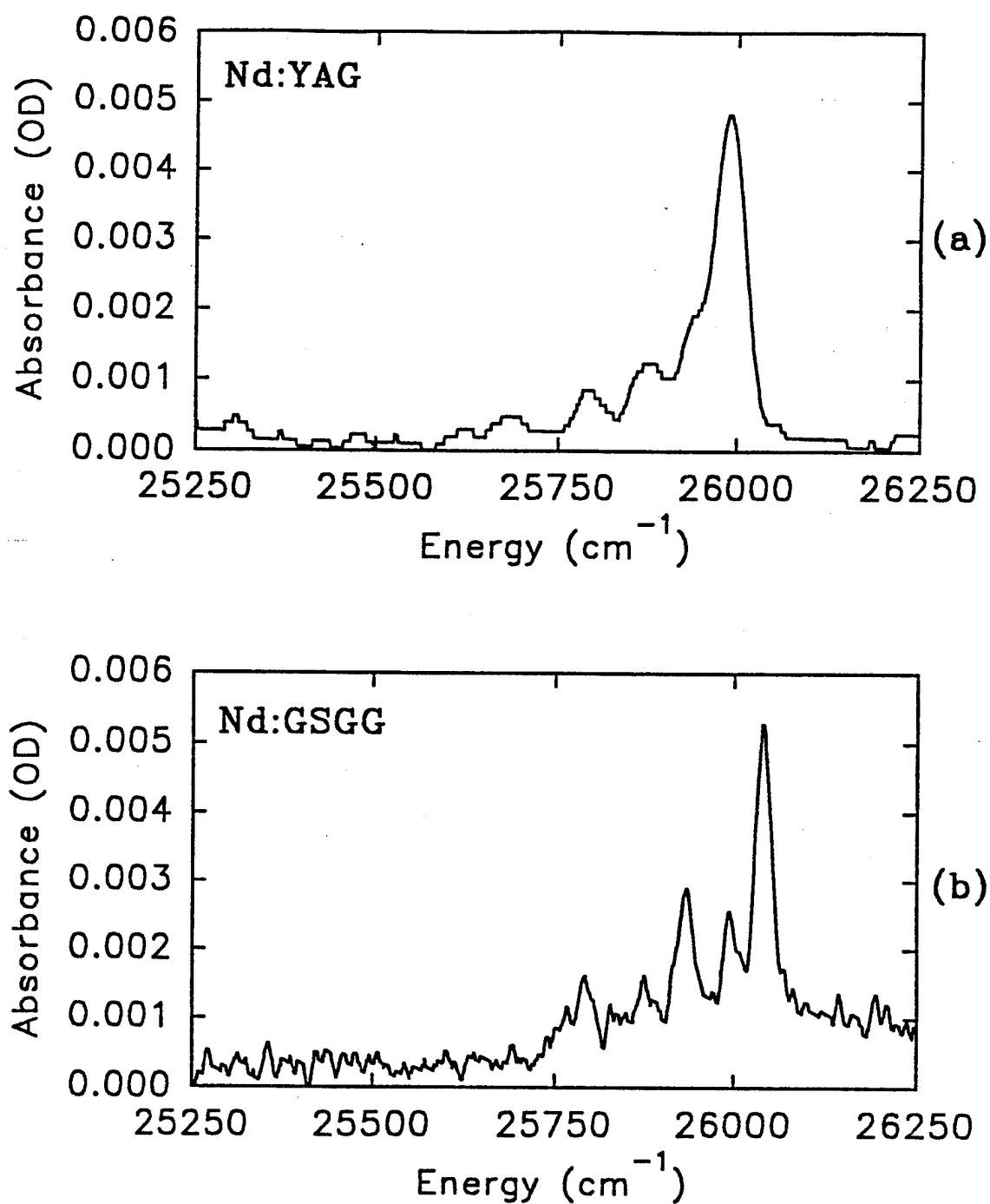
Figure 20. Absorption Spectra of $^2P_{3/2}$ Multiplet. (a) Nd:YAG and (b) Nd:GSGG.

TABLE IV

OSCILLATOR STRENGTHS FOR TRANSITIONS
FROM THE GROUND STATE
Nd:YAG AND Nd:GSGG

Band	Multiplet	Nd:YAG (1) λ (nm)	f ($\times 10^{-8}$) expt.	calc.	Nd:YAG (2) λ (nm)	f ($\times 10^{-8}$) expt.	calc.	Nd:GSGG (1) λ (nm)	f ($\times 10^{-8}$) expt.	calc.	Nd:GSGG (2) λ (nm)	f ($\times 10^{-8}$) expt.	calc.
5	$^4F_{3/2}$	879	126	183	879	126	183	878	139	175	878	139	173
6	$^4F_{5/2},{}^2H_{9/2}$	806	840	748	806	840	746	806	677	645	806	677	643
7	$^4F_{7/2},{}^4S_{3/2}$	747	768	867	747	768	865	746	688	720	746	688	722
8	$^4F_{9/2}$	683	69.5	62.9	683	69.5	62.8	681	64.0	53.3	681	64.0	53.3
9	$^2H_{11/2}$	636	34.0	17.5	636	34.0	17.5	641	26.0	14.9	641	26.0	14.8
10	$^4G_{5/2},{}^2G_{7/2}$	586	749	760	586	749	761	586	796	806	586	796	796
11	$^4G_{7/2}(2),{}^2K_{13/2}$	525	598	459	525	598	458	527	552	429	530	297	310
12	$^4G_{9/2}$										514	258	116
13	$^2D_{3/2},{}^2K_{15/2}$	473	220	78.2	481	118	55.7	474	187	71.1	480	112	51.1
14	$^4G_{11/2}$				459	106	22.1				459	87.5	19.5
15	$^2P_{1/2}$	434	32.3	44.9	434	32.3	44.8	433	39.2	49.8	433	39.2	48.8
16	$^2D_{5/2}$	423	2.85	4.14	423	2.85	4.13						
17	$^2P_{3/2}$	385	2.76	2.56	385	2.76	2.56	385	2.14	2.42	385	2.14	2.40
18	$^4D_{5/2},{}^4D_{3/2}$	355	890	931	355	890	928	354	935	961	354	935	944
	$^4D_{1/2},{}^2I_{11/2}$												

TABLE V

JUDD-OFELT PARAMETERS FOR
Nd:YAG AND Nd:GSGG

Material	Ω_2 $(\times 10^{-20})$	Ω_4 $(\times 10^{-20})$	Ω_6 $(\times 10^{-20})$	RMS-Error
Nd:YAG(1)	0.56	2.55	5.03	17
Nd:YAG(2)	0.57	2.54	5.02	15
Nd:YAG[a]	0.20	2.7	5.0	10
Nd:YAG[b]	0.37	2.29	5.97	-
Nd:GSGG(1)	0.65	2.33	3.79	13
Nd:GSGG(2)	0.66	2.29	3.73	9.3
Nd:GSGG[c]	0.35	2.35	3.23	14

a Ref. [88]
b Ref. [89]
c Ref. [90]

TABLE VI

TRANSITION PROBABILITIES AND BRANCHING RATIOS FROM THE $^2P_{3/2}$ MULTIPLET FOR Nd:YAG AND Nd:GSGG

Terminal Multiplet	Nd:YAG			Nd:GSGG		
	λ (nm)	A (s^{-1})	β (%)	λ (nm)	A (s^{-1})	β (%)
$^4I_{9/2}$	385	101	2.55	385	111	2.71
$^4I_{11/2}$	419	652	16.5	420	774	18.9
$^4I_{13/2}$	459	556	14.1	455	570	13.9
$^4I_{15/2}$	501	127	3.21	519	110	2.68
$^4F_{3/2}$	685	4.39	0.111	686	6.55	0.16
$^4F_{5/2}$	737	25.3	0.641	737	30.6	0.747
$^2H_{9/2}$	737	1140	28.9	737	1110	27.1
$^4F_{7/2}$	794	4.09	0.104	796	4.78	0.117
$^4S_{3/2}$	794	7.04	0.178	796	10.3	0.251
$^4F_{9/2}$	882	638	16.1	886	648	15.8
$^2H_{11/2}$	976	131	3.31	964	142	3.47
$^4G_{5/2}$	1120	2.37	0.0599	1120	3.47	0.0848
$^2G_{7/2}$	1120	0.00	0.00	1120	0.00	0.00
$^4G_{7/2}$	1440	5.64	0.143	1430	7.2	0.176
$^4G_{9/2}$	1440	161	4.07	1430	171	4.17
$^2K_{13/2}$	1440	392	9.92	1430	390	9.52
$^2D_{3/2}$	2070	0.326	0.00825	2050	0.502	0.0122
$^4G_{11/2}$	2070	1.23	0.0311	2050	1.48	0.036
$^2K_{15/2}$	2070	4.28	0.108	2050	4.24	0.104
$^2P_{1/2}$	3410	0.0755	0.00191	3470	0.109	0.00266
$^2D_{5/2}$	4290	0.0513	0.00130	3470	0.151	0.00369

TABLE VII

SUMMARY OF RADIATIVE LIFETIMES AND
BRANCHING RATIOS TO THE ^4I_J
MULTIPLETS FOR Nd:YAG
AND Nd:GSGG

Terminal Multiplet	Nd:YAG			Nd:GSGG		
	λ (nm)	τ μs	β (%)	λ (nm)	τ μs	β (%)
$^4I_{11/2}$	4760	58600		4620	51700	
$^4I_{13/2}$	2380	15500		2510	19900	
$^4I_{15/2}$	1670	19000		1490	10100	
$^4F_{3/2}$	879	270	100	878	264	100
$^4F_{5/2}$	806	200	99.8	806	197	100
$^2H_{9/2}$	806	1250	100	806	1300	100
$^4F_{7/2}$	747	180	100	746	190	100
$^4S_{3/2}$	747	152	100	746	162	100
$^4F_{9/2}$	683	230	99.7	681	239	99.7
$^2H_{11/2}$	636	3780	91.3	641	3830	92.3
$^4G_{5/2}$	586	104	98.6	586	88	98.5
$^2G_{7/2}$	586	237	97.2	586	212	97.4
$^4G_{7/2}$	525	146	92	527	127	93
$^2K_{13/2}$	525	915	47.9	527	968	48.9
$^4G_{9/2}$	525	131	94.6	527	119	95
$^2D_{3/2}$	473	397	76.8	474	393	77.2
$^4G_{11/2}$	473	99.1	90.7	474	93.6	90.8
$^2K_{15/2}$	473	681	33.6	474	693	33
$^2P_{1/2}$	434	235	64.7	433	202	62.2
$^2D_{5/2}$	423	443	30.7	433	490	31.8
$^2P_{3/2}$	385	253	36.3	385	244	38.2

TABLE VIII

OSCILLATOR STRENGTHS FOR TRANSITIONS
TO THE $^2P_{3/2}$ MULTIPLET FOR
Nd:YAG AND Nd:GSGG

Initial Multiplet	Nd:YAG			Nd:GSGG		
	λ (nm)	f ($\times 10^{-8}$)	ΔE (cm^{-1})	λ (nm)	f ($\times 10^{-8}$)	ΔE (cm^{-1})
$^4F_{3/2}$	685	0.924	-1230	686	1.20	-972
$^4F_{5/2}$	737	4.11	-200	737	4.33	-200
$^2H_{9/2}$	737	111	-200	737	94.4	-200
$^4F_{7/2}$	794	0.579	775	796	0.598	1040
$^4S_{3/2}$	794	1.99	775	796	2.57	1040
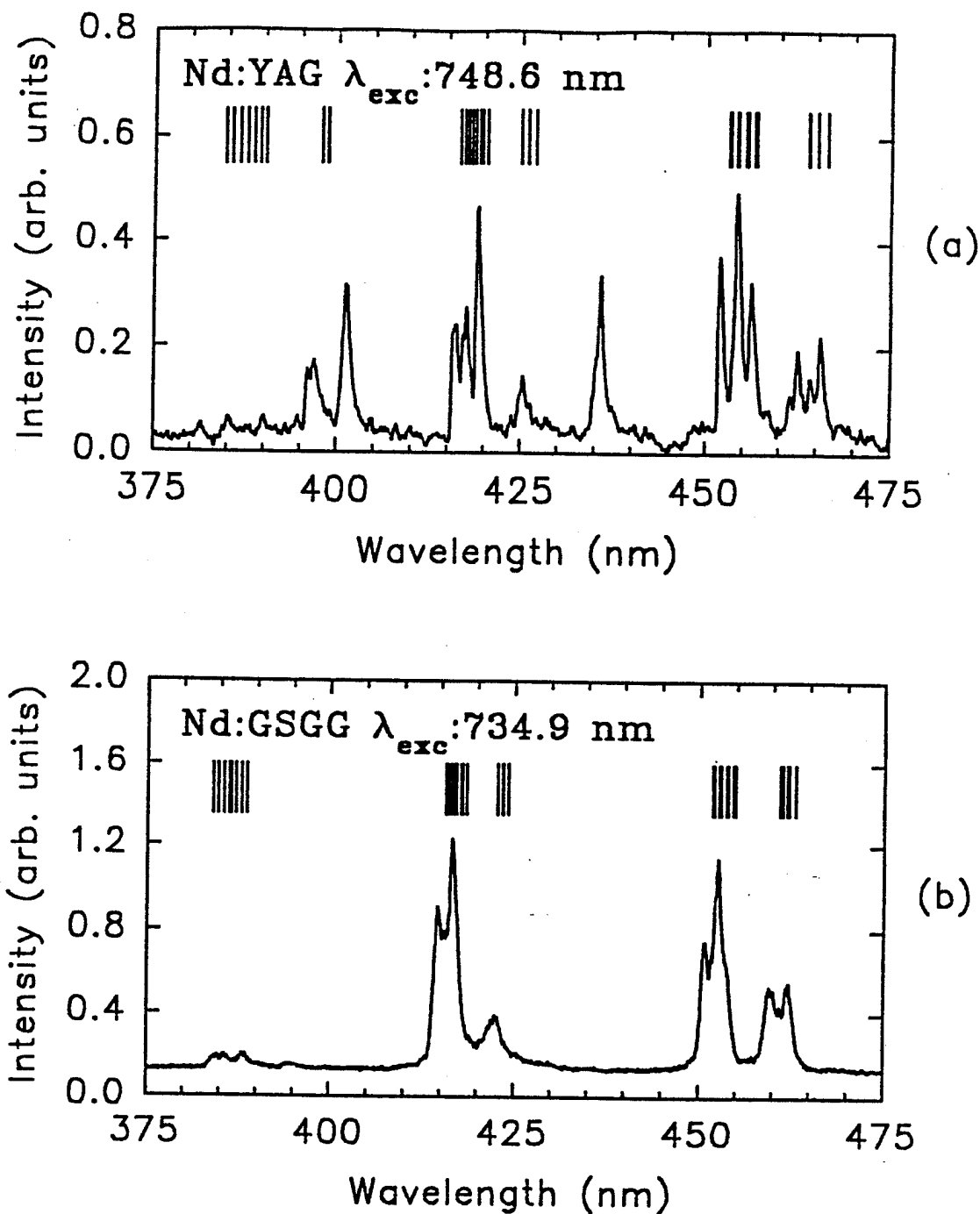
Figure 21. Fluorescence Spectra in 375-475 nm Spectral Range. (a) Nd:YAG and (b) Nd:GSGG. The Vertical Lines Indicate Emission Wavelengths Predicted by the Positions of the Stark Components of the $^2P_{3/2}$ and ^4I_J Multiplets.
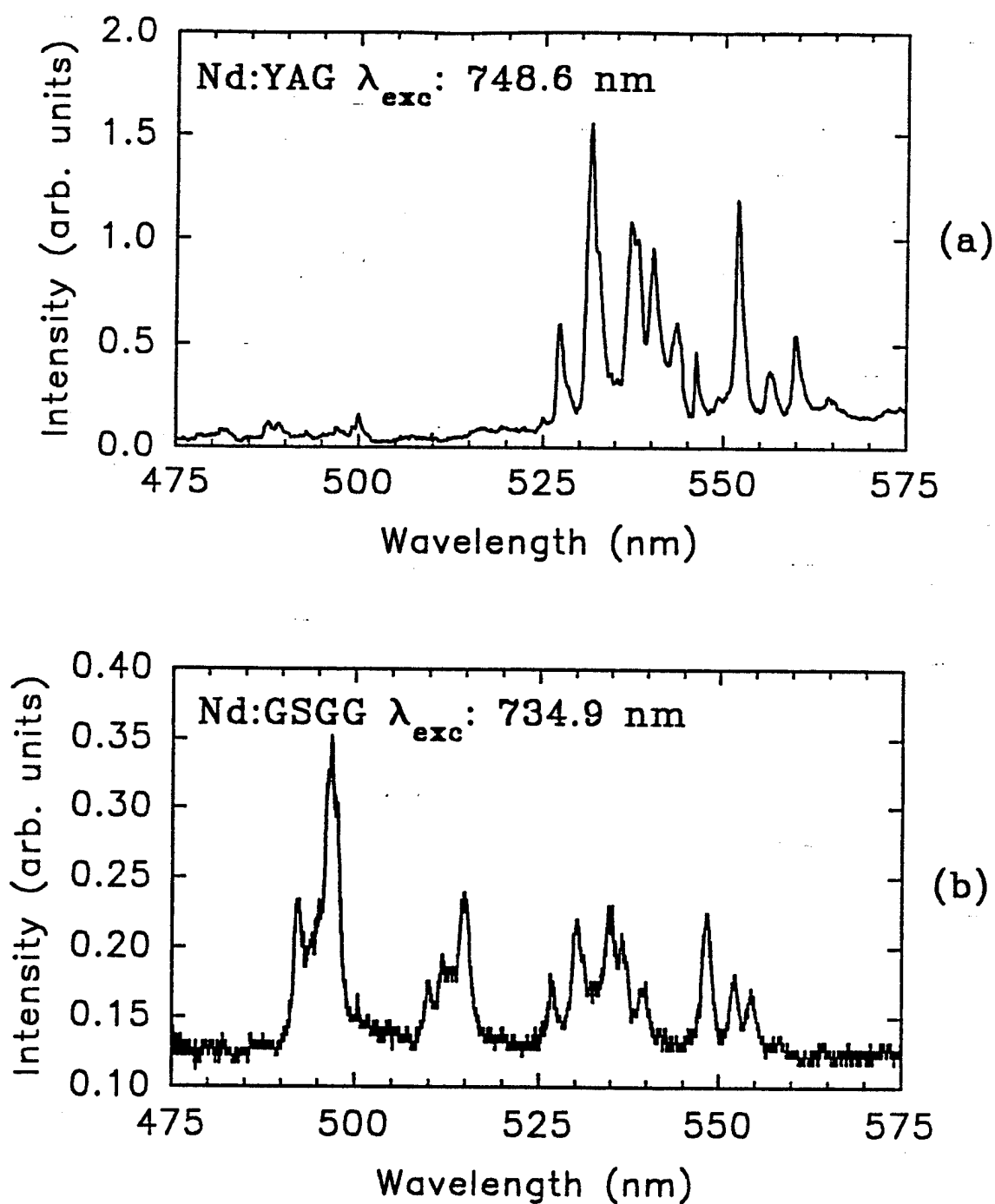
Figure 22. Fluorescence Spectra in 475-575 nm Spectral Range. (a) Nd:YAG and (b) Nd:GSGG.

alexandrite pump wavelengths for the samples differ slightly but in both cases the absorption band corresponding to the $^4F_{7/2} + {}^4S_{3/2}$ is excited directly. The presence of emission at higher energies than that of the pump photons indicates some type of multiple body process, ion-ion energy transfer upconversion, reabsorption of emitted photons, or excited state absorption of pump photons, occurs.

Determining the exact dynamics involved in this process would be extremely difficult considering the number and location of the multiplets present in the system. To help in determining the processes involved, excitation spectra for some of the emission peaks observed in the GSGG sample are presented in Figure 23. Excitation spectra for the 417 nm line, the 536 nm line, and the 1064 nm line are shown along with the absorption spectrum for transitions originating on the ground state in this spectral region. The 417 nm excitation spectrum contains peaks not seen in the other spectra. Additionally, the spectrum for the 417 nm emission line cuts off much more rapidly at wavelengths larger than 760 nm. The 536 nm and 1064 nm excitation spectra closely resemble the standard absorption spectrum for the region. These results are similar to those previously reported for Nd:YAG in [77].

Discussion of Results

Absorption

The results of the Judd-Ofelt analysis leads to some interesting conclusions. Two different sets of results and parameters found in the analysis for each sample along with previous results are listed in Tables IV and V. The two different sets of results and parameters in this work correspond to different methods of grouping the various multiplets when using Equation (18). For the entries labeled A the term assignments used are those found in Hua et al.[85]. An alternative grouping of the multiplets is used for the entries labeled B. In both cases for both samples an error within the 5-20 % usually encountered in these calculations is found.
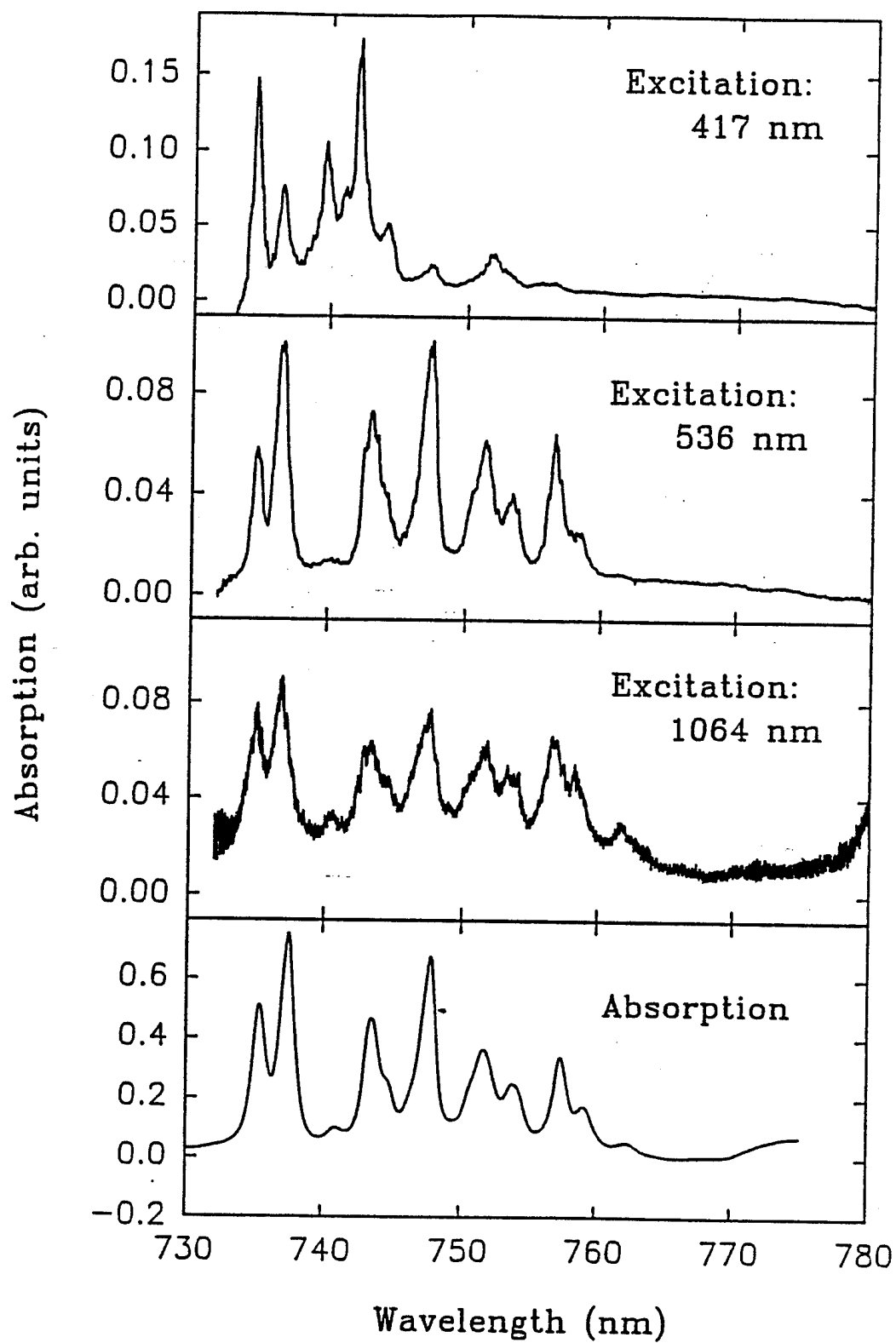
Figure 23. Nd:GSGG Excitation and Absorption Spectra 730-780 nm. Emission at (a) 417 nm, (b) 536 nm, (c) 1064 nm, and (d) Absorption Spectrum.

The Judd-Ofelt parameters determined are very close to those found previously by other authors. [88–90]

The grouping used for the results labeled A differs slightly from that used by others, especially in the region of 440-500 nm. This region of the absorption spectra for both samples is shown in Figure 24. This region corresponds to absorption by the $^2D_{3/2}$, $^2K_{15/2}$, and $^4G_{11/2}$ multiplets.

In the past, the absorption in this region was broken into two regions, one below and one above ≈ 470 nm. Term values were assigned to each of these regions individually.

These terms are not separated in the entries labeled A because of the extensive mixing of the Stark components of the three multiplets in this region [85–87] and the absorption spectra in the region. As seen from the spectra, determining the exact location to place the limits on the integration found in Equation (18) is difficult. The same problem is encountered in the 500-550 nm region for Nd:GSGG. For comparison. to previous work, the results of the analysis for the case in which these bands are separated are also listed (case B).

Comparison of the results for both cases and to those found previously show little difference. Although the rms-error is slightly reduced in case B, the differences between the measured and predicted oscillator strengths remain essentially the same. The increase in the number of transitions used in the second method does not lead to a significant reduction in the overall error associated with the calculation or lead to a significant change in the Judd-Ofelt parameters. When comparing these results to those found for these materials by others, the only significant difference is in the Ω_2 parameter. The value found here seems consistently larger than that reported elsewhere. For Nd^{3+} doped materials, the Ω_t parameter is not as reliable as the Ω_4 and Ω_6 parameters.[88] Ω_2 only depends on one absorption band, the $^4G_{5/2} + {}^2G_{7/2}$ band. The ratio of this oscillator strength to that of the $^4F_{5/2} + {}^4S_{3/2}$ band found here is larger than that found by others: 1.18 vs. 0.79 for GSGG and 0.89 vs 0.45 for YAG. This leads to a higher value for Ω_2. If this band is completely eliminated from the analysis and Ω_2 set to 0.00, as done by Krupke [88],
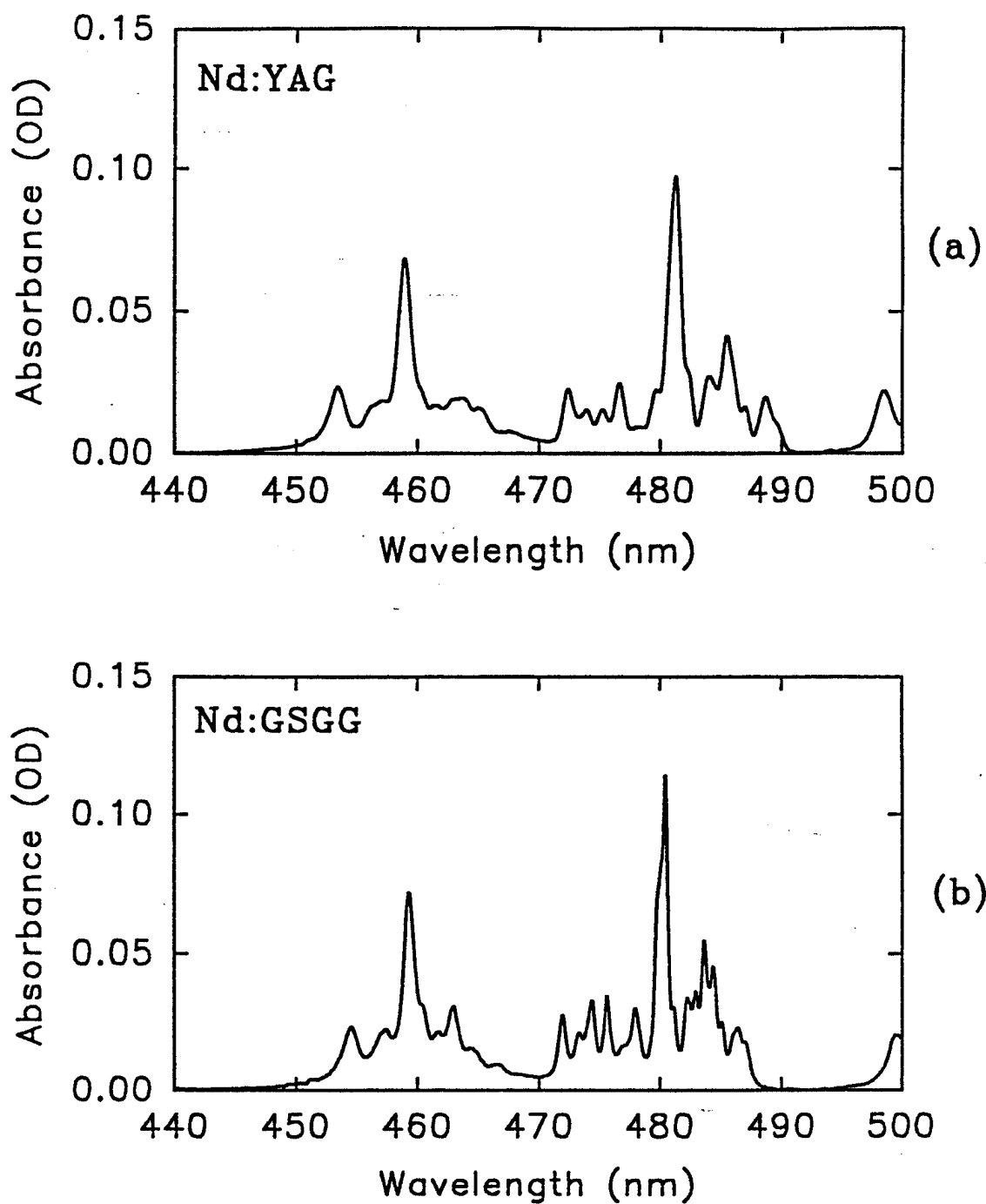
Figure 24. Absorption Spectra in 440-500 nm Spectral Range. (a) Nd:YAG and
(b) Nd:GSGG.

the results for Ω_4 and Ω_6 remain essentially unchanged. Analysis of the various doubly reduced unit tensor matrix elements indicates that slight differences in Ω_2 will not greatly affect any of the important transitions in the system.

Tables VI-VIII summarize much of the information acquired through the application of Equations (13, 16, and 17). In Table VI the transition probability rates for all transitions originating on the $^2P_{3/2}$ multiplet are listed along with the predicted branching ratios. Analysis of these values shows that a significant portion of the radiative emission occurs to states above the metastable state. From these states ions can either cascade non-radiatively to the metastable state or radiatively decay to a still lower level. In all cases, only a fraction of the ions excited to states above the metastable state bypasses the metastable state via fluorescence to the ^4I_J multiplets. Table VII summarizes the radiative lifetimes and the branching ratio to states below the metastable state. For those cases in which the lifetime has been experimentally measured [23–25,81,91] the measured lifetimes are significantly shorter than those listed here. This indicates that the non-radiative decay path for ions excited to these states is the dominant relaxation process.

In Table VIII the oscillator strengths for transitions between excited states that may be responsible for the excited state absorption of pump photons are listed. The ΔE noted is the energy deficiency (excess) involved in a transition terminating on the $^2P_{3/2}$ originating on one of these levels. It is interesting to note that the oscillator strength for a transition originating on the $^4F_{5/2} + {}^2H_{9/2}$ band is ≈ 100 times larger than that originating on the metastable state for both materials. A complexity in quantitatively determining the absorption cross sections for transitions in the spectral corresponding to these transitions is that the actual transition involved in an absorption process would be a Stark level to Stark level transition and not a multiplet to multiplet transition as calculated here. Calculation of Stark level to Stark level oscillator strengths is possible [92,93] but requires detailed knowledge of the radial wavefunctions for individual Stark levels which is not generally available.

Fluorescence

Analysis of the emission spectra in Figures 21 and 22 can be used to establish the origin of the blue emission observed here. The emission is broken into three main bands for each sample, corresponding to emission from the $^2P_{3/2}$ to the $^4I_{13/2}$, $^4I_{11/2}$, and $^4I_{9/2}$ multiplets. The vertical lines in Figure 21 are the wavelengths of predicted emission from the $^2P_{3/2}$ multiplet determined from the positions of the Stark levels identified earlier and the Stark level positions for the lower multiplets in Ref. [85,87]. Most of the lines observed correspond well with the predicted emission. The absence of large numbers of additional lines indicates little contribution from other higher lying multiplets, especially in the GSGG sample.

Previous work [34,74,76–80,82,83] has attributed the blue fluorescence in the 380 nm, 420 nm, 450 nm, and 460 nm regions to transitions originating on the $^4D_{5/2}$, $^4D_{3/2}$, and $^2P_{3/2}$ multiplets. The mechanisms cited for populating the upper state was excited state absorption (ESA) from the metastable state (either of pump or fluorescence photons) and ion-ion energy transfer upconversion (ETU) involving ions in the metastable state.

Some of these mechanisms are shown in Figure 25. Figure 25(a) shows possible ESA processes and Figure 25(b) shows possible ETU processes. The origin and dynamics of the blue and green emission is difficult to determine exactly. There are a number of different mechanisms which could lead to this emission and a number of possible upper states that could be the origin level. From experimental evidence and energy considerations, a number of these are shown to be less probable than others. Results indicate that processes involving the metastable state may not be the important process and ETU involving the pump and intermediate levels and/or ESA of pump photons from an intermediate state, process II in Figures 25(a) and 25(b), are the dominant mechanisms leading to blue emission.

The spectra in Figure 21 shows emission in the 380 nm region. The energy of a 735 nm pump photon alone is not large enough to excite an ion in the metastable state to the proposed upper state. (see ΔE in Table VIII) It is possible that the
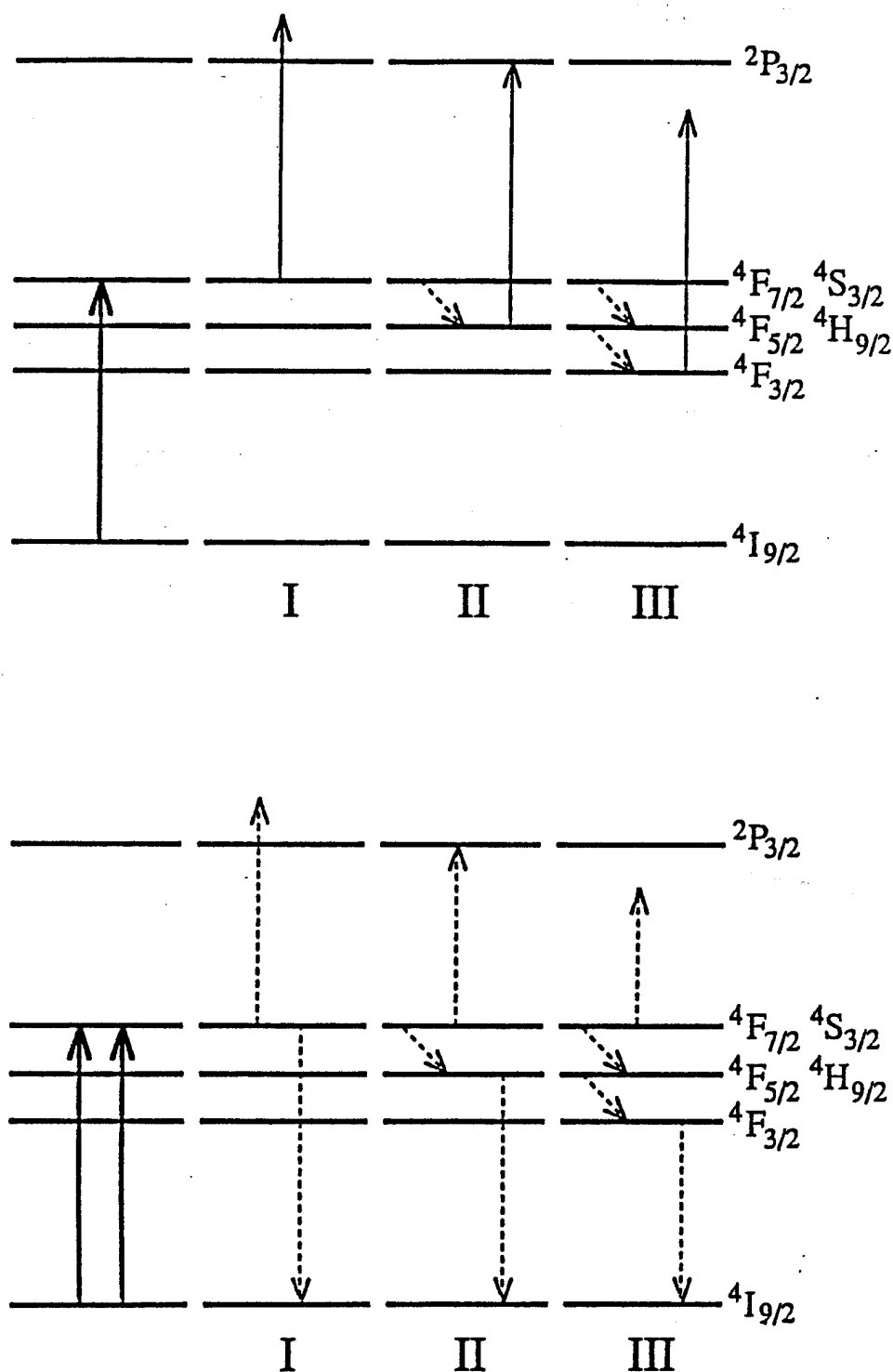
Figure 25. Possible Upconversion Processes. The Top Portion Shows Three Different Excited State Absorption Processes and the Lower Portion Shows Three Different Ion-Ion Energy Transfer Processes.

transition is phonon assisted but this requires absorption of a phonon with an energy of ΔE 1000 cm^{-1} . Although such high energy phonons may be present, at room temperature their number should be small. Additionally, the oscillator strength for the transition determined from the Judd-Ofelt analysis is much smaller than that for other transitions (Table VIII). Energy conservation also indicates that ETU involving ions in the metastable state is not the dominant process. Energy conservation for a transition involving the interaction of a metastable state ion with that of another metastable state ion or an ion in the intermediate band or pump band requires phonons with energy between 1000-3000 cm^{-1} .

Energy transfer upconversion involving ions in the pump and intermediate states could be a resonant process (Figure 25 II). Additionally, ESA of pump photons from the intermediate level (the $^4F_{5/2}$ + $^2H_{9/2}$ levels) is also a resonant process. If energy transfer upconversion is the dominant process then dramatic differences between the ground state absorption spectra and the excitation spectra for the emission are not expected. As long as ions are present in the Stark components of the multiplets involved the process occurs and emission is present.

Excitation spectra for GSGG for the emission at 417 nm is found to be much different than the ground state absorption spectra for the pump region (Figure 23). This is similar to the behavior that was found in YAG [77]. In both cases there are pump wavelengths for which there is strong absorption of the pump photons by the ground state but weak blue fluorescence and regions of weak ground state absorption with strong blue fluorescence. This suggests that the process is very sensitive to pump wavelength and indicates the dominant process is ESA of pump photons rather than ETU.

The Judd-Ofelt analysis can be used to help confirm the identity of the upper level involved in the blue emission by comparing predicted and measured branching ratios. It is known from the Judd-Ofelt analysis that emission from the $^2P_{3/2}$ manifold occurs at wavelengths throughout the visible and near infrared spectral regions. Emission from lower manifolds will overlap this emission in many cases. Thus determining the total integrated intensity of emission and the absolute

branching ratios from the $^2P_{3/2}$ multiplet is not possible. The integrated intensities and relative branching ratios for some of the transitions originating on the $^2P_{3/2}$ multiplet can be determined from Figure 21 and 22. Table IX shows these results and the predicted branching ratios. Only the emission to the three lowest multiplets found in Nd:YAG and Nd:GSGG is considered. It is assumed that the emission to $^4I_{13/2}$ is the amount predicted by the Judd-Ofelt analysis. This value is then used to find the total integrated intensity allowing the branching ratios to the other two lower multiplets to be calculated and compared to those determined from the Judd-Ofelt analysis. Note that the results for GSGG are closer to those predicted than those for YAG. Analysis of the emission from YAG (Figure 21 and 22)) shows a number of lines that can not be assigned to the $^2P_{3/2}$ multiplet. The strong line near 401 nm is the best example of this and has been assigned to the $^2L_{17/2}$ [94]. Additional lines in the spectrum not attributed to $^2P_{3/2}$ are not included in the integrated intensity calculation. However, it is possible that some of the emission in the regions associated with the $^2P_{3/2}$ emission is actually originating on higher lying states and affects the results. The similarities, however, between the predicted and experimentally determined branching ratios indicates the accuracy of the assignment of the $^2P_{3/2}$ manifold as the origin level.

Figure 22 shows emission in the 475-575 nm region. The generation of this green emission is usually attributed to ETU or ESA of NIR photons involving metastable state ions. The excitation spectra of green emission does not show the same wavelength dependence as the blue emission (Figure 21) and is nearly identical to the excitation spectra for the NIR emission and ground state absorption spectra. Energetically, ETU involving ions in the metastable state or ESA of photons at the NIR laser wavelength by metastable state ions can produce excited ions in the multiplets from which green emission is likely to occur. The fact that this emission occurs at pump wavelengths where the blue emission is absent indicates a separate mechanism than that yielding blue emission is responsible. The number of possible upper states and processes involved is such that a detailed assignment of the dynamics is not feasible.

TABLE IX

INTEGRATED INTENSITIES AND COMPARISON
OF BRANCHING RATIOS

Initial Multiplet:	$^2P_{3/2}$		
Terminal Multiplet:	$^4I_{9/2}$	$^4I_{11/2}$	$^4I_{13/2}$
Nd:YAG			
Integrated Intensity	13.4	119	84.3
Measured Branching Ratio	1.59	14.1	9.99
Predicted Branching Ratio	2.55	14.1	16.5
Nd:GSGG			
Integrated Intensity	34.2	255	233
Measured Branching Ratio	2.54	18.9	17.3
Predicted Branching Ratio	2.71	18.9	13.9

Summary and Conclusions

In summary, the combination of a detailed Judd-Ofelt analysis with fluorescence emission and excitation experiments allows for a more detailed analysis of the dynamics involved in monochromatically pumped Nd^{3+} materials. The results of both methods of performing the band groupings in the Judd-Ofelt analysis are similar. The analysis using the multiplet positions from the recent crystal field study by [85-87] is as accurate as that performed previously. Separation of the various manifolds in regions where the Stark components are highly interleaved is shown to be unnecessary.

The origin of a significant portion of the blue emission seen under alexandrite laser excitation is also established. Accurate positions of the Stark components for the upper state and the terminal levels allow for a detailed comparison of observed and predicted emission peaks. This information, combined with comparison of predicted to measured branching ratios, leads to the assignment of the $^2P_{3/2}$ manifold as the origin level for much of the blue emission. The observation of emission at wavelengths not able to be assigned to transitions originating in this state indicates that additional levels and processes are also involved in some cases.

The dynamics involved in producing emission at energies greater than those of the pump photons are also identified here. There are two separate mechanisms, one leading to emission in the 375-475 nm region and one leading to emission in the 475-575 nm region. Emission in the 475-575 nm region shows little pump wavelength dependence and involves energies that are reachable by ion-ion interactions involving metastable state ions or the absorption of photons at NIR wavelengths by metastable state ions. The emission in the shorter wavelength region shows a dramatically different pump wavelength dependence and the energies involved are such that it is unlikely that the metastable state is involved. Additionally, the oscillator strength for excited state absorption of pump photons from the $^4F_{5/2}, ^2H_{9/2}$ multiplets is found to be 100 times weaker than that from the level immediately

above it. This transition is also found to be nearly resonant at the pump wavelengths producing blue emission and non-resonant for pump wavelengths not producing blue emission. Thus it seems likely that the upconversion process involved in generating blue emission originates on this intermediate band and not on the metastable state.

SECTION IV

SPECTROSCOPIC AND LASING PROPERTIES
OF Nd:ZBAN

Introduction

Another material for use in diode pumped laser systems is Nd^{3+} doped fluoride glass. Although laser systems based on rare-earth doped heavy metal fluoride glasses, both in bulk and fiber form, have been reported previously, [95–97] the lasing properties of Nd^{3+} in this type of host have been reported only in a fiber configuration. The results of a study of the spectroscopic and laser properties of Nd^{3+} doped heavy metal fluoride glass in bulk form, including the results of a Judd-Ofelt analysis, are reported here. An alexandrite laser, to simulate diode laser pumping, is used to investigate the laser operation of this material. Two different methods are used to determine the emission cross section of the $^4F_{3/2}$-$^4I_{11/2}$ transition and the results are compared to those reported for an oxide glass, an oxide crystal, and a fluoride crystal host.

Blue and green emission from levels above the metastable state, common in Nd^{3+} doped materials, is observed here and is found to be associated with excited state absorption (ESA) of pump photons. The oscillator strengths for the various excited state absorption transitions that could produce this emission are determined from a Judd-Ofelt analysis in an effort to understand the processes producing this emission. The effect of one of these processes on the slope efficiency is modeled using a rate equation approach [98] and the results provide information on the importance of the excited state absorption on monochromatically pumped Nd:ZBAN laser systems. This model is also used to qualitatively discuss the effects

91

of the ESA mechanism on the efficiency of laser systems based on other Nd^{3+} materials.

Results and Analysis: Spectroscopic Properties

Spectroscopic measurements were made on a sample of Nd^{3+} in ZBAN fluoride glass of dimensions $0.945 \times 0.720 \times 0.335$ cm. The sample used in the study had a mole % composition as follows: 53.33% ZrF_4; 19.84% BaF_2; 3.14% AlF_3; 18.70% NaF; and 5.0% NdF_3 (ZBAN:Nd). The room temperature absorption spectra covering the spectral ranges of 250-2500 nm and 2500-3600 nm were measured using a Perkin-Elmer 330 Spectrophotometer and a Beckman Model 4240 Spectrophotometer, respectively. The absorption spectra and corresponding energy levels are shown in Figure 26. They agree well with earlier results for Zr-Ba-Nd based fluoride glass [99]. The widths of the energy levels shown in Figure 26(c) are determined from the full width half maximum (FWHM) of the corresponding absorption peaks and are associated with the unresolved Stark levels of the upper and lower multiplets involved in the transition. Figure 26(b) is an enlargement of the room temperature absorption spectrum shown in Figure 26(a) and exhibits the positions of the $^2P_{3/2}$, $^2D_{5/2}$, and $^4D_{3/2}$ multiplets. These levels have been found to be involved with excited state absorption of pump photons when monochromatically pumping into the $^4S_{3/2}+^4F_{7/2}$ and $^2H_{9/2}+^4F_{5/2}$ levels of Nd^{3+} doped materials [77,80,82–84]. The absorption spectrum of Nd^{3+} in ZBAN glass covering the spectral range of 720-820 nm is shown in Figure 27. This corresponds to the spectral range of a tunable alexandrite laser.

Emission spectra and lifetime measurements were made using a nitrogen laser-pumped dye laser system. The dye laser contained Rhodamine 590 dye lasing at 575 nm and had a pulse duration of 10 ns. Emission from the sample over the spectral range of 760-1180 nm was focused into a 1 m Spex monochromator and detected by an RCA 7102 photomultiplier tube. The emission spectrum was recorded with the use of a PAR Model 164 Boxcar Integrator and a strip chart
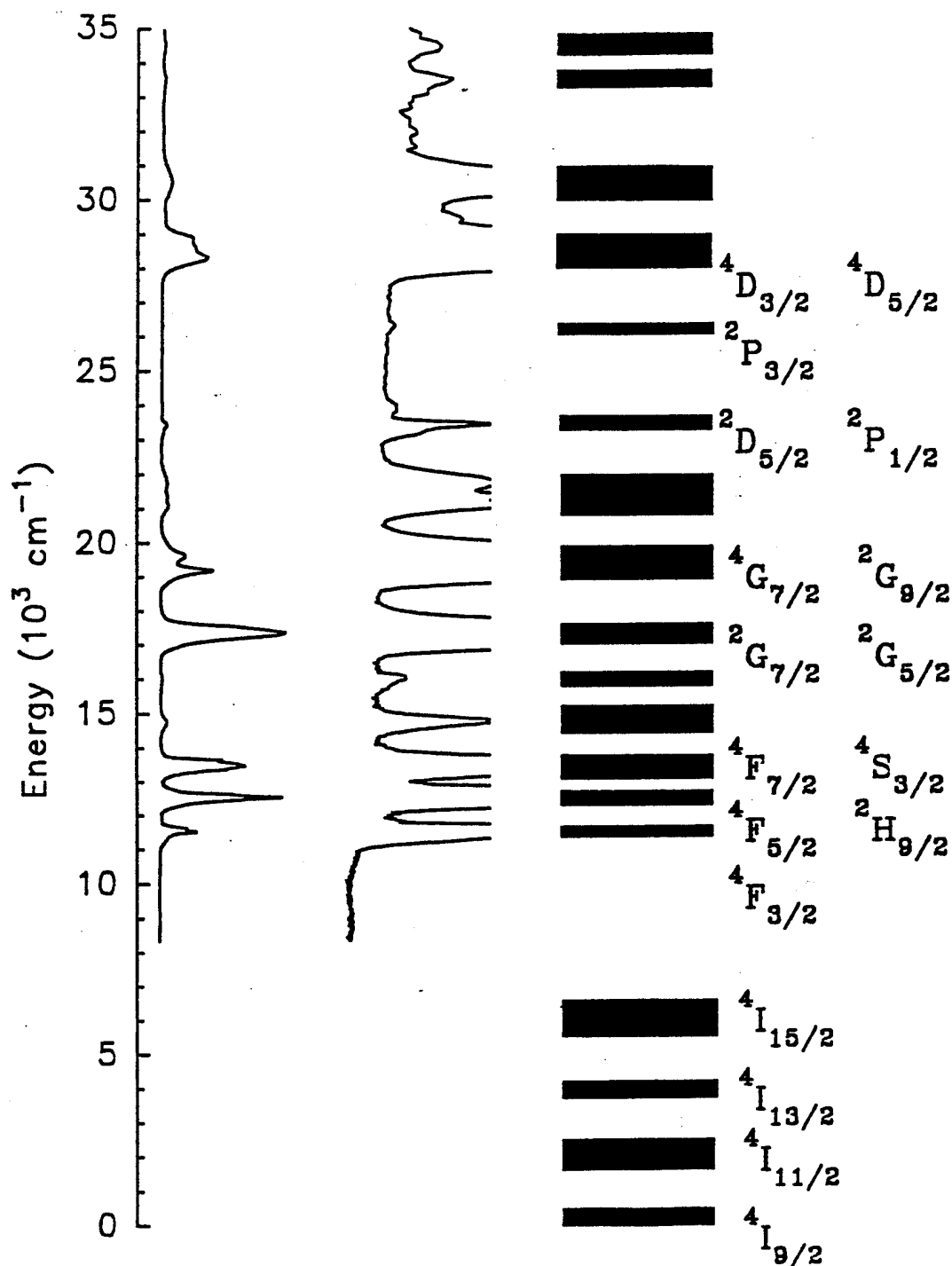
Figure 26. Absoption Spectra and Energy Level Diagram in Nd:ZBAN. (a) Absorption Spectrum of Nd:ZBAN.(b) The Absorption Spectrum in (a) Expanded to Show Details. (c) Energy Level Diagram of Nd:ZBAN with Widths Calculated from the FWHM of the Absorption Spectra.
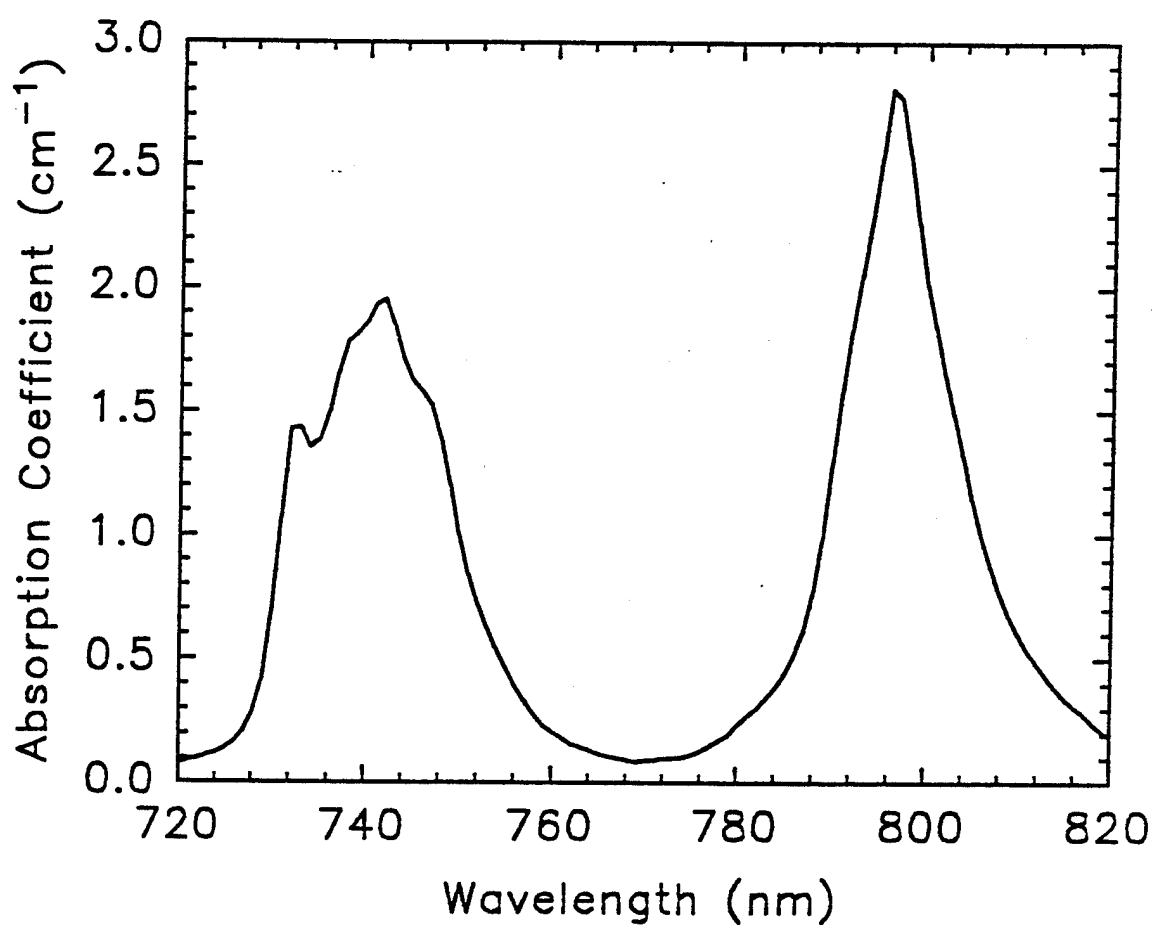
Figure 27. Absorption Spectrum of Nd:ZBAN in the Spectral Region of Alexandrite Laser Output.

recorder. For lifetime measurements an EG&G Model 4402-4420 boxcar averager signal processor combination was used.

The emission from the $^4F_{3/2}$ level of Nd^{3+} is shown in Figure 28 and can be used to determine the spectral width of the ground state manifold and the spectral location of the $^4I_{11/2}$ level shown in Figure 26. An effective linewidth of the $^4F_{3/2}$-$^4I_{11/2}$ transition, $\Delta\nu_{eff}$, can be determined by numerically integrating the emission line shape. A value for $\Delta\nu_{eff}$ of 278.8 cm^{-1} is obtained. The temperature dependence of the fluorescence lifetime is shown in Figure 29. The lifetime increases from 130 μs at room temperature to $\approx$ 400 μs at 10 K.

Table X contains the oscillator strengths determined experimentally and those calculated using the Judd-Ofelt theory along with the Judd-Ofelt parameters. The value of n for each transition was based upon that in Ref. [16]. A value of 1×10^{-6} was found for the rms deviation. For many of the weaker transitions the experimentally determined values differ significantly from those predicted from the model and in most cases the measured values for these transitions are larger than those predicted. The Judd-Ofelt parameters found here correspond well with those found in other fluoride glasses. [99–101] The Judd-Ofelt parameters can be used to calculate the oscillator strengths for excited state to excited state transitions also. Results of these calculations for transitions to the $^2P_{3/2}$ multiplet are listed in Table XI. Table XII lists the transition rates and branching ratios for emission from this multiplet. The lack of reduced matrix elements for transitions between the $^2D_{5/2}$ and $^4D_{3/2}$ multiplets and other excited states prohibits similar calculations for these multiplets.

The stimulated emission cross section can be determined from spectroscopically determined parameters using

$$\sigma_e = \frac{\lambda_p^2}{8\pi n^2 c} g(\nu) A\left[^4F_{3/2};^4 I_{11/2}\right] \tag{86}$$

where λ_p is the peak emission wavelength, n is the index of refraction of the material, $g(\nu)$ is the lineshape of the transition, and $A[^4F_{3/2};^4 I_{11/2}]$ is the radiative transition probability for this transition. The radiative transition probability is
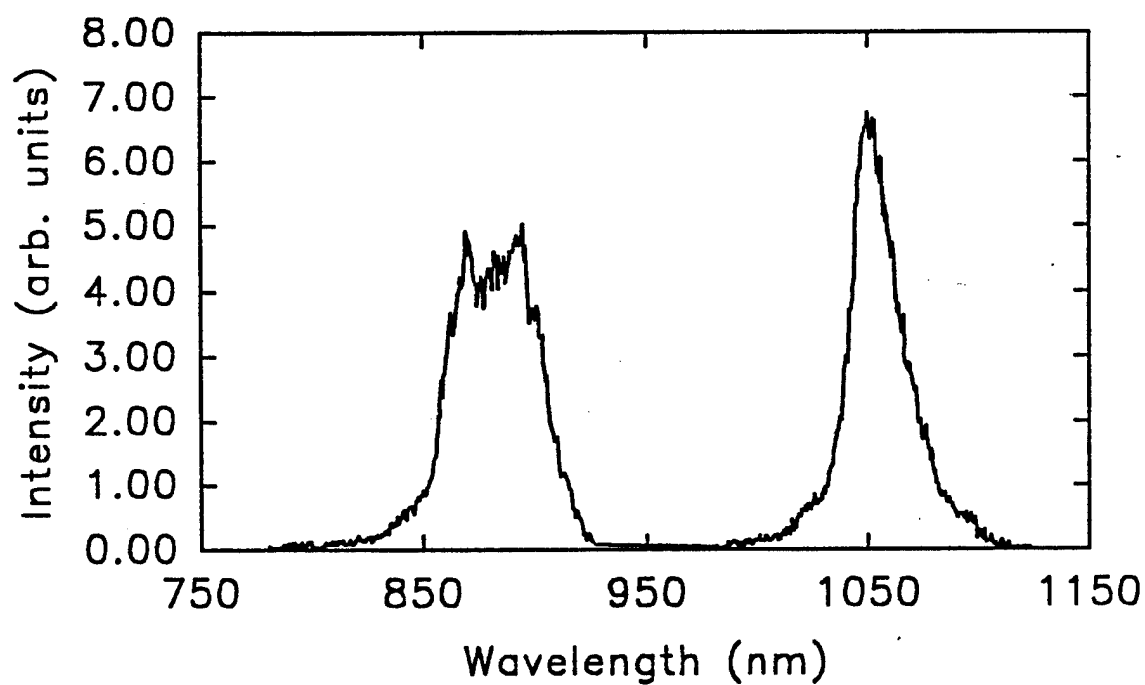
Figure 28. Room Temperature Emission Spectrum of Nd:ZBAN. Excitation at 575 nm. The effective linewidth of the $^4F_{3/2}$-$^4I_{11/2}$ transition is 278.8 cm^{-1}.
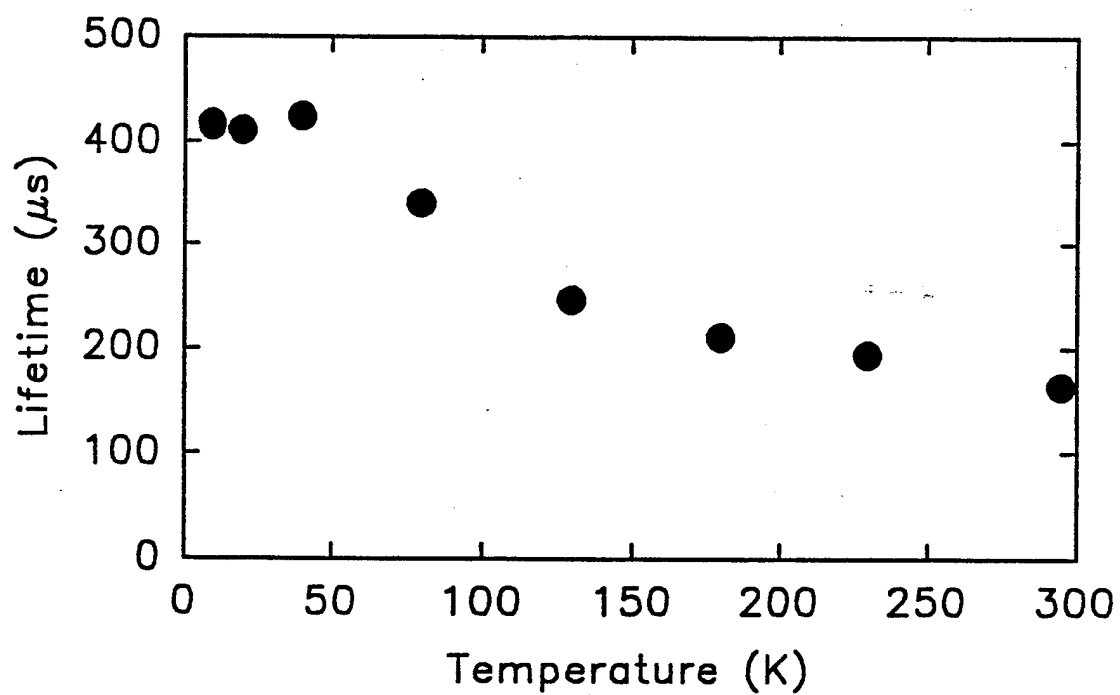
Figure 29.   Temperature Dependence of the Metastable State Lifetime of Nd:ZBAN.

TABLE X

OSCILLATOR STRENGTHS FOR TRANSITIONS
FROM THE GROUND STATE
FOR Nd:ZBAN

Band	Wavelength (nm)	Oscillator Strength ($\times 10^{-8}$)		Residuals ($\times 10^{-8}$)
		Measured	Calculated	
1	868	227.1	195.3	31.7
2	796	752.9	719.1	33.8
3	708	753.0	823.7	-70.7
4	677	102.2	58.6	43.5
5	624	35.4	16.4	19.0
6	576	1389.0	1401.0	-12.0
7	521	659.7	510.3	149.4
8	474	203.6	76.1	127.4
9	427	59.2	53.9	5.3
10	380	11.2	2.5	8.6
11	353	935.5	990.4	54.9
12	328	241.1	52.5	188.6

$$\Omega_2 = 3.09 \times 10^{-20}$$

$$\Omega_4 = 3.65 \times 10^{-20}$$

$$\Omega_6 = 5.74 \times 10^{-20}$$

Radiative Lifetime of the $^4F_{3/2}$-$^4I_{11/2}$ Transition

Measured	Calculated
420 μs	360 μs

TABLE XI

TRANSITION PROBABILITIES AND BRANCHING RATIOS FROM THE $^2P_{3/2}$ MULTIPLET FOR Nd:ZBAN

Terminal	λ (nm)	A (s^{-1})	β (%)
$^4I_{9/2}$	380	68.8	2.73
$^4I_{11/2}$	411	370.3	14.71
$^4I_{13/2}$	445	508.5	20.20
$^4I_{15/2}$	491	81.3	3.23
$^4F_{3/2}$	675	13.6	0.54
$^4F_{5/2},^2H_{9/2}$	727	770.1	30.59
$^4F_{7/2},^4S_{3/2}$	822	22.5	0.89
$^4F_{9/2}$	866	457.4	18.17
$^2H_{11/2}$	972	88.3	3.51
$^4G_{5/2},^2G_{7/2}$	1117	7.0	0.28
$^4G_{7/2},^4G_{9/2},^2K_{13/2}$	1404	123.7	4.91
$^2D_{3/2},^4G_{11/2},^2K_{15/2}$	1916	5.8	0.23
$^2P_{1/2},^2D_{5/2}$	3452	0.5	0.01

Total Transition Probablity Rate: 2517.8 s^{-1}

TABLE XII

OSCILLATOR STRENGTHS FOR TRANSITIONS TO
THE $^2P_{3/2}$ MULTIPLET
FOR Nd:ZBAN

Initial Multiplet	λ (nm)	f $(\times 10^{-8})$
$^4F_{3/2}$	676	4.01
$^4F_{5/2}$	727	6.32
$^2H_{9/2}$	727	101
$^4F_{7/2}$	820	0.78
$^4S_{3/2}$	820	8.26

difficult to determine directly but the probability rate for an electric dipole transition from the $| (S, L)J >$ manifold to the $| (S', L')J' >$ manifold can be obtained from the results of the Judd-Ofelt analysis. From Equation (13) a value for the radiative transition probability can be determined. For $\lambda_p = 1048$ nm the important rate is $A[^4F_{3/2};^4 I_{11/2}]$ and has a value of 1380 s^{-1}. Using Equation (86) yields a stimulated emission cross section of 3.2×10^{-20} cm^2 at this wavelength.

The fluorescence lifetime at room temperature is ≈ 130 μs which is much shorter than that predicted by the Judd-Ofelt analysis using Equation (15). Concentration quenching in Nd doped heavy metal fluoride glasses, previously reported [101–103], can account for this difference. The lifetime measured here at room temperature corresponds well with that determined in others glasses with similar concentrations of Nd^{3+}. The process responsible for this quenching is most likely a cross relaxation process in which a metastable state ion relaxes to the $^4I_{15/2}$ multiplet exciting a nearby ion from the ground sate to the $^4I_{15/2}$ multiplet. The longer lifetime found at low temperatures, nearly that predicted by the Judd-Ofelt theory and that found in low concentration glasses where cross relaxation is less important, indicates that the cross relaxation process is less important at low temperatures.

The emission cross section reported here for a Nd:ZBAN glass is slightly greater than that reported in ED-2, a standard oxide glass host, and much less than that in either crystal.(Table XIII) It is typical of that previously reported in a number of fluorozirconate glasses. [99,101,100,104] The radiative lifetime of the metastable state, determined from the Judd-Ofelt analysis, is nearly that reported for ED-2 and is close to that reported for other fluoride glasses.

Results and Analysis: Laser Properties

The emission of an alexandrite laser was used to side and end pump the sample in an optical cavity. The 30 cm long cavity consisted of a high reflector with a 50 cm radius of curvature and flat output couplers with varying transmittances. When end pumping a high reflector coated for high transmission over the pumping

TABLE XIII

COMPARISON OF Nd^{3+} EMISSION CROSS SECTIONS
AND RADIATIVE LIFETIMES IN
DIFFERENT HOSTS

	ED-2[a]	YAG[b]	YLF[c]	ZBAN
Emission Cross Section ($\times 10^{-20} cm^2$)	2.7	30.0	18	3.20
Raditive Lifetime μs	359	250	570	420
Peak Wavelength (nm)	1062	1064	1047	1048
Effective Linewidth (cm^{-1})	305	-	-	278

a From Ref. [105]
b From Ref. [5]
c From Ref. [106]

range was used. Laser output was monitored while the alexandrite pump laser was tuned over the range 735-760 nm. No lasing of the sample was detected for pump wavelengths outside this spectral range. The transverse pump geometry shown in Figure 30 was used to investigate the time resolved and emission properties of the Nd:ZBAN sample under alexandrite pumping. Time-resolved measurements were made of the output of the alexandrite laser and the output of the Nd:ZBAN glass laser using photodiodes and a Tektronix Model 2440 Digital Oscilloscope. A 2.0 neutral density filter was used in order to avoid saturation of the detector by the alexandrite pump pulse. The emission from the Nd:ZBAN sample was monitored while the material was lasing at 1.048 μm using a 0.25 m spectrometer and a C31034 photomultiplier tube which is sensitive in the visible spectral range. The signal was analyzed with a PAR model 164 boxcar averager and recorded on a strip chart recorder. Appropriate filters were used to eliminate scattered light from the alexandrite laser.

Measurements of the threshold energies and slope efficiencies with various output couplers were made using the experimental set-up shown in Figure 31. The pump beam was focused within the lowest order cavity mode using a convex lens. Simultaneous measurements of the average pulse energies of the alexandrite laser incident upon the sample and of the laser emission of the Nd^{3+} ions in the ZBAN glass were made using a dual probe energy meter.

Figure 32(a) shows the results of the the time-resolved measurements of the 1.048 μm laser emission and the alexandrite laser emission averaged signal over 256 pulses. The upper trace is the alexandrite pump pulse and the lower trace is the corresponding laser output of the Nd:ZBAN glass. Figure 32(b) shows the behavior of both the pump laser and the laser output from the sample for a single pump pulse. The short delay of the output from the sample with respect to the pump pulse is the time needed to establish the population inversion. After the short delay the traces show the relaxation oscillation and spiking characteristic of many solid state laser systems.

Oscilloscope

Alexandrite Laser

Trigger

CyL

CL

HR

Sample

Photodiode

OC

CL

Boxcar
Averager

Stripchart
Recorder

.25 m
Spectrometer

C31034
PMT

OC: Output Coupler
HR: High Reflector
CL: Convex Lens
CyL: Cylindrical Lens
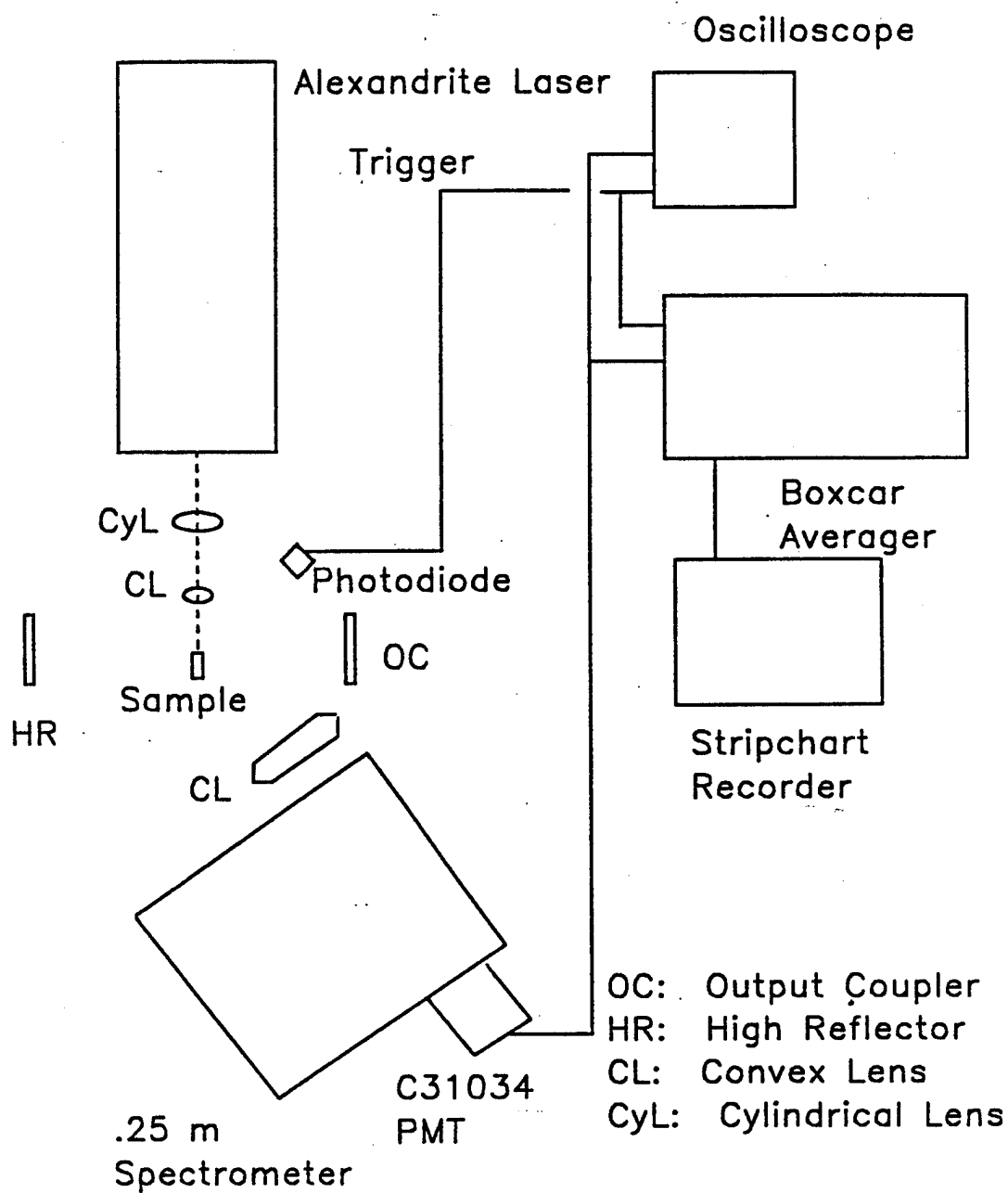
Figure 30. Experimental Set-Up for Transverse Laser Pumped Laser Experiments.

Alexandrite Laser

BS   Sample   BS

HR   OC   F

Probe   Probe

BS: Beam Splitter
HR: High Reflector
OC: Output Coupler
F :   Filter

Energy Meter
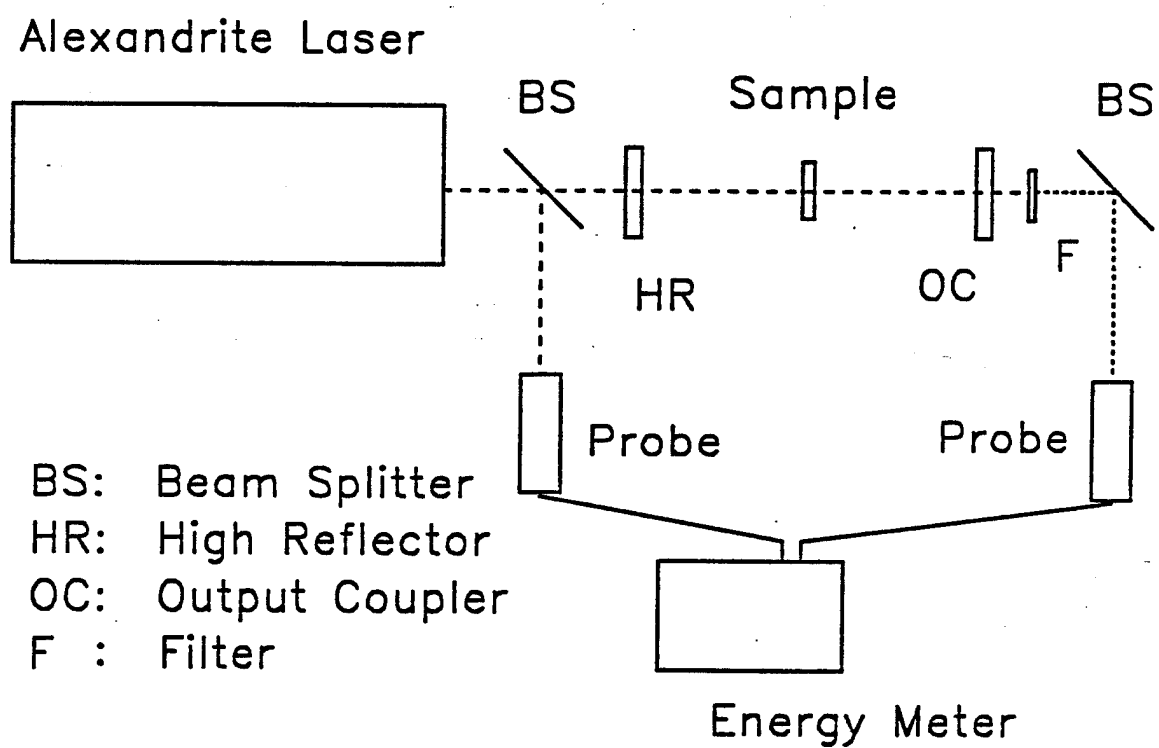
Figure 31. Experimental Set-Up for Longitudinal Laser Pumped Laser Experiments.
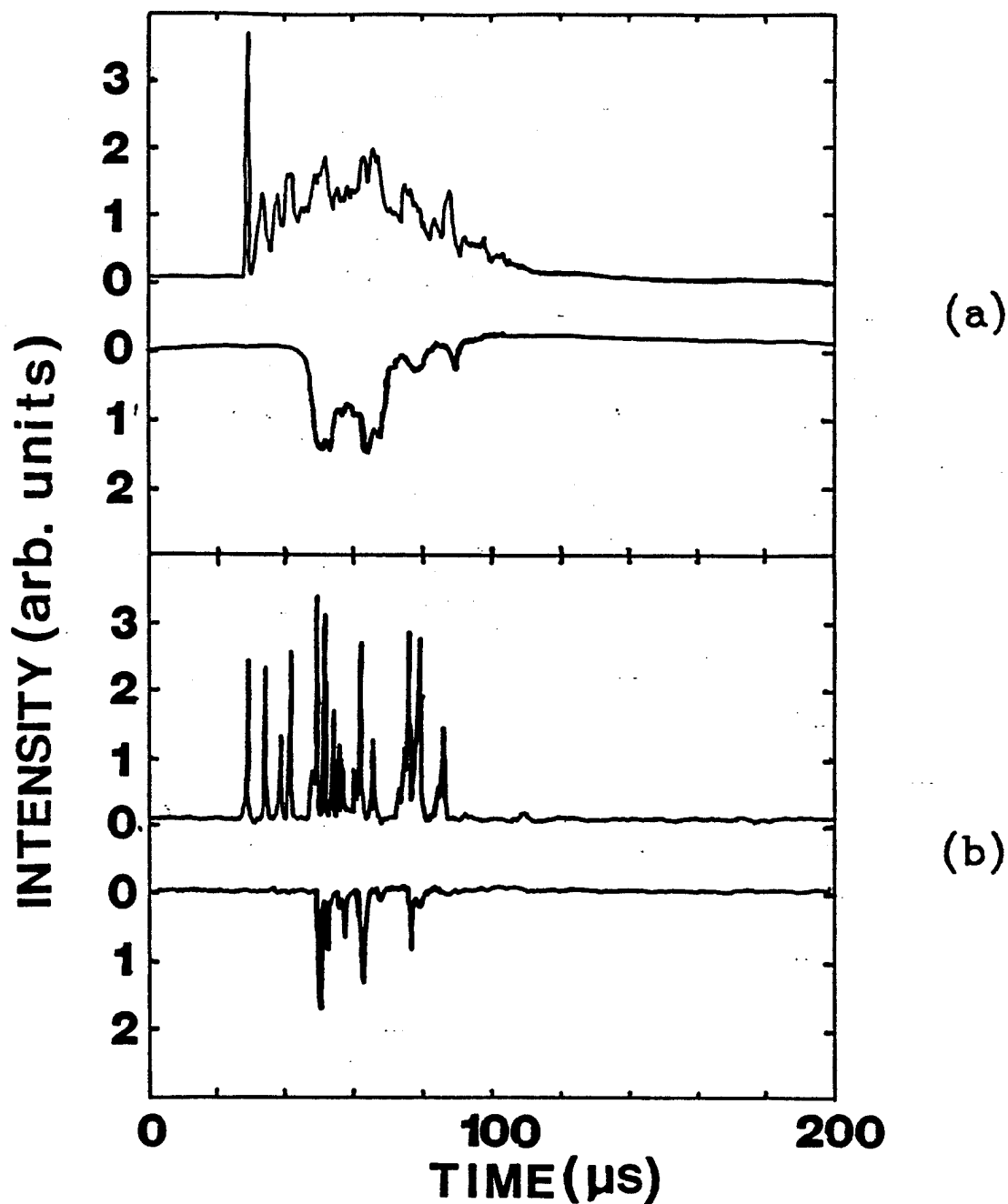
Figure 32. Temporal Output of Alexandrite Laser and Nd:ZBAN Laser (a) Output Intensity of Pump (Upper Trace) and Nd:ZBAN (Lower Trace) Averaged over 256 Pump Pulses. (b) Single Shot Time Resolved Output of the Pump Pulse (Upper Trace) and Nd:ZBAN Lasing Pulse (Lower Trace).

Figure 33 shows examples of the results obtained for measurements of the laser energy output as a function of pump energy absorbed. The deviation from a straight line relationship at high levels of power absorbed is due to several effects including saturation and thermal lensing.

The lasing thresholds and slope efficiencies can be obtained from the data above. Table XIV summarizes the results for the various pump wavelengths and output couplers. From these results, values for the passive losses in the system, the emission cross section and the relative effects of excited state absorption of pump photons on laser efficiency are determined.

The emission cross section is related to the threshold energy and mirror reflectivities by the expression [107,108]

$$-\ln(R) = M_e E_T - L \tag{87}$$

where E_T is the absorbed energy at threshold, L is the passive loss per pass through the cavity at the laser wavelength, R is the product of the effective reflectivities of the cavity mirrors, and M_e is the slope of the E_T vs.$\ln 1/R$ plot. R is given by [107,109]

$$R = R_{hr} \left(\frac{R_f^{1/2} + R_{oc}^{1/2}}{1 + (R_f R_{oc})^{1/2}} \right) \tag{88}$$

where R_f is the Fresnel reflection coefficient of the sample surface, R_{oc} is the reflectivity of the output coupler and R_{hr} is the reflectivity of the high reflector. The slope M_e can be written as [108]

$$M_e = \frac{8 f_B \sigma_{eff} \eta_p}{h \nu_p \pi d^2} \tag{89}$$

where η_p is the pump efficiency, f_B is the fraction of the population in the lower Stark component of the metastable state, $\pi d^2/4$ is the area of the pump beam, $h\nu_p$ is the energy of a pump photon, and σ_{eff} is the effective emission cross section. The effective emission cross section is defined as $\sigma_e - \sigma_{EA}$ where σ_e is the emission cross section and σ_{EA} is the excited state absorption cross section for photons at
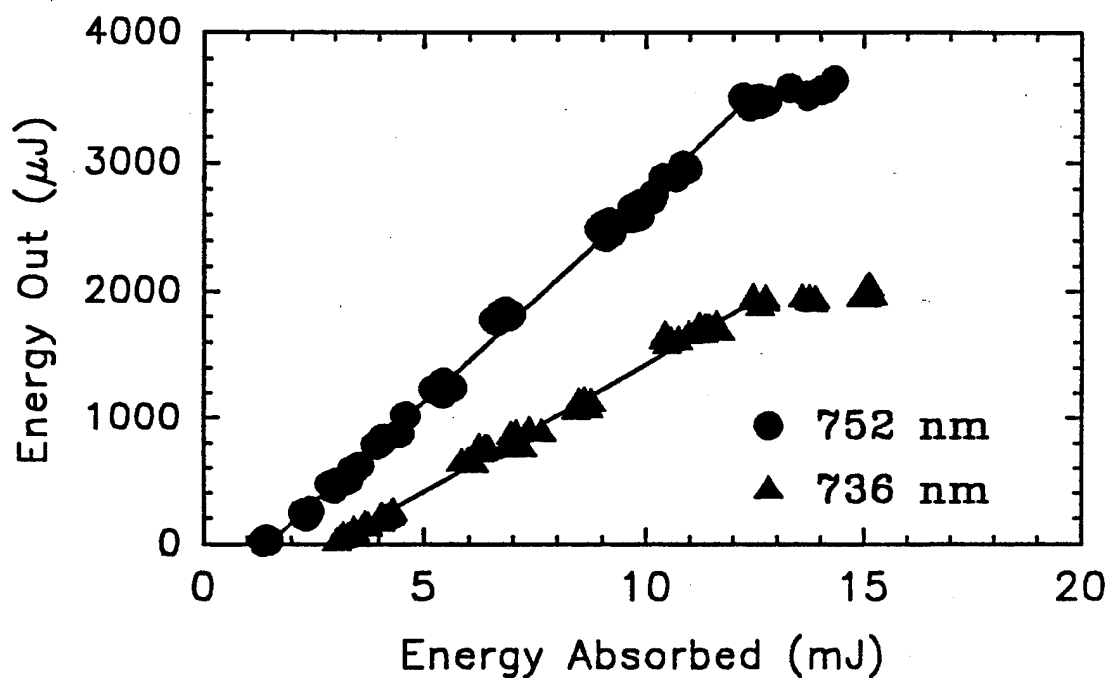
Figure 33. Nd:ZBAN Energy Out vs. Alexandrite Energy Absorbed. Data Shown for Pump Wavelengths of 752 nm (circles) and 736 nm (triangles). The Lines are a Best Fit to the Data.

TABLE XIV

SUMMARY OF THRESHOLD ENERGY AND
SLOPE EFFICIENCY MEASUREMENTS

Run	Pump Wavelength (nm)	Output Coupler	R	ET (mJ)	η_s %
1	752	2	0.93	1.08	36.4
2	752	3	0.85	2.73	20.8
3	752	1	0.93	1.49	32.2
4	752	2	0.93	1.74	31.8
5	736	1	0.93	2.95	20.2
6	736	2	0.93	2.28	33.1
7	736	3	0.85	4.44	16.0

the laser wavelength. Output couplers 1 and 2 have the same value of R_{oc} to within experimental error. Figure 34 shows a plot of $-\ln R$ vs. threshold energy absorbed. The lines drawn in Figure 34 pass through the average threshold energy of runs 1, 3, and 4 for the 752 nm case and runs 5 and 6 for the 736 nm case. From these plots values for M_e of 72/J and 51/J and values for L of 0.034 and 0.063 were obtained for 752 nm and 736 nm pump wavelengths respectively.

Rewriting Equation (89) yields

$$\eta_p \sigma_{eff} = \frac{h\nu_p \pi d^2 M_e}{8 f_B}. \tag{90}$$

The fractional Boltzmann population of the lower Stark component of the $^4F_{3/2}$ can be found from

$$f_B = \left[\exp\left(\frac{-\Delta E}{k_B T}\right) + 1\right]^{-1} \tag{91}$$

where ΔE is the Stark splitting of the metastable state, k_B is Boltzmann's constant, and T is the temperature in Kelvin. ΔE was approximated as 90 cm^{-1}, typical of the crystal field splitting for the $^4F_{3/2}$ multiplet. At room temperature $k_B T$ is 207 cm^{-1} giving a value for f_B of 0.61. The area of the pump beam was measured to be ≈ 0.001 cm^2. The effective emission cross section and pump efficiency for each wavelength used can be found from Equation (90)

$$\eta_p^{752} \sigma_{eff} = 1.57 \times 10^{-20} cm^2 \tag{92}$$

$$\eta_p^{736} \sigma_{eff} = 1.13 \times 10^{-20} cm^2 \tag{93}$$

where the superscripts label the pump wavelength.

It is possible to relate the measured slope efficiencies to $\eta_p \sigma_{eff}$. In the limit of low output coupling [110,111]

$$\eta_s = \frac{\lambda_p}{\lambda_l} \frac{\eta_p \sigma_{eff}}{\sigma_e} \frac{C_o}{C + L} \tag{94}$$
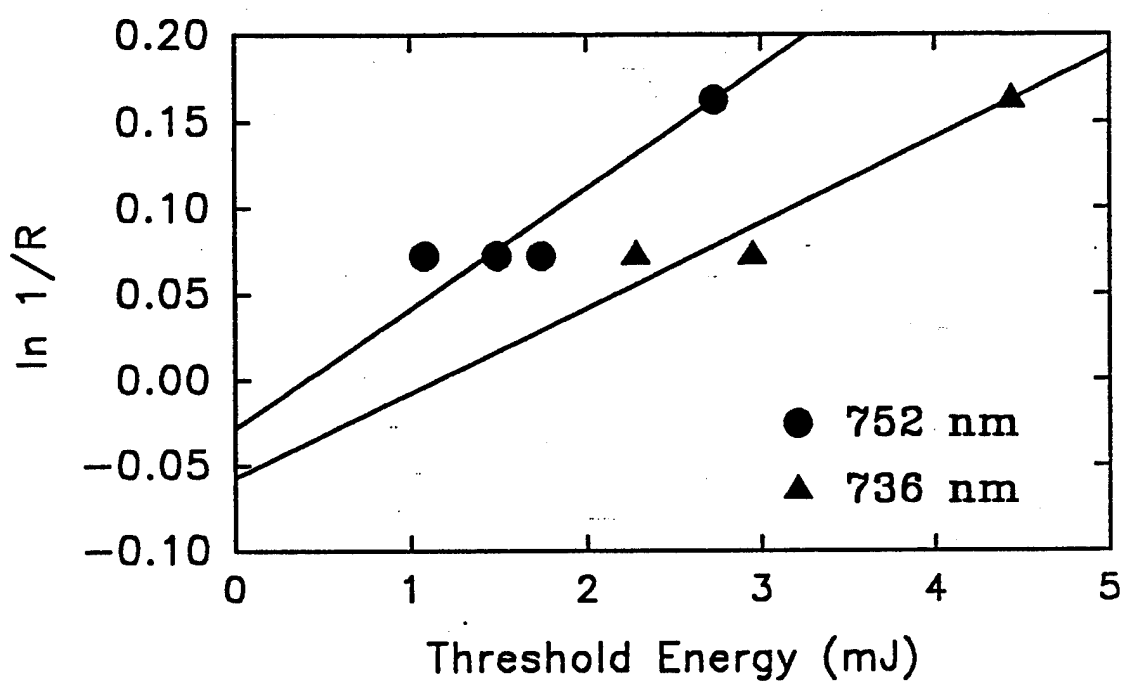
Figure 34. Plot of ln 1/R vs. Threshold Energy Absorbed. The y Intercepts are the Passive Losses in the System and the Slopes are Related to the Emission Cross Section. Data Shown for Pump Wavelengths of 752 nm (circles) and 736 nm (triangles).

where η_s is the slope efficiency, λ_p and λ_l are the pump and laser wavelengths respectively, C_o is the effective output coupling, C is the total transmission of the mirrors and the other parameters have their previous meanings. Rewriting and solving for σ_e gives

$$\sigma_e = \frac{\lambda_p}{\lambda_l} \frac{\eta_p \sigma_{eff}}{\eta_s} \frac{C_o}{C+L}. \tag{95}$$

Restricting the analysis to the lower transmission output couplers (1 and 2) and letting $C = C_o$ ($R_{hr} = 1$) values for σ_e of 2.25×10^{-20} cm^2 and 1.56×10^{-20} cm^2 are found from the parameters for 752 nm and 736 nm respectively.

One possibility that would produce different emission cross sections for different pump wavelengths is a change in pump efficiency with wavelength. Comparison of the values for $\eta_p \sigma_{eff}$ at the two different pump wavelengths indicates that the pump efficiency at 736 nm is less than that at 752 nm if the cross sections are wavelength independent. The effective emission cross section should be independent of pump wavelength giving $\eta_p^{736} = 0.72 \ \eta_p^{752}$. An increase in the energy absorbed for threshold and a lower slope efficiency at the 736 nm pump wavelength lead to the calculation of a reduced pump efficiency for this wavelength using Equations (87), (89), and (94).

Alternatively, the difference between the emission cross sections calculated from the slope efficiency measurements at the two wavelengths could be an indication of the uncertainties in the calculation. In this case the pump efficiencies are similar. Since the emission cross section should be independent of pump wavelength, differences between the values for 752 nm and 736 nm would be attributed to the uncertainties in the measured slope efficiencies, threshold energies and in the extrapolation used to find the passive losses.

Figure 35(a) shows an example of the emission spectra with an excitation wavelength of 755 nm and the emission spectra in Figure 35(b) is that for a pump wavelength of 735 nm. Note the similarities to the spectra observed for Nd:YAG and Nd:GSGG in Chapter IV. The analysis in this case is made more difficult by the broadened absorption and emission peaks in the fluoride glass and the lack

of detailed knowledge of the Stark level positions. The two green peaks centered at 530 nm and 595 nm have been reported earlier in other Nd^{3+}-doped materials [77,80,82–84] and can be attributed to transitions from the $^4G_{7/2}$ and $^2G_{9/2}$ energy levels to the ground state and the $^2G_{7/2}$ and $^2G_{5/2}$ levels to the ground state, respectively. The transitions leading to the blue (365-460 nm) emission spectra observed under alexandrite laser excitation (Figure 35) cannot be definitely identified but from conservation of energy arguments transitions from the $^2P_{3/2}$, $^4D_{3/2}$, and $^4D_{5/2}$ to the ^4I_J levels seem to be the most probable. The upper state could be populated via resonant excited state absorption of pump photons from the $^4F_{3/2}$, $^4F_{5/2}$, $^2H_{9/2}$ or $^4F_{7/2}$, $^4S_{3/2}$ multiplets. The oscillator strength for ESA process involving the $^2P_{3/2}$ and the $^4F_{5/2}$, $^2H_{9/2}$ multiplets is much larger than that for transitions originating on either the metastable level or the pump level, similar to the results for Nd:YAG and Nd:GSGG. (Table XII) However, other transitions to $^4D_{3/2}$ and $^4D_{5/2}$ multiplets from the pump level and to the $^2P_{3/2}$ from the metastable state are nearly resonant for the 735 nm pump wavelength. Both of these transitions are resonant to within 500 cm^{-1}, the energy of a high energy phonon in fluoride glasses [102,103], and will assist in populating the upper states. For the 755 nm pump wavelength the transition from the pump level to the $^2P_{3/2}$ multiplet is nearly resonant but the other transitions are not.

A comparison of Figures 35a and 35b leads to the following conclusions. At shorter pump wavelengths the blue emission is the most intense. As the excitation wavelength is shifted to lower energies the blue emission decreases and the green emission becomes more intense. This decrease in the blue emission can be attributed to the loss of resonance between the pump photon energy and the energy difference between the $^4F_{5/2}$,$^2H_{9/2}$ and $^2P_{3/2}$ multiplets and between the $^4D_{3/2}$ and $^4D_{5/2}$ multiplets and the pump level. The increase in intensity of the green emission may be due to nonresonant excited state absorption of pump photons with the energy mismatch compensated for by phonon emission and to increased output of the alexandrite laser at 755 nm as compared to 735 nm. The important observation, however, is the pump wavelength dependence of the emission. The
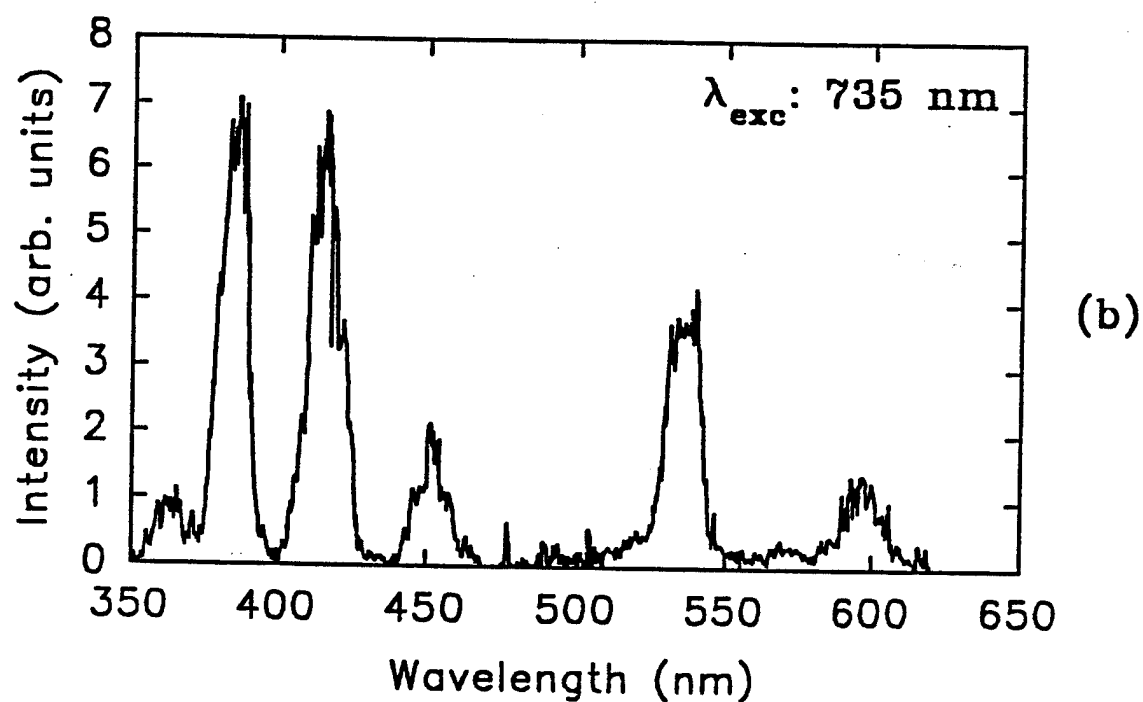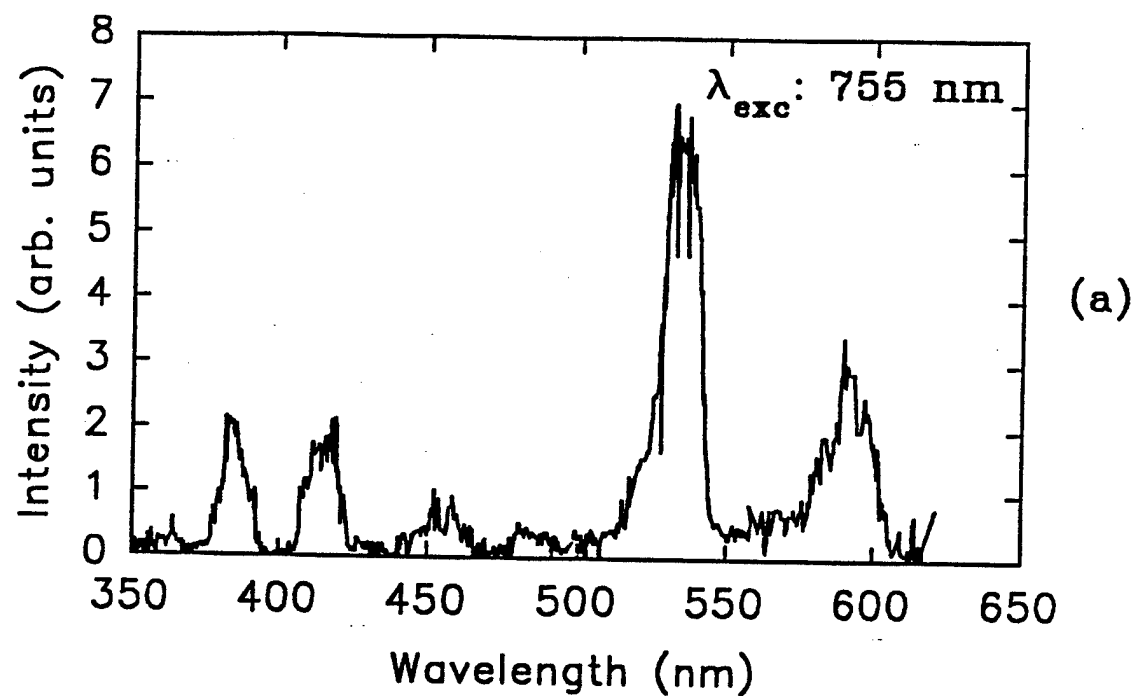
Figure 35. Emission Spectra of Nd:ZBAN in the Blue-Green Spectral Region with Alexandrite Excitation. Pump Wavelength of (a) 755 nm and (b) 735 nm.

relative intensities of the blue and green emission change with pump wavelength. Therefore the process leading to the emission is pump wavelength dependent and, of the processes that could lead to blue emission, only ESA of pump photons is pump wavelength dependent.

Excited State Absorption Model

Excited state absorption of pump photons (ESA) may be a loss mechanism in Nd^{3+} doped laser hosts.[77,84] Here a model which describes the effects of ESA on both the metastable state population and the total energy circulating in the cavity at the output wavelength is presented. The model used is a modified version of the standard Nd^{3+} four level model and is shown in Figure 36. Two additional levels are added, an intermediate level between the pump level and the metastable state and a second level at a higher energy than the pump level. The second level is located such that it is in resonance with the added intermediate level at the pump energy. Since the transition between levels 4 and 6 is in resonance with the pump laser it is possible for excited state absorption of pump photons to occur.

The rate equations describing this model are written as follows:

$$\dot{n}_1 = -R_{15} + R_{51} + A_{61}n_6 + A_{31}n_3 + W_{21}n_2 - W_{12}n_1 \tag{96}$$

$$\dot{n}_2 = +R_{32} - R_{23} + A_{32}n_3 - W_{21}n_2 + W_{12}n_1 + W_{eff}n_3 \tag{97}$$

$$\dot{n}_3 = -R_{32} + R_{23} - \tau_3^{-1}n_3 + A_{63}n_6 + W_{43}n_4 - W_{34}n_3 - W_{eff}n_3 \tag{98}$$

$$\dot{n}_4 = -R_{46} + R_{64} + A_{64}n_6 - W_{45}n_4 + W_{54}n_5 - W_{43}n_4 + W_{34}n_3 \tag{99}$$

$$\dot{n}_5 = +R_{15} - R_{51} + A_{65}n_6 + W_{45}n_4 - W_{54}n_5 \tag{100}$$
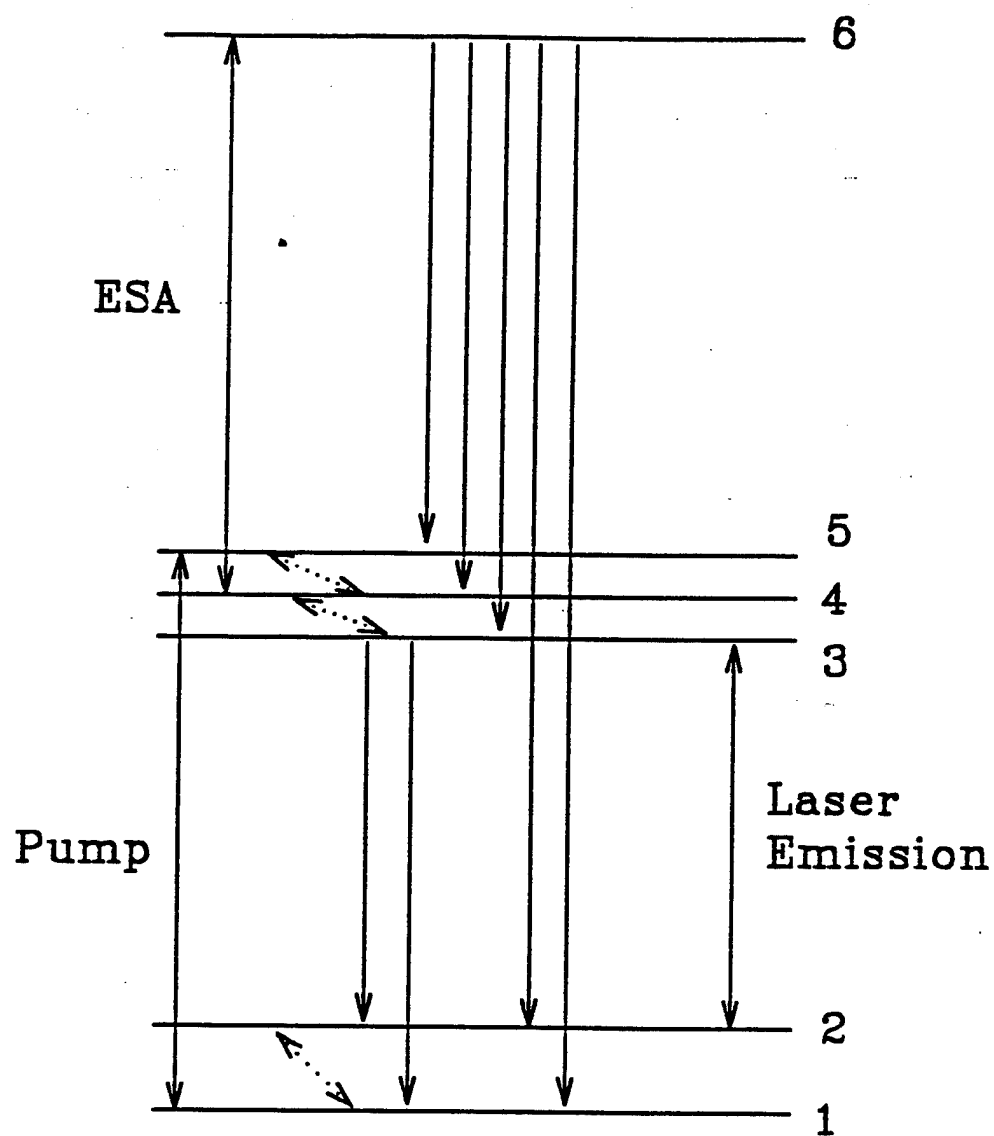
Figure 36. Model of Nd:ZBAN Laser System.

$$\dot{n}_6 = +R_{46} - R_{64} + \tau_6^{-1} n_6 \tag{101}$$

$$\dot{n}_p = +R_{32} - R_{23} - \tau_c^{-1} n_p + \omega_{el} n_3 \tag{102}$$

For transitions resonant with either the pump laser wavelength or the output laser wavelength both stimulated emission and absorption are included. Fluorescence is allowed from the metastable state to both the ground state, level 1, and the first excited state, level 2. Fluorescence from the upper excited state (6) can occur to each of the excited states and the ground state. Levels 2, 4, and 5 are assumed to decay only non-radiatively.

The population of each level and the photon density is determined from a numerical solution of the rate equations by a fourth order adaptive Runge-Kutta method. The parameters used are listed in Table XV and are representative of those for Nd^{3+} in a fluoride glass host. Non-radiative ion-ion cross relaxation, which reduces the lifetime of the metastable state, is modeled simply as an additional relaxation process (W_{eff}) populating the terminal laser level. The emission cross section for the pump transition is found from the measured absorption cross section and Equation (61). This equation and the spectroscopically determined emission cross section for the laser wavelength are used to find the absorption cross section at the output laser wavelength. Since the exact positions of the Stark levels are not known for the fluoride glass, Z_l and Z_u are approximated by their values in other Nd^{3+} materials.[5,86,87,112] Values for Z_l for the lower level of the pump transition vary from ≈ 2.1 to ≈ 2.7 and values for Z_u for the upper level of the pump transition vary from ≈ 3.0 to ≈ 3.8. A value for Z_l/Z_u for the pump transition used here is 0.7. For the laser transition, values for Z_l vary from ≈ 3.0 to ≈ 4.0 and values for Z_u vary from ≈ 1.6 to ≈ 1.8. This gives a value for Z_l/Z_u of 2 for the laser transition. The zero line energy, E_{zl}, is approximated as the energy of the transition so that $E_{zl} - h\nu$ is zero for both cases. The non-radiative rates listed in the table labeled by A are representative non-radiative decay rates in fluoride glasses found from the energy gap law, Equation (22), using values for

the parameters C and α found in Ref. [113]. The second set of rates, labeled B, are representative of rates much faster than those predicted by the energy gap law as suggested by recent measurements of small energy gap multiphonon rates. [24,27,91] The relaxation rate for the lower laser level is approximated based on recent measurements in a variety of materials. [24,26,27,91] The alexandrite pump laser pulse is modeled with a series of 300 ns pulses of constant flux separated by ≈ 4 μs in a 40 μs envelope. The flux used used corresponds to an incident energy of 17 mJ per 40 μs pulse train focused within the lowest order mode of the cavity.

The results of the numerical solution for the metastable state population and the photon density over the first 400 ns using the smaller multiphonon rates are shown in Figure 37. The solid line and long-dashed line represent the metastable state population for the cases $\sigma_{46} = 0$ (no excited state absorption) and $\sigma_{46} = 5 \times 10^{-18}$ cm^2, respectively (for simplicity, the emission cross section for this transition is assumed to be equal to the absorption cross section). The photon density with no ESA is shown by a short-dashed line while that with ESA is shown by a dotted line.

These results qualitatively display some of the effects of excited state absorption of pump photons on laser dynamics. When ESA of pump photons is possible the population of the metastable state grows significantly more slowly than when there is no ESA possible. In Figure 37 the population of level 3 when ESA is present rises more slowly than that when there is no ESA. The time at which lasing occurs is also shifted due to excited state absorption. The photon density in the cavity peaks at 298 ns when there is no ESA but doesn't peak until 342 ns when ESA is allowed. There are no significant differences between the ESA and no ESA cases when the larger multiphonon relaxation rates are used. For excited state absorption to be important, the metastable state population and the photon density must remain significantly below the values achieved when no ESA is possible.

It is possible to determine the loss in available output energy from the photon density. The stored energy in the cavity is related to the photon density by

TABLE XV

PARAMETERS USED IN Nd:ZBAN
RATE EQUATION MODELING

$A_{61} = 1029s^{-1}$ $A_{62} = 0s^{-1}$
$A_{63} = 14s^{-1}$ $A_{64} = 770s^{-1}$
$A_{65} = 705s^{-1}$ $A_{31} = 978s^{-1}$
$A_{32} = 1828s^{-1}$

$\sigma_{15} = 1.37 \times 10^{-20} cm^2$ $\sigma_{32} = 5.00 \times 10^{-20} cm^2$
$\sigma_{46} = 5.00 \times 10^{-18} cm^2$

A=0.7 B=0.5 C=1.0

$\tau_c^{-1} = 6.00 \times 10^7 s^{-1}$
$\Phi_p = 4.0 \times 10^{26} photons/cm^2 s$

$W_{21} = 1 \times 10^8 s^{-1}$ $W_{12} = 6.9 \times 10^4 s^{-1}$
$W_{eff} = 5000s^{-1}$

A[a]	B
$W_{54} = 2.9 \times 10^7 s^{-1}$	$W_{54} = 2.9 \times 10^9 s^{-1}$
$W_{45} = 9.7 \times 10^5 s^{-1}$	$W_{45} = 9.7 \times 10^7 s^{-1}$
$W_{43} = 1.9 \times 10^7 s^{-1}$	$W_{43} = 1.9 \times 10^9 s^{-1}$
$W_{34} = 4.1 \times 10^5 s^{-1}$	$W_{34} = 4.1 \times 10^7 s^{-1}$

---

a From Ref. [113]
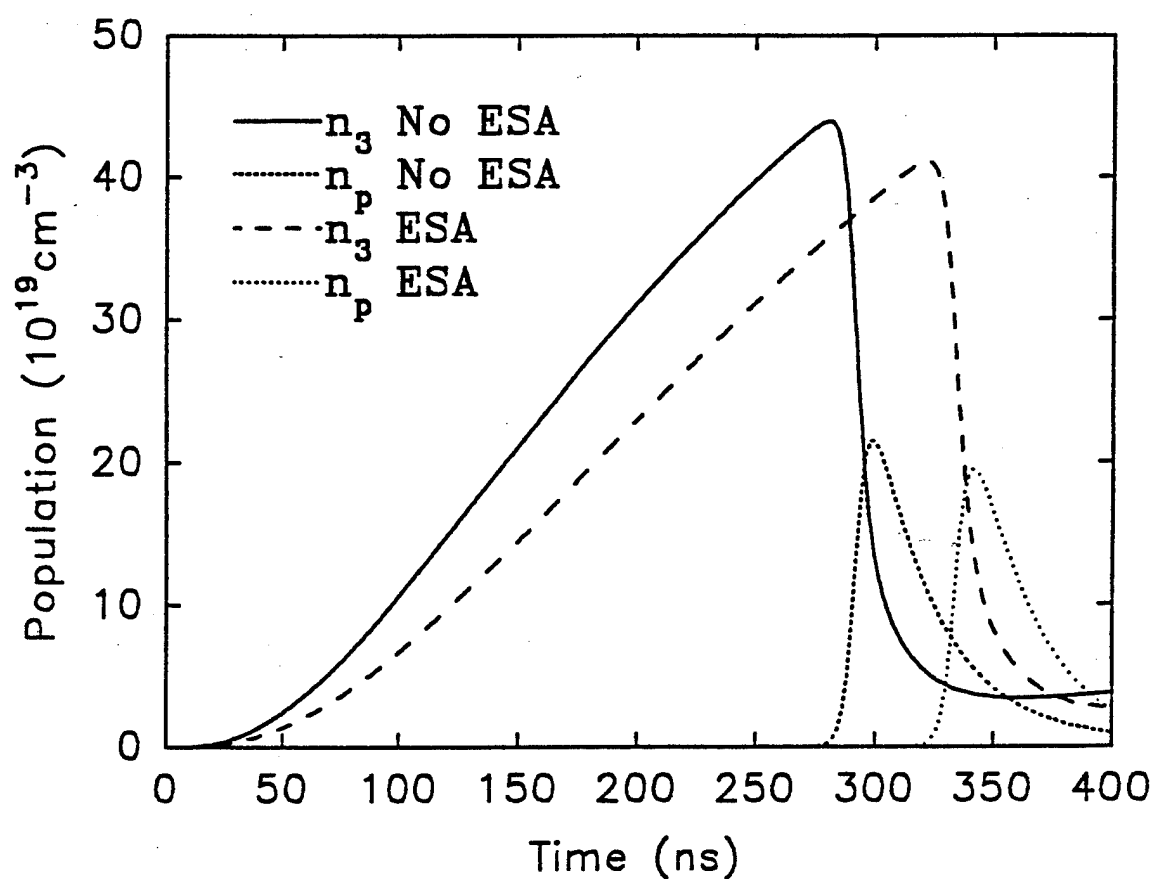
Figure 37. Plot of Metastable State Population and Photon Densities Predicted by the Rate Equation Model. The Solid Line and Long- Dashed Lines are the Metastable State Population Densities with and without ESA, Respectively, and the Short-Dashed Line and Dotted Lines are the Photon Densities with and without ESA, Respectively.

$$Energy \propto A \int n_p(t)dt$$

where A includes the energy per photon, the speed of light , and the area of the cavity mode. The value of $\int n_p(t)dt$ is determined by numerically integrating the photon density. For the case with the smaller non-radiative multiphonon rates, excited state absorption causes this value to decrease from 9.64×10^{13} to 8.32×10^{13} photons s/cm^3 , a reduction of $\approx 14\%$, reducing the available energy by a similar amount. Note that only one of the possible ESA processes is considered here and the additional processes mentioned earlier will further reduce the energy at the output wavelength.

The importance of ESA of pump photons is especially dependent on two sets of system parameters. One of the these sets are the branching ratios for emission from the upper state involved in the ESA transition. If the branching ratio for transitions from this state to levels below the metastable state is larger than that to levels above the metastable state the effects of ESA will be more important. Those ions that participate in ESA are lost to the metastable state since they radiatively decay to lower levels. If the reverse is true and transitions to states above the metastable state are more likely then the effects of ESA will be reduced since ions excited to upper states will relax back to the metastable state. In Nd:ZBAN the $^2P_{3/2}$ state is one of the upper state involved in ESA. The Judd-Ofelt analysis performed (Table XII) predicts that nearly 60% of the emission from the $^2P_{3/2}$ state occurs to levels above the metastable state. The effects of ESA in this system will be different in materials where these branching ratios are significantly different. If more of the emission from the upper level occurs to levels below the metastable state then ESA may be more important while if more of the emission occurs to levels above the metastable state ESA will be less important. Also, if non-radiative multiphonon decay depopulates the upper state, the effects of ESA will be reduced.

The second set of parameters which determines the importance of ESA is the combination of the non-radiative decay rate from the level from which ESA is occurring and the product of the flux and the absorption cross section for the process. This can easily be seen by examining Equation (99), governing the population of the intermediate level from which ESA is occurring and Equation (101) governing the decay of the upper excited state. Although values for the non-radiative decay rates W_{54} and W_{43} are difficult to determine, the energy gap law can be used to give approximate values. Using the energy gap law and one set of parameters for C and α a non-radiative rate of 1.92×10^7 s^{-1} is obtained for the $^4F_{5/2}$-$^4F_{3/2}$ transition. The second set of parameters yields a much larger rate. For ESA to be an important loss mechanism the product of Φ_p and σ_{46} must be of at least the same order of magnitude as W_{43}, so the effects are expected to be smaller when the non-radiative multiphonon rates are larger. The lack of significant changes in the metastable state population density and photon density when the larger relaxation rates are used is evidence of this. Additionally, since more transitions are resonant or nearly resonant for a 736 nm pump wavelength compared to 752 nm pump wavelength the effective cross section for the former transition is expected to be higher than that for the latter. Thus the effects of ESA are larger for a 736 nm pump wavelength than that for 752 nm. This seems to be indicated by the analysis of the pumping efficiencies.

For reasonable values of the absorption cross section for the ESA transition, the requirement that $\Phi_p \sigma_{46} \approx W_{43}$ requires the high fluences encountered only when using a high peak power pulsed laser as a pump source. As shown in Figure 32 the output of the alexandrite laser used here is not a smooth pulse. The spiking in the pump laser due to relaxation oscillations provides the high fluences necessary for ESA to be important. The non-radiative decay rates in fluoride glasses are known to be lower than those in many other laser materials.[101–104] Thus the requirement above is more easily met in fluoride glasses than in other materials, such as Nd:YAG. Previously reported wavelength dependent slope efficiency changes in Nd:YAG [77] can be attributed to difficulties in determing the energy

absorbed in the cavity mode of the system. Even in the fluoride glasses, however, if the actual non-radiative rates are closer to the larger values used here or are much faster than those predicted by the energy gap law, as recently found in other Nd^{3+} doped materials for small energy gaps, [24,27,91] then the effects of ESA will be reduced. In this case, additional mechanisms such as sequential two photon absorption and non-resonant transitions originating on the metastable state will be much more important in any explanation of a decrease in slope efficiency with pump wavelength.

Summary and Conclusions

The two different methods used to calculate to stimulated emission cross section yield different results, the spectroscopic method producing a result which is larger than that found by using the measured laser properties. A very critical factor in the latter method is the determination of f_B. It is assumed here that the upper level for the lasing transition is the lower Stark component of the $^4F_{3/2}$ manifold. If the laser transition actually originates on the upper Stark component, as found in many Nd^{3+} doped systems, then the value of f_B would be a factor of two smaller, effectively doubling the values calculated using the method based on laser efficiency measurements and bringing them closer to that determined spectroscopically. The difference between the emission cross sections calculated from the slope efficiency measurements at the two wavelengths arises from two possibilities: either uncertainties in the measured slope efficiencies, threshold energies and the extrapolation used to find the passive losses or changes in pump efficiency with wavelength.

Excited state absorption of pump photons is identified as a possible mechanism for reducing the pumping efficiency at certain wavelengths. The wavelength dependence of the blue emission under alexandrite excitation provides evidence for an ESA process. Although the exact transitions involved and the actual dynamics of the system are not definitively identified, evidence indicates that the $^2P_{3/2}$ multiplet is one of the multiplets involved in the blue emission. A model of

the ESA process quantitatively shows that this process can be an important loss mechanism under certain conditions. If high peak power pulsed lasers are used as pump sources, if the multiphonon decay rate from the intermediate level is slow and if the branching ratios for emission from the upper state involved are such that much of the emission from the upper state bypasses the metastable state then ESA is important. The results presented here indicate that excited state absorption of pump photons should be considered in the selection of host materials to insure the criteria for this effect to be important are not met.

PART B

NONLINEAR OPTICAL MATERIALS

SECTION V

THEORETICAL BACKGROUND

Linear Optics

Lorentz model

There are several formalisms to describe light-material interaction, but by far the most intuitive is the classical Lorentz model[117]. The model is as follows: let us assume that our material is made up of N nuclei per unit length, each having a single electron in orbit. The electric field of an incident electromagnetic wave will induce a polarization in the electronic cloud of first row of atoms. The atoms will behave as a dipole, oscillating with the same frequency as the incident wave. The phase of the dipole oscillation, however, lags the phase of the incident field. In other words, re-radiated light from the dipoles has the same frequency but a different phase from the incident wave. This means that the resultant wave, incident plus re-radiated, will have a phase different from the incident. This wave will now be the incident wave for the next row of atom which in turn will encode an additional phase change on it. Light emerging from the back surface of the medium, therefore, has undergone a phase change proportional to N. The phase change can be interpreted as an increase in the optical path length of the light due to the presence of the atoms. The increase is dependent on the material and is described by the refractive index coefficient. Such a model can easily be represented by a simple harmonic oscillator with equation of motion given by:

$$\frac{d^2x}{dt^2} + \Gamma\frac{dx}{dt} + \omega_o^2 x = -\frac{e}{m}E(\omega)e^{-i\omega t} + c.c. \tag{103}$$

with x denoting the displacement of the electron, m its mass, e its charge, ω_o its natural frequency, γ a damping constant and E the oscillating field of the applied light. This equation has a solution,

$$x = -\frac{e}{m}E\frac{e^{-i\omega t}}{\omega_o^2 - i\gamma\omega - \omega^2} + c.c. \tag{104}$$

Therefore, the complex susceptibility of the material with N molecules per unit volume, with f_j electrons in each molecule with binding frequency, ω_j, and damping constant, γ_j, is[118]:

$$\tilde{\chi} = \frac{Ne^2}{m}\sum_j \frac{f_j}{\omega_j^2 - i\gamma_j\omega - \omega^2} \tag{105}$$

In the above we have used the relation $P = -Nex = \chi E$. This susceptibility is related to the complex index of refraction of material through the dielectric constant, $\tilde{\epsilon}$:

$$\tilde{n}^2 = \tilde{\epsilon} = 1 + 4\pi\tilde{\chi} \tag{106}$$

Wave Equation

The above model, though intuitive, is too simplistic for our application. Alternatively, we may approach the problem from Maxwell's equations and neglect the microscopic nature of interactions. The light-atom interaction can then be studied from a semi-classical formalism. To show the form of the wave equation in a medium, we will first start with Maxwell's equations. Following reference [119], Maxwell's equations in Gaussian units are:

$$\nabla \cdot \mathbf{D} = 4\pi\rho_{free} \qquad \text{(Gauss's law)}$$

$$\nabla \cdot \mathbf{B} = 0 \qquad \text{(no name)}$$

$$\nabla \times \mathbf{E} = -\frac{1}{c}\frac{\partial \mathbf{B}}{\partial t} \qquad \text{(Faraday's law)}$$

$$\nabla \times \mathbf{H} = \frac{1}{c}\frac{\partial \mathbf{D}}{\partial t} + \frac{4\pi}{c}\mathbf{J} \qquad \text{(Ampère's law)}$$

(107)

where the symbols have their usual meaning and bold letters denote vector quantities. These are supplemented by additional relations known as material equations. For an isotropic medium, these equations are:

$$\mathbf{D} = \tilde{\varepsilon}\mathbf{E}$$
$$\mathbf{J} = \tilde{\sigma}\mathbf{E} \qquad (108)$$
$$\mathbf{B} = \mu\mathbf{H}$$

Here, $\tilde{\varepsilon}$, $\tilde{\sigma}$, and μ are the complex dielectric constant, conductivity and the magnetic permeability, respectively. In addition, we have assumed that the macroscopic polarization, P, is proportional to the applied field, E:

$$\mathbf{P} = \frac{1}{4\pi}(\tilde{\varepsilon} - 1)\mathbf{E} = \tilde{\chi}\mathbf{E} \qquad (109)$$

where $\tilde{\chi}$ is the material susceptibility. This equation is the same as its more common representation, $\mathbf{D} = \mathbf{E} + 4\pi\mathbf{P}$.

Having taken care of some definitions, we take the curl of the Faraday's equation:

$$\nabla \times (\nabla \times \mathbf{E}) = -\frac{1}{c}\frac{\partial}{\partial t}(\nabla \times \mathbf{B}) \qquad (110)$$

Using the identity, $\nabla \times (\nabla \times \mathbf{E}) = \nabla(\nabla \cdot \mathbf{E}) - \nabla^2\mathbf{E}$ and Ampere's equation we get:

$$\nabla(\nabla \cdot \mathbf{E}) - \nabla^2\mathbf{E} = -\frac{\mu}{c}\frac{\partial}{\partial t}\left(\frac{\tilde{\varepsilon}}{c}\frac{\partial \mathbf{E}}{\partial t} + \frac{4\pi\tilde{\sigma}}{c}\mathbf{E}\right). \qquad (111)$$

If we assume that $\rho_{free} \approx 0$, this reduces to:

$$\nabla^2 \mathbf{E} = \frac{\mu\tilde{\varepsilon}}{c^2}\frac{\partial^2 \mathbf{E}}{\partial t^2} + \frac{4\pi\mu\tilde{\sigma}}{c^2}\frac{\partial \mathbf{E}}{\partial t} \tag{112}$$

which is the general wave equation in a conducting medium.

We could have done this work in the Fourier space. The equation obtained is the scalar wave equation, also known as Hemlholtz equation. The advantage of Hemlholtz equation to Eq. 112 is that the latter is an ordinary differential equation. We can achieve the same effect if we assume a solution of the form $\sim E e^{-i\omega t}$ for the wave equation[119]. With this assumption, Eq. 112 reduces to the Hemlholtz equation:

$$\nabla^2 \mathbf{E} + \frac{\omega^2}{c^2}\mu\tilde{\epsilon}\mathbf{E} = 0 \tag{113}$$

where $\tilde{\epsilon}$ is the complex dielectric constant and is related to $\tilde{\varepsilon}$ and $\tilde{\sigma}$ by:

$$\begin{aligned}
\tilde{\epsilon} &= (\tilde{\varepsilon} + i\frac{4\pi\tilde{\sigma}}{\omega}) \\
&= (\{\varepsilon_R + i\varepsilon_I\} + i\frac{4\pi}{\omega}\{\sigma_R + i\sigma_I\})
\end{aligned} \tag{114}$$

The real and imaginary parts of $\tilde{\epsilon}$ will dictate phase and absorption of a light within a medium, respectively. For materials with small conductivity (insulators, undoped semiconductors) we can neglect contributions due to $\tilde{\sigma}$. In these cases we can define a complex refractive index as:

$$\sqrt{\tilde{\epsilon}} = \tilde{n} = n + i\frac{\alpha}{2k_o} \tag{115}$$

with $k_o = \omega/c = 2\pi/\lambda$ being the wavevector in free space, α the absorption coefficient and n the real index of refraction. The terms index of refraction and the refractive index are used interchangeably. However, we will refer to $\tilde{n}$ as the refractive index and n as the index of refraction.

Up to this point, we have not yet specified any special limitations on the material parameters, $\tilde{\epsilon}$ and $\tilde{n}$. They can be constants or functions of the spatial coordinated. Depending on the medium, they can be purely real (vacuum) or

highly complex (metals). Additionally, they may exhibit dispersion with respect to the incident fields frequency. The only constraint that will be imposed for now is that they are not functions of electric field. Later, in the nonlinear optics section, we will even relax this constraint.

Propagation in free space

The first case that will be investigated is the simplest one, in vacuum. Here, dielectric function is purely real and has a numerical value of 1. In effect, this states that the wave will travel at the speed of light, c, and will not be absorbed. Furthermore, the dispersionless vacuum means that the pulse shape of the wave will not be altered by propagation. Therefore, the time dependence will not play a role and we can use the Helmholtz's scalar wave equation to describe the propagation.

The approach that we take to solve this problem is based on Huygen's principle[119]. It states that every point in space is a source of radiation of spherical waves of the form, $E \sim E_o e^{ikr}/r$. Where the strength of the field, E_o, depends on the strength of the primary source of radiation at that point. Each of these points will inturn behave as a source of a secondary spherical wave. Now, the field at every point on a wavefront is the summation of the fields at that point from all the points preceding it. This point will become clearer as the discussion continues but for now we will restrict ourselves from an in depth explanation of the origin of this principle. The interested reader may refer to any optics books such as ref. [119]. Fresnel added a postulate that these secondary waves will interfere with each other (Huygen-Fresnel Principle). So for example, we can have a source of light, followed by an infinite screen with an opening in it. Then, according to the principle, the light on the other side of the screen is made up from interference of a series of spherical lights originating at the opening. We can use this principle to find the scalar field at any point given the field at the earlier point. This is given by

$$E(P_2) = -\frac{ik_o}{2\pi} \int\limits_S E(P_1) \frac{e^{ikr}}{r} dS \tag{116}$$

In the above, the integration is over all possible secondary sources, and e^{ikr}/r is the field at a distance, r, from a source, $P1$, of a secondary wave. The strength at the origin of the secondary wave is $E(P1)$, and it determines the contribution from that source. The phase factor, i, is necessary for a correct reconstruction of the wave[119], and it means that the secondary wave is out of phase with respect to the primary.

Using Fig. 38 we can expand r in terms of (x_1, y_1, z_1) and (x_2, y_2, z_2) to find:

$$r = (z_2 - z_1)\sqrt{1 + \left(\frac{x_2 - x_1}{z_2 - z_1}\right)^2 + \left(\frac{y_2 - y_1}{z_2 - z_1}\right)^2} \tag{117}$$

If we define $Z = (z_2 - z_1)$ and assume that $Z \gg (x_2 - x_1)$ and $(y_2 - y_1)$ we can use binomial expansion $(1 + x)^{1/2} \simeq 1 + x/2$ to get:

$$r \simeq Z\left(1 + \frac{1}{2}\left[\frac{x_2 - x_1}{Z}\right]^2 + \frac{1}{2}\left[\frac{y_2 - y_1}{Z}\right]^2\right) \tag{118}$$

Rewriting in terms of polar coordinate we have:

$$r \simeq Z + \frac{1}{2Z}\{\rho_1^2 + \rho_2^2 - 2\rho_1\rho_2\cos(\theta_1 - \theta_2)\} \tag{119}$$

Finally, we substitute this into Eq. 116:

$$E(\rho_2, z_2) = -\frac{i}{Z\lambda}e^{ikZ}e^{i(k/2Z)\rho_2^2} \int E(\rho_1, z_1)e^{i(k/2Z)\rho_1^2}\rho_1 d\rho_1 \int e^{(-ik/Z)\rho_1\rho_2\cos(\theta_1 - \theta_2)}d\theta_1$$

We can write the angular integral using zeroth order Bessel function[120]:

$$E(\rho_2, z_2) = -\frac{i}{Z\lambda}e^{ikZ}e^{i(k/2Z)\rho_2^2} \int E(\rho_1, z_1)e^{i(k/2Z)\rho_1^2}J_o(k\rho_1\rho_2/Z)\rho_1 d\rho_1 \tag{120}$$

This is the Kirchoff's diffraction integral and can be used to evaluate a field at any point given the field at earlier location. It should be noted that the time dependence in the field is implicitly implied.

Propagation in a homogeneous medium

Having formulated free space propagation we turn our attention to propagation in a medium. For simplicity we use a nonconducting ($\sigma = 0$) homogeneous medium. Returning to Helmholtz equation:

$$\nabla^2 \mathbf{E} + k_o^2 \tilde{\varepsilon} \mathbf{E} = 0 \tag{121}$$

we will assume that $\tilde{\varepsilon}$ is a constant and dispersionless. For a field of the form $\mathbf{E} = \mathcal{E}e^{i\phi}$, the above reduces to:

$$2i\frac{\partial \mathcal{E}}{\partial z}\frac{\partial \phi}{\partial z} - \mathcal{E}\left(\frac{\partial \phi}{\partial z}\right)^2 + k_o^2 \tilde{\varepsilon}\mathcal{E} = 0 \tag{122}$$

In the above we have invoked the slowly varying amplitude and phase approximation (SVAPA). This assumption states that amplitude and phase of the field are not significantly altered within one wavelength[121]. In general, this is an excellent approximation for a thin, absorbing medium.

To have Eq. 122 satisfied, it is necessary to have the real and the imaginary parts of the equation be independently zero. Remembering that the dielectric function, $\tilde{\varepsilon}$, is a complex quantity, the equations become:

$$\mathcal{E}\left(\frac{\partial \phi}{\partial z}\right)^2 = k_o^2 \varepsilon_R \mathcal{E}$$

$$2\frac{\partial \mathcal{E}}{\partial z}\frac{\partial \phi}{\partial z} = -k_o^2 \varepsilon_I \mathcal{E} \tag{123}$$

These two can be solved to give two uncoupled differential equations for the amplitude and the phase variation due to a media:

$$\frac{\partial \phi}{\partial z} = k_o\sqrt{\varepsilon_R}$$

$$\frac{\partial \mathcal{E}}{\partial z} = -\frac{k_o \varepsilon_I}{2\sqrt{\varepsilon_R}}\mathcal{E} \tag{124}$$

We can also relate these equations to the complex refractive index, $\tilde{n} = n + i\alpha/2k_o$ since,

$$\tilde{\varepsilon} = \left(n + i\frac{\alpha}{2k_o}\right)^2$$

$$\varepsilon_R + i\varepsilon_I = \left(n^2 - \frac{\alpha^2}{4k_o^2}\right) + i\left(\frac{n\alpha}{k_o}\right)$$

$$(125)$$

In the limit of SVAPA, $n^2 \gg \alpha^2/4k_o^2$, so we get $n \simeq \sqrt{\varepsilon_R}$ and $\alpha \simeq k_o\varepsilon_I/\sqrt{\varepsilon_R}$. Therefore, it can be concluded that:

$$\frac{\partial\phi}{\partial z} = k_o n \quad \Rightarrow \quad \phi = nk_o z$$

$$(126)$$

$$\frac{\partial\mathcal{E}}{\partial z} = -\frac{\alpha}{2}\mathcal{E} \quad \Rightarrow \quad \mathcal{E} = \mathcal{E}_o e^{-\alpha z/2}$$

which is exactly as expected. The first equation is the simple restatement of the role of index of refraction in alteration of the optical path length. The second is better known as Beer's law of exponential absorption of light in absorbing media.

An important point that must be re-emphasized is that these equations are strictly valid for a monochromatic light. In the event that the dispersion of the material is significant or the incident field has a time dependence it is necessary to use the time dependant wave equation (Eq. 112). However, that approach will readily reduce to the above if the thickness of the sample is smaller than the length of the pulse in space ($c \times pulsewidth$)[122]. It will be seen that for the experiments presented in this thesis this condition holds. Therefore, we will stick with this formalisms throughout this work.

Diffraction from a thick grating

As a final application of the Helmholtz equation in linear optics, we will apply it to a medium with a periodic modulation in its dielectric constant of a form:

$$\tilde{\varepsilon} = \tilde{\varepsilon}_o + \tilde{\varepsilon}_1(1 + \cos(\mathbf{q} \cdot \mathbf{r})) = \tilde{\varepsilon}'_o + \tilde{\varepsilon}_1 \cos(\mathbf{q} \cdot \mathbf{r}) \tag{127}$$

with $|\mathbf{q}| = 2\pi/\Lambda$ and $\varepsilon_o \gg \varepsilon_1$. In this case Eq. 121 becomes:

$$\nabla^2 \mathbf{E} + k_o^2 \tilde{\varepsilon}(x, z)\mathbf{E} = 0 \tag{128}$$

An incident plane wave with wave-vector, $\mathbf{k}_i$, and amplitude A_i will undergo diffraction from such a pattern much like X-ray diffraction off a periodic lattice in a crystal. At certain exit angles, light from this grating will coherently sum. This is dictated by the Bragg condition[123]:

$$\mathbf{k}_m = \mathbf{k}_i + m\mathbf{q} \text{ with } m = 0, \pm 1, \pm 2, \dots \tag{129}$$

Where $\mathbf{k}_m$ is the wave vector of the diffracted beam and has a magnitude equal to that of the incident beam, i.e. $|\mathbf{k}_m| = |\mathbf{k}_i|$. We can solve the Helmholtz equation by assuming a solution made from an infinite number of plane wave with wave-vector $\mathbf{k}_m$. For an H-polarized wave, the Helmholtz equation becomes a scalar equation with $E \sim E(x, z)$ given by:

$$E(x, z) = \sum_{m=-\infty}^{\infty} S_m(z) \exp(i\mathbf{k}_m \cdot \mathbf{r}) + c.c. \tag{130}$$

where $\mathbf{k}_m$ is the wave vector within the material[124]. If this is substituted into Eq. 128, assuming that:

$$\mathbf{q} = \mathbf{q}_x = q \tag{131}$$

we get:

$$\sum_m \left[\frac{\partial^2 S_m}{\partial z^2} + 2i(\mathbf{k}_i)_z \frac{\partial S_m}{\partial z} - \{(\mathbf{k}_m \cdot \mathbf{k}_m) + k_o^2(\tilde{\varepsilon}_o' + \frac{\tilde{\varepsilon}_1}{2}\left(e^{i\mathbf{q}\cdot\mathbf{r}} + e^{-i\mathbf{q}\cdot\mathbf{r}}\right))\}S_m \right] e^{i\mathbf{k}_m \cdot \mathbf{r}} = 0 \tag{132}$$

Using the Bragg condition (Eq. 129):

$$\sum_m \left[\frac{\partial^2 S_m}{\partial z^2} + 2i(\mathbf{k}_i)_z \frac{\partial S_m}{\partial z} - (k_i^2 - k_o^2 \tilde{\varepsilon}_o')S_m + \frac{k_o^2 \tilde{\varepsilon}_1}{2}(S_{m+1} + S_{m-1}) \right] e^{i\mathbf{k}_m \cdot \mathbf{r}} = 0 \tag{133}$$

This equation must be satisfied for all values of m. Therefore, in SVAPA, we have:

$$2i(\mathbf{k}_i)_z \frac{\partial S_m}{\partial z} + (k_o^2 \tilde{\varepsilon}_o' - k_i^2)S_m + \frac{k_o^2 \tilde{\varepsilon}_1}{2}(S_{m+1} + S_{m-1}) = 0 \qquad (134)$$

This is known as the coupled-wave equation[125]. If we assume that the grating is thick, only the zeroth and first order terms survive. Assuming that the incident beam makes an angle, θ, with the z-axis and using $k_i^2 = \tilde{n}^2 k_o^2$ where $\tilde{n}^2 = \tilde{\varepsilon}_o$ the above reduces to:

$$\frac{\partial S_o}{\partial z} = i\frac{k_o \tilde{\varepsilon}_1}{2\tilde{n}\cos\theta}S_o + i\frac{k_o \tilde{\varepsilon}_1}{4\tilde{n}\cos\theta}S_1$$

$$\frac{\partial S_1}{\partial z} = i\frac{k_o \tilde{\varepsilon}_1}{2\tilde{n}\cos\theta}S_1 + i\frac{k_o \tilde{\varepsilon}_1}{4\tilde{n}\cos\theta}S_o \qquad (135)$$

The solution to this set of coupled first-order differential equation with the boundary condition of $S_o(z=0) = A_i$ and $S_1(z=0) = 0$ is:

$$S_o = A_i \exp\left(i\frac{k_o \tilde{\varepsilon}_1}{2\tilde{n}\cos\theta}z\right)\cos\left(\frac{k_o \tilde{\varepsilon}_1}{4\tilde{n}\cos\theta}z\right)$$

$$S_1 = iA_i \exp\left(i\frac{k_o \tilde{\varepsilon}_1}{2\tilde{n}\cos\theta}z\right)\sin\left(\frac{k_o \tilde{\varepsilon}_1}{4\tilde{n}\cos\theta}z\right) \qquad (136)$$

The dielectric change, $\tilde{\varepsilon}_1$, can be related to the more commonly used material parameters, n and α:

$$\tilde{\varepsilon} = \tilde{n}^2 = n + i\alpha/2k_o$$

$$\tilde{\varepsilon}_1 = \triangle\tilde{\varepsilon} \simeq 2\tilde{n}\triangle\tilde{n} = 2\tilde{n}(\triangle n + i\triangle\alpha/2k_o) \qquad (137)$$

Therefore,

$$S_o = A_i \exp\left(i\frac{k_o \triangle n}{\cos\theta}z\right)\exp\left(-\frac{\triangle\alpha}{2\cos\theta}z\right)\cos\left(\frac{k_o \triangle n + i\triangle\alpha/2}{2\cos\theta}z\right)$$

$$S_1 = iA_i \exp\left(i\frac{k_o \triangle n}{\cos\theta}z\right)\exp\left(-\frac{\triangle\alpha}{2\cos\theta}z\right)\sin\left(\frac{k_o \triangle n + i\triangle\alpha/2}{2\cos\theta}z\right) \qquad (138)$$

The two waves, transmitted and diffracted, are given by:

$$E_m = \frac{1}{2} \left\{ S_m \exp\left(-\frac{\alpha}{2\cos\theta} z\right) \exp\left(i\frac{k_o n}{\cos\theta} z\right) + c.c. \right\} \qquad (139)$$

The intensity of the transmitted and diffracted beams, normalized to the input intensity, I_i, is:

$$\frac{I_o}{I_i} = \exp\left(-\frac{\alpha + \triangle\alpha}{\cos\theta} z\right) \left[\cos^2\left(\frac{k_o \triangle n\, z}{2\cos\theta}\right) + \cosh^2\left(\frac{\triangle\alpha\, z}{4\cos\theta}\right) - 1\right]$$

$$\eta = \frac{I_1}{I_i} = \exp\left(-\frac{\alpha + \triangle\alpha}{\cos\theta} z\right) \left[\sin^2\left(\frac{k_o \triangle n\, z}{2\cos\theta}\right) + \sinh^2\left(\frac{\triangle\alpha\, z}{4\cos\theta}\right)\right]$$

$$(140)$$

Which is the desired solution and somewhat more general than the one in ref.[124]. A few points of interest about this result. $\triangle\alpha$ and $\triangle n$ are the average values for the absorption and index changes in the grating. In addition there is a energy transfer between the two beams, extension of which is determined by the change in the optical path length due to the presence of the grating.

<div align="center">Nonlinear Optics</div>

Nonlinear Polarization

Up to this point we have assumed that the polarizability of the material was a constant. At this stage we will relax this requirement. This will lead to the branch of optics known as nonlinear optics. In terms of the Lorentz model presented earlier, when the intensity of the incident light is increased, a simple harmonic oscillator model is no longer sufficient for description of light-atom interaction. It can, however, be modified by inclusion of higher order terms, i.e. Eq. 103 becomes:

$$\frac{d^2 x}{dt^2} + 2\Gamma\frac{dx}{dt} + \omega_o^2 x + ax^2 + bx^3 + \cdots = -\frac{e}{m} E(\omega) e^{-i\omega t} + c.c \qquad (141)$$

where all the terms have their previous meaning. We are, also, assuming that there is only one incident wave with a single frequency. The additional terms result in an anharmonic behavior of the electronic displacement, x. In this case, the oscillation

of the electron will be at a frequency dictated by a combination of the frequency of the incident light and its higher harmonics[122]. Equation 141 does not have an exact solution, but if the higher order terms are small (as they usually are), we can solve it to successive order of approximation by Taylor series expansion of x in terms of the applied field, E. Alternatively, we can perform this expansion in the polarization of the atom in the form:

$$P = \chi^{(1)}E + \chi^{(2)}EE + \chi^{(3)}EEE + \cdots \tag{142}$$

where $\chi^{(n)}$ is a tensor of rank $n+1$ and tensoral multiplication is implied. Each tensor element will also exhibit dispersion. The effect of this field dependence can be categorized as follows:

(i) Production of fields at different frequencies.

(ii) Alteration of the macroscopic parameters, n, and α.

For each order both of the above cases occur with a strength dictated by the dispersion dependence of the tensor elements. For example, $\chi^{(2)}$ tensor accounts for both, second harmonic generation and the linear electro-optic effect. The $\chi^{(3)}$ term gives rise to third harmonic generation and the Optical Kerr effect. Table XVI list some of the common processes in nonlinear optics and the order of the process [126].

Waves in a Nonlinear Medium

Here we will focus on the effects of field dependant polarization on the macroscopic material parameters. Interested reader can refer to ref. [117] for frequency conversion properties. Furthermore we will use the field dependent susceptibility formalism since in this case we can retain all the information we derived in the linear optics section with a simple modification to the susceptibility,

$$\chi = \chi^{(1)} + \chi^{(2)}E + \chi^{(3)}EE + \cdots \tag{143}$$

TABLE XVI Nonlinear optical processes and their order.

Process	Order n	$-\omega_\sigma; \omega_1, ..., \omega_n$	K
Linear absorption/emission and refractive index	1	$-\omega; \omega$	1
Optical rectification (optically-induced d.c. field)	2	$0; \omega, -\omega$	$\frac{1}{2}$
Pockels effect (linear electrooptic effect)	2	$-\omega; 0, \omega$	2
Second-harmonic generation	2	$-2\omega; \omega, \omega$	$\frac{1}{2}$
Sum- and difference-frequency mixing, parametric amplification and oscillation	2	$-\omega_3; \omega_1, \pm\omega_2$	1
d.c. Kerr effect (quadratic electrooptic effect)	3	$-\omega; 0, 0, \omega$	3
d.c.-induced second-harmonic generation	3	$-2\omega; 0, \omega, \omega$	$\frac{3}{2}$
Third-harmonic generation	3	$-3\omega; \omega, \omega, \omega$	$\frac{1}{4}$
General four-wave mixing	3	$-\omega_4; \omega_1, \omega_2, \omega_3$	$\frac{3}{2}$
Third-order sum- and difference-frequency mixing	3	$-\omega_3; \pm\omega_1, \omega_2, \omega_2$	$\frac{3}{4}$
Coherent anti-Stokes Raman scattering	3	$-\omega_{AS}; \omega_P, \omega_P, -\omega_S$	$\frac{3}{4}$
Optical Kerr effect (optically-induced birefringence), cross-phase modulation, stimulated Raman scattering, stimulated Brillouin scattering	3	$-\omega_S; \omega_P, -\omega_P, \omega_S$	$\frac{3}{2}$
Intensity-dependent refractive index, optical Kerr effect (self-induced and cross-induced birefringence), self-focusing, self-phase and cross-phase modulation, degenerate four-wave mixing	3	$-\omega; \omega, -\omega, \omega$	$\frac{3}{4}$
Two-photon absorption/ionisation /emission	3	$-\omega_1; -\omega_2, \omega_2, \omega_1$ or $-\omega; -\omega, \omega, \omega$	$\frac{3}{2}$ $\frac{3}{4}$

which implies that

$$\tilde{\varepsilon} = 1 + 4\pi\tilde{\chi} = 1 + 4\pi(\chi^{(1)} + \chi^{(2)}E + \chi^{(3)}EE + \cdots) \tag{144}$$

since χ is complex,

$$\varepsilon_R = 1 + 4\pi(\chi_R^{(1)} + \chi_R^{(2)}E + \chi_R^{(3)}EE + \cdots)$$
$$\varepsilon_I = 4\pi(\chi_I^{(1)} + \chi_I^{(2)}E + \chi_I^{(3)}EE + \cdots) \tag{145}$$

To write this in terms of the refractive index, we recall that while ε and χ are tensors, $1/n$ has tensoral properties. Full tensoral treatment of the problem can be greatly simplified with proper choice of the principle axis. In this case, the refractive index and the dielectric function can be treated as constants and are related by, using Eq. 144,

$$\frac{1}{n^2(E)} = \frac{1}{\varepsilon} = \frac{1}{\varepsilon}\left(1 + \frac{4\pi\chi^{(2)}E}{\varepsilon} + \frac{4\pi\chi^{(3)}EE}{\varepsilon} + \cdots\right)^{-1} \tag{146}$$

Since $\varepsilon \gg \chi^{(n)}E^{(n-1)}$, field dependence of the index components are:

$$\frac{1}{n^2(E)} \simeq \frac{1}{n^2(0)} - \frac{4\pi\chi^{(2)}E}{\varepsilon^2} - \frac{4\pi\chi^{(3)}EE}{\varepsilon^2} + \cdots \tag{147}$$

Using $d(n^{-2}) = -2dn/n^3$ we get

$$\triangle n = \frac{2\pi}{n_o}(\chi^{(2)}E + \chi^{(3)}EE + \cdots) \tag{148}$$

Therefore an incident light will undergo additional phase and amplitude modulation. So, using Eq. 126:

$$\frac{\partial\phi}{\partial z} = k_o(n + \frac{2\pi}{n}\chi_R^{(2)}E + \frac{2\pi}{n}\chi_R^{(3)}EE + \cdots)$$

$$\frac{\partial\mathcal{E}}{\partial z} = -\frac{1}{2}(\alpha + \frac{4\pi k_o}{n}(\chi_I^{(2)}E + \chi_I^{(3)}EE + \cdots))\mathcal{E} \tag{149}$$

and therefore,

$$n = n_o + \frac{2\pi}{n_o}(\chi_R^{(2)}E + \chi_R^{(3)}EE + \cdots)$$

$$\alpha = \alpha_o + \frac{4\pi k_o}{n_o}(\chi_I^{(2)}E + \chi_I^{(3)}EE + \cdots)$$

(150)

At this point two types of applied fields are considered:

(i) *d.c. field with amplitude E_1.* A d.c. field (external, internal or induced by other nonlinear processes) will alter the refractive index, $\tilde{n}$, through $\chi^{(2)}$ and $\chi^{(3)}$ tensors. Changes due to $\chi^{(2)}$ through the linear electrooptic coefficient are known as the Pockel effect. Changes due to $\chi^{(3)}$ through the quadratic electrooptic coefficient are known as the d.c. Kerr effect. In the presence of both terms, Pockel effect usually dominates those due to Kerr effect. Quantitatively, we represent these effects as:

$$n = n_o + \frac{1}{2}n_o^3 r E_1 + \cdots$$

$$\alpha = \alpha_o + \frac{1}{2}n_o^3 r' E_1 + \cdots$$

(151)

where r and r' are the linear electro-optic and electro-chromatic coefficients and are related to $\chi^{(2)}$, (see appendix B). In the above we have omitted the d.c. Kerr effect which will not be used in this work.

(ii) *Oscillating field with amplitude E_2 and frequency ω.* In the event of an oscillating field, the average (over an optical cycle) of first order changes due to $\chi^{(2)}$ will be zero. Second order changes can occur through optical rectification followed by electrooptic effect. However, these effects are of order of $\left[\chi^{(2)}\right]^2$ which are in general negligible. Therefore, the first dominant nonlinear terms is due to $\chi^{(3)}$. In this case, the index of refraction is altered by the intensity of the field which has nonzero average over one optical cycle. Therefore, in this case we have:

$$n = n_o + n_2 I_2$$
$$\alpha = \alpha_o + \beta I_2 \tag{152}$$

Where n_2 and β are the Kerr and two photon absorption coefficients respectively. They can also containing all the terms arising from $\chi^{(3)}$, including the d.c. Kerr and the third order photo-chromatic coefficients.

Therefore, we can write the index in terms of a d.c. field and an intensity as follows:

$$n = n_o + \tfrac{1}{2}n_o^3 r E + n_2 I$$
$$\alpha = \alpha_o + r'E + \beta I \tag{153}$$

Origins of refractive index changes

Thusfar, we have focused on the results of nonlinearities in the susceptibility tensor of a material. At this point we will present the role of the material in the magnitude of the changes. The work will be divided in the categories based on the response time of different material properties.

Bound Electrons.   By far the fastest rise and decay time for optical nonlinearities are those due to bound electrons. By bound electrons, we are referring to the electrons which do not participate in conduction. In particular, we will be using the valence band electrons as the model for the calculations. This problem has been studied extensively   [127], [128], [129] and has more recently been invoked to a wide range of solids. We will follow, closely, the works of these authors which use the same method for the determination of the nonlinear parameters. The basic approach is to determine the material parameters involved in the two photon absorption process. A Kramer-Kronig transformation of the result will yield the corresponding index changes. For two, co-linearly polarized beams with polarization, $\hat{n}$, with vector potential of

$$\mathbf{A} = \hat{n}(A_{01}\cos(\omega_1 t) + A_{02}\cos(\omega_2 t + \phi)) \tag{154}$$

the interaction with the bands is given by[130]:

$$H_{int} = -\frac{e}{m_e c}\mathbf{A} \cdot \mathbf{P}$$ (155)

Here, m_e, and $\mathbf{P}$ are the electron mass and momentum operator, respectively. Using 'Dressed' states which are the system's eigenstates comprises of the atom *and* the field, the transition probability is given by the S-matrix[130]:

$$S = -\frac{i}{\hbar}\int dt \int d^3x \psi_f^* H_{int}\psi_i$$ (156)

We will use a Valkov-type wavefunction[131]:

$$\psi_i(\mathbf{k},\mathbf{r},t) = u_i(\mathbf{k},\mathbf{r})\exp\left[i\mathbf{k}\cdot\mathbf{r} - \frac{i}{\hbar}\int E_i(\tau)d\tau\right]$$ (157)

where i is used to designate a band with E_i given by[129]:

$$\begin{aligned}
E_c &= E_g + \frac{\hbar^2 k^2}{2m_c} - \frac{e\hbar}{m_c c}\mathbf{k}\cdot\mathbf{A}(\tau) + \triangle E_{cv} \\
E_v &= \frac{\hbar^2 k^2}{2m_v} - \frac{e\hbar}{m_v c}\mathbf{k}\cdot\mathbf{A}(\tau) + \triangle E_{vc}
\end{aligned}$$ (158)

with $\triangle E_{ij}$ designating the time independent ac Stark shifts. The resulting S-matrix is:

$$S = \frac{i\pi}{\hbar}\frac{e\hat{\mathbf{n}}\cdot\mathbf{P}_{vc}}{m_o c}\sum J_m(\eta_1)J_n(\eta_2)$$

$$\times[A_{01}\{\delta((m+1)\omega_1 + n\omega_2 + \omega_{vc}) + \delta((m-1)\omega_1 + n\omega_2 + \omega_{vc})\}$$ (159)

$$+ A_{02}\{\delta(m\omega_1 + (n+1)\omega_2 + \omega_{vc}) + \delta(m\omega_1 + (n-1)\omega_2 + \omega_{vc})\}]$$

where

$$\mathbf{P}_{vc} = \frac{i}{\hbar}\int d^3x u_c^*(\mathbf{k},\mathbf{r})\nabla u_v(\mathbf{k},\mathbf{r})$$

$$\hbar\omega_{vc} = E_g - \triangle E_{vc} + \triangle E_{cv} + \frac{\hbar^2 k^2}{2m_{cv}}$$

$$\frac{1}{m_{cv}} = \frac{1}{m_c} - \frac{1}{m_v}$$ (160)

$$\eta_i = \frac{eA_{oi}\mathbf{k}\cdot\hat{\mathbf{n}}}{m_{vc}c\omega_j}$$

At this point, we consider the different processes resulting in two photon absorption. For simplicity, a two parabolic band model with $m_v = -m_c$ with a spin degeneracy of 2 for each band is used for the calculations. First, for degenerate two photon absorption we have, $A_{02} = 0$, $m = -1$, and $n = 0$. Ignoring changes due to optical stark effect (assuming $J_n(x) \simeq x^n/2^n n!$), the change in the transition rate due to this process is[129]:

$$
\begin{aligned}
\triangle W &= \sum \int \frac{d^3 k}{(2\pi)^3} \left[\frac{\pi e^2 A_{01}^2}{2m_o m_{cv} c^2 \omega_1} \right]^2 |\hat{\mathbf{n}} \cdot \mathbf{P}|^2 \\
&\times |\hat{\mathbf{n}} \cdot \mathbf{k}|^2 \frac{1}{2\pi\hbar} \delta \left(E_g + \frac{\hbar^2 k^2}{2m_{vc}} - 2\hbar\omega_1 \right) \\
&= \frac{2^4 \pi}{5} \frac{e^4}{n_1^2 c^2} \frac{E_g}{2\sqrt{m_c}} \frac{I_1^2}{(\hbar\omega)^6} (2\hbar\omega_1 - E_g)^{3/2}
\end{aligned}
\tag{161}
$$

In the above we have assumed that $\mathbf{P}_{vc}$ is parallel to $\mathbf{k}$ resulting in factor of $1/5$ for the angular integration and used $I_1 = n_1 \omega_1^2/8\pi c$ and $|\mathbf{P}_{vc}|^2/m_o^2 \approx E_g/2m_c$. Using $\triangle W = \beta I^2/2\hbar\omega$, we get

$$
\beta(\omega) = 2K \frac{\sqrt{E_p}}{n_1^2 E_g} F_2 \left(\frac{\hbar\omega}{E_g} \right)
\tag{162}
$$

where

$$
F_2(x) = \frac{(2x - 1)^{3/2}}{2(2x)^5}
$$
$$
E_p = \frac{m_o}{m_c} E_g \simeq 21 \text{ ev}
\tag{163}
$$

$$
K = \frac{2^9 \pi}{5} \frac{e^4}{\sqrt{m_o} c^2}
$$

resulting in β with units of cm/GW. The scaling parameter for K deviates with different approaches. A value of 3100 has been shown to yield the best fit to the empirical data obtained[129]. The above solution is a special case of the nondegenerate two photon absorption coefficient with

$$
F_2^{TPA} = \frac{(x_1 - x_2 - 1)^{3/2}}{2^7 x_1 x_2^2} \left(\frac{1}{x_1} + \frac{1}{x_2} \right)^2
\tag{164}
$$

TABLE XVII Functional forms of F(x)

Contribution	$F_2(x_1; x_2)$
Two-Photon Absorption	$\dfrac{(x_1 + x_2 - 1)^{3/2}}{2^7 x_1 x_2^2}\left(\dfrac{1}{x_1} + \dfrac{1}{x_2}\right)^2$
Raman	$\dfrac{(x_1 - x_2 - 1)^{3/2}}{2^7 x_1 x_2^2}\left(\dfrac{1}{x_1} - \dfrac{1}{x_2}\right)^2$
Linear Stark	$-\dfrac{(x_1 - 1)^{3/2}}{2^6 x_1 x_2^2}\dfrac{1}{x_2^2}$
Quadratic Stark	$-\dfrac{1}{2^{10} x_1 x_2^2 (x_1 - 1)^{1/2}}\left[\dfrac{1}{x_1 - x_2} + \dfrac{1}{x_1 + x_2}\right]$

Other calculations using other methods have resulted in similar expressions with the different value of K. Including other two photon processes of Raman transitions, linear and quadratic Stark effects, we obtain the same expression as Eq. 162 but different $F_2(x)$. Table XVII is the resulting F_2 expressions taken from ref. [129] for each of the processes. The total two photon absorption coefficient is thus,

$$\beta = 2K\frac{\sqrt{E_p}}{n_1^2 E_g}\left(F_2^{TPA} + F_2^{RAM} + F_2^{LSE} + F_2^{QSE}\right) \tag{165}$$

Having found the frequency dependence of absorption changes $\triangle\alpha = \beta I$ we can determine the corresponding nonlinear refraction coefficient, n_2, via Kramers-Krönig relation[126]:

$$\triangle n(\omega_1; \omega_2; I) = \frac{c}{\pi}\int d\omega'\frac{\triangle\alpha(\omega'; \omega_2; I)}{\omega'^2 - \omega_1^2} \tag{166}$$

The above is strictly valid if the optical intensity is kept constant[126] but can be used to a good accuracy to determine the Kerr coefficient. In this case we obtain

$$\begin{aligned}
n_2 &= 2K\frac{\hbar c^2\sqrt{E_p}}{20\pi n_o E_g^4}G_2\left(\frac{\hbar\omega}{E_g}\right)\\
&= K'\frac{\sqrt{E_p}}{n_o E_g^4}G_2\left(\frac{\hbar\omega}{E_g}\right)
\end{aligned} \tag{167}$$

TABLE XVIII Functional forms of G(x)

Contribution	$G_2(x)$
Two-Photon Absorption	$\frac{1}{(2x)^6}\left[-\frac{3}{8}x^2(1-x)^{-1/2}+3x(1-x)^{1/2}\right.$ $\left.-2(1-x)^{3/2}+2\Theta(1-2x)(1-2x)^{3/2}\right]$
Raman	$\frac{1}{(2x)^6}\left[-\frac{3}{8}x^2(1+x)^{-1/2}-3x(1+x)^{1/2}\right.$ $\left.-2(1+x)^{3/2}+2(1+2x)^{3/2}\right]$
Linear Stark	$\frac{1}{(2x)^6}[2-(1-x)^{3/2}-(1+x)^{3/2}]$
Quadratic Stark	$\frac{1}{2^{10}x^5}\left[(1-x)^{-1/2}-(1+x)^{-1/2}\right.$ $\left.-\frac{x}{2}(1-x)^{-3/2}-\frac{x}{2}(1+x)^{-3/2}\right]$

With K' having values in the range of $0.8 - 1.5 \times 10^{-8}$. Table XVIII lists the functional forms for $G_2(x)$.

Free Carriers. Upto this point we have neglected any contribution due to free carriers. This, in general is a good approximation for a widegap semiconductors and insulators. Particularly, contributions to the index of refraction due to free carriers are more than 1000 times smaller than those due to bound electrons in these materials. However, variations in the spatial positions of these carriers can result in significant alteration of the behavior of a light in that medium. For example, if carriers are placed in a sinusoidal nature within a sample, an incident light will undergo diffraction as discussed earlier.

To include the contributions due to free carriers, we need merely to replace the complex dielectric constant, $\tilde{\varepsilon}$, with the more general complex dielectric coefficient, $\tilde{\epsilon}$. In doing so, we are introducing the effects of the free carriers through the complex conductivity, $\tilde{\sigma}$. In this case, using Eq. 114

$$\sqrt{\varepsilon_R} \rightarrow \sqrt{\epsilon_R} = \sqrt{\varepsilon_R - 4\pi\sigma_I/\omega}$$
$$\varepsilon_I \rightarrow \epsilon_I = \varepsilon_I + 4\pi\sigma_R/\omega$$

(168)

In terms of the index of refraction, n, and absorption coefficient α, we have:

$$n = \sqrt{\epsilon_R} = \sqrt{\varepsilon_R}\sqrt{1 - 4\pi\sigma_I/\omega\varepsilon_R}$$

$$\alpha = \frac{\omega\epsilon_I}{c\sqrt{\epsilon_R}} = \frac{\omega}{c\sqrt{\epsilon_R}}(\varepsilon_I + 4\pi\sigma_R/\omega) \tag{169}$$

Using the fact that the changes in the index of refraction due to free carriers is much smaller than the background index, n, the above reduces to

$$n = n_o - \frac{2\pi\sigma_I}{\omega n_o}$$

$$\alpha = \alpha_o + \frac{4\pi\sigma_R}{n_o c} \tag{170}$$

where n_o, and α_o are given by Eq. 125. The above equation states that the additional free carriers will *decrease* the index of refraction. We can use the Drude-Lorentz model for conductivity by ignoring the ω_o term in Eq. 103 and using $J = \sigma E$, to get:

$$\tilde{\sigma} = \frac{Nf_o e^2}{m(\gamma - i\omega)} = \frac{e^2 N_{free} f'}{m(\gamma - i\omega)} \tag{171}$$

where for sake of completeness, we have included an oscillator strength, f'. Defining $\tau = 1/\gamma$, we have,

$$\tilde{\sigma} = \sigma_R + i\sigma_I = \frac{e^2 N_{free} f''}{m}\left[\frac{\tau}{1 + \omega^2\tau^2} + i\frac{\omega\tau^2}{1 + \omega^2\tau^2}\right] \tag{172}$$

Combining Eq. 170 and Eq. 172, in the high frequency limit, $\omega\tau \gg 1$, we have

$$\triangle n = -\frac{2\pi e^2 N_{free} f'}{nm\omega^2} = -\gamma N_{free}$$

$$\triangle\alpha = \frac{4\pi e^2 N_{free} f'\tau}{ncm\omega^2} = \kappa N_{free} \tag{173}$$

The above is a simplified version of the results obtained from a band filling model. In this model, the change in the real part of the dielectric function is calculated directly. Such a quantum mechanical calculation yields[132]

$$\triangle n = -\frac{2\pi e^2 N_{free}}{nm\omega^2} \frac{E_{gap}^2}{E_{gap}^2 - (\hbar\omega)^2} \tag{174}$$

This theory has all the same features as the classical analog with $f' = E_{gap}^2/[E_{gap}^2 - (\hbar\omega)^2]$. This difference is due to the fact that in the classical case we set $\omega_o = 0$ which ignores any coupling to higher lying bands.

Photorefractive effect. In addition to changes brought about directly, free carriers can also contribute to changes in the refractive index through interaction with ionized impurities or oppositely charge carriers. Such interaction is only possible in electro-optic crystals (no center of inversion) and is known as the photorefractive effect. This effect is most commonly associated with laser induced grating experiments and as such we will focus on its behavior in these experiments.

Let us assume that two σ-polarized, plane wave beams propagating in the z-direction are crossed at an angle, θ, in a crystal. The interference of the beams results in an intensity distribution given by:

$$\begin{aligned} I_{tot} &= I_A + I_B + 2\sqrt{I_A I_B}\cos(\vec{q}\cdot\vec{r}) \\ &= 2I\{1 + \cos(2k_x x)\} \end{aligned} \tag{175}$$

where

$$\vec{q}\cdot\vec{r} = (\vec{k}_A - \vec{k}_B)\cdot\vec{r} = 2k_x \tag{176}$$

with k_i being the wave vector for the i beam. We have also assumed that they have equal wave vector magnitudes, k and intensity, I. Absorption of light through single and/or two photons results in generation of free carriers with a spatial profile of I_{tot}, i.e.

$$N = 2N_o\{1 + \cos(2k_x x)\} \tag{177}$$

The generated carriers will migrate from the highly concentrated region of the peak to the less concentrated valleys of the light induced grating. This motion may arise due to diffusion, drift, photovoltae or a combination of these process[124].

To get a better intuitive understanding we will assume that the carrier motion is dominated by electrons.

Immediately after the generation, each region is still neutral. Once the electrons initiate their motion from the bright regions to the dark regions, a charge distribution builds up. In particular, the bright regions will lose electrons and become slightly positive (leftover holes and ionized donors) and the dark regions will become slightly negative (excess electrons). After a while, there will be a charge distribution given by

$$\rho_{sc} = \rho_o \cos(2k_x x) \tag{178}$$

Using Gauss's law $\nabla \cdot E = 4\pi\rho/\varepsilon$ we get an electric field of the form

$$E_{sc} = E_o \sin(2k_x x) \tag{179}$$

Figure 39, from ref. [133], summarizes the buildup of a space-charge field. This field can now interact with the material through the linear (or quadratic electro-optic) coefficients to produce an index change of the form:

$$
\begin{aligned}
\triangle n &= \frac{1}{2} n_o^3 r_{eff} E_{sc} \\
&= \triangle n_o \sin(2k_x x)
\end{aligned}
\tag{180}
$$

The periodicity of this index change is $\pi/2$ out of phase from the instantaneous change arising from the generation of the free carriers. A probe beam incident on such a grating will diffract in the same manner as described earlier.

Other Mechanisms. In terms of the basic Lorentz model, any changes in the electronic cloud of atoms will result in a change in the polarizability and subsequently, the refractive index. There are several mechanism that may induce this change. Below we will consider a few of them relevant to this work.

In materials with dopants, transitions within a dopant can lead to significant index changes[134]. In terms of our model, this means that the responsible electron is in an orbital which may have a significantly different "cloud" from the ground

state. The significance is determined by the host as well as the dopant[134]. In this case the susceptibility is given by:

$$\chi = \chi_o^{(1)} + \{\chi_1^{(1)} - \chi_o^{(1)}\}N_1/N + \cdots \tag{181}$$

where, χ_o and χ_1 are the susceptibility of the material with the dopants in the ground and excited states, respectively. The population of the excited ions, N_1, is directly related to the intensity of the exciting beam and is, therefore, quadratic in the field amplitude. This means that changes due to population changes are third order susceptibility changes. A detailed analysis of the derivation of this contribution and typical magnitude for certain ions is found in ref. [134], [122].

Alternatively, it is possible to alter the cloud by introduction of an electric field or a temperature change. Here, the interaction of the atomic orbitals with the surrounding atoms is modified. This, inturn, will modify the index of refraction. In terms of the macroscopic quantities, density and temperature, we can represent this as:

$$\triangle n = \left(\frac{\partial n}{\partial \rho}\right)_T \triangle \rho + \left(\frac{\partial n}{\partial T}\right)_\rho \triangle T \tag{182}$$

Where the origin of the changes is irrelevant. Changes in the density occur in the presence of an electric field, a structural change or temperature changes. Changes in temperature are a result of heating, either directly or indirectly such as optical absorption.

An applied field alters the electronic cloud of a material and thereby changing the macroscopic density of the medium. Therefore, the first term in the above equation will be the responsible term for index changes. This effect is known as electrostriction and for a CW beam is represented as [122]

$$\triangle \rho(E) = \frac{\gamma}{2\pi v^2}|E(\omega)|^2 \tag{183}$$

In the above γ is the Electrostrictive coefficient and v is the velocity of sound. We have also assumed that the responsible field is the optical field itself.

In the presence of absorption additional changes are present due to an increase in the local temperature. Ignoring the effects of diffusion, the temperature change is given by:

$$\triangle T(r) \simeq \rho c \int I(r,t)dt \tag{184}$$

where, ρ, c, and I are the density, heat capacity and the input intensity respectively. This change in the temperature will result in the change in the index by (i) changing the density of the material and (ii) changing the polarizability of the atoms. Assuming that density is a function of temperature only, the total change in the refractive index in the presence of absorption is[135]:

$$\triangle n(\rho, T) = \left(\frac{\partial n}{\partial \rho}\right)_T \triangle \rho(T) + \left(\frac{\partial n}{\partial T}\right)_\rho \triangle T$$

$$\tag{185}$$

$$= \left(\frac{\partial n}{\partial \rho}\right)_T \left(\frac{\partial \rho}{\partial T}\right) \triangle T + \left(\frac{\partial n}{\partial T}\right)_\rho \triangle T$$

The two terms can be combined to give:

$$\triangle n(\rho, T) = \frac{dn}{dT} \triangle T \tag{186}$$

In the above dn/dT is known as the thermo-optic coefficient. To obtain a quantitative measure of this coefficient we use the Lorentz-Lorenz model for the macroscopic index of refraction;

$$\frac{n^2 - 1}{n^2 + 2} = \frac{4\pi}{3} \frac{N\alpha'}{V} \tag{187}$$

Where N, α', and V are the number of atoms, polarizability of each atom and volume respectively. Using

$$\frac{\partial \rho}{\partial T} = \beta \rho$$

and

$$\frac{\partial \alpha'}{\partial T} = \Phi \alpha'$$

we get:

$$\frac{dn}{dT} = -\frac{(n^2 - 1)(n^2 + 2)}{6n}(\beta - \Phi) \tag{188}$$

Note that changes in the index arising from an increase in the density are negative while those due to polarizability are positive. The contribution of each term depends on the material used and the time scales involved. In general, the effects due to density changes are slower and smaller than temperature changes in polarizability. However it is possible to select materials with zero or negative thermo-optic coefficients[135].
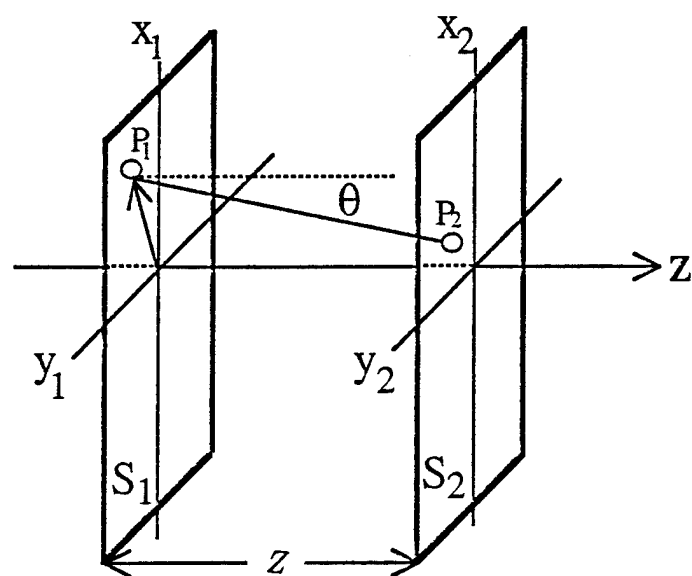
Figure 38. Coordinate specification for a propagating light.
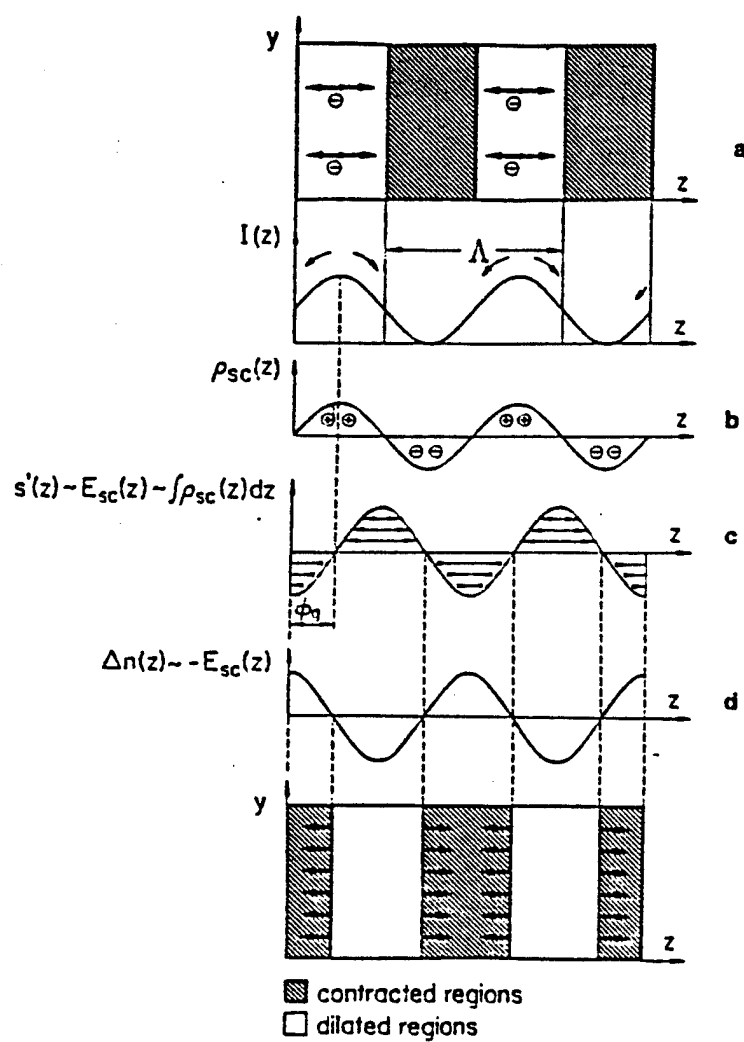
Figure 39. Schematic of the buildup of a space charge field from an laser induced grating.

SECTION VI

DILUTED MAGNETIC SEMICONDUCTORS

Introduction

Dilute magnetic semiconductors (DMS) have been the subject of numerous investigations in the recent years. Most popular are $A^{II}MnB^{VI}$, where Mn^{2+} ions are embedded in a $II - VI$ semiconductor host. Structurally, in $A^{II}B^{VI}$ semiconductors, the group II cations (A) have 2 valence electrons and the group VI anions (B) have 6 valence electrons in the outer shells. It is the formation of bond between these atoms which gives rise to the semiconducting behavior of the host material. From an ionic bonding approach bonds are formed by transfer of the 2 valence electrons of the cation to the electron deficient orbital of the anion. Therefore, in the band formation view point, the valence band extremum is due to the filled outer shell of the anions. Similarly the minimum of the conduction band is due to the empty outer shell of the cations. For example in CdTe the valence band is composed of the p-type orbitals of Te and the conduction band, the s-type orbitals of Cd. From a molecular orbital approach, the 2 valence electrons of the cations and the 6 valence electrons of the anions will hybridize to form a pair of bonding and antibonding s-p^3 orbitals [136]. The overlap of the bonding orbitals results in the p-type valence and the overlap of antibonding orbitals results in the s-type conduction bands.

The s-p^3 orbital formation means that the cation and the anion are bonded tetrahedrally, i.e. each having 4 nearest neighbors in a tetrahedral coordination leading to the zincblend and wurtzite structures found in $A^{II}B^{VI}$ semiconductors. Recall that zincblend consists of two interpenetrating fcc sublattices shifted along

154

the (111) axis and wurtzite consists of two interpenetrating hcp sublattices shifted along (001) axis [123].

By far the most popular magnetic ions in DMS is Mn^{2+} ions. Apart from the fact that Mn^{2+} ions have a high spin angular momentum ($S=5/2$) and will be electrically neutral in the $II-VI$ host, $A^{II}MnB^{VI}$ with high concentration of Mn can be grown without significant alteration of the crystallographic nature of the host [137]. This is a unique property most commonly associated with the presence of filled d-orbitals in Mn ions. The high solubility leads to several interesting physical properties.

First, the addition of Mn will result in alteration of the lattice parameter and the band gap of the host in a continuous way. This allows the customization of the semiconducting and optical properties of these materials where needed such as in quantum wells.

Second, depending on Mn concentration, DMS can exhibit paramagnetic, antiferromagnetic and spin glass behaviors in the same host. This allows the study of the effects of spin-spin correlation and the role of super exchange on the magnetic properties observed.

Third, interactions among the Mn ions and the conduction band electrons lead to effects which are unique to the DMS. These include giant Faraday rotation, giant negative magnetoresistance and large Zeeman splittings. These are referred to as sp-d exchange interactions since it is believed that they arise from interaction between the Mn d-electrons and the sp band.

Although numerous investigations have been performed on the nonlinear optical properties of $II-VI$ semiconductors, a relatively few experiments on the nonlinear optical properties of DMS have been reported. With this in mind, experiments were performed to determine the nonlinear optical and carrier dynamics of $Cd_{1-x}Mn_xTe$ and $Cd_{1-x}Mn_xSe$ samples with several Mn concentrations.

TABLE XIX Physical parameters of the DMS used

Sample	x	Bandgap (eV)	Thickness (mm)
CdSe	0.0	1.7	0.7
	0.1	1.8	0.7
	0.2	1.9	0.7
+In	0.3	2.0	0.7
	0.4	2.1	0.7
CdTe	0.0	1.5	0.9
	0.1	1.6	1.0
	0.25	1.8	0.7
	0.45	2.0	2.4

Nonlinear Optical Properties

The nonlinear optical properties of semiconductors can be categorized as those arising from the bound electrons and free carriers. The nonlinearities due to the bound electrons are instantaneous and will follow the temporal shape of the pulse. In the case of the third order susceptibility tensor, these result in the two photon absorption, β, and the bound electron nonlinear refraction, n_2, coefficients. In the last chapter we should that these parameters are bandgap dependant and have been estimated for a variety of materials. Nonlinearities due to free carriers, however, have been less investigated. We shall focus on the effects of free carriers on the optical nonlinearities. To utilize the bulk properties of the material, two photon absorption will be used to generate the free carriers. Therefore, it is necessary to determine this coefficient in order to estimate the number of generated carriers. The experiments were designed for simultaneous determination of these properties.

Experimental Setup

Table XIX lists the characteristics of the CdMnSe and CdMnTe samples used

for the experiment. The CdMnSe samples were cut and positioned with their c-axis parallel to the polarization of the incident light. In the CdMnTe samples the (111) crystal direction was set parallel to the propagation direction of the incident beams.

For this investigation we used a mode-locked, Q-switched, Nd:YAG laser operating at 1.06 μm with a FWHM of 27 ps. Since photon energies of the laser are less than the bandgap of the DMS studied, free carrier generation takes place primarily via two photon absorption (TPA). The generated carriers will then modulate the absorption coefficient and index of refraction of the material. In particular, if the excitation pulse has a Gaussian intensity profile, the spatial profile of the generated electrons will be radial and the material will behave as an absorptive lens. The absorptive nature of the material will be due to two photon absorption of bound electron and the subsequent single photon absorption of the generated carriers. However, the effects due to free carriers will persist while they remain in the conduction band. It is possible to isolate these effects by introduction of a weak probe beam delayed long enough from the pump beam to insure no interaction yet much shorter than the carrier lifetime. The post sample spatial profile of a delayed probe beam can then be used to determine the effect of the carriers only. If the number of generated carriers were known, it would be a relatively simple task to determine the changes induced by them.

Figure 40 shows the experimental setup used to study the third order nonlinearities in our samples. The probe beam is delayed 100 ps from the pump beam to insure that there are no interactions between the beams. Both beams are passed through a $1m$ focal length lens and have the same beam radius of $590\mu m$ at the front surface of the sample. Each sample was placed 29cm behind the focal plane of the lens. The samples were 'thin' compared to the Rayleigh range of the beams ($\sim$30 times smaller) to insure applicability of the thin medium formalism[138,139]. The energy of the pump beam was varied by a waveplate-polarizer combination and that of the probe was kept fixed at a level where no self-induced optical nonlinearities were measurable. The apertures placed in front of the detectors are to

monitor the total and the on-axis transmission of each beam. The detected energy at each meter was stored in a computer as a function of the input energy of the pump beam.

Theoretical

We can use the formalisms developed in the previous chapter to put the above in a more quantitative bases. Using Eqs. 153 and 173 , the amplitude, I_1, and the phase changes, ϕ_1, of the incident pump beam are given by:

$$\frac{dI_1}{dz} = -\alpha I_1 - \beta I_1^2 - \sigma N I_1 \tag{189}$$

$$\frac{d\phi_1}{dz} = k(n_2 I_1 + \sigma_r N) \tag{190}$$

where for the laser photon energies ($\hbar\omega < E_{gap}$) the carrier concentration, N, is given by:

$$\frac{dN}{dt} = \beta \frac{I_1^2}{2\hbar\omega} \tag{191}$$

Here, k is the wave vector of the incident pump beam, α is the absorption coefficient of the material, σ is the free carrier absorption cross section (FCA), and σ_r is the nonlinear refraction coefficient of the free electrons (FCN). In Eq. 191 any recombination of the carriers is neglected since the lifetime of the carriers are much greater than the 27 ps pulsewidth of the laser. In the above we have also ignored any losses due to second harmonic generation of the pump beam. This is valid since phase matching condition is not satisfied for our crystal orientation. Furthermore, second harmonic of the pump beam has photon energy greater than the bandgap and is, therefore, absorbed by the valence electrons. This SHG followed by single photon absorption leads to a small correction in the value of the two photon absorption coefficient and will be ignored here. Separate experiments investigating the SHG signal emerging from the back surface of these materials show that the above assumption is valid.

A similar set of equations can be used for the delayed probe beam, I_2. However, any changes of the probe beam amplitude and phase are a result of the pump beam generated free carriers only. In other words:

$$\frac{dI_2}{dz} = -\alpha I_2 - \sigma N I_2 \tag{192}$$

$$\frac{d\phi_2}{dz} = k\sigma_r N \tag{193}$$

But the number of generated carriers is still determined by the pump beam intensity:

$$\frac{dN}{dt} = \beta \frac{I_1^2}{2\hbar\omega} \tag{194}$$

The field at any plane past the sample can, then, be calculated by a zeroth order Hankel transform of the field at the exit plane. The above equations were solved numerically and the field at the aperture was determined for a number of input pump beam intensities.

Results and Discussion

Two photon and free carrier absorption. To determine the values for two photon and free carrier absorption the _total_ energy of the pump and the probe were measured versus their energies incident on the sample. Experimentally, this means that the aperture in front of the detector was fully open. In this case, all of the light from the two beams is collected and changes in the phase front resulting in the lensing behavior of the material will not play any roles. The transmission coefficients, hence, are solely determined by the two photon and free carrier absorption coefficients. For the probe beam, these changes are a result of the free carrier absorption only. Mathematically, we need to solve Eqs. 189 191 and 192 to determine the transmittivity of the samples. In these equations the two unknowns are β and σ. Since we are employing two separate beams, it should be possible to determine their magnitude exactly.

Figure 41 (a) and (b) shows the transmission coefficients of the pump and probe beams obtained in a fully open aperture experiment performed on CdTe. The lines in the graphs correspond normalized transmission of the pump and probe beams for various values of β and σ. While it is apparent that a "fit" to the pump beam transmission can be obtained for a number of β and σ values, use of both graphs will uniquely determine each coefficient. This procedure was repeated for all the samples.

Figure 42 (a) shows the magnitude of two photon absorption coefficient in $Cd_{1-x}Mn_xSe$ and $Cd_{1-x}Mn_xTe$ for different x values. Both hosts exhibit similar features, a decrease in the TPA coeff. with an increase in the Mn concentration, x. As stated earlier, an increase in x results in an increase in the bandgap. Therefore, the figure shows a decrease in the TPA coeff. with an increase in the bandgap. This is to be expected from the discussions in the origin of optical nonlinearities section. Figure 42 (b) shows the magnitude of the free carrier absorption for various Mn concentrations. Here, we see different behavior from the two materials. In CdMnSe, free carrier absorption cross-section remains constant for all values of x. In CdMnTe, however, the cross-section decreases with an increase in the Mn concentration. The origin of this is not understood and warrants further investigation.

With these parameters determined, we can used Eq. 191 to determine the number of carriers generated by the pump beam. This is an important parameter in determination of the free carrier absorption cross-section or nonlinear refractive index changes. Figure 43 (a) and (b) are the total number of carrier per unit length generated by the pump beam. For CdMnSe the number of generate carriers decrease with increase in Mn concentration. This is to be expected since the FCA coefficient in this material remains constant while the TPA coefficient decrease with addition of Mn. For the CdMnTe, however, number of free carriers in pure CdTe is the same as that with 10% Mn. The number increases for the 20% Mn conc. before decreasing for the 45% concentration. The reason for this behavior is associated with the non-constant behavior of the FCA cross-section. Since both

the TPA and FCA are decreasing with increase in Mn concentration, the total number of carriers generated will depend on both coefficients. It is, therefore, possible for a higher Mn concentrated sample with smaller TPA coefficient to have greater number of free carriers.

Nonlinear refraction. Having determined the TPA and FCA coefficients we focus on the nonlinear refraction of the samples. Nonlinearities can arise from bound and free electrons. In the presence of free carriers, changes in the refractive index are dominated by the electrons. This means omission of the n_2 terms in the phase changes described earlier. Including the phase change equations, there are three parameters to be considered; β, σ, and σ_r. The first two were determined earlier, so all that is left is the free carrier nonlinear refraction (FCN) coefficient, σ_r. This terms will cause the phase of the wave front to experience a change proportional to the number of generated carriers. Since the generation takes place via two photon absorption of the pump beam, the phase changes will have a radial distribution, $\phi(r)$. This radial phase change is similar to that experienced by a beam passing through a lens. Therefore, the FCN can be viewed as inducing a lensing behavior in the sample. In our experiment, this means that the radius of the beam at the detector will change with an increase in the pump beam generated free carrier concentration. In other words, the on-axis intensity of the beams will be different, in the presence of material lensing, from its value with no lensing. We can determine the on-axis intensity by monitoring the energy of the transmitted beam through a small diameter aperture placed in front of the detectors.

If the sample behaves as a negative lens, the on axis intensity will show a decrease greater than a purely absorptive sample. Figure 44 shows the normalized transmission coefficient of the probe beam obtained in a small aperture experiment performed on CdTe. The solid line is the best fit using the old values of β and σ found earlier and σ_r as an adjustable parameter. We observed a decrease in probe beam transmittivity followed by a sharp saturation at higher pump beam intensities. Comparing the probe transmissions in figures 41 and 44 , we see that

it decreases more rapidly in the small aperture experiment than in the case of an open aperture experiment. This suggests that the free carriers induced lensing behaves as a negative lens, as expected from the discussion in chapter 2. The sharp saturation in the transmission coefficient, however, could not be fitted or described by Eq. 192 - 194. In particular, a fit could only be obtained if the value of σ_r were to decrease with an increase in the pump beam energy or, in other words with carrier concentration.

In the theories considered so far we had neglected nonlinearities in the free carrier concentration. In trying to keep most of our previous features, we look at concentration dependence of each factor in the FCN coefficient. From Eq. 174

$$\sigma_r = -\frac{2\pi e^2}{n_o \omega^2 m^*} \frac{E_g^2}{E_g^2 - (\hbar\omega)^2} \tag{195}$$

two factors to be considered are E_g and m^*. In the first case we see that an increase in the number of carriers will increase the bandgap by blocking the possible transition to the bottom of the conduction band. Actually, this band filling model was used to determine the above expression. So This factor is accounted for in the theory. The other factor is the effective mass at the bottom of the band, m^*. At high electron concentrations, states higher than the bottom of the conduction band are occupied. It has been shown that the effective mass of the electrons has an energy dependence given by[140]:

$$m^* = m_o^*(1 + 2\frac{E - E_c}{E_{gap}}) \tag{196}$$

with $E - E_c \approx E_f$, where E_f is the Fermi energy. When carrier concentrations exceed a critical value, N_c, the quasi-Fermi level will be within the conduction band and thus the effective mass of the carriers will differ from the dilute case. In general, the location of the Fermi level with respect to the bottom of the band is dictated by the Fermi integral [141] but for our case it can be approximated by $E_f \approx a(\ln(N/N_c))^2$. This means that the effective mass of electrons are given by:

$$m^* = m_o^*(1 + b(\ln(N/N_c))^2) \tag{197}$$

TABLE XX Values of b and N_c used for the fit

Sample	x	b coeff.	N_c ($10^{17} cm^{-3}$)
CdSe	0.0	0.3	3.5
	0.1	0.35	6.0
	0.2	0.35	6.0
+In	0.3	0.52	8.0
	0.4	0.3	2.0
CdTe	0.0	0.8	5.0
	0.1	0.6	3.0
	0.45	0.2	1.0

which implies that[142]:

$$\sigma_r = \begin{cases} \sigma_{ro} & for\ N < N_c \\ \dfrac{\sigma_{ro}}{1 + b(\ln(N/N_c))^2} & for\ N \geq N_c \end{cases} \tag{198}$$

So, the slope of the transmission coefficient at low pump beam intensities (for $N < N_c$) is dictated by σ_{ro} and the saturation level by b and N_c values.

The calculations were redone with this new FCN coefficient. Figure 45 shows the result of re-fitting the CdTe results using the above equation with b and N_c as adjustable parameters. The 0.3 and $5 \times 10^{17} (cm^{-3})$ values used for these parameters are typical values expected for this material.

This was done for all the samples. Figure 46 shows the $|\sigma_{ro}|$ values obtained for different Mn concentrations. We see that for both hosts an increase in concentration results in a decrease in σ_{ro}. Again this is as predicted by the theory presented earlier since a decrease in FCN is to be expected with an increase in E_g. Table XX lists the values used for b and N_c for best fits. The values for N_c are $\sim 10^{17}$ and for b are $0.2 - 0.8$. These are material dependent but have the correct order of magnitude expected from these parameters.

In principle, all the relevant parameters have been found. We have an additional set of data, namely the pump beam transmission for small aperture experiment. We can use this as a test for the values found. Figure 47 is the small aperture transmission of the pump and the theoretical prediction using the values determined before. We see an excellent agreement between the data and the fit with *no* adjustable parameters. Similar results were obtained for all samples. A small deviation from the data is observed at higher pump intensities. This corresponds to uncertainties in the b and N_c values. Since the saturation in the small aperture transmission is dependant on two coefficients, and we used probe beam results as the bases for analysis only, more than one set of fitting parameters are possible. Using both pump and probe beam data, however, each of the two parameters can be uniquely determined. The important point is that correct behavior can be predicted with the inclusion of the concentration dependant effective mass.

Carrier Dynamics

The decay of the nonlinear optical behavior described above is dictated by the electron recombination time and diffusion coefficient. This decay time is usually of order of a few nanoseconds. This time is faster than most electronic detection systems. It is, therefore, necessary to use other means for this measurement. By far, the most common technique is pulsed probe degenerate four wave mixing. Basically, two pulses of light are overlapped, spatially and temporally, in the sample. The interference of the two "write" beams in the sample will set up a grating. The intensity of the light is chosen so that in the light regions of the grating, nonlinearities in the optical properties are present. In the dark regions, of course, this does not happen. We therefore have a sinusoidal modulation in the refractive index of the material. A third beam, "probe", incident on this grating will undergo diffraction as discussed in Chapter 2. The lifetime of the grating depends on the lifetime of the source of optical nonlinearity. For the case of bound electrons this lifetime is almost instantaneous. If high photon energy ($E > E_g$) or intensity is used, single or two photon generated carriers will be responsible for index modulation in the

grating. Then the lifetime of the grating is dictated by the carrier recombination and diffusion coefficients. By delaying the arrival time of the probe beam and monitoring its diffraction, we can determine the lifetime of the grating. This gives us an insight into the carrier dynamics of these materials.

Experimental Setup

Figure 48 shows the forward propagating laser induced grating technique used. Single 27 ps pulse from a mode-locked, Q-switched Nd:YAG laser was split into three pulses. Computer controlled optical delay lines were placed in the path of each beam to control its arrival time. The two pump beams passed a waveplate-polarizer combination to allow continuous change in their energies. The energy ratio between the two pump beams was kept at 1:1 and they were focused to a 1 mm radius and crossed at the sample. Their crossing angle, 2θ, was 9.5^o in air, which corresponds to a grating spacing of 6.5 μm. The plane of probe beam propagation was at an angle of 2° to the plane of the pump beams propagation. Therefore, the scattered and the transmitted probe were out of the plane of the pump beams which allowed for easy detection of the total energy in them. The probe beam energy was kept constant and had a beam radius of 0.3 mm at the sample. The smaller radius of the probe helps minimize effects arising from the Gaussian nature of the pump beam spatial profile. The energy of the transmitted and the scattered probe beam was monitored by two LaserPrecision energy meters. This was done as a function of the pump beam energy and the probe beam delay.

The CdMnSe crystals were positioned such that the polarization of the write beams were parallel to the c-axis. In the case of CdMnTe, the propagation wavevector of the pump beams were parallel to the (111) crystalographic direction. In both materials the probe beam polarization was set at 90° from the pump beams.

Theoretical

Crossing two beams propagating in the $x - z$ plane, each with intensity, I, and wavelength, λ, polarized in the y-direction results in an interference pattern given by:

$$I(x,t) = I(t)\{1 + \cos(2\pi x/\Lambda)\} \tag{199}$$

where the grating spacing, Λ, is related to the crossing angle, 2θ, by:

$$\Lambda = \lambda/(2\sin\theta) \tag{200}$$

Inside a material, $I(x,t)$ will generate free carriers via single and two photon absorption. The generated carriers will then change the refractive index of the material through FCA and FCN coefficients:

$$\begin{aligned} \triangle n &= \sigma_r N \\ \triangle \alpha &= \sigma N \end{aligned} \tag{201}$$

This generated grating will scatter a probe beam in the direction satisfied by the Bragg condition. The scattering efficiency, η, is given by:

$$\eta = \frac{I_{scatt}}{I_{input}} = e^{-(\alpha+\langle\triangle\alpha\rangle)z/\cos\theta}\{\sin^2(\frac{\pi z}{2\lambda\cos\theta}\triangle n_o) + \sinh^2(\frac{z}{8\cos\theta}\triangle\alpha_o)\} \tag{202}$$

and the transmitted probe beam efficiency is:

$$T = \frac{I_{trans}}{I_{input}} = e^{-(\alpha+\langle\triangle\alpha\rangle)z/\cos\theta}\{\cos^2(\frac{\pi z}{2\lambda\cos\theta}\triangle n_o) + \cosh^2(\frac{z}{8\cos\theta}\triangle\alpha_o)\} \tag{203}$$

with

$$\begin{aligned} \triangle n_o &= \sigma_r\{N(peak) - N(valley)\} \\ \triangle \alpha_o &= \sigma\{N(peak) - N(valley)\} \\ \langle\triangle\alpha\rangle &= \sigma\frac{1}{\Lambda}\int_0^\Lambda N(x)dx \end{aligned} \tag{204}$$

where $N(peak)$ and $N(valley)$ are the number of electrons in the light and dark regions of the grating, respectively.

The decay of the grating can occur through both, (i) recombination of the carrier and (ii) movement of the free electron from the light region of the generated grating to the dark region. In the latter case, presence of an electron in the dark region will reduce the contrast between the light and the dark regions. Since the scattering efficiency is related to the differences between the two regions, this means a decrease in scattering. So any time dependence of the scattering enters the equation through the time dependence of the free carriers. This is determined by the diffusion equation[143]:

$$\frac{\partial N(x,t)}{\partial t} + \frac{N(x,t)}{\tau(N)} - \nabla(D(N)\nabla N) = \frac{\beta}{2\hbar\omega}I^2(x,t) \tag{205}$$

where, in general, the lifetime, τ, and the diffusion coefficient, D, are carrier concentration dependent. The term on the right accounts for carrier generation via two photon absorption. In general, analytical solution to this equation is not possible due to the concentration dependence of the coefficients.

For a first order approximation to Eq. 205, we assume a low power input pulse with a Dirac delta function temporal profile. In this case, we expect low concentrations of generated carrier and can, therefore, ignore any concentration dependence of τ and D. Then, Eq. 205 reduces to:

$$\frac{\partial N(x,t)}{\partial t} + \frac{N(x,t)}{\tau_R} - D\nabla^2 N = \frac{\beta}{2\hbar\omega}I^2(x,t) \tag{206}$$

For a pulse spatial profile given by Eq. 199, this can be solved analytically [144]:

$$\begin{aligned} N(x,t) = \quad & N_o\{3/2 + 2\exp\left(-\frac{4\pi^2 Dt}{\Lambda^2}\right)\cos\left(\frac{2\pi x}{\Lambda}\right) + \\ & \frac{1}{2}\exp\left(-\frac{8\pi^2 Dt}{\Lambda^2}\right)\cos\left(\frac{4\pi x}{\Lambda}\right)\}\exp\left(-\frac{t}{\tau_R}\right) \end{aligned} \tag{207}$$

which is also valid if the pulse duration is much smaller than the lifetime of the carriers. This is certainly true in our case where the pulse width is 27 ps in duration

and the carrier lifetimes are a few nanoseconds. Using the above solution for N, we see that the time dependence of $\triangle \alpha_o$, $\triangle n_o$ and $\langle \triangle \alpha \rangle$ is:

$$\triangle \alpha_o, \triangle n_o \sim \exp\left(-t\left[\frac{1}{\tau_R} + \frac{4\pi^2 D}{\Lambda^2}\right]\right) \sim \exp(-t/\tau_g) \qquad (208)$$

$$\langle \triangle \alpha \rangle \sim \exp\left(-t/\tau_R\right)$$

This is an important result. It states that the grating decay time is different from the increased absorption decay time. This will be used later to separate the values of the two parameters, D and τ_R.

As a next approximation, a Taylor series expansion for the coefficients is used:

$$\begin{aligned} \gamma(N) &= \gamma_1 + \gamma_2 N + \cdots \\ D(N) &= D_o + D_1 N + \cdots \end{aligned} \qquad (209)$$

where $\gamma = 1/\tau$. So, Eq. 205 becomes:

$$\frac{\partial N}{\partial t} + \gamma_1 N + \gamma_2 N^2 - D_o\frac{\partial^2 N}{\partial x^2} - D_1\frac{\partial}{\partial x}\left(N\frac{\partial N}{\partial x}\right) = \frac{\beta}{2\hbar\omega}I^2(x,t) \qquad (210)$$

Next, we define,

$$I(x,t) = A\exp(-a^2 t^2)\{1 + \cos(2\pi x/\Lambda)\}$$

$$n = N/N_{\max} \qquad (211)$$

$$t' = \gamma_1 t$$

$$x' = x/\Lambda$$

which upon substitution into Eq. 210 results in a dimensionless equation:

$$\frac{\partial n}{\partial t'} + n + \varepsilon n^2 - \delta_o\frac{\partial^2 n}{\partial x'^2} - \frac{\delta_1}{2}\frac{\partial^2 n^2}{\partial x'^2} = \frac{\sqrt{\pi}\gamma_1}{2a}\exp(-2a^2 t'^2/\gamma_1^2)\{1 + \cos(2\pi x')\} \qquad (212)$$

where

$$\begin{aligned} \varepsilon &= \gamma_2 N_{\max}/\gamma_1 \\ \delta_o &= D_o/\gamma_1\Lambda^2 \\ \delta_1 &= D_1 N_{\max}/\gamma_1\Lambda^2 \end{aligned} \qquad (213)$$

The coefficient in front of the generation term is to insure that $n_{\max} = 1$. The effects of the nonlinear terms, ε and δ_1, on the spatial and temporal nature of the carrier concentration can now be investigated by solving Eq. 212 numerically. For realism, values of $2 \times 10^8 (s^{-1})$, 2.5 (cm^2/s), 6.5 μm, and 22 ps were used for γ_1, D_o, Λ, and $1/a$ respectively.

To determine the effects of ε, Eq. 212 was solved with $\delta_1 = 0$. Figure 49 shows the dependence of the spatial profile of generated carriers on ε for three delay times (a) 20 ps (b) 1.11 ns (c) 3.53 ns after the arrival of the pump beams. The solid line corresponds to $\varepsilon = 0.0$, dashed line to $\varepsilon = 0.33$ and dotted to $\varepsilon = 0.67$. We see that as time progresses the number of carriers in the nulls of the grating increase. This is due to the diffusion of the carriers from the highly populated to the less populated areas. In the figure, the overall area underneath each curve represents the total number of carriers and its decreases as a function of time indicates recombination process. Comparison of the area and the values in the nulls of the profiles for different times indicates that the main mechanism of grating erasure is due to recombination.

Next, setting $\varepsilon = 0.0$, Eq. 212 was solved for a number of δ_1 values. Figure 50 shows the dependence of the spatial profile of the generated carriers on δ_1 for the delay times used before. Here, the solid line corresponds to $\delta_1 = 0.0$, dashed line to $\delta_1 = 0.009$ and dotted to $\delta_1 = 0.028$. In this case, we see that the number of carriers in the null of the grating increases as a function of time and value of δ_1. In particular, at any given time, the number of carriers in the null of the grating increases with δ_1. This is to be expected since an increase in δ_1 means an increase in the diffusion. As before, however, we see that the main mechanism for grating erasure remains the recombination process.

From the above and using Eqs. 202 and 204 we can determine the lifetime of the grating. Figure 51 shows the scattering efficiency as a function of the probe beam delay for different (a) ε and (b) δ_1. From the figure it can be concluded that an increase in ε or δ_1 results in shortening of the grating lifetime. Furthermore, the

grating decay departs from a single exponential nature observed in the low carrier concentration regime.

Results and Discussion

Figure 52 shows the scattering efficiency of the probe beam as a function of the delay and the pump beam energy for CdTe. There are two interesting time regimes to be considered, (i) delay=0 and (ii) delay > 0.

In the first case, we see that the scattering efficiency increases with the pump beam energy followed by saturation and a subsequent decrease in the scattered signal. This behavior is typical for scattering from a phase grating (first term in Eq. 202). In a highly degenerate semiconductor, however, the contributions from the absorption grating (second term in Eq. 202) can be significant. Furthermore, these contributions may oppose those due to a pure phase grating[143]. To elucidate the significance of the absorption grating, using Fig. 43 carrier concentrations in the peaks of the grating were determined for this geometry. A maximum concentration of 4×10^{17} cm^{-3} suggests that any contribution from the absorption grating can be neglected. Figure 53 shows the scattering efficiency for different carrier concentrations at zero delay. As before, Fig. 43 was used for the conversion. The fit to the zero delay efficiency of CdTe was obtained using a value of 2.6 for the magnitude of σ_r, in excellent agreement with the result found earlier.

The behavior at times greater than zero delay is dictated by the time behaviors of $\triangle n_o$ and $\langle \triangle \alpha \rangle$. We can focus on the time response from $\triangle n_o$ by re-defining the scattering efficiency as:

$$\eta = \frac{I_{scatt}}{I_{trans} + I_{scatt}} \qquad (214)$$

We can do this since the energy of both, scattered and transmitted probe beam were measured during the experiment. From Eq. 208, an exponential decay of $\triangle n$ and $\triangle \alpha$ is expected with the decay time, τ_g, dictated by the recombination lifetime of the carriers and the ambipolar diffusion coefficient. Substitution of this result into Eqs. 202, 203 and 214 predicts a time dependence for the scattering

efficiency of the form $\eta(t) \sim \sin^2(a \exp(-t/\tau_g))$. For small values of a, this reduces to $\eta(t) \sim \exp(-2t/\tau_g)$. Figure 54 is a plot of the time dependence of the scattering efficiency for a number of pump generated carrier concentrations. The single exponential response means that the concentration dependence of the D and τ_R can be neglected here.

A fit to the time delay results was done for all of the samples using a single exponential function. This results in a value for τ_g which contains the ambipolar diffusion coefficient and the recombination lifetime. Therefore, another measurement is needed to uniquely determine the relative contributions of each parameter.

It is possible to determine the recombination lifetime of the carriers from the time dependence of the total probe beam energy emerging from the sample. From Eq. 202 we see that attenuation of the probe beam can occur by (i) scattering in the Bragg direction and (ii) absorption by the carriers. The latter will be present for the scattered beam also, and is insensitive to the spatial nature of the carrier concentration. Furthermore, this absorption persists throughout the duration that the electrons are in the conduction band. Therefore, by monitoring the total energy of the post sample probe beam, scattered + transmitted, as a function of time, it is possible to determine the carrier lifetime. In terms of the parameters stated earlier, we now look for $I_{out} = I_{trans} + I_{scatt}$. In this case, the time response is dictated by $\langle \triangle \alpha \rangle$ which, from Eq. 208, depends on the recombination lifetime only. Figure 55 shows the total probe energy after the sample vs. time for different carrier concentrations for CdTe. The time dependence of the signal has no saturation effects, which further emphasizes that the saturation observed in the FWM scattering efficiency was not caused by a saturation in the generated free carriers. This graph was used to determine the lifetime of the electrons in the band. It was found that for the concentrations reached the decay, τ, was a constant.

Figure 56 shows the lifetime of the electrons as a function of Mn concentration. The lifetimes of CdTe decreased with addition of Mn while for CdSe, with an exception of 30%, there was a dramatic increase. This increase is expected

since addition of Mn will increase the bandgap which will reduce the coupling between the conduction and valence bands and, therefore, increasing the lifetime of carriers[141]. The decrease in the 30% concentration is thought to be related to the Indium doping of this sample. Doping will increase the number of traps and defects which increase the coupling between the bands. In the case of CdMnTe, it is thought that the decrease in the lifetime is due to an increase in the Te defect caused by addition of Mn. This also results in a scattering of light in CdMnTe sample which was not observable in the CdMnSe samples.

Finally, with the two lifetime, τ_R and τ_g, it should be possible to determine the magnitude of the ambipolar diffusion coefficient. This was done for CdTe and a value of 2.5 cm^2/s was estimated which is in good agreement with previous measurements. This results means that it is possible to determine both coefficients from the same experiment. This is an important point since the general method for this determination was to perform the experiment for several grating spacings. This increases the error in the numerical value of this coefficient since change in the crossing angle will change the interaction length which can not be accounted for in the simple theory used. Unfortunately in the other samples the value of D could not be determined since τ_g was dictated by the lifetime of the carriers, τ_R. The reason for this is believed to be the decrease in τ_R with an increase in Mn for CdMnTe samples. In the case of CdMnSe, the presence of the superimposed photorefractive grating maybe responsible for this.

Conclusions

Table XXI is a summary of the measured parameters for each samples. There are a few points of interest. First, the two photon absorption, β, and the nonlinear refraction, σ_r, coefficients decrease with an increase in the Mn concentration. This is to be expected, since addition of Mn will result in an increase in the bandgap of the DMS and these coefficients are inversely proportional to the bandgap. Secondly, the free carrier absorption cross section remained constant for $Cd_{1-x}Mn_xSe$ but decreased for $Cd_{1-x}Mn_xTe$. The origin of this is not known but it may be
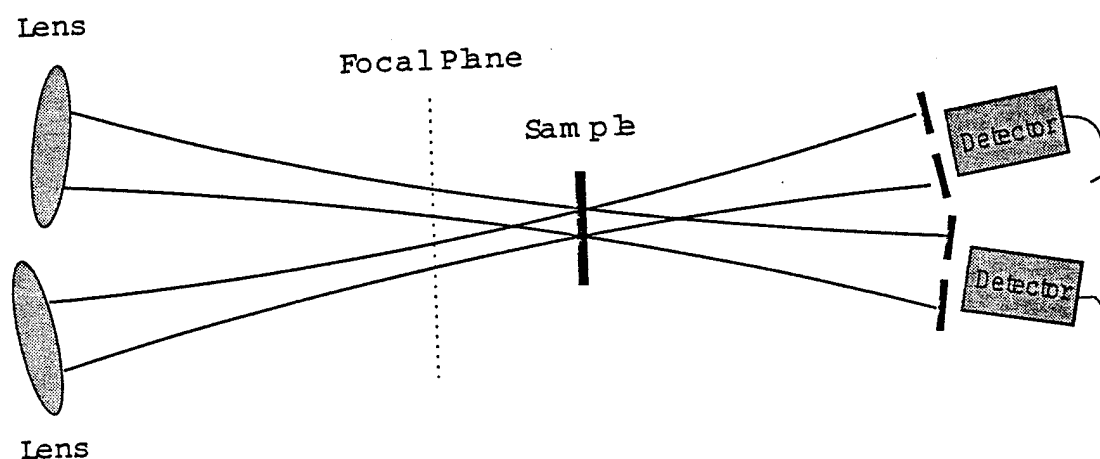
Figure 40. Experimental setup for measuring the nonlinear optical properties.

TABLE XXI Nonlinear optical parameters of DMS.

Material	$\beta(cm/GW)$	$\sigma(10^{-18}cm^2)$	$\sigma_{ro}(10^{-21}cm^3)$	$\tau(ns)$
CdSe	35	5	-2.7	4.4
$Cd_{0.9}Mn_{0.1}Se$	20	5	-1.5	7.0
$Cd_{0.8}Mn_{0.2}Se$	15	5	-2.0	12.0
$Cd_{0.7}Mn_{0.3}Se:In$	10	5	-1.1	2.2
$Cd_{0.6}Mn_{0.4}Se$	2.5	5	-0.6	71.4
CdTe	20	20	-2.5	4.8
$Cd_{0.9}Mn_{0.1}Te$	15	13	-2.5	*
$Cd_{0.6}Mn_{0.4}Te$	6.5	5	-0.75	*
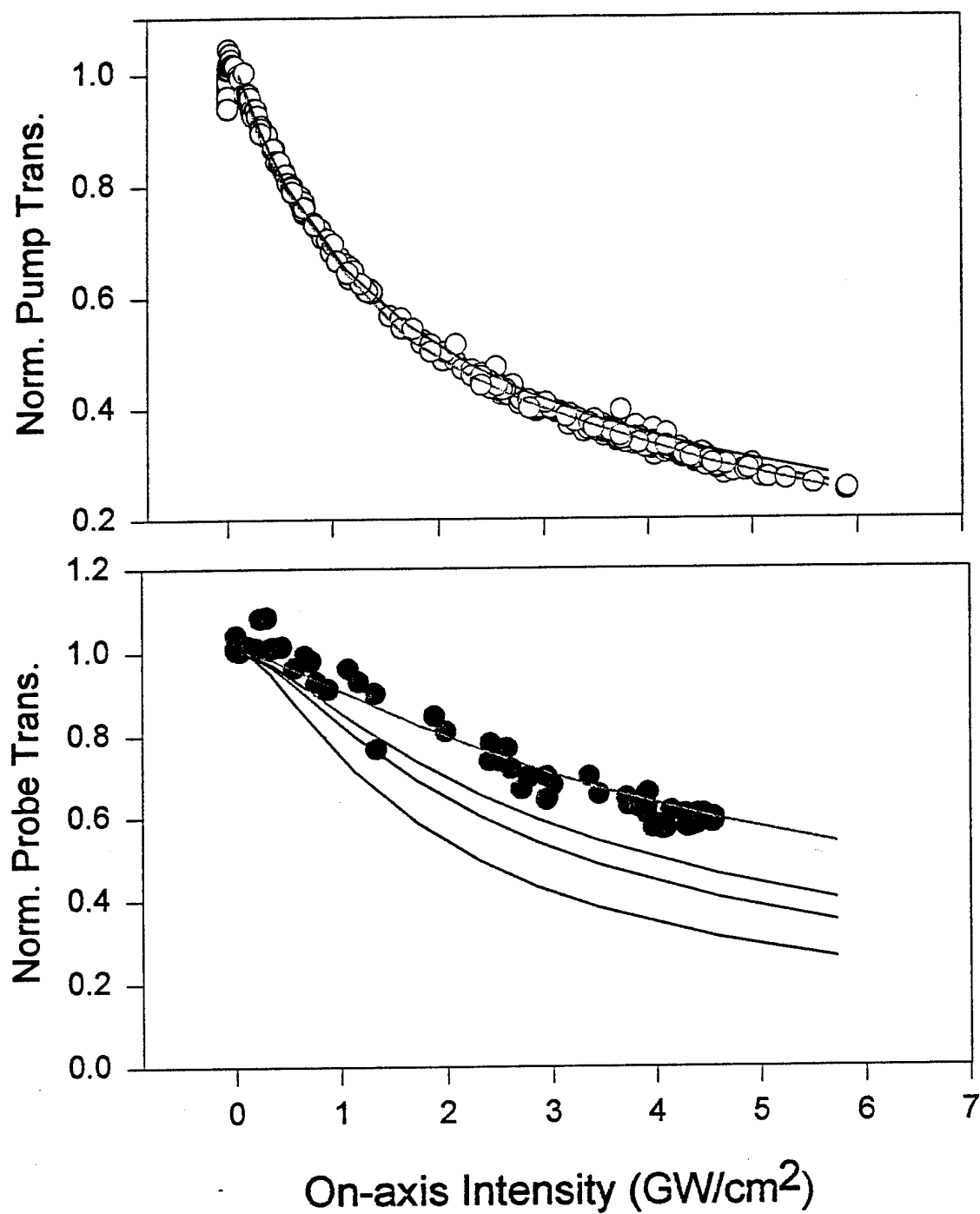
Figure 41. Results of the open aperture experiment on CdTe for (a) Pump beam and (b) Probe beam. The circles are the data points and the lines are the solutions of Eqs. 87, 89 and 90 at the detectors.
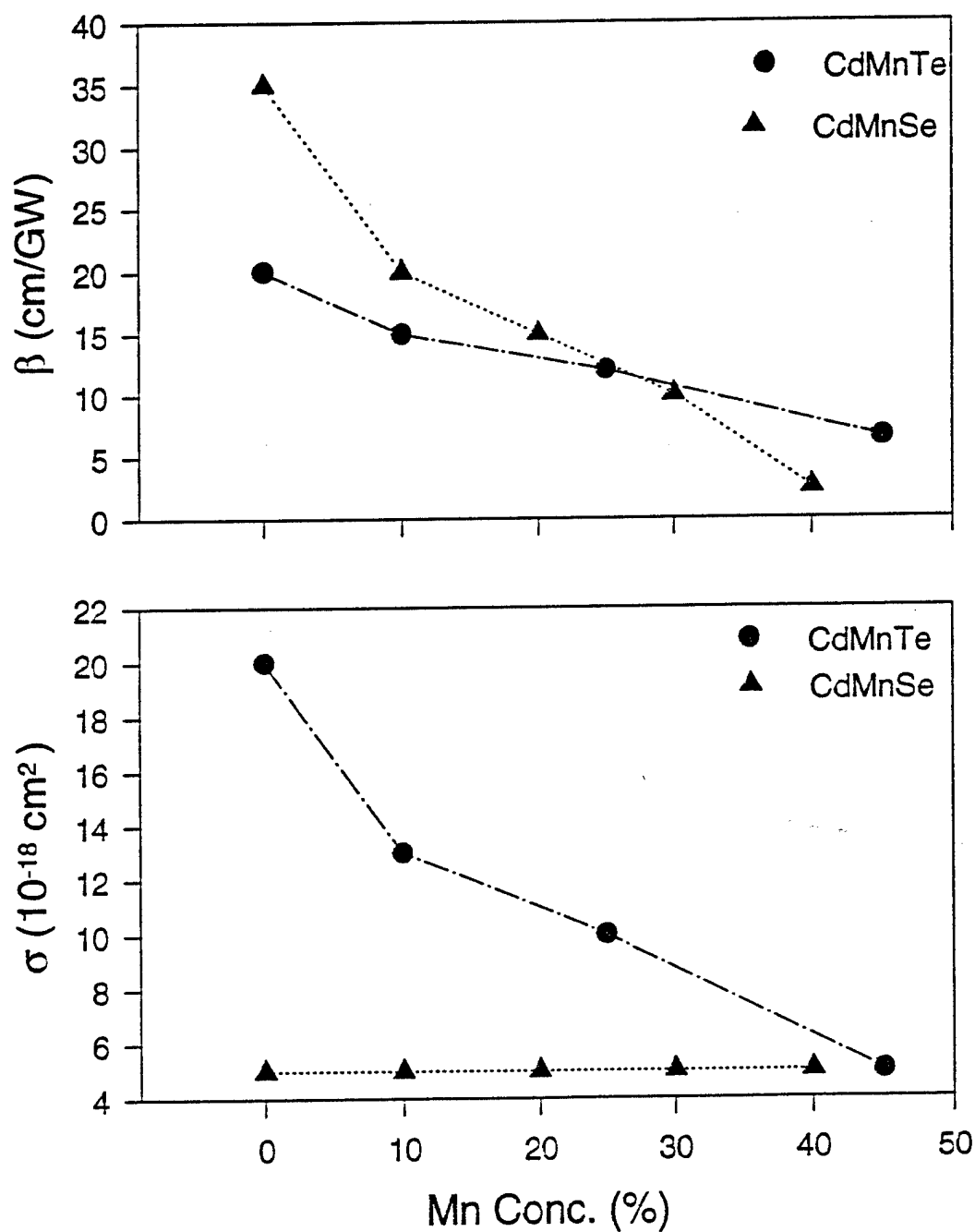
Figure 42. Parameters obtained for the (a) two photon and (b) free carrier absorption coefficients for different Mn concentrations.
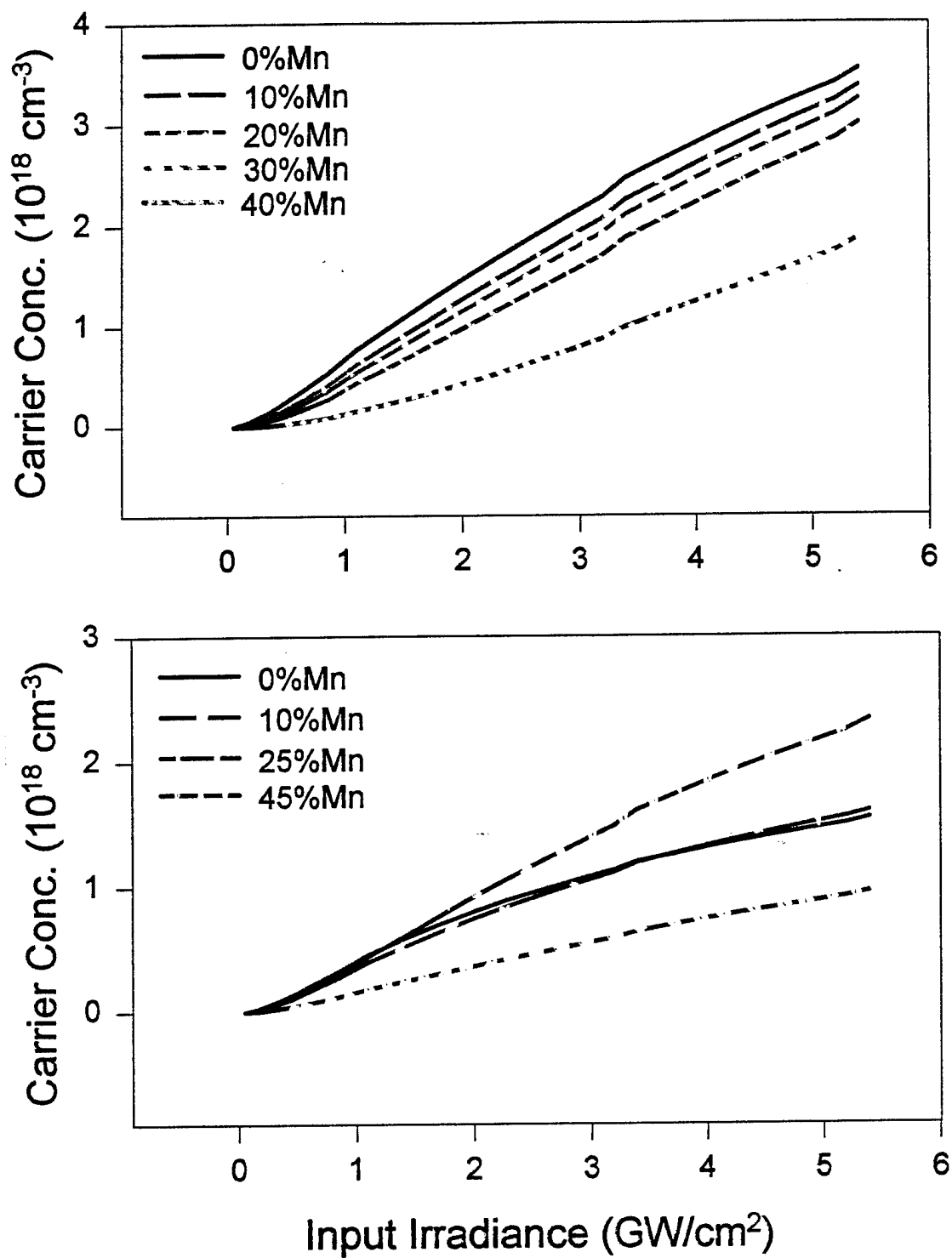
Figure 43. Number of generated carriers per unit length using Eq. 89 for (a) CdMnSe and (b) CdMnTe.
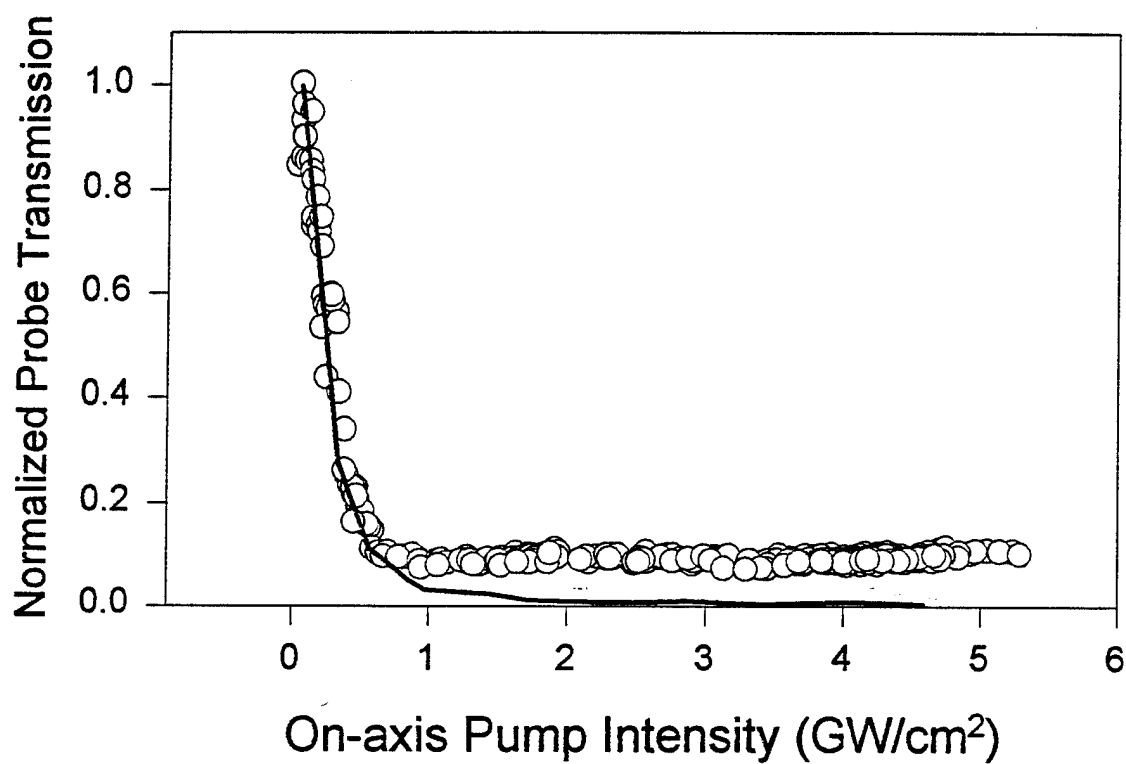
Figure 44. Results of the closed aperture experiment on CdTe for the probe beam. The fit was obtained using Eqs. 90, 91 and 92.
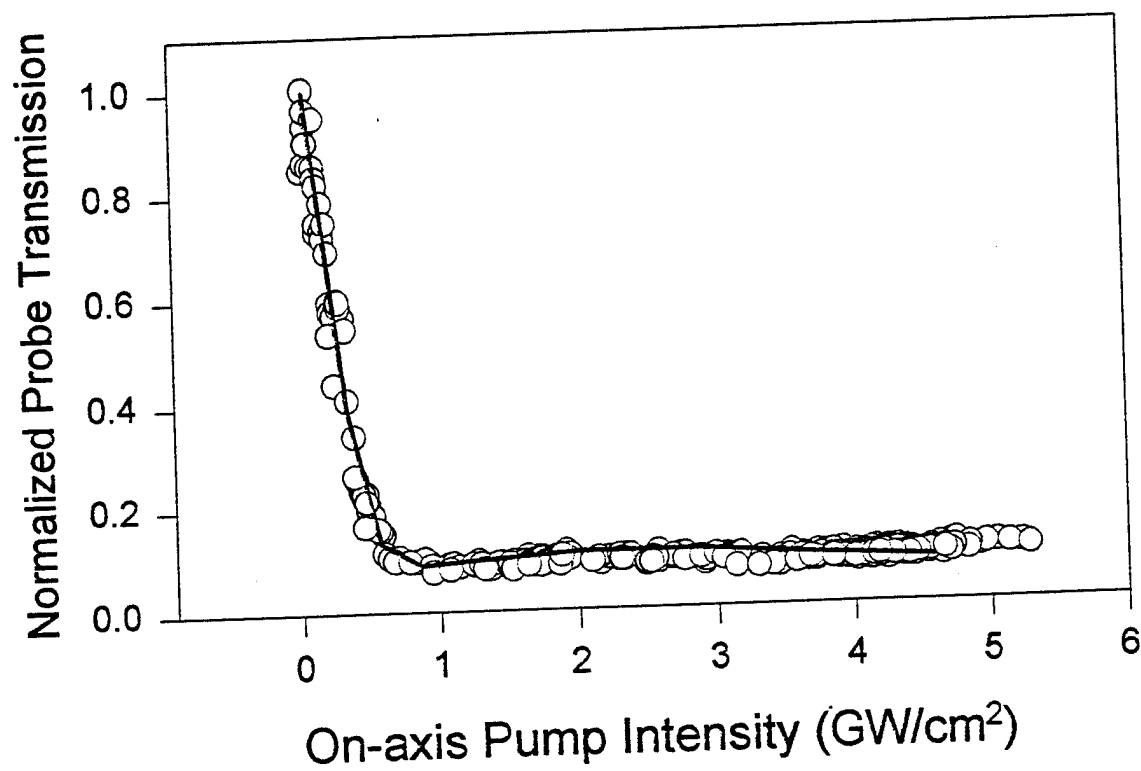
Figure 45. Results of the closed aperture experiment on CdTe for the probe beam. The fit was obtained using Eq. 96 for σ_r.
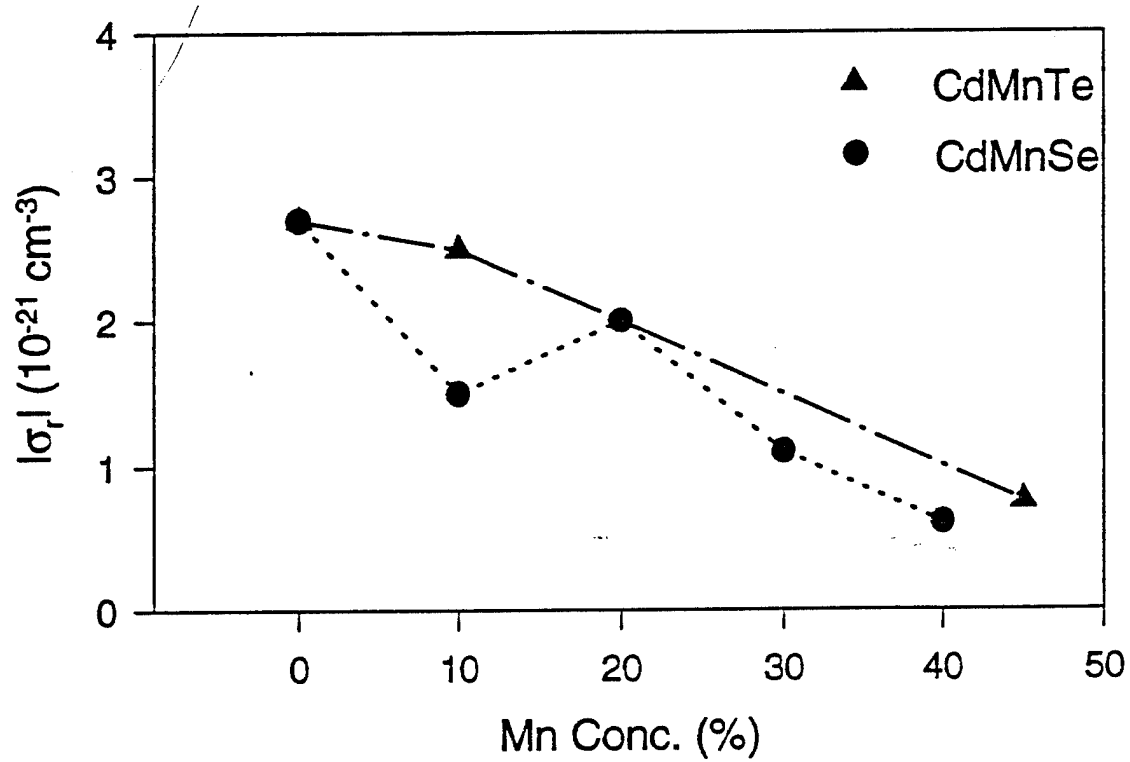
Figure 46. Magnitude of $|\sigma_{ro}|$ as a function of Mn concentration.
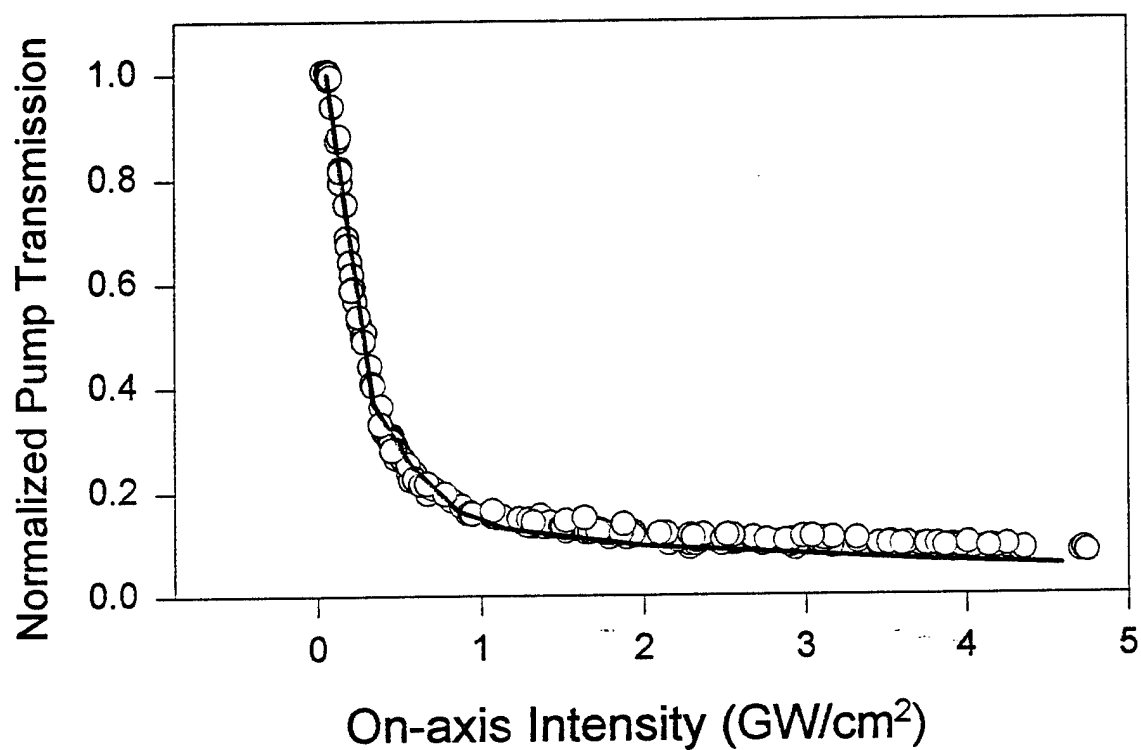
Figure 47. Results of the closed aperture experiment on CdTe for the pump beam. The line is from the parameters obtained from the other data set with no fitting parameters.
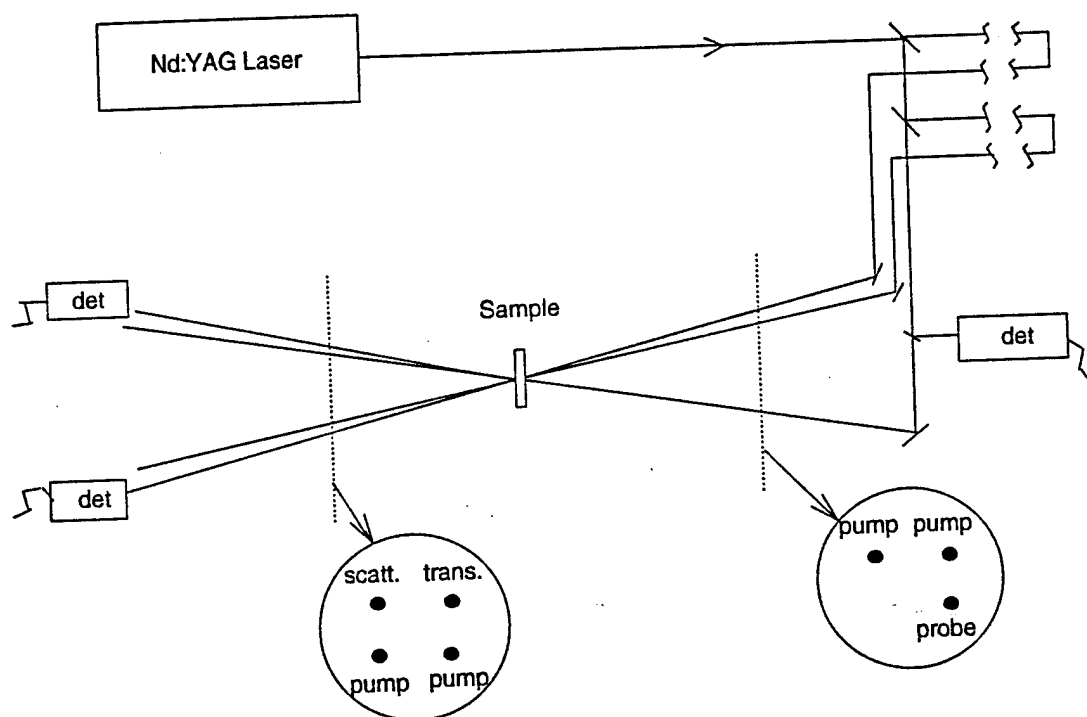
Figure 48. Experimental setup used for pulsed probe degenerate four wave mixing experiment.
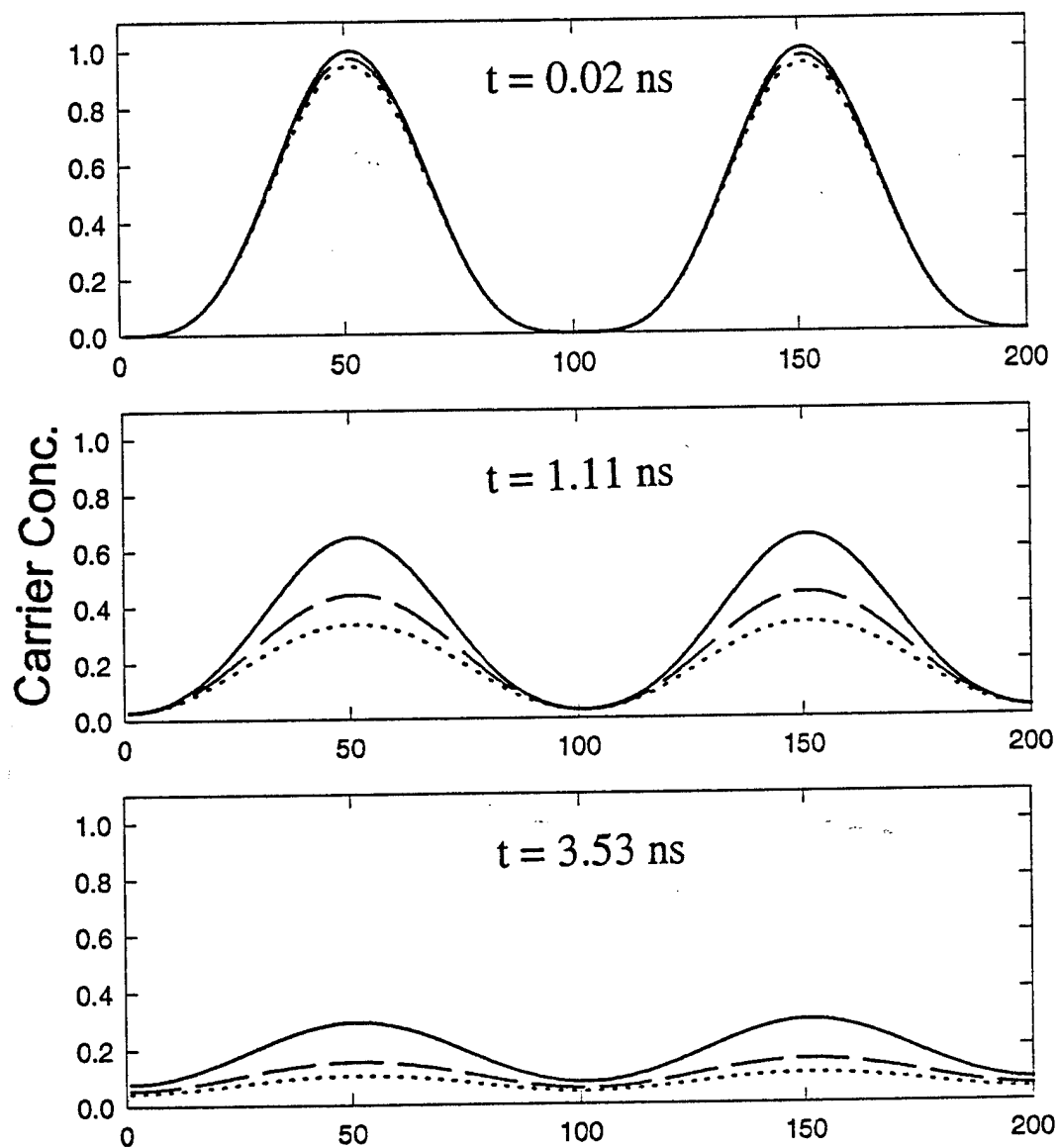
Figure 49. Dependence of the spatial profile of generated carriers on ε for three delay times (a) 20 ps (b) 1.11 ns (c) 3.53 ns after the arrival of the pump beams. In all cases $\delta_1 = 0.0$.
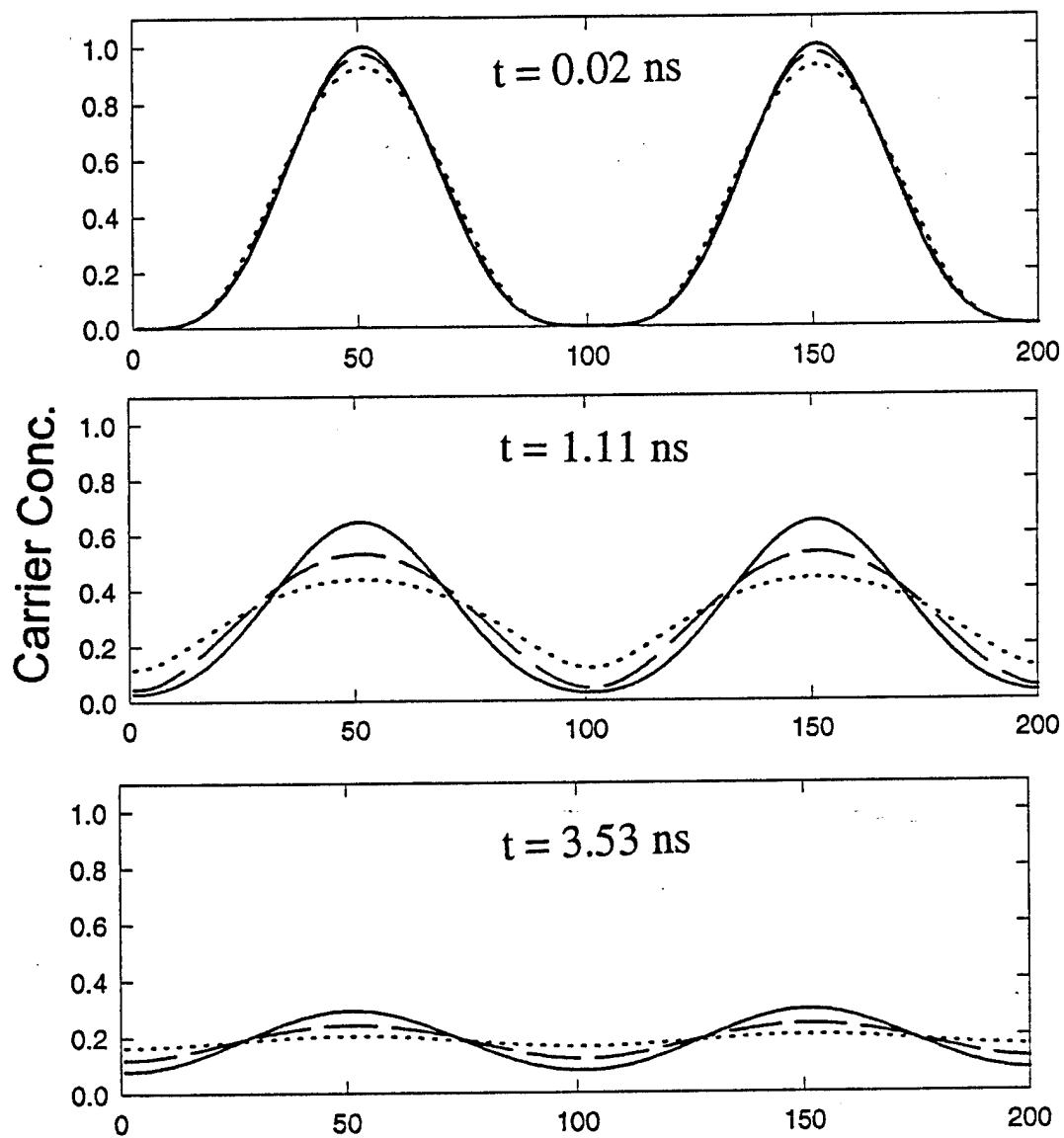
Figure 50. Dependence of the spatial profile of generated carriers on δ_1 for three delay times (a) 20 ps (b) 1.11 ns (c) 3.53 ns after the arrival of the pump beams. In all cases $\varepsilon = 0.0$
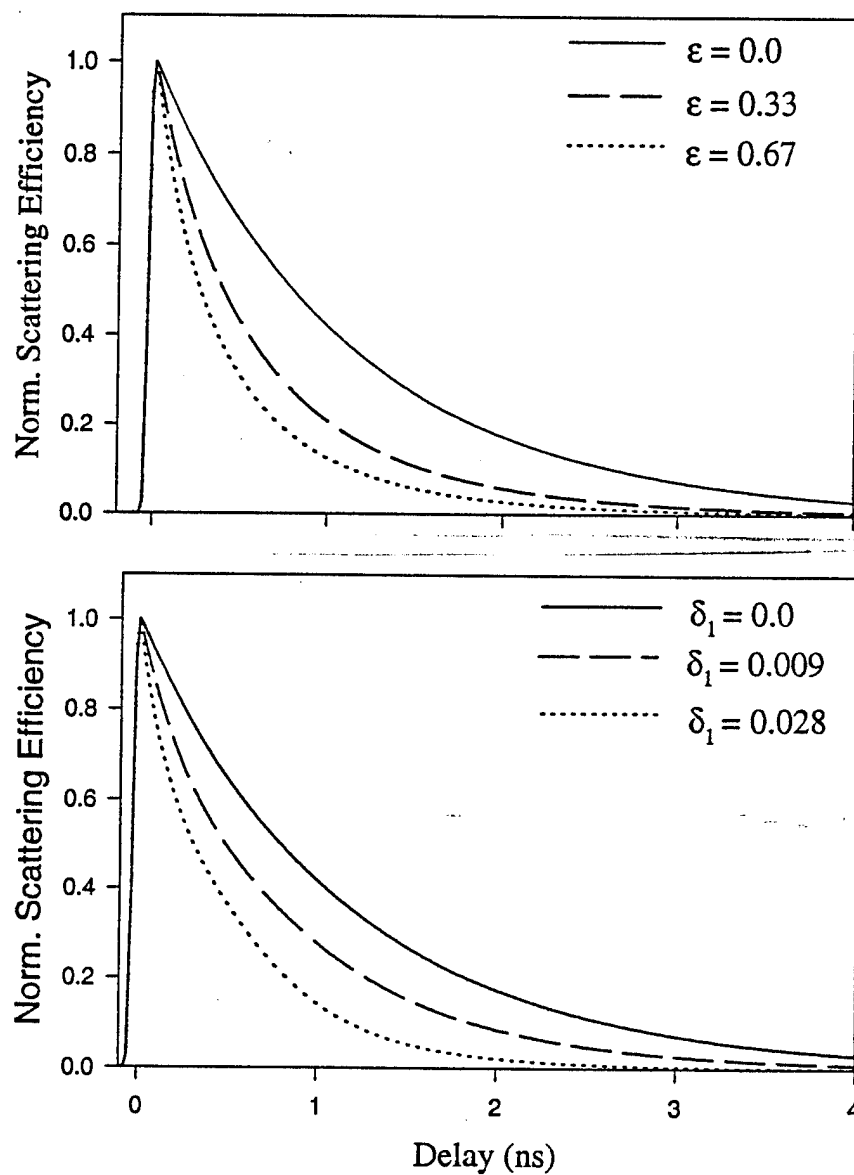
Figure 51. Scattering efficiency as a function of probe delay and (a) ε and (b) δ_1.

related to the strain present in $Cd_{1-x}Mn_xTe$ due to addition of Mn. Finally, the recombination lifetime of $Cd_{1-x}Mn_xSe$ increased with the Mn concentration with the exception of $x = 0.30$ value, which may be due to presence of In in these samples. Furthermore, from the fits it was concluded that for the carrier concentrations achieved ($\sim 10^{17}\ cm^{-3}$), the concentration dependence of the recombination lifetime plays an insignificant role in the recombination process.
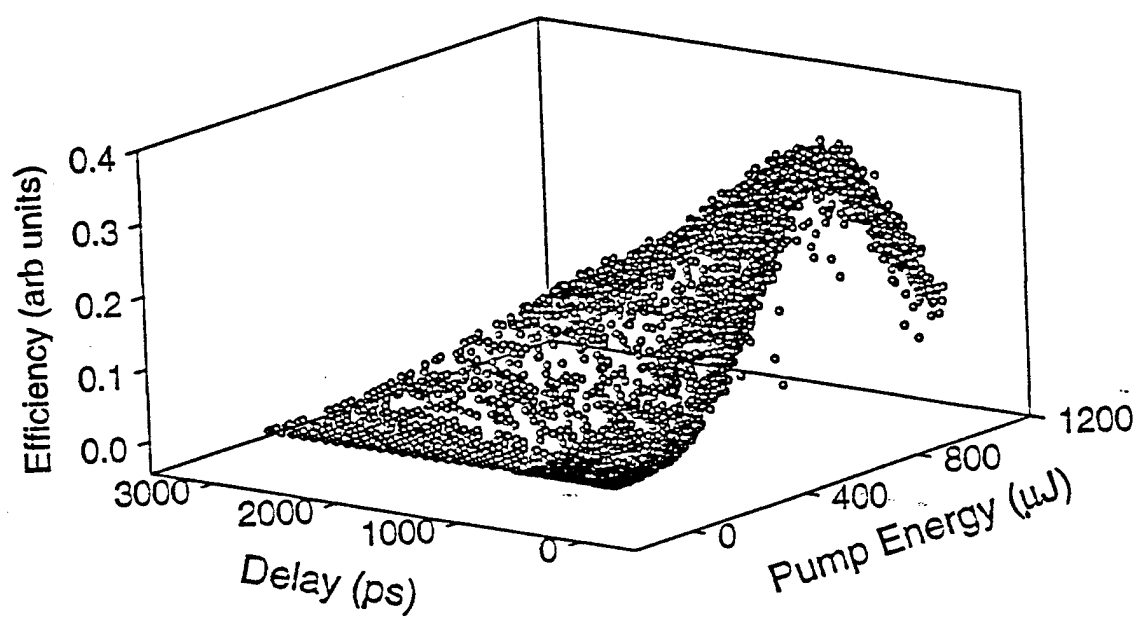
Figure 52. Scattering efficiency of the probe beam as a function of the pump beam energy and probe beam delay.
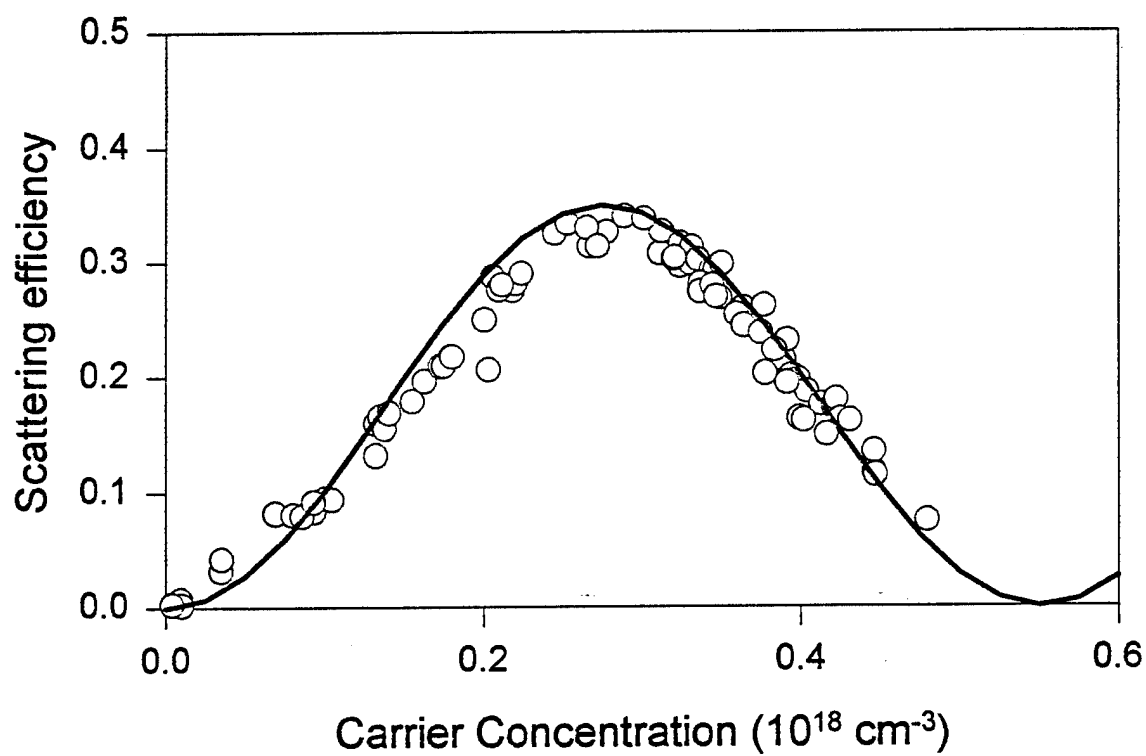
Figure 53. Scattering efficiency of the probe beam at zero delay as a function of carrier concentration.
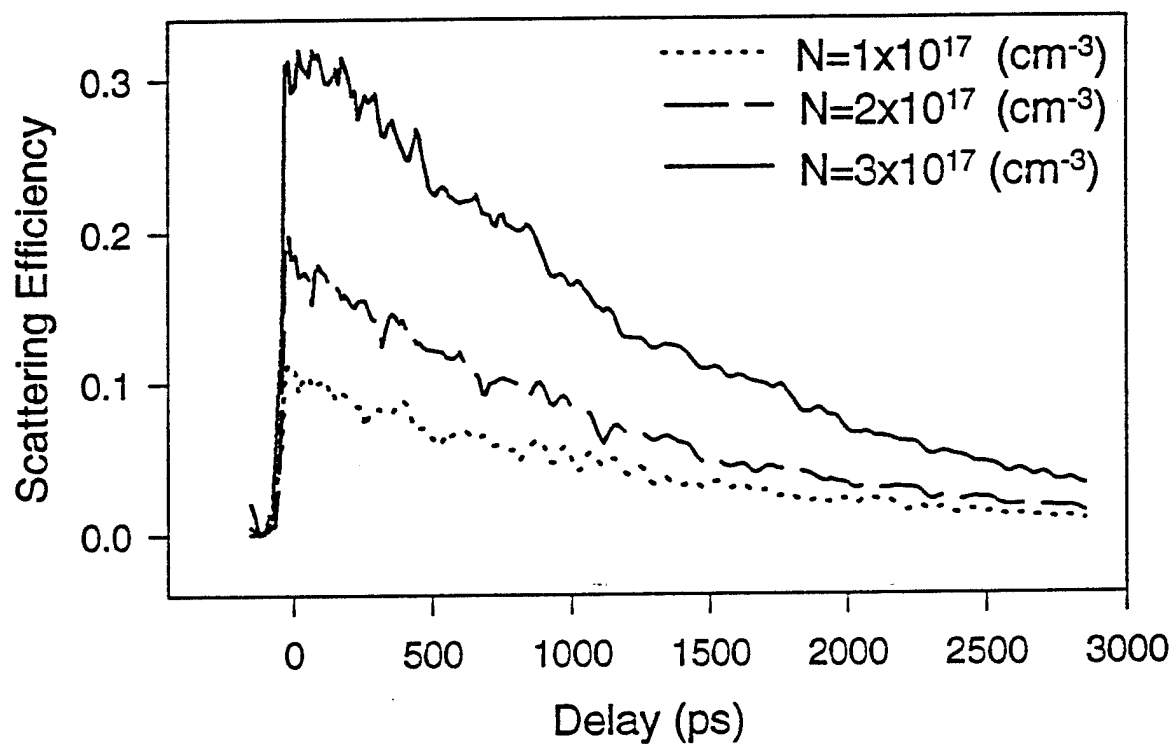
Figure 54. Scattering efficiency of the probe beam as a function of the delay for a number of pump generated carrier concentrations.
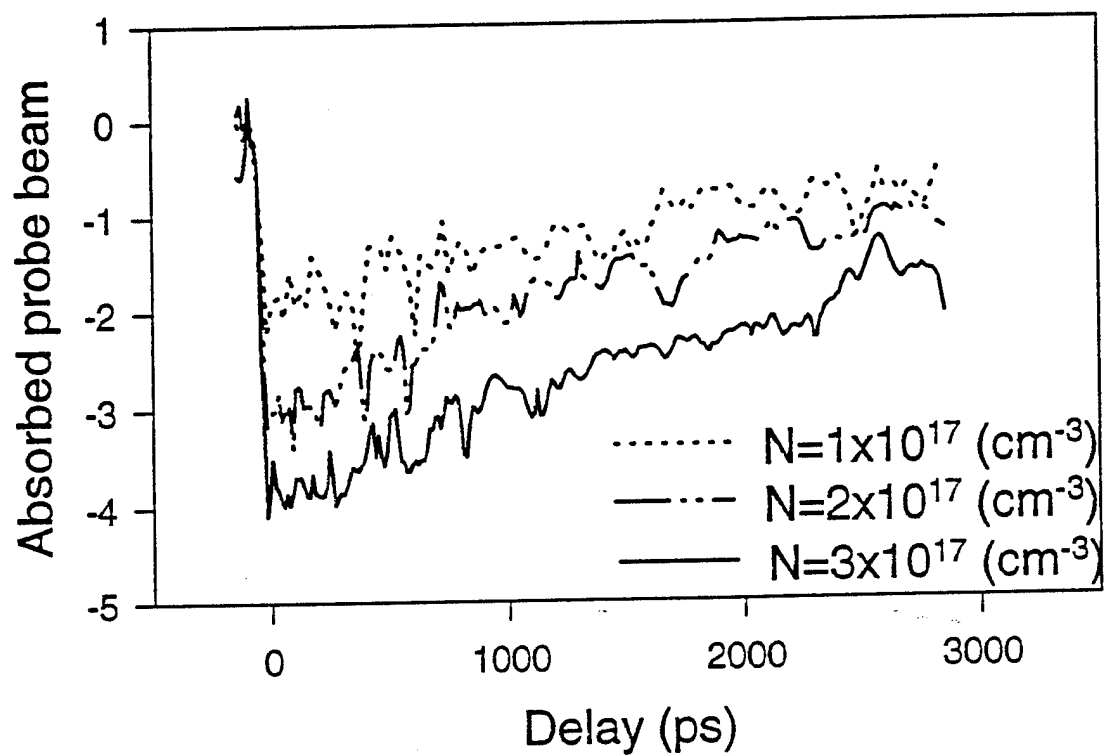
Figure 55. Loss in the probe beam energy vs delay for different carrier concentrations.
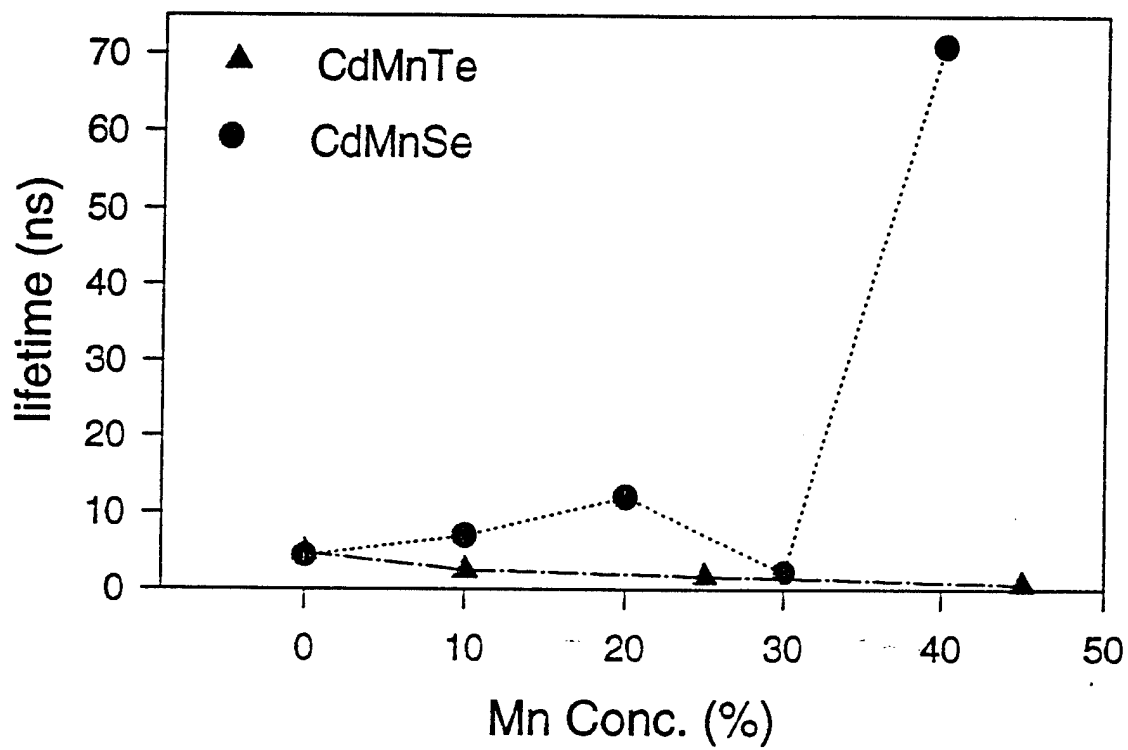
Figure 56. Life time of the electrons as a function of the Mn concentration in CdMnSe and CdMnTe.

SECTION VII

PHOTOREFRACTIVE CRYSTALS

Introduction

By far the most studied materials used for optical switching and memory storage are the photorefractive crystals. Photorefractive effect relies on the linear electro-optics effect for index changes. Since, linear electro-optic effect is the first order correction to the index with respect to an applied electric field, the index change arising from it is much larger than index changes due to third order susceptibility tensor. The linear electro-optic coefficients in insulating crystals are larger than the in semiconductors[133]. Therefore, focus is placed on insulating crystals with a large electro-optic coefficient, r. Their study is usually done using four-wave-mixing experiments. Two pump beam will interfere in the sample producing a periodic pattern of light and dark regions in the sample. Generated carriers in the light region will migrate to the dark regions via diffusion or drift. The field setup by the displaced carriers and the site of their generation will modulated the index of refraction via the linear electro-optic effect[133]. For insulator with large defect levels, continuous (cw) beam can be used to generate the carriers. Using high intensity pump beams allows band to band generation via two photon absorption (TPA) which can increase the efficiency and rise time of the signal.

The nonlinear optical responses to short laser pulses have previously been reported in photorefractive materials such as $Bi_{12}SiO_{20}$[145–151], $Bi_{12}GeO_{20}$ [151], $BaTiO_3$ [152,153], $KNbO_3$ [154], $LiNbO_3$ [155], $KTa_xNb_{1-x}O_3$[156], and Bi_2TeO_5[157] using nanosecond and picosecond pulses. The time scales for the electrooptic signals in these crystals range from less than 100 ps for $BaTiO_3$ up to 1 ms for $KNbO_3$. Here we present the results of short pulse experiments performed on a number of

191

Bismuth germanite (BGO), Bismuth tellurite (BTO) and Strontium Barium niobate (SBN) crystals. Since TPA is an important carrier generation mechanism, the two-photon absorption coefficient, β, is determined in these materials. Then, the results of FWM experiments are presented.

Sillenites, with the composition of $Bi_{12}MeO_{20}$ (Me=Si, Ge, Te), crystallize in a T23 cubic structure where the Bi^{3+} and Me^{4+} ions occupy octahedral and tetrahedral sites, respectively. Because of their large photoconductivity, sillenites have the greatest known photorefractive sensitivity of oxide-type crystals[158,133,159,160]. Their large photoconductivity is related to the absorption shoulder on the band edge which is characteristic of the undoped crystals[161]. This shoulder is due to Bi-ions in the Me^{4+} sites (Bi "anti-site")[160,162,163] and it can be suppressed with the addition of 1-5% Al or Ga oxide into the melt[161,164]. Preparing colorless, undoped $Bi_{12}SiO_{20}$ (BSO) crystals by hydrothermal growth, has recently been achieved [165].

The outstanding photorefractive sensitivity of sillenites permits the use of low laser beam intensities to induce refractive index gratings. The high absorption coefficient near the shoulder predicts that one-photon excitation processes are sufficient in low intensity, continuous wave (CW) photorefractive experiments. This should manifest itself in a quadratic dependence of the four wave mixing (FWM) diffraction efficiency on the write beam intensity. All models describing CW FWM use this one photon absorption approximation since the photorefractive efficiency is trap limited in the intensity range where multi-photon absorption is expected[133,166]. Additional shallow traps in Al:BGO which were revealed by thermoluminescence[167] and photochromic[168] investigations may be attractive for photorefractive applications since they predict a fast photorefractive response in these materials. One-photon excitation in Al:BGO, however, is only effective in a narrow energy range in the near UV[168].

The fast photorefractive response of the sillenites has been observed in short pulse laser excitation experiments[169–175,157]. The peak intensity of short pulse lasers is often large enough to induce two photon absorption in photorefractive

oxides[176–179]. Despite the expected interest in the topic only one preliminary observation has been reported concerning nonlinear absorption in sillenites[178]. The possibility of nonlinear absorption has been recognized in a picosecond pulse photorefractive process as "enhanced excitation" [174]. The measured write beam intensity dependence of the FWM diffraction efficiency, however, has not been analyzed from this aspect in the nanosecond pulse experiments[169,172].

Bismuth tellurite (Bi_2TeO_5) is a new nonlinear optical material that has recently become obtainable with a quality suitable for optical applications [180]. This material is one of the stable forms among the numerous compositions identified in the phase diagram of the Bi_2O_3-TeO_2 system [181,182]. It crystallizes in an orthorhombic crystal structure (C_{2v}^{15}) with no center of symmetry at room temperature. The early investigations were performed on microcrystallie samples but these observations are questionable since Bi_2TeO_5 is not the only crystallizing composition in the Bi_2O_3-TeO_2 system [182]. The growth of Bi_2TeO_5 single crystals using the Czochralski method has been reported [180,183,184], and some electric [183,185], optical [180,184,186–188], and acoustic [186] data have been published for single crystals. The undoped Bi_2TeO_5 crystal is transparent in the 400-7000 nm range [180,184,188]. The position of the absorption edge exhibits an orientation anisotropy when measured with polarized light [188]. Strong anisotropy has also been observed in the refractive indices [186,187], and the reflectivity spectra [188].

The first nonlinear optical properties of Bi_2TeO_5 were observed on microcrystalline samples [183,184]. Recently, photorefractive effects have been reported in Bi_2TeO_5 single crystals using both continuous wave and picosecond pulse write beams [189–192]. The decay of the photorefractive signal in Bi_2TeO_5 has multiple components with several contributions to the signal already identified. Among others, there is along lived FWM signal which lasts for more than two years without any fixing procedure[191]. FWM experiments with picosecond-duration laser pulses have been performed and indicated the existence of two-photon processes in

Bi$_2$TeO$_5$ [192]. However, without a direct measurement it was not possible to estimate the contribution of the nonlinear absorption to the creation of photorefractive gratings.

The last ferroelectric material studied is Strontium Barium Niobate (Sr$_x$Ba$_{1-x}$Nb$_2$O$_6$), SBN:100x. It has been extensively studied for applications in optical storage and processing in the continuous wave (cw) laser regime[193–195]. SBN crystals are ferroelectric with an open tungsten-bronze structure. The Sr^{2+} and Ba^{2+} ions have a 15- and 12-fold site, respectively while the niobium occupies a 6-fold site. They posses a tetragonal symmetry (point group 4mm) at room temperature [193]. Proper Sr-Ba ratio can result in a very large Pockel coefficients in these materials namely, r$_{33}$.

SBN displays excellent nonlinear optical properties, in particular, they are an attractive photorefractive materials because of their large r$_{33}$ electrooptic coefficient. Additionally, SBN is one of only a handful of materials that exhibit self-pumped phase conjugation[195]. Material properties can be tailored by varying the crystal composition and by incorporating impurity ions at open lattice sites.

<div align="center">Two Photon Absorption</div>

Theoretical

When light passes through a crystal, its amplitude is attenuated by surface reflections, absorption, scattering, and absorption of the second harmonic of the incident light. In a non-phase matched, optical quality crystal used here, the losses are primarily due to refection and absorption. Considering only single reflection from the front and back surfaces, the change in the beam irradiance, I, is given by:

$$\frac{dI}{dz} = -\alpha I - \beta I^2 - \sum_i \sigma_i N_i I \tag{215}$$

where α, and β are the single and two photon absorption coefficients and $\sigma_i N_i$ accounts for absorption due to free carriers, excited states and pump beam repopulation of the trap levels (generally termed excited state absorption). Here N_i is the number of absorption centers and σ_i is the cross-section for each center.

If we ignore the last term, excited state absorption, Eq.215 has a solution:

$$I(x,y,z,t) = \frac{I(x,y,0,t)e^{-\alpha z}}{1 + \dfrac{\beta}{\alpha} I(x,y,0,t)(1 - e^{-\alpha z})} \tag{216}$$

where we have assumed propagation in the z direction. Including a single reflection from the front and back surface we get:

$$I(x,y,z,t) = \frac{(1-R)^2 I(x,y,0,t)e^{-\alpha z}}{1 + \dfrac{\beta}{\alpha}(1-R) I(x,y,0,t)(1 - e^{-\alpha z})} \tag{217}$$

where R is the reflection coefficient.

The experimentally determined values is the incident and transmitted energy of the laser. From this measurement, the transmittivity, T, of the material can be determined. For a sample of thickness l, this is given by:

$$T = \frac{\int \int \int I(x,y,l,t)\,dx\,dy\,dt}{\int \int \int I(x,y,0,t)\,dx\,dy\,dt} \tag{218}$$

We will consider two types input pulses (i) spatially and temporally Gaussian beams and (ii) uniform spatial and Gaussian temporal beams. The first case was studied in the previous chapter. It results in:

$$T = \frac{2\alpha(1-R)\exp(-\alpha l)}{\sqrt{\pi}\beta I_o(1-\exp(-\alpha l))} \int_0^\infty \ln\left[1 + \frac{\beta}{\alpha}(1-R)I_o(1-e^{-\alpha l})\exp(-x^2)\right] dx \tag{219}$$

For the second case, the radial integration results in the area of the beam and we get:

$$T = \frac{(1-R)^2 \exp(-\alpha l)}{\sqrt{\pi}\tau} \int_{-\infty}^\infty \frac{dt}{1 + \dfrac{\beta}{\alpha}(1-R)I_o e^{-(t/\tau)^2}(1 - e^{-\alpha z})} \tag{220}$$

In both of the above case we assumed that:

$$I_o = \frac{E_o}{\pi^{3/2}\omega^2\tau} \tag{221}$$

where E_o, ω, and τ are the energy, e^{-1} radius, and e^{-1} time of the laser pulse.

Bi_2TeO_5 (picosecond)

experimental. Single crystals of Bi_2TeO_5 were grown by the Czochralski method in the research Laboratory for Crystal Physics, Budapest, Hungary. The details of material preparation and crystal growth can be found in ref. [180]. In these experiments high-purity undoped samples were used. The Fe concentrations of selected samples was measured by atomic absorption spectroscopy to be less than 10^{-5} mole/mole. This resulted in better optical quality and lower linear absorption in the transparent region than found in the crystals used in the earlier investigations [188,190]. The Bi_2TeO_5 single crystals have a (100) cleavage plane along which parallel, mirror-flat surfaces can easily be obtained. In the present measurements the laser beams were incident on such a freshly cleaved (100) surface. the other two edges of the samples were oriented by X-ray diffraction and cut by a diamond saw parallel to the [001] and [010] crystallographic directions. Throughout this paper we use the orientation convention from ref. [196] which corresponds to the a=1.16, b=1.646, and c=0.552 nm unit cell parameters.

In the nonlinear absorption experiment a Continuum Model YG671C Q-switched and mode locked Nd:YAG laser was used as the excitation source. The frequency doubled (532 nm) output of the laser has a pulse duration of about 13 ps and a repetition rate of 10 Hz. The laser beam profile in the TEM_{00} mode had a Gaussian intensity distribution. The optical setup for the nonlinear absorption measurements is shown in Fig. 57. For simplification, the lenses and irises that were used are not shown in the figure. Two types of measurements have been conducted. First, the energy transmission was determined by measuring the attenuation of strong (pump) laser pulses through the sample (part a in Fig. 57). The polarization of the pump beam was vertical. The incident and transmitted

laser pulse energies were measured by a Laser Precision Corporation Model Rm 6600 two-detector energy meter. The fluence dependence of the signal from the two detectors was calibrated without a sample.

In another experiment a weak time delayed probe beam was also applied (part b in Fig. 57). Here the probe beam attenuation was detected as a function of the pump beam fluence at different delay times with respect to the pump pulse. The delay time of the probe pulses were controlled by a motor driven optical delay line. The zero delay between pump and probe pulses was determined by adjusting for the maximum intensity of the picosecond FWM signal from a CS_2 sample as was described in ref. [197]. The polarization of the probe beam was horizontal and its incident fluence was kept fixed at 0.5 $\mu J/cm^2$ for each pump beam investigated. The transmitted probe beam was detected by a fast photodiode and analyzed by a TEKTRONIX Model 2440 digital oscilloscope. A polarizer placed after the sample and the 0.4o crossing angle between the pump and probe beams provided good beam separation even when the pump beam was four hundred times stronger than the probe beam.

High fluence (20 mJ/cm^2) write pulses, applied at a frequency of 10 Hz for several minutes, resulted in an observable color change in the illuminated part of Bi_2TeO_5 samples [192]. Typically, a yellow spot appeared which was darker than the practically colorless surrounding area of the undoped sample. In the present experiments this permanent coloration was avoided by only using a short series (16 shots) of laser pulses in the same crystal area. The coloration was checked by examining the transmission of the weak probe beam before and after the pump beam exposure. At the highest pump fluences investigated only a slight coloration was observed but the 532 nm absorption was negligible when a few shots were applied to the same spot. Signal averaging was done by repeating the series of pulses four times using a fresh crystal area for each series. Thus each experimental point in the figures represents the average of 64 individual laser pulses.

<u>results and discussion</u>.   Figure 58 shows the energy transmission of Bi_2TeO_5
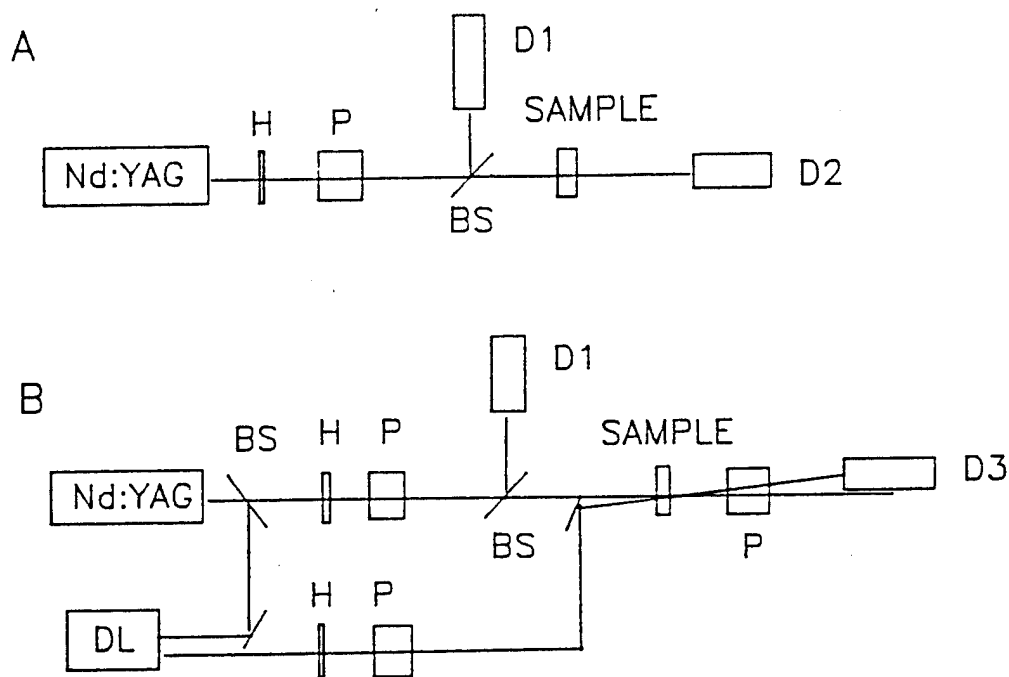
Figure 57. Experimental setups for measuring the nonlinear absorption by (a) Two photon absorption and (b) free carrier absorption.
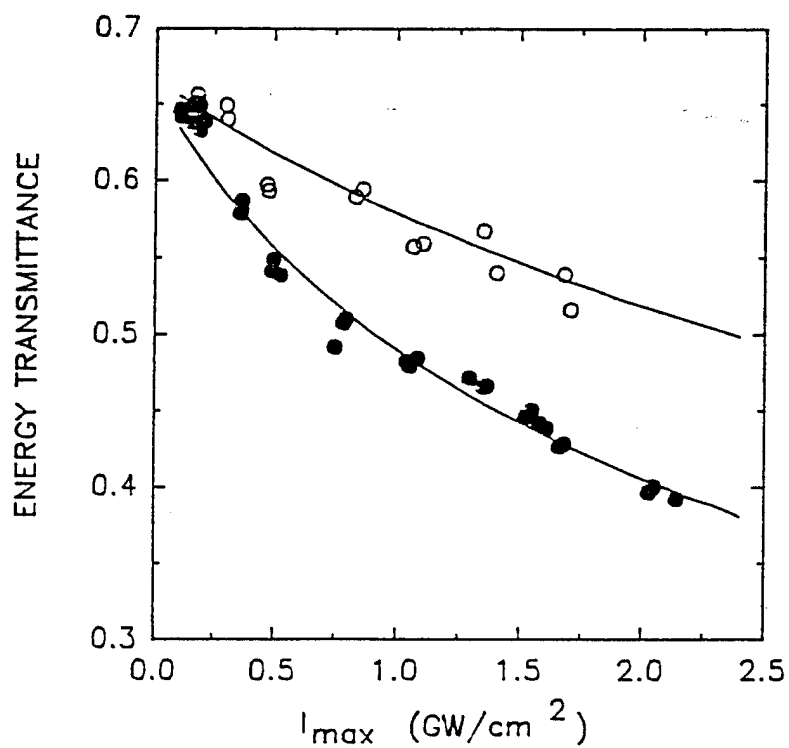
Figure 58. Energy Transmission vs Io with polarization parallel to [001] direction of BiTeO.

as a function of the maximum irradiance of the laser pulses for two different crystal samples. The 4.4 mm thick sample (filled circles) is a crystal of improved quality while the 1.2 mm thick sample (open circles) is from the same standard crystals used in the four-wave mixing experiments. In the experiments presented in fig. 58 the laser beam polarization was parallel to the [001] axis. The data for beam polarization parallel to the [010] axis are shown in fig. 59. The solid line is the fit to the data obtained using Eq. 219. The fit was done using Mathematica package with β as the only adjustable parameter. The values for the absorption coefficient, α and the reflectivity, R where taken from literature values of these materials published earlier. Table XXII shows the optical parameters used in fitting for both polarization directions. As expected α and β depend on the crystal quality. In the 4.4 mm thick sample a slight orientation anisotropy is observed in both α and β for the [001] and [010] polarization directions.

We notice from the results that the TPA coefficient of the thicker samples is lower than the thinner samples. This can be attributed to a number of effects including the excited state absorption neglected in our calculations. To elucidate the effect of excited state absorption, a delayed probe beam was introduced. Figure 60 shows the attenuation of the delayed probe beam as a function of the pump beam intensity for a 4.4 mm thick Bi_2TeO_5 sample. The data in fig. 60 are the ratio of the transmitted probe beam energy with and without the pump beam. Two probe beam delay times were chosen, 30 ps (open circles) which is slightly longer than the duration of the laser pulses and 2 ns (filled circles) which is expected to be longer than the decay time of the free charge carriers [192]. From the data, we see that the exclusion of the excited sate absorption will not result in significant alteration in the values of TPA obtained. In particular, a decrease of <4% in the total transmission was seen at input intensities of 2 GW/cm^2.

Figure 60 also shows that at high pump intensities an absorption induced by the strong pump beam is smaller after 2 ns than after 30 ps. We expect an increase in the excited state absorption if it was due to the retraped electrons by
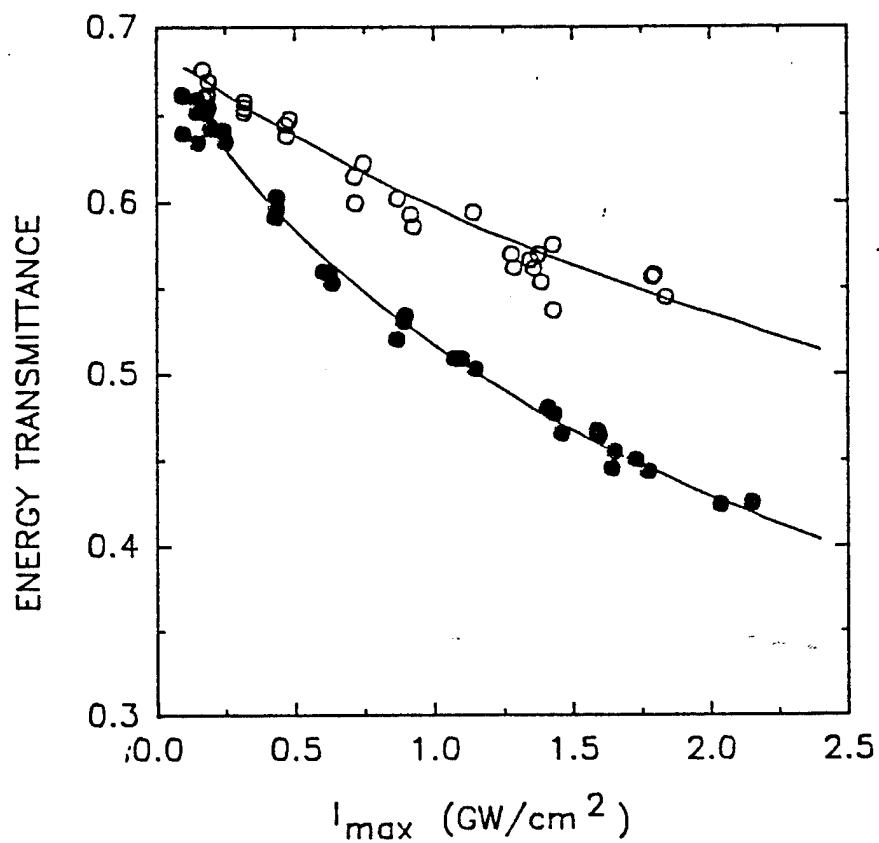
Figure 59. Energy Transmission vs Io with polarization parallel to [010] direction of BiTeO.

TABLE XXII Optical parameters used in the fitting of the TPA measurements.

Parameter	Polarization	Data
Reflectivity [a]	[001]	0.172
	[010]	0.158
Sample from standard quality crystal [b], $d = 1.2$ mm		
Linear abs. coeff. (α)	[001]	0.25 cm^{-1}
	[010]	0.25
Two-photon abs. coeff. (β)	[001]	4.7 cm/GW
	[010]	4.7
Sample from improved quality crystal, $d = 4.4$ mm		
Linear abs. coeff. (α)	[001]	0.09 cm^{-1}
	[010]	0.07
Two-photon abs. coeff. (β)	[001]	3.2 cm/GW
	[010]	3.0
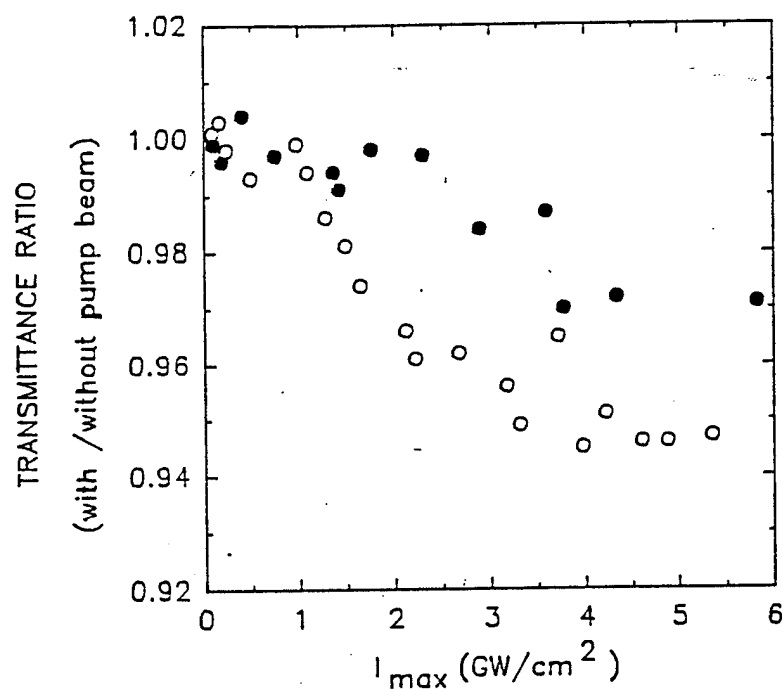
Figure 60. Probe beam attenuation due to the generated carriers at 30 ps (open circles) and 2 ns (filled circles) delay.

the defects. The decrease at 2 ns suggests that the main contribution to the excited states absorption is from the free carrier absorption.

SBN (picosecond and femtosecond)

experimental.   The nominally undoped and iron-doped, optical quality $Sr_{0.60}Ba_{0.40}Nb_2O_6$ (SBN:60) single crystals used in the experiments reported here were grown using the Czochralski technique. The iron concentration of the doped crystal was 0.012 weight percent and it is expected that iron is present in both its Fe^{2+} and Fe^{3+} charge states. An automatic diameter control unit was used in the growth of the iron-doped sample to obtain striation free crystals. Individual samples were cut from the boule, optically polished, and completely poled to a single domain using fields less than 10 kV/cm[193]. The dimensions of the samples were $5.0 \times 5.7 \times 5.7$ mm^3 and $5.9 \times 6.1 \times 6.1$ mm^3 for the undoped and iron-doped respectively.

The subpicosecond source used was the amplified output of a Spectra-Physics model 3500 synchronously pumped femtosecond dye laser. The pump source for the dye laser was a Spectra-Physics model 3800 cw, mode-locked Nd:YAG laser whose pulses were compressed via the standard optical fiber/grating pair method and then frequency doubled to 532 nm. The 580 nm, 350-450 fs duration dye laser pulses were then amplified by a three stage pulsed dye amplifier (PDA). The PDA was pumped by an injection seeded, Q-switched Spectra-Physics model GCR-3 Nd:YAG laser. Single high energy subpicosecond pulses were obtained by operating the amplifier in its single shot mode. For the picosecond laser studies the source was the frequency doubled output of a Continuum model YG571C Q-switched and mode locked Nd:YAG laser producing single 20 ps pulses at 10 Hz. An individual pulse was then separated using a mechanical shutter.

In the experiment to determine the two photon absorption (TPA) coefficient single laser pulses were passed through the sample and the energy transmission coefficient was measured as a function of incident pulse energy. The incident energy was varied using a polarizing beam splitter preceded by a polarization rotator. The polarization was maintained such that it was the same as a write

pulse in the FWM experiments described below; perpendicular to the c-axis of the crystal. The incident and transmitted laser pulse energies were measured with a Laser Precision model Rm-6600 universal radiometer with two model RJP-735 probes. The spatial profile of the picosecond laser source at the sample surface was determined using a 15 micron pinhole and a photodiode. A Gaussian profile having a e^{-1} radius of $r_0 = 0.061$ cm was observed. The Gaussian temporal profile was measured via autocorrelations to have a half width $\tau = 13$ ps at the e^{-1} point. The spatial and temporal profiles of the femtosecond laser at the sample surface were such that they were best modeled as uniform (crossectional area=3.14 $\times 10^{-2}$ cm^2) and Gaussian (half width at e^{-1}, $\tau = 240$ fs) respectively.

results and discussion. The energy transmission coefficient was measured for a single 13 ps pulse through a sample by monitoring both the incident and transmitted energies. Data were collected for a range of incident energies and the results for the undoped and iron-doped samples are plotted in Fig. 61. Equation 219 was fit to this data using the commercial program Mathematica while allowing β to vary as free parameters. α was also allowed to vary in the fit but its value was restricted to ±10% of the value determined using a Cary 2400 spectrophotometer. The solid lines in the figure represent the results of the fitting procedure. The parameters for the undoped sample were, $\alpha = 0.05$ cm^{-1} and $\beta = 2.3$ cm/GW, and for the Fe-doped sample they were, $\alpha = 0.1$ cm^{-1} and $\beta = 2.15$ cm/GW. A value for the reflection coefficient was calculated by using the published value for the index of refraction of SBN:60[198]. This value was confirmed to be valid for our samples by a simple Brewster's angle experiment and calculation. The resulting value for the intensity reflection coefficient is $R = 0.16$.

Figure 63 is a plot of transmission coefficient versus incident intensity for the experiment using the subpicosecond laser source. The solid line represents a fit of Eq. 220 to the data where, once again, β is a free parameter. The resulting value for the TPA coefficient is 2 cm/GW, in reasonable agreement with that measured for the shorter wavelength of 532 nm.

Using the subpicosecond laser system we have eliminated the possibility of significant contribution from free carrier absorption by monitoring a weak probe pulse delayed 2 ps behind the original strong one. The probe was a split component of the strong pulse and 1000 times less intense. A mechanical delay line was used to obtain the 2 ps time difference. If there were free carrier absorption, the probe pulse would have been attenuated increasingly as the strong pulse energy is increased. Transmitted probe pulse energies were recorded as a function of incident strong pulse energies. The numbers were compared with the probe transmission recorded when the strong pulse was blocked from entering the sample. Except for a small *increase* in transmission of the probe pulse at the lower energies its transmission was unaffected by the presence of the strong pulse. This result supports, to a good approximation, the exclusion of single photon free carrier absorption in our calculation of β. The increased transmission at low pump pulse energies could be due to an initial saturation of the linear absorption.

$Bi_{12}GeO_{20}$ (picosecond)

experimental. Single crystals of BGO were grown by the Czochralski technique at the Research Laboratory for Crystal Physics in Budapest. The Starting Bi_2O_3 and GeO_2 compounds were obtained by a conversion from 5N purity Bi and Ge metals, respectively. The technical details for the crystal growth can be found in ref.[170]. Three kinds of BGO crystals were prepared:

BGO1 — undoped BGO grown from the standard stoichiometric melt composition.

BGO2 — grown from stoichiometric melt composition with 2 mole % Al_2O_3 added to the melt.

BGO3 — also grown with 2 mole % Al_2O_3 dopant but the Bi_2O_3 content was reduced proportionally to the dopant.

The experimental setup used for the nonlinear absorption measurement was the same as that used in the BiTeO experiment. In this case, however, the delayed probe beam was omitted. The laser used was a frequency doubled (λ =532 nm), mode-locked, and Q-switched Nd:YAG laser operating at 10 Hz with pulse width of 13 ps. Single pulses were focused in the sample using a 1m focal length lens. The lens produced a e^{-1} beam radius of 270 μm at the front surface of the sample and a Rayleigh length of $\sim$ 20 cm. The polarization of the beam was oriented parallel to the c-axis of the crystals and its energy was controlled by a waveplate-polarizer combination. The 6% beam splitter preceding the lens provided a reference pulse for the determination of the incident energy of the laser. The energy of each pulse, transmitted and reference, was monitored by a dual probe Laser Precision RM-6600 energy meter. The calibration of the reference was done by monitoring the transmitted versus reference pulse energies in the absence of a sample. The energy of each individual transmitted and reference pulse was recorded in a computer via GPIB interface.

results and discussion.   Figure 63 shows the energy transmission coefficient as a function of maximum irradiance for the BGO1 sample. The circles and triangles are for the sample thickness of 1mm and 5mm, respectively. Figures 64 and 65 show the results obtained for experiments performed on the heavily Al-doped BGO2 and BGO3 samples. Equation 219 was integrated numerically and fitted to the data obtained using the commercial program "PeakFit". α and R were determined by direct absorption measurement using two different sample thicknesses. Therefore, only one adjustable parameter, β, was used in the fitting procedure

Table XXIII summarizes the values of the physical parameters measured for these materials. The TPA coefficients of the thicker samples have a smaller numerical value than those for the thinner samples. This difference may be due to the assumptions used in the derivation of Eqs.215-219:

i) It was assumed that the beam radius in the sample remained constant. This assumption is not valid for thick samples or samples which exhibit lens type
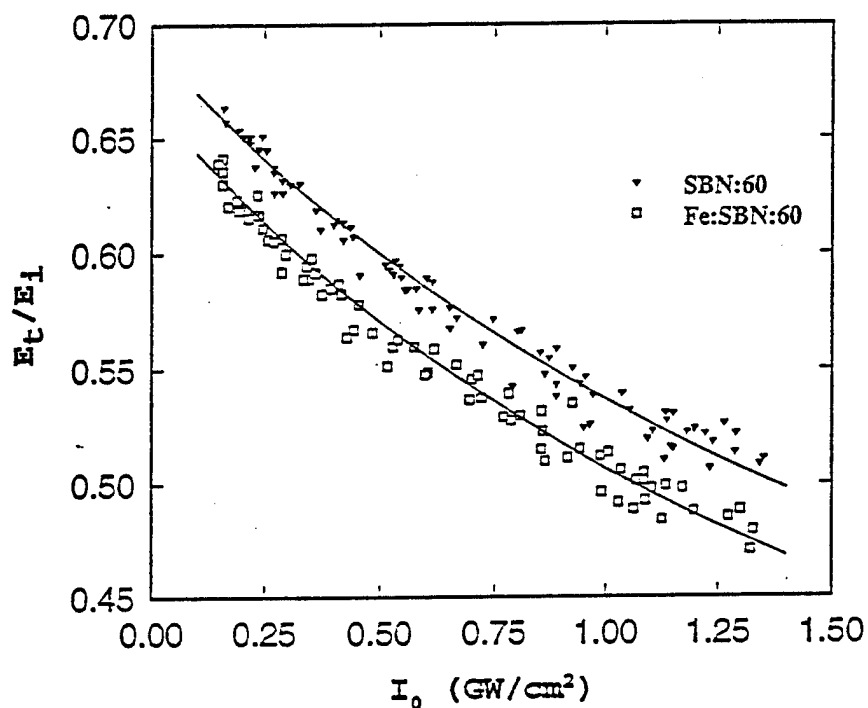
Figure 61. Picosecond two photon absorption of SBN and Fe:SBN and the fit (solid lines).

TABLE XXIII Physical parameters found for BGO crystals

Sample	Dopant	Thickness	α	R	β
		(mm)	(cm^{-1})	(%)	(cm/GW)
BGO1	----	1	0.30	18	2.6
BGO1	----	5	0.30	17	2.2
BGO2	Al	1	0.12	19	2.3
BGO2	Al	5	0.12	18	1.9
BGO3	Al	1	0.12	19	2.3
BGO3	Al	5	0.12	19	1.9
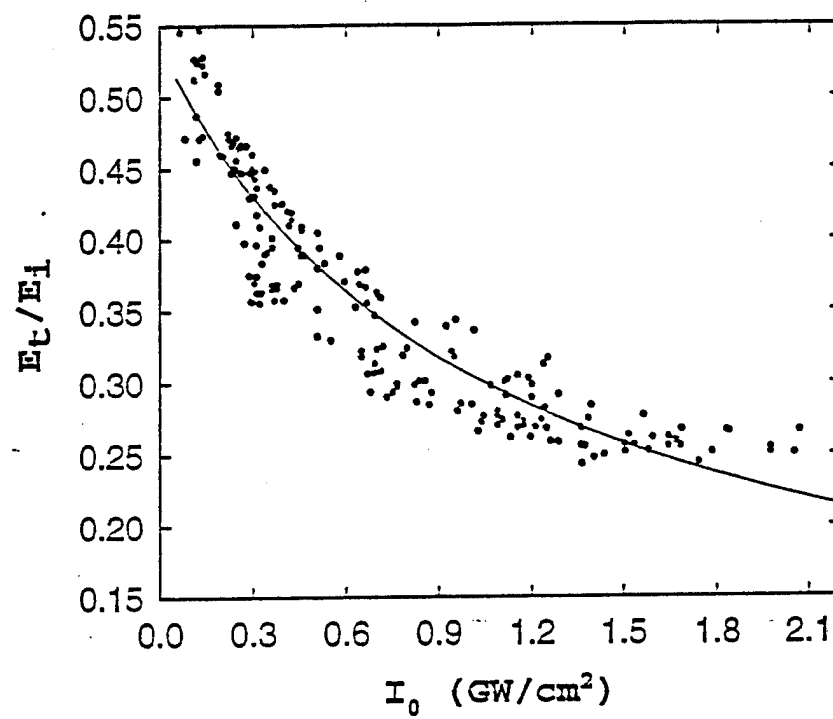
Figure 62. Femtosecond nonlinear absorption in SBN and Fe:SBN with fit (solid lines).
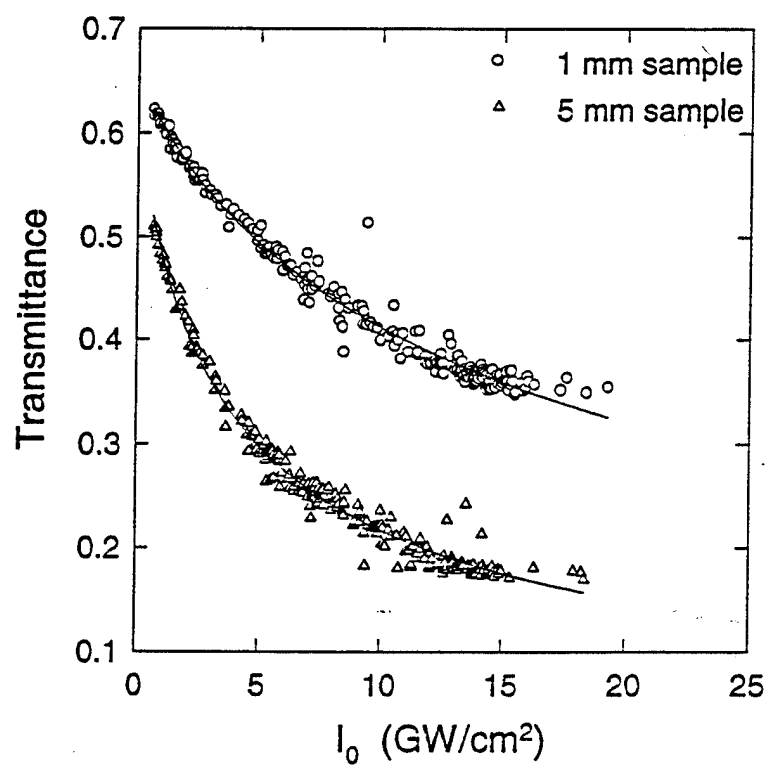
Figure 63. Transmission of light versus input intensity for BGO1 crystal. The solid line is the fit.

nonlinearities. For photon energies used ($\hbar\omega/E_{gap} \succ 0.7$), both bound and free electrons result in self defocusing[129]. The reduction in the on-axis irradiance due to this defocusing is greater in the thicker samples. Therefore, the true average on-axis irradiance in the thicker sample is smaller than the front surface value used in the above calculations. This will result in an under estimation of the value of the two photon absorption coefficient for the thicker samples.

ii) Various nonlinear processes which are observable at high input irradiance, such as absorption by the two photon generated free carriers, were ignored. These effects reduce the total transmission coefficient and are less significant in the depth of the crystals where a part of the incident laser light has already been absorbed. Thus, the thinner samples will demonstrate a greater decrease per unit length in the transmission coefficient which can be interpreted as an enhancement of the TPA coefficient.

It is thought that the observed dependence of the TPA coefficient on the crystal thickness is due to a combination of the above effects. Such behavior has also been observed in BTeO crystals. In those experiments, the free carrier absorption was monitored and a 3% decrease in the transmission coefficient was found for a 1.2 mm sample while a 4.4 mm sample exhibited a 5% decrease. The nonlinear nature of the thickness dependence of the free carrier absorption in the BTeO crystals suggests that the thickness dependence of β is primarily due to the free carrier absorption rather than self defocusing mechanism. Regardless, for any given sample thickness it can be seen that the Al doping (BGO2 and BGO3) slightly reduces TPA coefficients. It is also of interest to note that the effects of the Bi-Ge Stoichiometry were not quantified by the numerical values of the TPA coefficients.

Photorefractive Properties

SBN (picosecond and Femtosecond)

experimental. In the FWM experiment a single pulse was split into two parts of equal energy (hereafter referred to as 'write' pulses) which were focused such that they overlapped spatially and temporally in the sample ideally producing a spatially harmonic interference pattern. The angle between the paths of the pulses was 3.2° measured in air. A low power, cw He-Ne laser aligned at the Bragg angle for maximum diffraction from the grating was also focused in the sample. The beam geometry and crystal orientation was the usual photorefractive configuration used for FWM studies in SBN[199], i.e. the π-polarized He-Ne laser beam was crossed in the sample with the two σ-polarized write beams which were oriented with respect to the crystal such that they produced a grating wavevector that was parallel to the c-axis (see Fig. 66). To improve the signal-to-noise ratio the probe beam propagation direction was aligned out of the plane containing the write pulses. The diffracted beam was detected using a photomultiplier tube with a rise time of approximately 2 ns and a digital storage oscilloscope. An interference filter at the He-Ne laser wavelength was used to ensure that no stray light from the pulsed laser entered the photomultiplier tube.

results.

Picosecond-pulse excitation With excitation pulses of 20 ps duration and 532 nm wavelength there were two distinct temporal features seen in the FWM signal for both samples. Typical data obtained for the undoped sample are shown in Fig. 67. After the initial unresolved build-up the first decay of the FWM signal is in the 100 ms time scale. This was followed by a comparatively slow rise that reaches its maximum after a few minutes (Fig. 67(b)). In the case of a total write beam energy of 78 μJ the second rise is complete in approximately four minutes and

decays to half the peak height, in the continuous presence of the He-Ne laser, after another fifteen minutes.

Typical FWM data obtained using the Fe:SBN sample are shown in Fig. 68. Similar to the signal from the undoped sample, there exists two stages to the signal in the time frame studied, however the time scales associated with them are very different. The decay of the first signal is complete in less than 25 ms and is followed by a rise of the second signal that is complete in less than 20 seconds. For pulse energies lower than those shown in Figs. 68(a) and 68(b), e.g. Fig. 68(c), the detected signal is observed to drop below the background level in the time regime just after the first signal decay. This means that there must be a process that had decreased the total amount of background light that is randomly scattered from the sample to the detector. For both samples the cross-sectional area of interaction for the two write pulses was 2.7×10^{-5} cm^2.

Subpicosecond-pulsed excitation In a manner similar to that which was seen using the ps pulses, excitation using 400 fs, 580 nm pulses produces two temporal features to the diffracted signal in the time scale of interest in these experiments. Typical data for the undoped sample are shown in Fig. 69. The first feature in Fig. 69(a) is a peak that has a rise time of 300-600 ns which is time resolved in Fig. 69(b). The initial spike in the data seen in Fig. 69(b) is due to gratings formed on the time scale of the temporal overlap of the two write pulses and is not of interest in this work. This signal decays into the microsecond time scale where it competes with the rise of the second signal. The time constants associated with the second peak depend strongly upon the intensity of the write pulses. It has been observed to last as long as thirty seconds or as short as few hundred milliseconds.

Experiments on the Fe-doped samples were not performed using the subpicosecond laser system.

discussion. The first signal in both the picosecond and subpicosecond experiments is associated with scattering from a grating that is set up by an optically

induced absorption change in the bright regions of the interference pattern of the two write pulses. In order to demonstrate that intense light at both 580 nm and 532 nm induces absorption at 632.8 nm in SBN:60, one of the write pulses and the He-Ne laser were crossed in the sample and the transmitted He-Ne laser beam was monitored with the same detection scheme as discussed above for FWM. The results of the experiment using the picosecond and subpicosecond laser are shown in Figs. 70(a) and 70(b), respectively. In both cases, the time dynamics of the induced absorption are the same as those of the first signal in the FWM experiments. This suggests that, for the time scales associated with the first peak in the FWM signals, an absorption grating dominates any contribution from a photorefractive index grating.

This experiment was carried out using the iron-doped sample as well and, within our model of induced absorption, since the FWM signal decays more rapidly in this sample it would be expected that the induced absorption decays faster as well. On the contrary, however, the induced absorption experiment showed that the depletion lasted longer (see Fig. 71). This observation helps explain why the decay of the FWM signal is followed by a drop in the signal below the background level for total write pulse energies less than ~ 40 μJ (not observed at higher intensities because the rise of the second peak begins earlier for increasing intensities and competes with the decay of the first signal). A comparison of the time scales for both experiments in Fe:SBN reveals that the levels responsible for the induced absorption remain populated following the decay of the absorption grating. The grating decay rate is then associated with the rate at which the absorbing level in the dark regions of the interference pattern are populated. This action decreases the contrast ratio of the grating and therefore the diffracted signal. It is this spatially uniform residual absorption that decreases the amount of randomly scattered light that reaches the detector and causes the signal to drop below the background level. Since the absorption grating signal in the undoped sample follows the decay of the absorption, the difference in signal behavior can most likely by attributed to increased carrier mobility associated with iron-doping. Increased mobility is

supported by the observation that the photorefractive signal develops an order of magnitude faster in the iron-doped sample.

Kogelnik[125] presented the coupled wave solution for diffraction from thick absorption gratings. With the probe beam incident at the Bragg angle and having its polarization parallel to the plane of incidence, the diffraction efficiency for such a grating is given by[125]

$$\eta = \exp(\frac{-\alpha d}{\cos\theta_0}) \sinh^2(\frac{\alpha_1 d \cos(2\theta_0)}{4\cos(\theta_0)}) \tag{222}$$

where α_1 is the average value of the absorption change, d is the interaction length, and θ_0 is the Bragg angle measured inside the crystal given by $\theta_0 = \sin^{-1}(\frac{\lambda_p}{2\Lambda n})$ (isotropic diffraction). λ_p is the vacuum wavelength the probe beam (632 nm), $\Lambda = \lambda_w/2\sin\theta$ is the grating spacing with $\lambda_w \equiv$ write laser wavelength and $\theta \equiv$ crossing angle measured inside the crystal, and n is the dark index of refraction of the crystal. Using the results of the induced absorption experiment where no grating is present, $\alpha_1 d$ is Eq. 222 can be calculated for a given value of incident pulse intensity

$$\alpha_1 d = -Ln(\frac{I_d}{I_a}), \tag{223}$$

where I_d is the depleted value of the He-Ne transmission intensity following the strong pulse and I_a is the He-Ne transmission intensity in the absence of the strong pulse. Since in FWM experiment, the peak intensity in the bright regions of the interference pattern is given by I=$I_t(1 + m)$, where m is the modulation index of the grating and I_t is the total intensity of the write pulses, we can estimate the expected contribution of the absorption grating to the total experimental efficiency. The result is that the diffraction efficiency observed can not be fully accounted for by Eq. 222. With the large values of the induced absorption produced, a contribution from the unshifted refractive index grating (according to Kramers-Kronig relation) is needed. For the lowest values of the write intensities used, the diffraction efficiency using SBN approaches that predicted by Eq. 222. However, using the Fe-doped sample, the signal is an order of magnitude larger.

With the experiments described thus far it is not possible to determine the physical mechanisms responsible for the induced absorption. It is proposed that the induced absorption is a result of the population of an impurity or defect site that did not have significant population before excitation. Further, it is thought that significant population of this level is realized with the aid of a large number of two photon band-to-band transitions followed by trapping at the site(s) that absorb near 632 nm. The TPA coefficient at 532 nm, as discussed in the previous section, is 2.3 cm/GW for undoped SBN:60. With an intensity of 2.5 GW/cm^2 the intensity depletion of a laser beam due to TPA is more than an order of magnitude greater than that due to the linear absorption. Below this value of intensity the transient probe beam depletion becomes an unmeasurable effect with our detection system. After excitation the free carriers populate an absorbing level at a rate that is roughly inversely proportional to the rise time of the induced absorption. As discussed the primary physical mechanisms leading to the decay of the grating are different for the two samples. For undoped SBN:60 the decay is thought to be primarily due to the depopulation of the absorbing level either through recombination or trapping at other site(s) that do not absorb at 632.8 nm.

The subsequent rise of the diffracted signal after the decay of the absorption grating is explained as due to the usual charge displacement photorefractive effect[200]. It can only be observed when the beam geometry is such that photorefractive effects are possible. At this time the mechanism of charge transport as well as the sign of the charge carrier is not apparent. In cw FWM experiments electrons have been found to be the dominant carrier[193]. However, competition from holes cannot be ignored in the pulsed regime because the direct band-to-band transitions that are associated with nonlinear absorption create a large number of holes. Their contribution to the grating depends on their relative mobility with respect to the electrons. The physical processes leading to the photorefractive index grating are currently under investigation.

Bi$_2$TeO$_5$ (picosecond)

experimental.   Single crystals of Bi$_2$TeO$_5$ were grown by Czochralski method in the Research Laboratory for Crystal Physics, Budapest, Hungary. The details of material preparation and crystal growth can be found in ref. [180]. For the present experiments undoped, Cr-doped (10^{-4} mole/mole), and Fe-doped (5 x 10^{-5} mole/mole) samples were used. The Cr and Fe impurity concentrations of the undoped Bi$_2$TeO$_5$ crystals were 1.0 x 10^{-6} and 1.2 x 10^{-5} and mole/mole, respectively. These built-in dopant concentrations were determined by Atomic Absorption Spectroscopy.

In the pulsed four-wave mixing experiments, a Quantel International Model YG571c Q-switched and mode locked Nd:YAG laser was used as the excitation source. Each frequency doubled (λ =532 nm) pulse had an energy of 18 mJ/pulse, duration of about 18 ps with a repetition rate of 10 Hz. The two write beams were crossed in the sample at various angles creating gratings in the [010] crystallographic direction. The σ-polarized probe beam was either a third weak component of the Nd:YAG laser pulse, or the 632.8 nm cw output of a He-Ne laser. In the first case (degenerate FWM) an optical delay line was used in the probe beam path to follow the evolution of the diffracted signal beam in the time range from 100 ps before to 2 ns after the write pulses. The diffracted signal was detected by a photodiode and analyzed by a boxcar signal averager. When the cw He-Ne probe beam was used, the scanning mode of the boxcar signal averager provided the time evolution of the diffracted signal. In most of the photorefractive measurements the cleaved (100) surface was exposed to the incident laser beams. Throughout this section we will use the orientation convention introduced in ref. [196].

results.   Figure 72 shows the FWM diffraction efficiency as a function of the probe beam delay for different Bi$_2$TeO$_5$ samples. The time evolution of the FWM signal from Bi$_2$TeO$_5$ crystals, using 18 ps pulses for write and probe beams, is similar to those published for other photorefractive oxide materials using similar experimental conditions [201,204–207]. Each curve in Fig. 72 consists of a sharp

peak positioned at 0 ps delay and a decaying part with a superimposed damped oscillation covering the time scale from about 20 ps to 2 ns. The basic character of the time evolution is the same for the undoped and doped Bi_2TeO_5 samples. Slight differences have been observed in the absolute signal intensity and the lifetime and relative intensities of the three contributing signal components in the different samples.

The time evolution of the FWM signal in the microsecond to millisecond range is shown in Figure 73. These data were obtained by using 18 ps write pulses and a cw probe beam for detection . The FWM diffraction efficiency for undoped Bi_2TeO_5 shows a continuous decrease up to about 50 μs, then a slight increase was observed between 50 μs and 1 ms, followed by another decaying region. The rate of decay for the microsecond range signal is 0.033 μs^{-1} while for the millisecond range signal it is 0.026 ms^{-1}. The latter decay rate is in good agreement with the data obtained in the previous CW FWM experiments [191].

discussion.   The CW FWM experiments on Bi_2TeO_5 have shown strong photorefractive signal with multicomponent decays [190]. Excited state population grating, refractive index modulation due to the space charge induced electro-optic effect, and a contribution due to ion displacements are identified in the photorefractive process [190]. In the Cr-doped samples, an absorption grating was also detected. The relatively low saturation limit of the observed FWM diffraction efficiency indicates that the photorefractive effect in undoped Bi_2TeO_5 crystals is limited by the charge carrier or charge trap concentrations [190]. This saturation limit is increased by using Fe or Cr dopants in both CW and short pulse induced FWM [190,192].

The characteristic feature of the fast photorefractive response of the crystal have already been analyzed for undoped Bi_2TeO_5 [192]. The detailed analysis based on the dependence of the FWM signal on the write beam intensity, write beam crossing angle, crystal orientation, write- and probe beam polarization [192]. The

laser excitation process was also investigated and significant two-photon absorption was observed [192,208].

The interaction of the laser beams with bound charges is the major contribution to the sharp peak at 0-delay. This signal component decays in the picosecond time scale. There is an additional component to the instantaneous signal due to the creation of free carriers. This component persists as long as the free carrier lifetime or the time it takes for the carriers to diffuse to the dark regions of the light interference pattern. The free carrier grating is considered as the main contribution to the signal component decaying in the few nanosecond time scale [192]. The damped oscillatory modulation of the nanosecond FWM signal is attributed to the generation of acoustic phonons by the laser pulse impact. The compression due to the acoustic phonons moves along the refractive index grating and its contribution to the refractive index grating created in the FWM processes is periodically constructive and destructive [192].

The Fe and Cr dopants do not modify the basic character of the FWM signal induced by short laser pulses significantly. However, the amplitude of all three signal components discussed above are larger for the doped crystals than for the undoped one. Also, the damping of the phonon induced oscillations different for the doped and undoped crystals. The decaying factor of the oscillation was found 0.89 ns^{-1} for undoped Bi_2TeO_5 samples under the standard experimental condition, while this factor is 1.24 ns^{-1} for the Cr-doped and 0.49 ns^{-1} for the Fe-doped samples.

The interpretation of the longer lived FWM signals decaying in the microsecond and millisecond range is more difficult. It was shown for $BaTiO_3$ and $Bi_{12}SiO_{20}$ that the intense short pulse induced FWM signals, decaying in this time interval, are associated with electro-optically induced, phase shifted gratings [201,209,210]. The build-up of the photorefractive grating is much faster in the pulsed writing than in the CW writing process. This was attributed to an enhanced diffusion of the charge carriers in the former case. Two models have been developed to explain tis fast diffusion. In the model of ref. [211] the charge recombination time

is short compared to the pulse length, and consequently only the high fluence of the pulsed beams can saturate the charge number density. Under these conditions the diffusion rate is modified. The other explanation is a saturation of the charge traps due to the high irradiance of the write beams. This increases the effective trapping time of the charge carriers [209].

A signal decaying in a few tens of milliseconds has already been identified in the CW FWM measurements of Bi_2TeO_5 and attributed to an impurity related excited state population grating [190]. In those measurements the write beam intensity was smaller by orders of magnitude than that of the present pulsed write beams and only one photon excitation was considered. Consequently, the displacement of the excited charge carriers was only in its initial stage and the unshifted component due to excited state population grating was predominant in the millisecond time regime after CW writing [190]. In the 18 ps pulse writing process, however, the free charge carriers are generated in large numbers by two-photon excitation and, according to the models discussed above, they may be spatially shifted before recombination or trapping occurs. A small shift of the charge carriers appears to occur even on the nanosecond time scale [192].

The FWM signal components decaying in microsecond and millisecond range may be related to the presence of shallow traps as has b been shown to be the case for other photorefractive crystals. In several oxide crystals impurity ions have been found to provide these shallow levels. Since a small concentration of iron impurities (about 20 ppm) is in the undoped Bi_2TeO_5 crystals, the iron ion electron levels are possible options as the source of the shallow traps in this material too.

A thermal excitation of the shallow traps and a subsequent re-trapping leads to a long range migration of the charge carriers with a trap-modulated mobility. In this way the contribution of the phase shifted grating becomes more and more dominant in the signal at longer times as was observed in the CW FWM measurements [190,191]. The CW FWM experiments have demonstrated the existence of a variety of different charge carrier traps and the deep traps are responsible for the longer time scale signals (seconds to minutes) [190,191]. The space charge

field generated in the photorefractive process also leads to ionic displacements in Bi_2TeO_5. Oxygen ions can easily be shifted in the space charge field since there are large number ($\sim$18%) of open oxygen position in the crystal structure [157].

The build-up of the phase shifted photorefractive signal component is significantly faster with the 18 ps writing pulses than it was observed for the CW writing process which was investigated earlier [190,191]. The faster build-up of the phase shifted grating in short pulse writing experiments compared to the CW write process, also leads to a faster build-up of the long lived FWM component (>2 years) which was attributed to the displacement of oxygen ions [190,191].

Another possible contribution to the signal on the microsecond-millisecond time scale is a thermal grating. Since the thermal properties of Bi_2TeO_5 crystals have not been investigated this possibility can not currently be evaluated.

The most interesting character of the time evolution of the FWM signal is the local maximum in the ms time range (Fig. 73). This indicates a rearrangement in the photorefractive grating during the time evolution. A mathematical modeling is in progress to distinguish among the possible options. Simultaneous presence of unshifted and phase shifted gratings, absorption and refraction index gratings as well as their decay and transfer to each other will be considered.

Conclusions

The experiments performed on different photorefractive crystals in pico and femto second time regimes resulted in TPA coefficients of a few cm/GW. In pulsed experiments, intensities of up to 5 GW/cm^2 are easily attainable. In these cases the two photon absorption can exceed the single photon absorption by up to two orders of magnitude. In such cases the electron generation is dominated by TPA. Since the scattering efficiency in a FWM experiment on these samples, dictated by their photorefractive behavior, depends on the number of generated carriers, an increase in the efficiency and response time can be expected if short pulse excitation is used. The limit on the efficiency, then, is dictated by the trapp density and not the generation rate.

Single picosecond and subpicosecond light pulses were used in independent experiments to induce refractive index gratings in SBN:60 and doped Bi_2TeO_5. In SBN crystals, the time evolution of the gratings appear to have at least two stages which are responsible for two distinct peaks in the FWM signal. The first peak is associated with induced absorption at the probe wavelength. In a single beam experiment, where no grating was present, it was shown that significant probe beam depletion is seen following intense excitation. This depletion is explained as induced absorption due to the population of an impurity or defect site and is associated with the first peak in the FWM signal because the time scales of the two phenomena overlapped. The second peak is explained as resulting from a grating due to a charge displacement photorefractive effect. It can only be observed when the beam geometry is such that photorefractive effects are possible.

In Bi_2TeO_5, the effect of dopants was investigated on the fast decaying photorefractive signal components (<2 ns) of Bi_2TeO_5. It was found that Cr and Fe doping resulted in only a moderate gain in the diffraction efficiency. This is unusual for oxide crystals where dopants generally increase the FWM signal by orders of magnitude, especially when combined by appropriate treatments to get the optimum ratio of empty traps and charge carrier source [212,213]. The dominant FWM signal components in the microsecond to seconds regime was attributed to electro-optically induced, phase shifted gratings involving impurity related traps with several different trap depths. The fast development of the real photorefractive signal is consistent with enhanced charge diffusion due to the higher density of free carriers created by the 18 ps laser pulses.
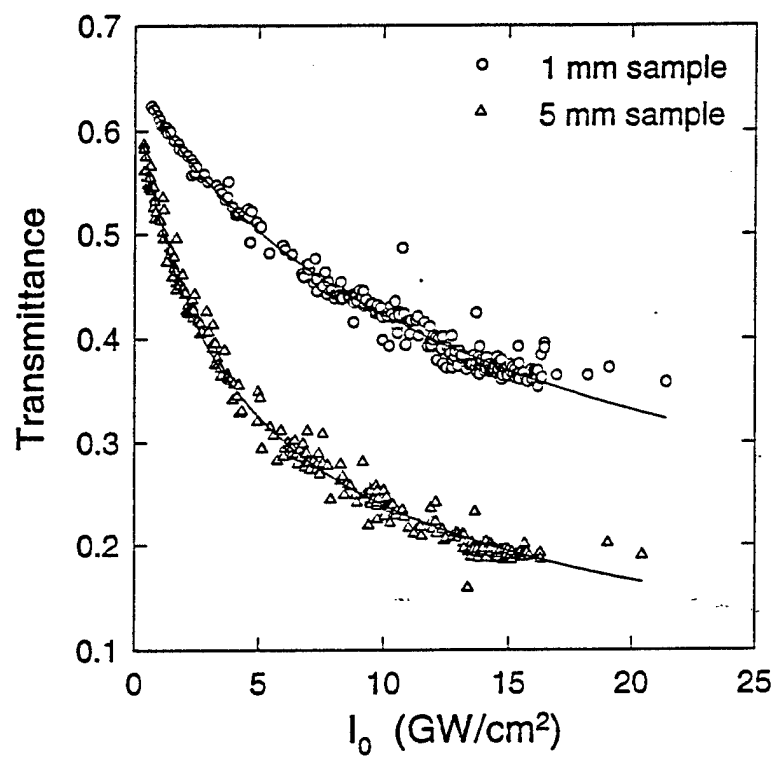
Figure 64. Transmission of light versus input intensity for BGO2 crystal. The solid line is the fit.
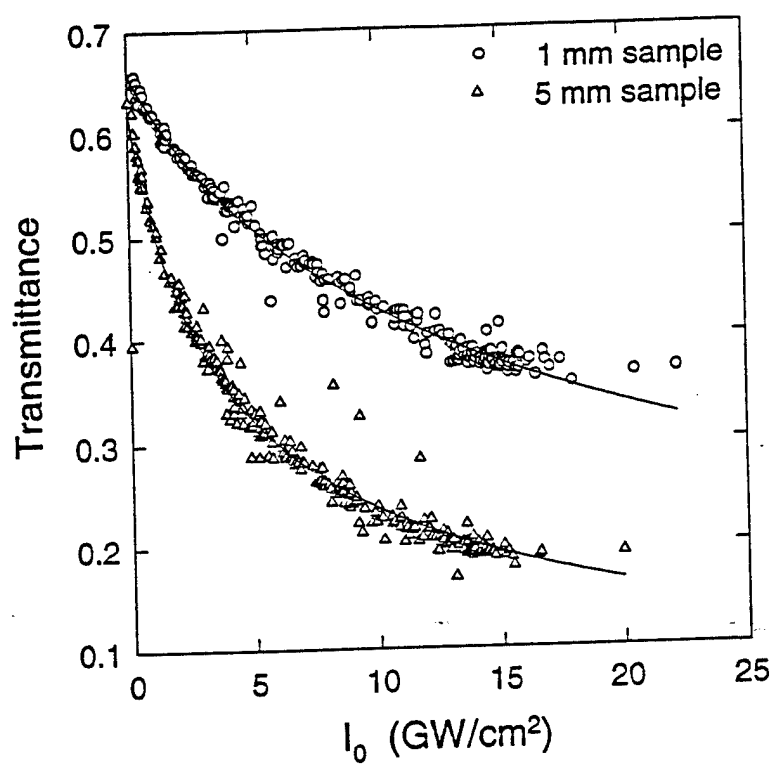
Figure 65. Transmission of light versus input intensity for BGO3 crystal. The solid line is the fit.
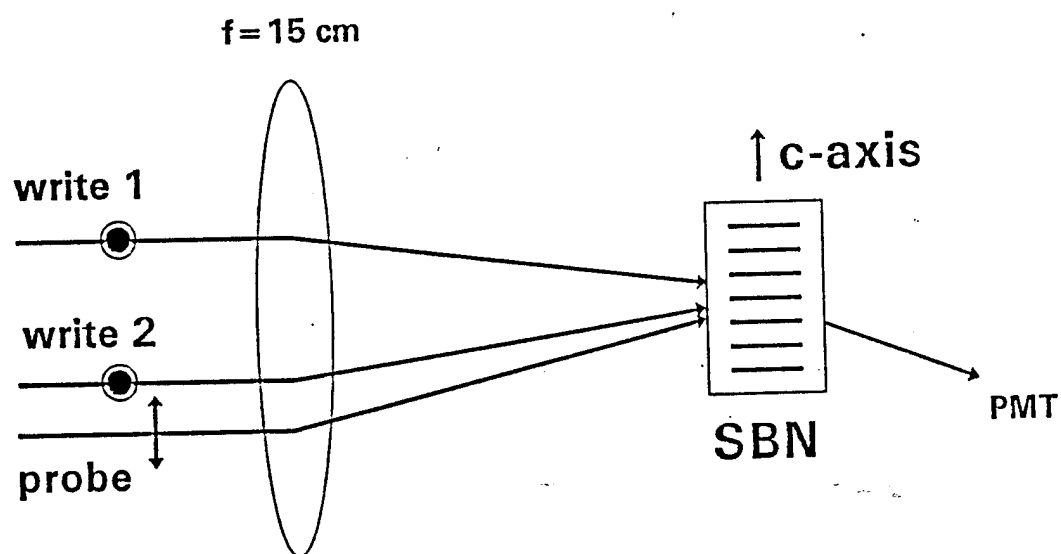
Figure 66. Beam geometry for FWM experiments. π-polarized cw He-Ne probe beam and σ-polarized subpicosecond ($\lambda = 580$ nm) or picosecond ($\lambda = 532$ nm) write pulses.
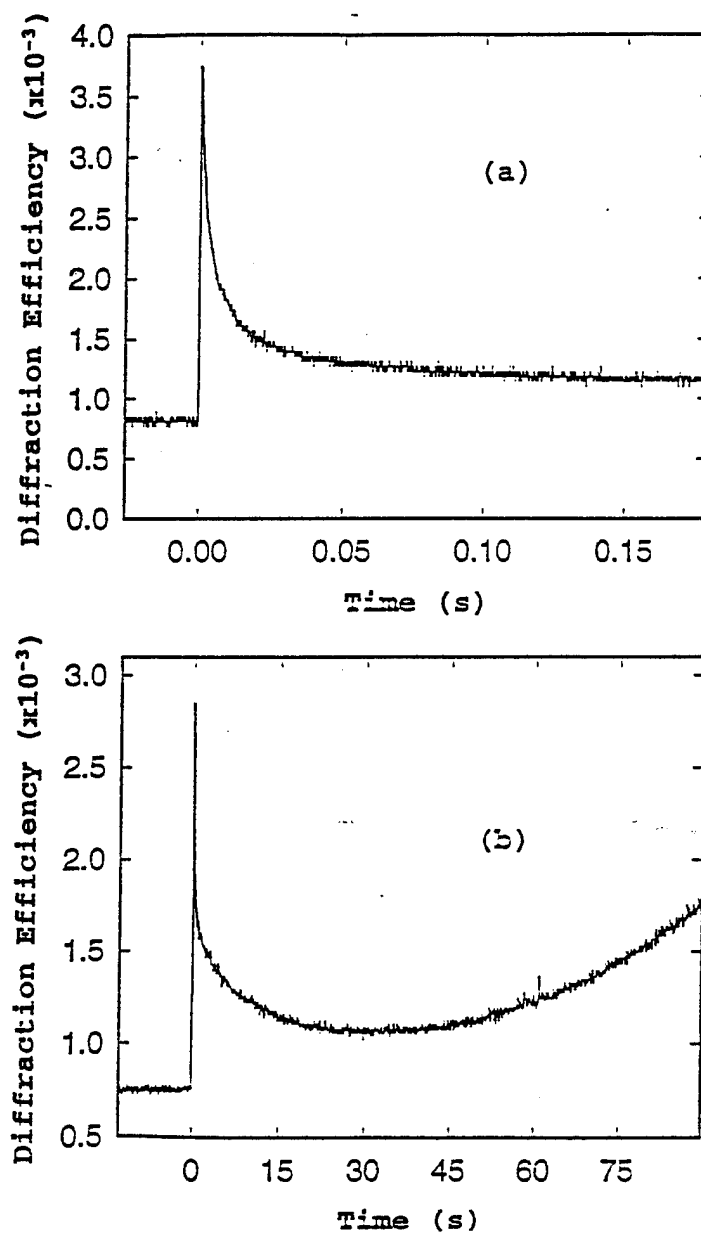
Figure 67. FWM signal following picosecond excitation in SBN:60 with write beam energies of (a) 47 μJ and (b) 46.4 μ J.
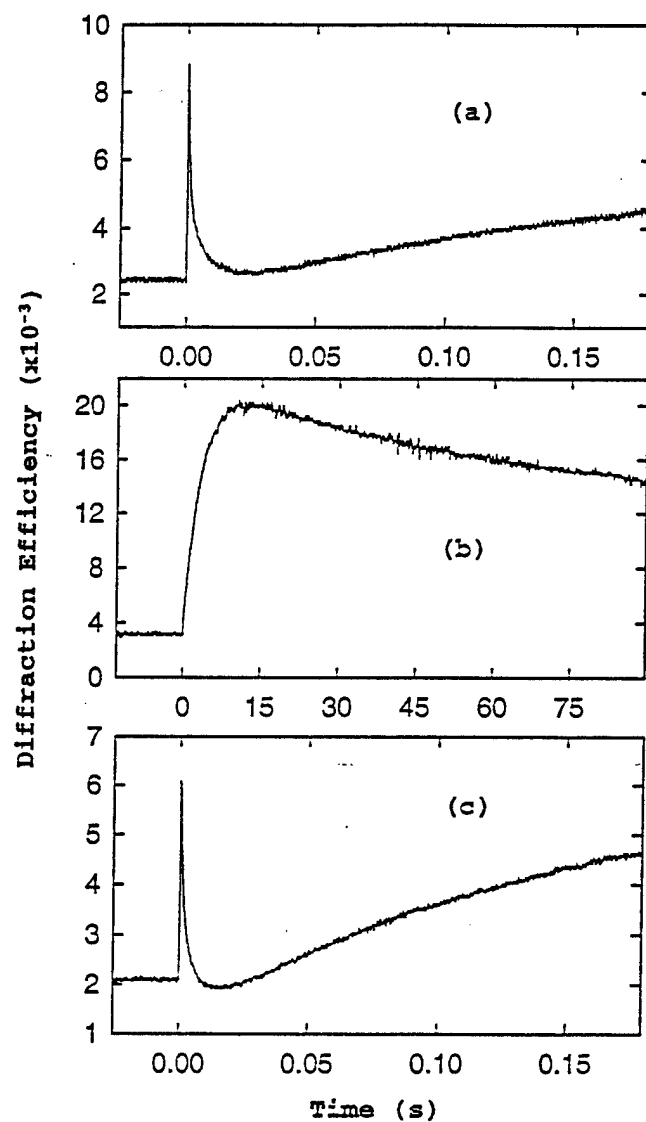
Figure 68. FWM signal following picosecond excitation in SBN:60 with write beam energies of (a) 42.8 μJ (b) 50 μ J and (c) 18.5 μ J.
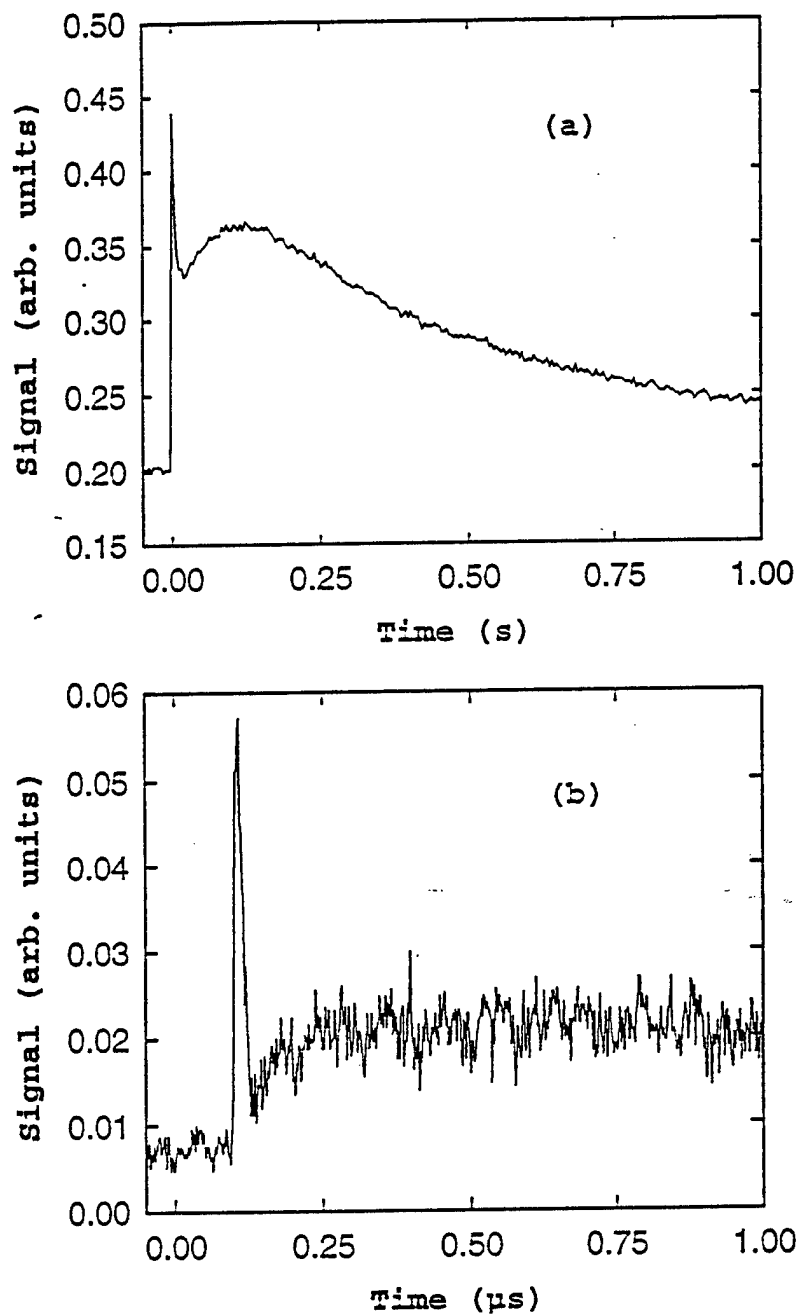
Figure 69. FWM signal following subpicosecond excitaion in SBN:60 in the time scale of (a) seconds and (b) microseconds.
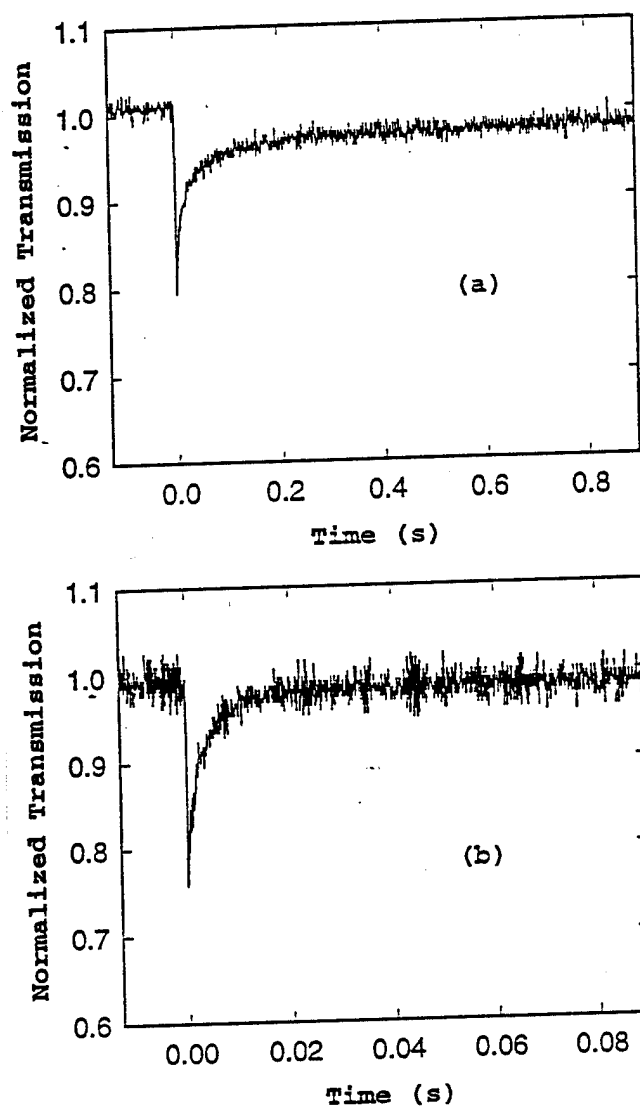
Figure 70. Probe beam depletion following (a) 46.1 μJ picosecond excitation and (b) 1.1 μJ subpicosecond excitaion.
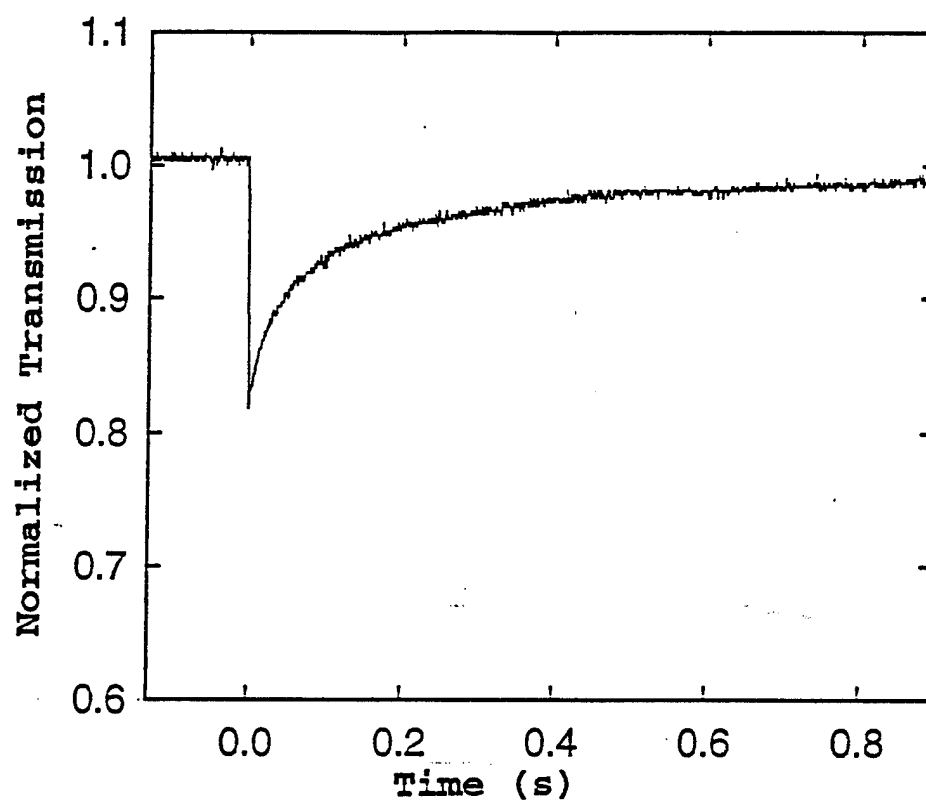
Figure 71. Probe beam depletion following 41.4 μJ picosecond excitaion..
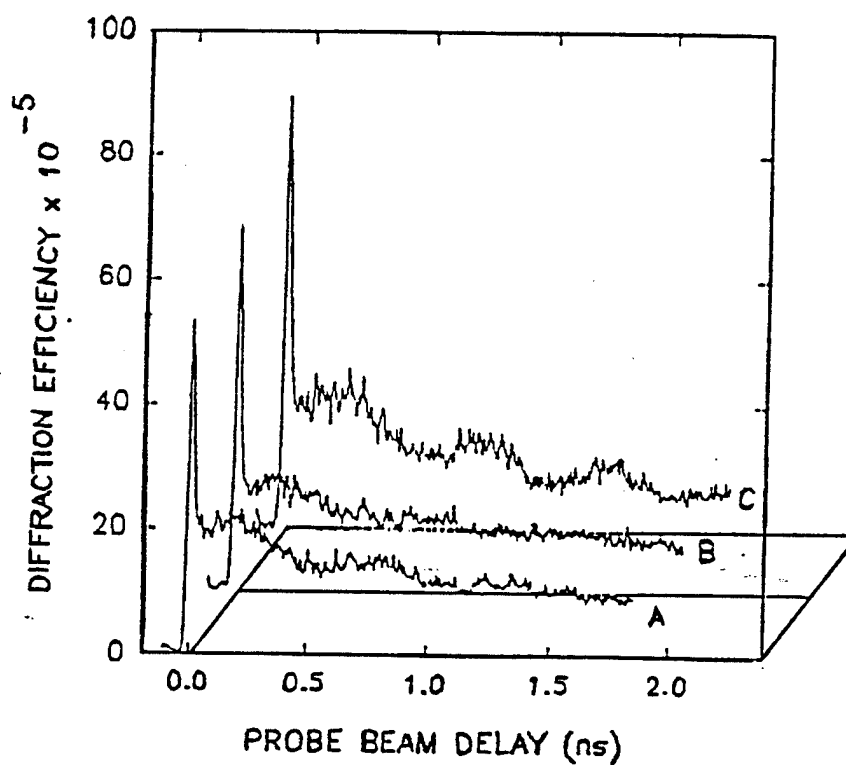
Figure 72. The time evolution of the FWM signal in undoped (curve A), Cr doped (curve B) and Fe-doped (curve C) Bi_2TeO_5.
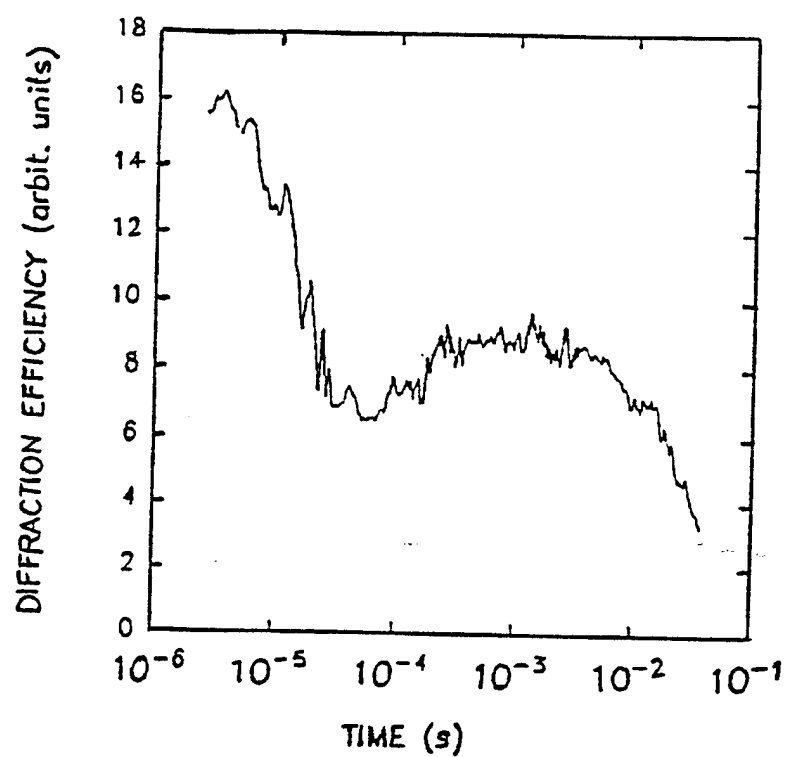
Figure 73. The time evolution of FWM signal from microsecond to millisecond time regimes.

SECTION VIII

RARE-EARTH DOPED GLASSES

Introduction

The last class of materials that has generated interest as possible memory storage materials are rare-earth doped glasses. Unlike the materials studied in the previous chapters, glasses are random structure with no translational symmetry. Much like the photorefractive crystals they are insulators, but unlike them the bonding between its various constituents is primarily covalent. The role of an ion in a glass is categorized as either network former (F) or network modifier(M). The network formers participate in the covalent bonding that compose the structure such as SiO_2, GeO_2. Presence of the modifier ions breaks the covalent bonding by competing for the shared electrons in the bonds. It has been shown that the role of an ion in the structure can be determined from its charge-to-radius-squared, Q/r^2 value. In particular, atoms with a large Q/r^2 display covalent bonding and as such will behave as network formers. As the value for Q/r^2 decreases, the bonding becomes more ionic and the ion becomes a network modifier. In oxide glasses studied here the oxygen is the bridging atom with a large Q/r^2 ratio. Addition of the network modifiers such as Na^+ breaks the covalent bonding between oxygen and its adjacent atoms turning the oxygen into a non-bridging oxygen. These free radicals have a very strong response to an incident electromagnetic wave and are dominant contributors to the glass' dielectric function. Ions with closed outer shell electrons, such as rare-earths, display interatomic transitions in addition to acting as a modifier ion. Excitation of these atoms through interatomic transitions can alter the dielectric function of the glass. most of these alterations are transient, however permanent index changes have been reported previously in rare-earth

doped phosphate and silicate glasses [214–220]. These gratings were produced using four-wave-mixing (FWM) techniques and resonant excitation of the trivalent rare-earth ions into excited states that undergo efficient radiation less relaxation. The transient component of the grating was attributed to a population grating of the rare-earth ions and a model based on a thermally induced change in the local glass structure at the site of the rare-earth ions was proposed to explain the formation of the permanent gratings [214–220].

The conventional view of glass as a structural network with modifying ions dispersed in the interstities can provide the essentials of this model if some of these ions have the ability to change their positions. In phosphate, silicate, germanate, and borate glasses the rare-earth (RE) dopant ions are in network-modifier positions, surrounded by nonbridging oxygen ions [221–225]. When the excited RE ions relax nonradiatively several high energy vibrational modes are created. The local heating associated with these vibrational modes produces a change in the structure of the local environment of the RE ions by causing the ions in that region of the material to move from one configuration to another. This leads to double-minima potential wells for the configuration coordinates of the RE ion electronic energy levels. The mechanism for switching the host ions between two equilibrium positions requires structures with high frequency local vibrational modes such as those associated with structural defects (lateral or nonbridging groups of ions) and further requires that the RE ions are strongly coupled to these vibrational modes[215]. The two-potential-well-model (TPWM) also assumes that the index of refraction of the material changes depending on which structural configuration is present.

There are still important questions to be answered concerning the exact nature of the local structural change in the glass and the origin of the refractive index difference for the two configuration. In order to answer these questions information is required as to how the chemical composition of the glass alters the characteristics of the permanent refractive index gratings produced. Also important is learning how to either optimize or minimize the production of these gratings. This is critical in understanding the general phenomenon of laser-induced index changes that have

been observed in both bulk and fiber materials[226], since this effect can form the basis of important optical devices or can be detrimental to optical transmissions. With this in mind, this paper extends the previous work to include new types of lithium borate, lead silicate, lead borate-germanates, and lead germanate glasses. The results of this work are combined with the previous results on phosphate and silicate glasses to understand the effects of the chemical composition of the glass on its ability to produce gratings with high scattering efficiencies.

Experimental Results

LIG's in lithium-borate glasses

To determine the effects of different glass modifier ions on the ability to produce gratings with high scattering efficiencies, six Eu^{3+}-doped lithium-borate glasses (LiB) were investigated. These had identical compositions except for one modifier ion which was changed through the series of metallic elements: Mg, Ca, Ba, Zn, Al, and Pb. These glasses were selected since: (i) the general optical properties of Eu^{3+}-doped glasses have been previously analyzed[223], (ii) in the range of B_2O_3 mole % used in these samples it is assumed that only fourfold coordinated boron atoms exist[227,228], and (iii) previous experiments have demonstrated permanent laser induced gratings in this type of glass[217]. The compositions of these glasses are listed in Table XXIV.

Gratings were produced in each sample at room temperature using the technique described previously[214–220]. Crossed beams from an argon laser tuned to the absorption transition of the $^5D_2$ level of the Eu^{3+} ions were used to write the gratings. The scattering efficiencies η of these gratings were measured using the output of a low power He-Ne laser for the read beam. A typical result for the time evolution of the FWM signal is shown in Fig. 74 for the LiB4 glass. In all six LiB glasses the signal builds up slowly in time reaching a maximum in about 30 min. It was observed that in each sample when the write beams were chopped off, the signal beam intensity decayed rapidly to about 70% of its maximum value in

TABLE XXIV Composition of glass samples

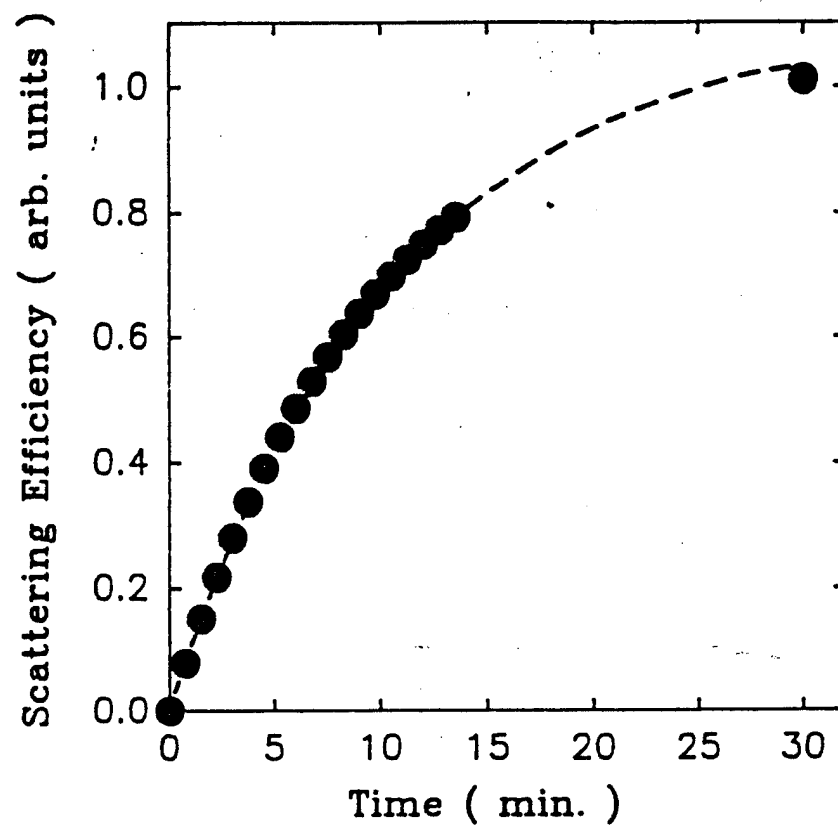| Sample	Network Former (mol %)	Network Modifier (mol %)		Eu^{3+} content (mol %)
LiB1	60.0 B_2O_3	15	Li_2O	5 Eu_2O_3
		20	BaO	
LiB2	60.0 B_2O_3	15	Li_2O	5 Eu_2O_3
		20	MgO	
LiB3	60.0 B_2O_3	15	Li_2O	5 Eu_2O_3
		20	CaO	
LiB4	60.0 B_2O_3	15	Li_2O	5 Eu_2O_3
		20	ZnO	
LiB5	60.0 B_2O_3	15	Li_2O	5 Eu_2O_3
		20	Al_2O_3	
LiB6	60.0 B_2O_3	15	Li_2O	5 Eu_2O_3
		20	PbO	
PbB	67.7 B_2O_3	24	PbO	5 Eu_2O_3
		3.3	BaO	
PbBGe	40.0 B_2O_3	24.0	PbO	5 Eu_2O_3
	27.7 GeO_2	3.3	BaO	
PbGe	67.7 GeO_2	24	PbO	5 Eu_2O_3
		3.3	BaO	
PbSi1	67.7 SiO_2	24	PbO	5 Eu_2O_3
		3.3	BaO	
PbSi2	57.7 SiO_2	34	PbO	5 Eu_2O_3
		3.3	BaO	

Figure 74. Time evolution of the buildup of the FWM signal in LiB4 sample at room temperature with write beam power of 70 mW.

TABLE XXV Relevant parameters of the modifier ions.

Glass	Modifier ion	Mass ($\times 10^{-24}$ g)	Q	r (Å)	Relative Q/r^2	SCB_{M-O}
LiB1	Ba	120	2	2.8	1.1	90
LiB2	Mg	35	2	2.0	2.0	79
LiB3	Ca	53	2	2.5	1.5	84
LiB4	Zn	76	2	2.1	1.8	66
LiB5	Al	38	3	1.8	3.4	116
LiB6	Pb	147	2	2.3	1.4	131

a time given by the Eu^{3+} ion $^5D_0$ level lifetime. This initial decay was followed by a slow decrease in the signal intensity over a period of about 15 min. In these lithium-borate glasses the signals leveled off at about 40% of their initial values and remained there for several days, the longest period investigated. The results obtained for this time evolution of the signal from the LiB4 sample are shown in Fig. 75.

It was found that the scattering efficiency of the permanent LIG in these LiB glasses was strongly dependent on the nature of the network modifier ions. Previous results from phosphate and silicate glasses also show efficiency changes with different modifier ions[214–220]. Table XXV lists the values of Q, r, and the mass are for each of the modifier ions used here along with relative values of Q/r^2.

In Fig. 76 the experimental values of the scattering efficiencies are plotted vs Q/r^2 for the samples studied. To illustrate the effects of the mass of the modifier ions, the efficiency is plotted vs the mass for the Group II alkali metals Mg, Ca, and Ba in Fig. 77. Another parameter that is used to characterize different modifier ions is the bond strength between modifier and oxygen ions. The values of the strength-of-the-chemical-bond (SCB_{M-O}) between the various modifier ions and oxygen ions are listed in Table XXV and the dependence of the scattering efficiency on SCB_{M-O} is shown in Fig. 78. Further discussion of these results is left to a later section.
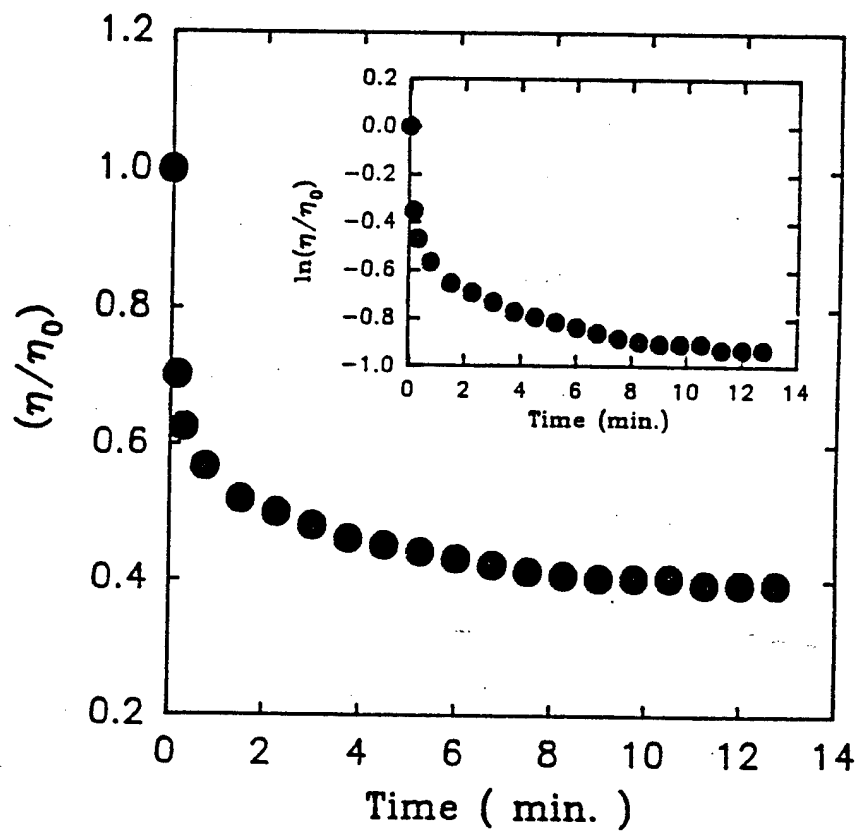
Figure 75. Time evolution of the scattering efficiency of the LIG in LiB4 after the write beams were choped off.
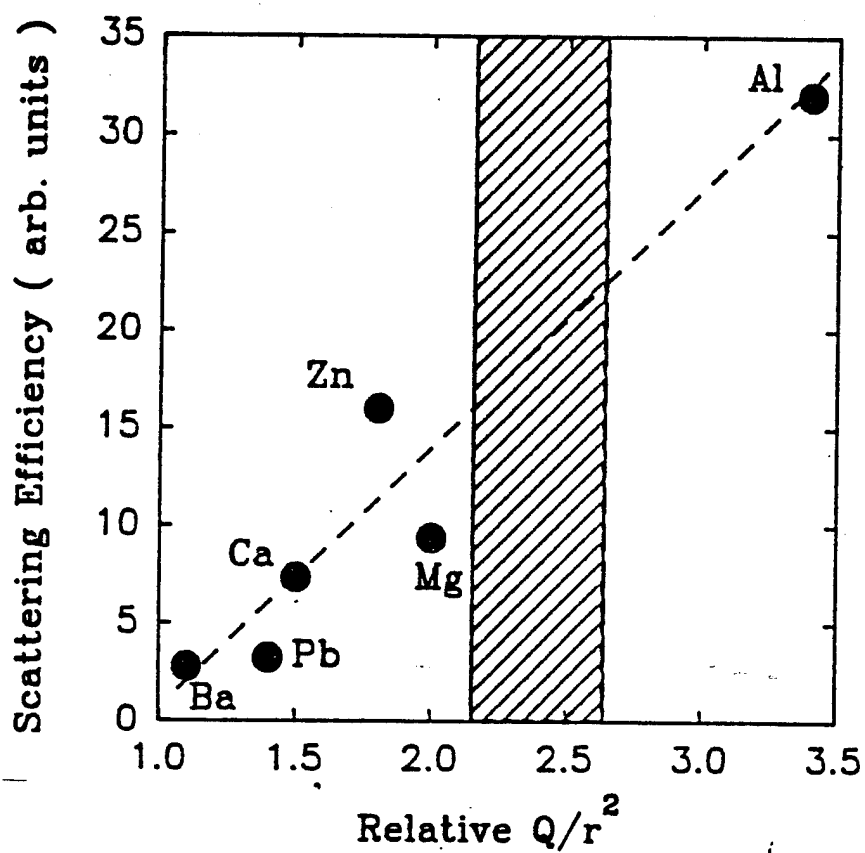
Figure 76. Scattering efficiency of LIG in the LiB samples as a function of Q/r^2 of modifiers. The area bounded by vertical dashes contains the values of Q/r^2 for rare-earth ions..
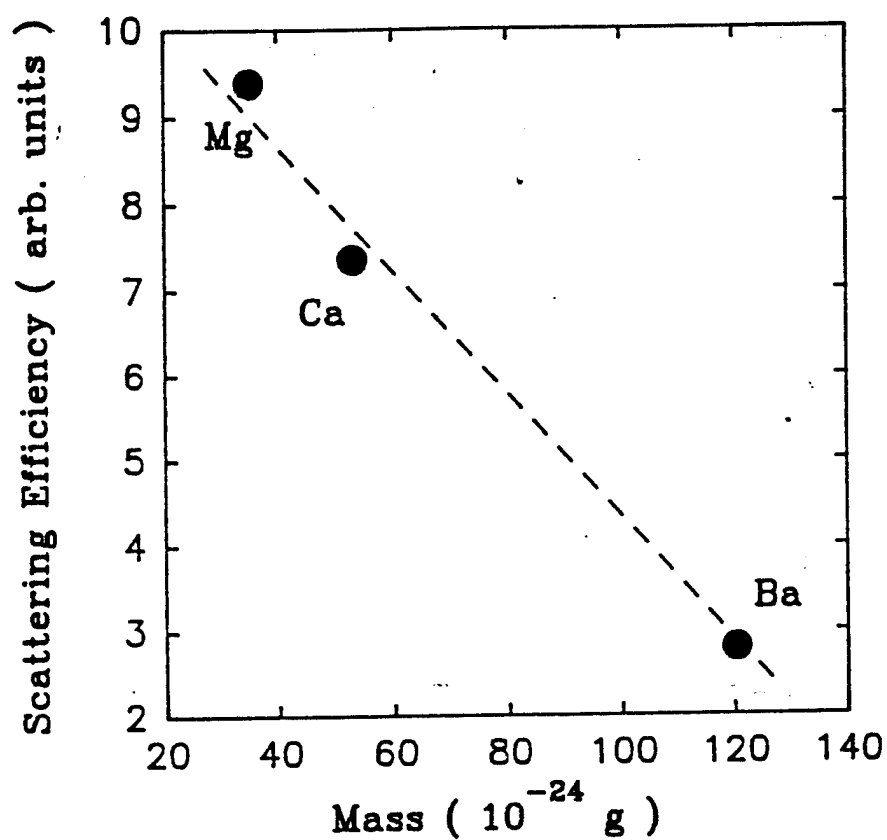
Figure 77. Scattering efficiency of LIG as a function of the mass of the modifier
ions created at room temperature in LiB samples containing the
Group II modifier ions Mg, Ca and Ba.

Figure 78. Scattering efficiency of the LiB glasses as a function of the strength of chemical bond between modifier and oxygen ions.

Effects of bond-strength and glass composition

Since the strength of the chemical bond between the network former ions and the oxygen ions (F-O) and the relative concentration of the network former and network modifier ions are two important parameters that determine the structure of the glass, five additional glasses were selected to study the influence of these parameters on the scattering efficiency of the permanent LIG. The compositions of these glasses are also listed in Table XXIV. They were selected since: (i) the strength of the chemical bonding between the network former and oxygen ions, SCB_{F-O}, increases as the network former ion changes with germanate<silicate<borate [229]; (ii) glasses are formed by all compositions in the system B_2O_3-GeO_2 [230]; and (iii) in the range of F_xO_y mole % selected, all of the network former ions are fourfold coordinated [231]. The scattering efficiency of the permanent LIG was found to decrease as the network former was changed to increase the SCB_{F-O} as shown in Fig. 79. In this figure a rule of additivity [232] was employed to estimate the SCB_{F-O} in the sample PbBGe.

Interpretation

Transient gratings

In all the samples investigated, both permanent and transient gratings were created. The initial signal decay having a time scale of the order of a few milliseconds is consistent with the decay of the Eu^{3+} population grating. The slow decay of the LIG signal to the stable value that was observed here in the lithium borate glasses was not seen in the earlier experiments on the phosphate and silicate glasses. This difference can be explained by the different thermal properties of the different types of glasses.

The structural units that form the amorphous nature of these glasses have several possible configurations. The permanent gratings result from a periodic modulation in the configurations of these units. Each unit has a characteristic
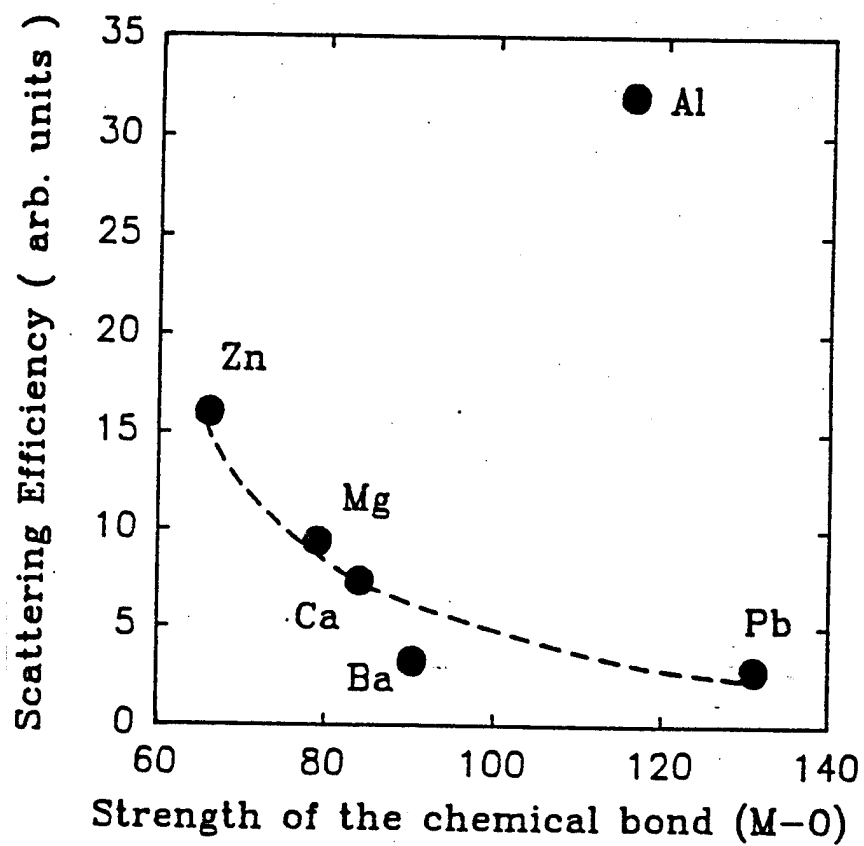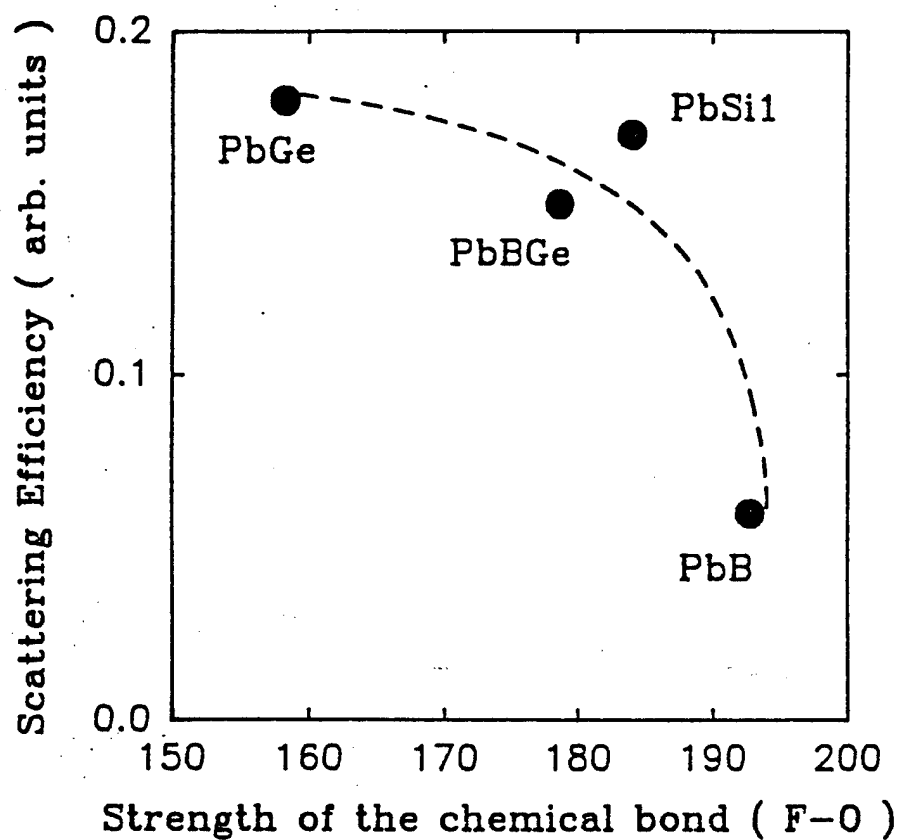
Figure 79. Scattering efficiency of LIG in four glasses as a function of the strength of chemical bond between the former and oxygen ions.

time for the change from one equilibrium configuration to another that will depend upon the temperature. For a given relaxation mechanism in a bulk sample, there generally exists a distribution of relaxation times resulting from the distribution of structural units. For a thermally activated mechanism the distribution of relaxation times is given by [233]

$$\tau = \ = \tau_o \exp(E_a/RT)$$

$$= \frac{\hbar}{kT} \exp(-\Delta S_a/R) \exp(E_a/RT)$$

(224)

where τ is the relaxation time, τ_0 is the pre-exponential factor, h is Planck's constant, k_B is Boltzmann's constant, R is the gas constant, T is the absolute temperature, ΔS_a is the activation entropy, and E_a is the activation energy. A distribution in relaxation times can be caused by either a distribution in the pre-exponential factor, which is related to the activation entropy, or by a distribution in the activation energies. An example of the slow decay observed in the LIG scattering signal is shown in the inset of Fig. 75 where the values of ln (η) vs time are plotted for the LiB4 sample. The nonlogarithmic dependence of the signal decay observed here is consistent with a distribution in the characteristic times of the thermally induced structural relaxation. Although it is not known whether the width of the distribution of the relaxation times in a specific glass is caused by the per-exponential term or by the activation energy, other studies of glass structural changes have been centered on the latter[233].

Effects of the network modifier ions on the FWM scattering efficiency of the LIG's

The lithium-borate glasses show a monotonic increase in scattering efficiency as Q/r^2 of the network modifier ion increases (Fig. 76). The significance of these results will be discussed in the first instance for the Mg, Ca, and Ba modifier ions since they are common Group II elements and expected to have similar chemical properties. While it is ultimately the different mass that distinguishes these elements, the appropriate parameter that has the most influence on the scattering

efficiencies is the bond strength. The $\sim$300% increase in scattering efficiency from the Ba to the Mg ions is associated with a 400% increase in Q/r^2 and 400% decrease in mass, but only a 12% decrease in the SCB_{M-O}. Since Ba, Ca, and Mg are from the same group it is not surprising that the same dependence of the efficiency on Q/r^2 and mass is observed.

When comparing results from glasses having modifier ions from different parts of the periodic table, the importance of the Q/r^2 and SCB_{M-O} parameters becomes apparent. For example, Ca and Zn modifier ions have the same charge but Zn is the heavier ion (Table XXV). If these tow ions were part of the same group of elements it would b expected that the Zn sample would show the lower scattering efficiency. In fact the opposite is observed (Fig.76). Compared to Ca, Zn has the better values of the important parameters Q/r^2 and SCB_{M-O} for grating information. The results show that for a given mass, large values of Q/r^2 and small values of SCB_{M-O} are the desired properties for the modifier ions.

In order to understand the m mechanism of grating formation, it is necessary to consider the effects different values of Q/r^2 and SCB_{M-O} have on the ions involved in the process. It has been pointed out before that the rare-earth dopant ions and the network modifier ions compete in attracting the nonbridging oxygen ions[220]. A measure of this attraction is the charge-to-radius-squared ratio, Q/r^2. In Fig. 76 the area bound by the vertical dashed lines represents typical values for Q/r^2 for rare-earth ions. The increase in scattering efficiency with increasing Q/r^2 of the modifier ions is interpreted in the following manner.

In samples having modifier ions with low values of Q/r^2, the Eu^{3+} ions are less effective at attracting the nonbridging oxygen ions. Since the permanent gratings are produced by rearrangements of the nonbridging oxygen ions low values of modifier ion Q/r^2 result in lower asymmetry between altered and unaltered regions at the Eu^{3+} ion sites. This in turn results in a less efficient modulation of the refractive index. As the values of Q/r^2 for the modifier ions increase to approach the values for the rare-earth ions, they become better at stabilizing structural changes involving different arrangements of nonbridging oxygen ions. This leads

to a greater modulation in the refractive index which is consistent with the observed dependence of the scattering efficiency.

It is well known that the bond st4rength between the atoms in simple oxides is a strong influence on heir tendency to form glass [234] and it has been shown here to be an important factor in grating formation. For the Group II elements Mg, Ca, and Ba an increase in grating scattering efficiency is observed when the SCB_{M-O} decreases (Fig. 78). Qualitatively this is understood as a stronger bonding between network modifier and oxygen ions results in a less efficient rare-earth-oxygen ion interaction and subsequent lower scattering efficiency. When comparing results between modifier ions from different parts of the periodic table the SCB_{M-O} does not appear to be a strong factor. For example, the samples with Pb and Ba ions exhibit similar scattering efficiencies but these ions have very different values of SCB_{M-O}.

In summary, when attempting to predict the properties of permanent LIG's produced in samples with different modifier ions, it is necessary to consider the positions of the ions relative to each other in the periodic table. For ions from the same part of the table and having similar chemical properties, the SCB_{M-O} and Q/r^2 parameters are equally good in predicting the expected response. However, for ions from different parts of the periodic table it appears that only the Q/r^2 parameter can be relied on to give some idea of the trend in the efficiency.

When examining the results shown in Fig. 78 of the scattering efficiency as a function of SCB_{M-O}, it is apparent that some comment is required for the glass with Al modifiers. It is well known that Al_2O_3 is a conditional glass former which, in many cases, becomes a part of the main structure of the glass instead of acting as a modifier [235,236]. This is in contrast to the role played by the rest of the modifier ions investigated here which almost always occupy interstitial positions with respect to the main structure of the glass formers. In behaving more like a former than a modifier, Al ions becoming more involved in the covalent bonding of the glass rather than in localized ionic bonding. Thus the values of Q/r^2 may be interpreted as describing the degree of covalence to the modifier-oxygen

interaction with large values of Q/r^2 for the modifier ion being associated with a m ore covalent interaction. This fact in itself may lie behind the observation of a very high scattering efficiency from this sample, however, the existence of additional oxygen ions should also be considered.

The glass samples discussed here are formed when nonglass forming oxides of the form MO (e.g., PbO, MgO) are added to glass forming oxides of the type F_xO_y (B_2O_3 for the borate glasses here). However, if the nonglass forming oxide is of the type M_mO_n (e.g., Al_2O_3) the number of oxygen ions is increased relative to the number of glass forming cations F [237]. Thus in lithium borate glasses studied here there are 50% more oxygen ions introduced when Al_2O_3 is present relative to one of the other modifier oxides. Unless the coordination number of the cation F is changed these additional oxygens cannot form linkages between neighboring F cations but must exist as single bonded oxygens, i.e., oxygens that are bonded to only one F cation. At the present time it is not clear if the very high scattering efficiency for the Al_2O_3 sample is the result of the increase in the number of nonbridging oxygen ions or the nature of Al_2O_3 as a conditional glass former.

Effects of the network former ions on the FWM scattering efficiency of the LIG's

The four glasses PbB, PbBGe, PbGe, and PbSi1 have the same network modifier composition but vary in the type and composition of network former (Table XXIV). This variation produces a change in the SCB_{F-O} between samples. In Fig. 79 the values of the grating scattering efficiency were plotted as a function of the SCB_{F-O} and show a decrease in efficiency as SCB_{F-O} increases in the order B-O>Si-O>Ge-O. This can be understood in a similar manner as the influence of the SCB_{M-O} on the efficiency. Qualitatively the ability of the Eu^{3+} ions to interact with the oxygen ions diminishes with the increasing strength of the interaction between network former and oxygen ions.

The two samples PbSi1 and PbSi2 contain the same elements but differ in the ratio o network former and modifier ions. In Fig. 80 the scattering efficiencies of
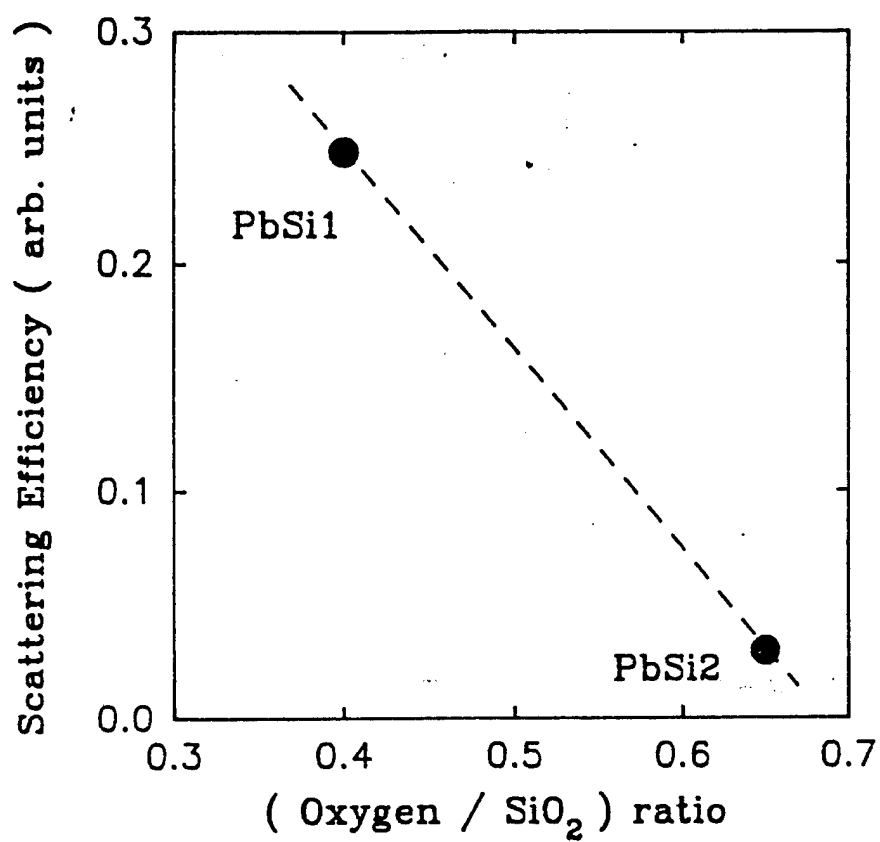
Figure 80. Scattering efficiency as a function of the ration of oxygen/SiO_2.

the permanent LIG's from these two samples are plotted vs the concentration ratio (oxygen/SiO$_2$) where the oxygen concentration is that contributed by the modifier ions. In PbSi2 t5he additional PbO increases the nonbridging oxygen content and might be expected to improve the scattering efficiency over PbSi1. However, the opposite dependence is observed and it appears that the role of PbO as an oxygen donor in increasing the efficiency is more than offset by the presence of additional heavy Pb modifier ions that decrease the efficiency.

Mechanism of erasure

It has been shown before that the permanent LIG's can be erased by heating the glass. This process involves the thermally activated relaxation of the structural modification created in the local environment of the Eu^{3+}ions. Additionally,the permanent signal can be erased optically by switching on only one of the write beams in resonance with the transition to the $^5D_2$ level of Eu^{3+}. In this case the optical excitation of the Eu^{3+} ions by the single beam creates a *uniform* structural modification in the local environment of the Eu^{3+} ions as before, i.e., the single beam removes the spatial modulation of the structure.

Of particular interest is the observation that a new, permanent LIG can be recreated at exactly the same point in the sample after optical erasure. Figure 81 shows a sequence of grating buildup and erasure curves in a Eu^{3+} silicate glass. In the upper part of this figure the erase beam intensity was 0.25 times the light intensity in the grating peak regions, while in the lower part it was 3.6 times. These results show that the efficiency of recreating a permanent LIG after optical erasure depends upon the actual intensity of the erasure beam.

Some insight into the processes taking place during the optical erasure and recreation can be obtained from an analysis of the time dependence of the signal. The contrast between grating peaks and valleys is provided by regions about Eu^{3+} ions that have undergone local structural change. During optical erasure, the time evolution of the concentration of these localized regions follows a simple rate equation [238]
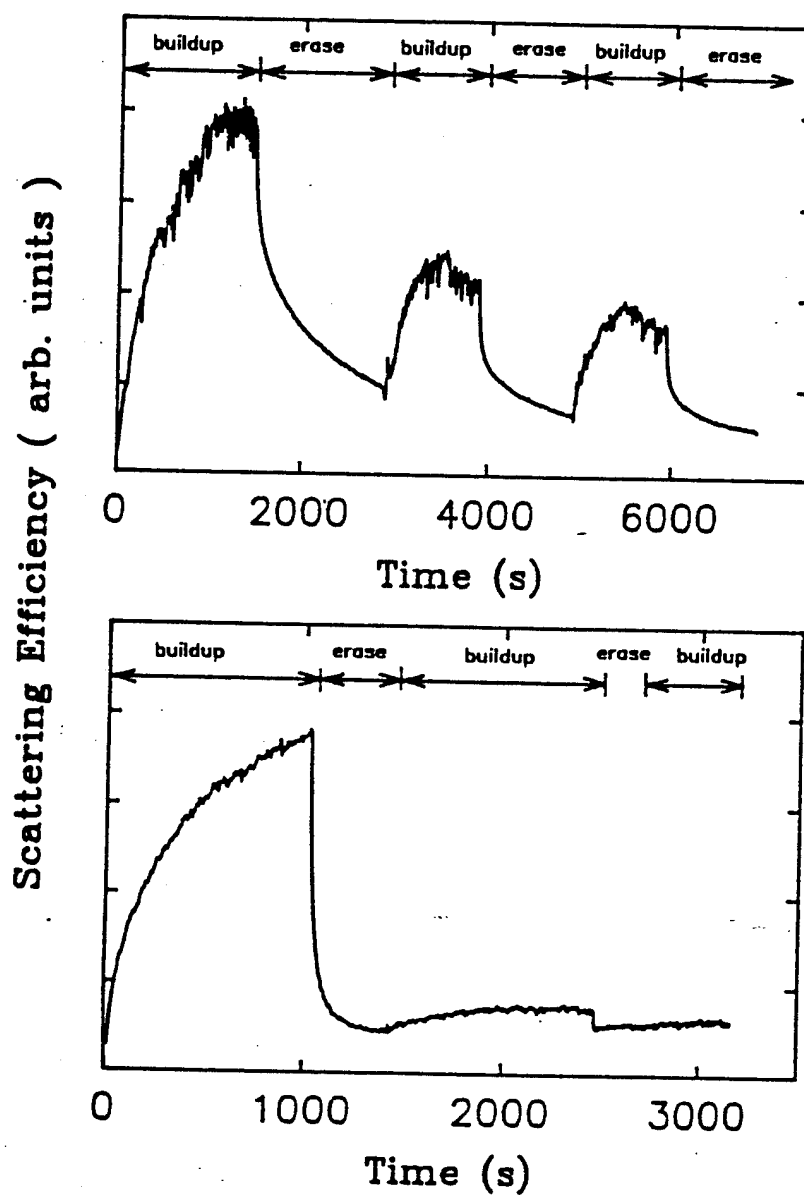
Figure 81. Time dependence of the Scattering efficiency for a series of grating creation and optical erasure experiments done in the same location. In the upper part the erasing beam was 0.25 times the intensity in the grating peak and the lower 3.6 times.

$$\frac{dn}{dt} = -n^x K \exp(-E/kT) \tag{225}$$

where E is the activation energy for the relaxation of the structural modification, K is a constant with units of s^{-1} and x is an integer that describes the order of the kinetics. The signal measured is the scattering efficiency, η, which is proportional to the square of the concentration of centers. Then

$$\frac{dn}{dt} \sim \frac{1}{n}\frac{d\eta}{dt} \tag{226}$$

and the expression describing the rate of change of the scattering efficiency is

$$\frac{d\eta}{dt} \sim -\eta^{(x+1)/2} \tag{227}$$

This equation describes the change in the signal as a function of time with the rate of change depending on the interaction between x groups of ions. With an initial condition of $\eta=\eta_0$ at $t=0$, the solution of Eq. (4) is

$$\left(\frac{\eta}{\eta_o}\right)^{(1-x)/2} = C\eta_o^{(x-1)/2}t + 1 \tag{228}$$

The experimental data of a single optical erasure curve, shown in Fig. 82 were analyzed and the term $(\eta/\eta_0)^{(1-x)/2}$ was plotted vs time for different integer values of x. The value of x giving the best straight line fit is interpreted as the order of tHe kinetics. The data points shown in Figs. 83 (a) and 83 (b) are optical erasure results analyzed using the model with a second and third order kinetics parameter, respectively. These results show a straight line was obtained for $x=3$. This suggests that the optical erasure involves a kinetic process between three neighboring structural units.

The interpretation of this is that there is an elastic interaction between these neighboring units that are trying to undergo simultaneous and perhaps competing structural changes. The third order kinetics arise as any individual unit is influenced by the changes taking place on either side of it in this one dimensional system defined by the grating wave vector. The center of each unit is a Eu^{3+}
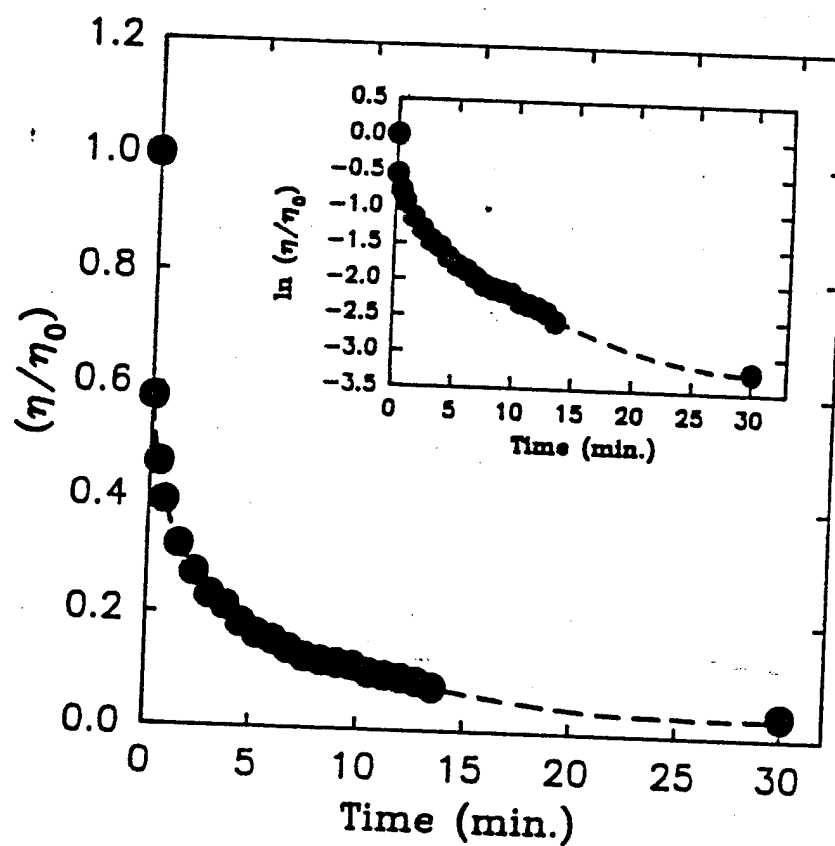
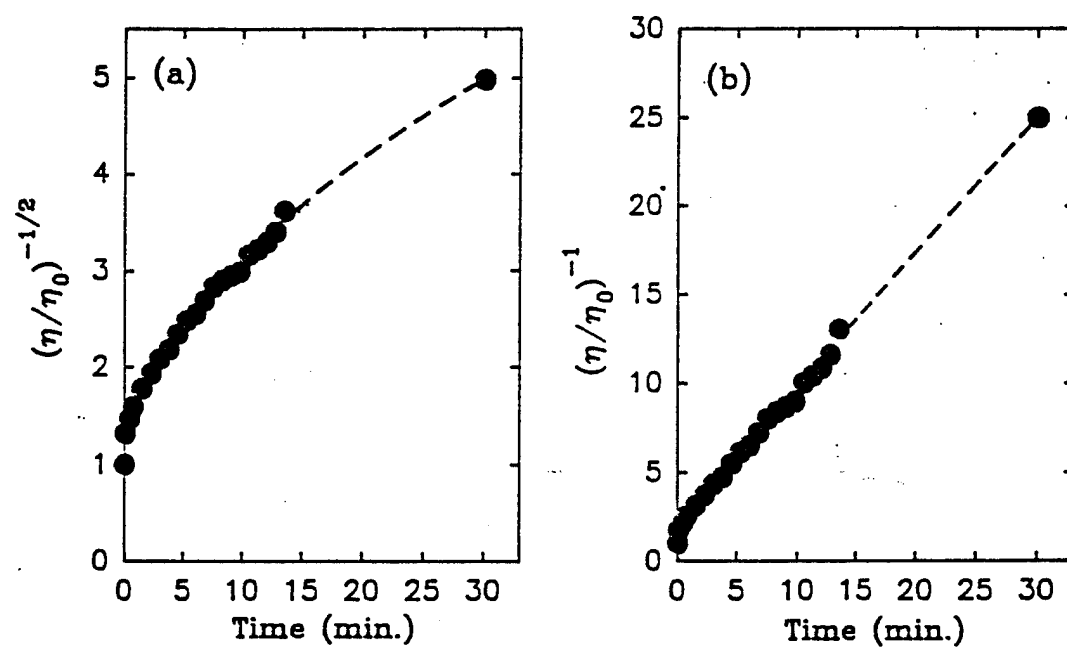Figure 82. The nonlogarithmic time dependence of optical erasure.

Figure 83. Scattering efficiency data and fit for different kinematic orders (a) $x = 2$ and (b) $x = 3$.

ion (or cluster) that acts as the catalyst for introducing thermal energy into the system. In both grating creation and optical erasure the equilibrium stabilization of the neighboring structural modifications can only be accomplished when the units are significantly far apart to eliminate the elastic interaction between them. In this picture only one of two optically active Eu^{3+} ions that are closer together than some critical distance R_0 will be at the center of a stabilized structural modification. This critical distance will be a function of the structure of the glass, the temperature and the optical intensity being used. This may also explain the saturation effects observed in some of the permanent LIG experiments. The scattering efficiency from a LIG in a metaphosphate glass containing 50 mol % of Eu^{3+} was considered to be saturated when compared to the intensity from a 10 mol % Eu^{3+} sample.[5] The theory predicted a 50-fold increase in scattering efficiency whereas only an 8-fold increase was observed. This saturation may be related to the onset of the regime where the elastic interaction between neighboring structural units extends over the distance between adjacent Eu^{3+} ions.

Discussion

The experimental results presented here show that the chemical composition of the glass host plays a major role in determining the scattering efficiencies of the LIG. By observing the response from different samples a set of empirical rules were developed to predict the relative scattering efficiency of a particular glass. For samples with modifier ions from the same part of the periodic table the charge-to-radius-squared ratio Q/r^2 and the strength of the chemical bond between modifier and oxygen ions SCB_{M-O} are parameters that can be used to predict the relative grating efficiency. For samples with modifier ions from different parts of the periodic table only the Q/r^2 parameter can be relied on to give some idea of the trend in efficiencies. The data show that large values of Q/r^2 and small values of SCB_{M-O} are desired for high scattering efficiencies.

The efficiency of forming a permanent LIG also depends on the glass former ions of the host. These affect the LIG's both through determining the number

of nonbridging oxygen ions present and through restricting the polarizability determined by the strength of the former ion-oxygen chemical bond. This was also observed recently in thermal lensing experiments on the same glasses used here [135]. A pulsed laser operating at 457 nm with a duration of 7 ns was used to thermally induce changes in the refractive index. Since the wavelength used did not correspond to any Eu^{3+} absorption it was concluded that the nonbridging oxygen ions were responsible for the changes in refractive index. The results obtained on glasses with different types of former ions were consistent with those obtained in the experiments described here.

The dependencies of the permanent LIG's on host chemical composition are consistent with the local structural modification model proposed previously[214–220]. The nature of the two possible local structures appears to be due to the relocation of the nonbridging oxygen ions near to the rare-earth ions. Multiple local configurations of coordination spheres of rare-earth ions in glasses are well known from other types of investigations. For example, computer simulations of the molecular dynamics of rare-earth doped glass showed the RE oxygen coordination number increasing with the mass of the modifier ion [239,240].

On an experimental level it has been shown that the certain rare-earth doped silicate crystals undergo a structural phase transition at elevated temperatures that may be similar to those modification response for grating formation[241]. In these crystals the time scales for the transitions are the order of several minutes which are similar to the time scales measured here for the LIG buildup. Such a long buildup would indicate the mechanism for grating creation is not photoionization as has been recently suggested[242]. During the grating buildup large numbers of high frequency local vibrational modes are produced on a local scale by the efficient nonradiative decay of the $^5D_2$ level. Under such conditions it is reasonable to conclude that elevated temperatures are produced in the local environment of the Eu^{3+} ion and structural changes occur with corresponding changes in Eu^{3+}-oxygen coordination number and bond lengths.

Having established that structural changes occur in the creation of a permanent LIG, it remains to question the origin of the different values of the refractive index. It was suggested previously[220] that the local change of crystal field of the rare-earth ion changes the radial integral of the $4f{\to}5d$ transition which is the dominant contribution to its polarizability. This predicts a reasonable value for the observed Δn.

However, a second source of variation in the local polarization is density changes due to different positions of the ions. In LIG experiments there are rearrangements of the nonbridging oxygen ions involved in the structural modifications. A change in their position of 0.1 A can produce a local polarization change leading to a refractive index change of $\Delta n=10^{-5}$, which is the order of magnitude of the observed LIG modulation depth. Thus, the index change may be associated with a polarization change between the two structures that has its origin either in the rare-earth ion or in the nonbridging oxygen ions.

During grating formation the spatial regions undergoing structural modifications experience a decrease in density. This is inferred since the high temperature phase has an increase in volume that results from an increase in the Eu^{3+}-oxygen bond lengths. Consequently, to maintain uniformity there is an increase in the density in the dark regions.

Assuming a simple one dimensional picture, it is possible to write a density

$$\rho = N/x \tag{229}$$

where x is the coordinate along the grating direction and N is the concentration in this direction. Then the change in density between light and dark regions varies as

$$\Delta\rho \sim \frac{N}{x^2}\Delta x = \rho_o \frac{\Delta x}{\Lambda_g} \tag{230}$$

where Λ_g is the grating spacing , ρ_0 the equilibrium density and Δx the coordinate change cause by the structural modification. Since the scattering efficiency is determined by the density fluctuations, the dependence of $\Delta\rho$ on Λ_g predicts

a general trend of increasing scattering efficiency with decreasing grating spacing. However, at some point the spacing between neighboring fringes will become sufficiently small such that the increased density in the dark regions would exceed some critical value determined by the bond strengths and the scattering efficiency should saturate and possibly start to decrease.

After a steady state permanent LIG has been produced in the sample,the periodic density function can be expressed as

$$\rho(x) = \rho_o - \Delta\rho_{P1}\sin(k_g x) \tag{231}$$

where ρ_0 is the original density, k_g is the grating wave vector, and $\Delta\rho_{P1}$ is the change in density caused by the write beams with total power $P1$. In this case the scattering efficiency would be proportional to the square of $\Delta\rho_{P1}$. Optical erasure is done by blocking one of the write beams which results in a constant density function given by

$$\rho(x) = \rho_o - \Delta\rho_{P2} \tag{232}$$

Since the intensity of a single beam is 1/4 of the peak intensity during grating buildup $\Delta\rho_{P2} < \Delta\rho_{P1}$. Now during rewriting of the grating the density in the light regions again returns to i its former value of $\rho_0 - \Delta\rho_{P1}$ but the dark regions remain at the erasure density of $\rho_0 - \Delta\rho_{P2}$. Figure 84 shows plots of these functions. As can be seen, after optical erasure and rewriting the density fluctuation is smaller than before and the grating does not full recover its previous scattering efficiency.

It is known from previous work that the choice of the rare-earth dopant ion in the glass composition has an important effect on the efficiency of any permanent LIG's produced. Both Eu^{3+} and Pr^{3+} have been shown to produce permanent gratings while Nd^{3+} and Er^{3+} do not. The appropriate feature of the former two ions is that they have electronic excited levels that efficiently relax nonradiatively through the emission of high energy local vibrational modes. In Nd^{3+} the lack of a grating was attributed to cascade relaxation between closely spaced energy levels that involved only low energy vibrational modes. When pumped to high energy
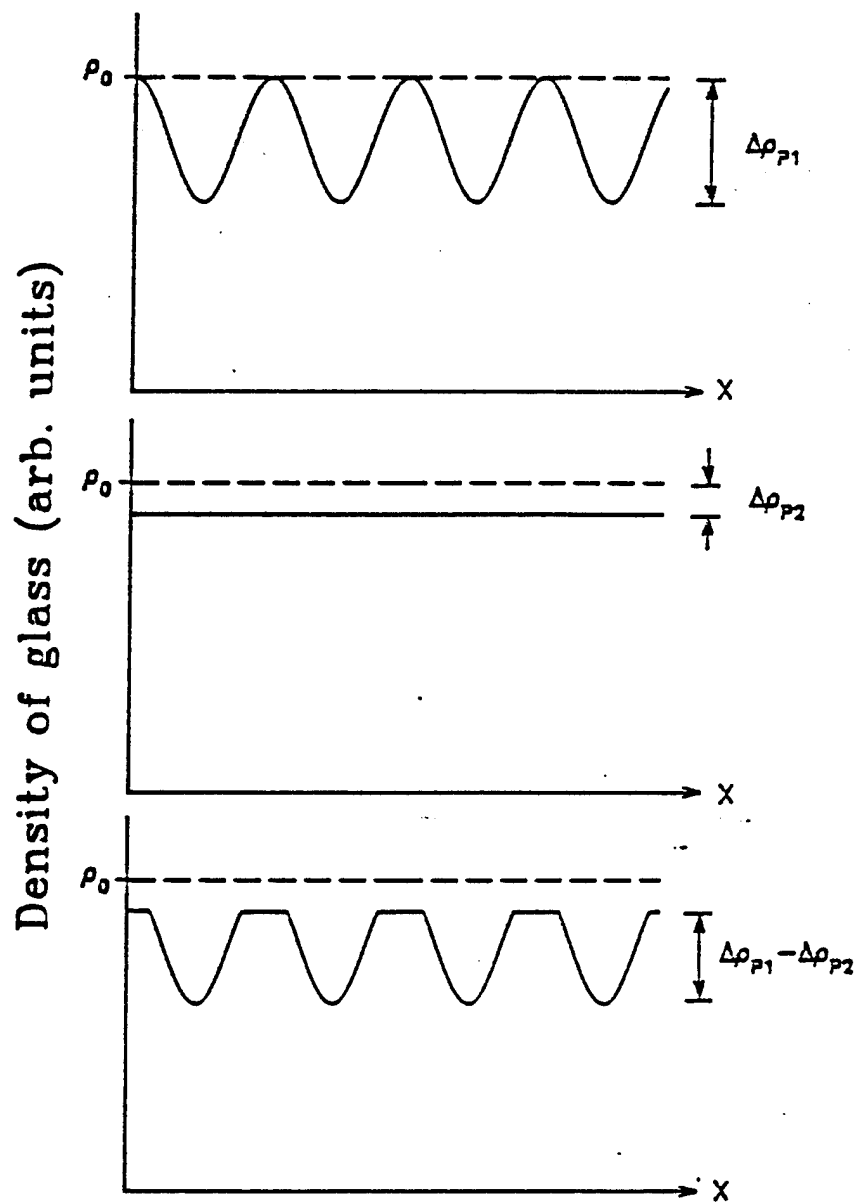
Figure 84. Schematic figure showing the density during LIG creation and erasure. Top: the sinusoidal decrease in initial creation, middle: uniform decrease after eraseure, bottom: smaller grating recovery.

excited levels, Er^{3+} ions under go predominantly radiative decay and this was suggested to be the reason for the absence of a permanent grating [216]. However, recent experiments [242] have not produced permanent gratings when Er^{3+}ions were excited to lower energy levels where efficient nonradiative relaxation does occur. Clearly a different explanation is required and the lack of a permanent grating in Er^{3+} samples may be associated with several different effects. One reason may be the difference in ionic size between Er^{3+} and Pr^{3+}, Eu^{3+} ions and the difference this makes in their interaction with the surrounding nonbridging oxygen ions. Also, based on observations from rare-earth silicate crystals [241] it is more difficult for Er^{3+} doped samples to undergo phase transitions at elevated temperatures that produce the difference between modified and unmodified regions that are observed in permanent LIG's. This was associated with the differences in Si-O bond interactions in the various rare-earth samples [243].

SECTION IX

BIBLIOGRAPHY

1. A. L. Schawlow and C. H. Townes, Phys. Rev. **112**, 1940 (1958).

2. T. H. Maiman, Nature **187**, 493 (1960).

3. P. P. Sorokin and M. J. Stevenson, IBM J. Res. Dev. **5**, 56 (1961).

4. L. F. Johnson and K. Nassau, Proc. IRE **49**, 1704 (1961).

5. A. A. Kaminskii, **Laser Crystals 2ed** (Berlin, Springer-Verlag, 1990).

6. G. H. Dieke, **Spectra and Energy Levels of Rare Earth Ions in Crystals** (Interscience, New York, 1968).

7. B. G. Wybourne, **Spectroscopic Properties of Rare Earths** (Interscience, New York, 1965).

8. L.A. Riseberg and M.J. Weber, in **Progress in Optics Vol. 14**, ed. E. Wolf (North Holland, New York, 1976) p89.

9. B.R. Judd, Phys. Rev. **127**, 750 (1962).

10. G.S. Ofelt, J. Chem. Phys. **37**, 511 (1962).

11. H. W. Moos, J. Lumin. **1**, 106 (1970).

12. M. J. Weber, Phys. Rev. **157**, 262 (1967).

13. T. Miyakawa and D. L. Dexter, Phys. Rev. B **1**, 2961 (1970).

14. J. C. Wright, in **Topics in Applied Physics Vol. 15**, ed. F. K. Fong (Springer-Verlag, Berlin, 1976) p239.

15. F. Auzel, Proc. IEEE **61**, 758 (1973).

16. R. Reisfeld and C.K. Jorgensen, **Lasers and Excited States of Rare Earths** (Berlin, Springer-Verlag, 1977).

17. B. Di Bartolo, **Energy Transfer Processes in Condensed Matter** (Plenum, New York, 1984).

18. B. R. Judd, **Operator Techniques in Atomic Spectroscopy** (McGraw-Hill, New York, 1963).

19. R. D. Peacock, in **Structure and Bonding Vol.22**, ed. J. D. Dunitz, P. Hemmerich, R. H. Holm, J. A. Ibers, C. K. Jorgensen, J. B. Neilands, D. Reinen, and R. J. P. Williams (Springer-Verlag, New York, 1975) p83.

20. W.T. Carnall, H. Crosswhite, and H.M. Crosswhite, Energy Level Structure and Transition Probabilities of the Trivalent Lanthanides in LaF_3 , The Johns Hopkins University Reasearch Report, unpublished.

21. A. Kiel, "Multiphonon Spontaneous Emission in Paramagnetic Crystals", in **Quantum Electronics Vol. 1**, ed. P. Grivet and N. Bloembergen (Columbia University Press, New York, 1964) p765.

22. L. A. Riseberg and H. W. Moos, Phys. Rev. **174**, 429 (1968).

23. T. Kushida, S. Kinoshita, T. Ohtsuki, and T. Yamada, Solid State Comm. **44**, 282 (1982).

24. T.T. Basiev, A. Yu. Dergachev, Yu. V. Orlovskii, Rev. Roum. Phys. **34**, 789 (1989).

25. J. Cruz, G. Giuliani, and H. M. van Driel, Opt. Lett. **15**, 282 (1990).

26. K. Palambo, S. Matthews, S. Sheldrake, and D. Capps, in **Advanced Solid State Lasers and Compact Blue-Green Lasers Technical Digest, 1993** (Optical Society of America, Washington, D.C., 1993), **Vol. 2**, p61.

27. C. Bibeau, S. A. Payne, and H. T. Powell, in **Advanced Solid State Lasers and Compact Blue-Green Lasers Technical Digest, 1993** (Optical Society of America, Washington, D.C., 1993), **Vol. 2**, p64.

28. T. Forster, Ann. Phys. (Liepzig) **2**, 55 (1948).

29. D. L. Dexter, J. Chem. Phys. **21**, 836 (1953).

30. M. Inokuti and F. Hirayama, J. Chem. Phys. **43**, 1978 (1965).

31. C. M. Lawson, R. C. Powell, and W. K. Zwicker, Phys. Rev. B **26**, 4836 (1982).

32. J. K. Tyminski, R. C. Powell, and W. K. Zwicker, Phys. Rev. B **29**, 6074 (1984).

33. R. C. Powell, S. A. Payne, L. L. Chase, and G. D. Wilke, Phys. Rev. B **41**, 8593 (1990).

34. R. M. Macfarlane, F. Tong, A. J. Silversmith, and W. Length, Appl. Phys. Lett **52**, 1300 (1988).

35. W. Length and R. M. Macfarlane, J. Lumin. **45**, 346 (1990).

36. W. J. C. Grant, Phys. Rev. B **4**, 648 (1971).

37. A. I. Burshstein, Sov. JETP Phys. **35**, 882 (1972).

38. S. Chandrasekhar, Rev. Mod. Phys. **15**, 1 (1943).

39. H. B. Rosenstock, Phys. Rev. **187**, 1166 (1969).

40. V. M. Kenkre, Phys. Rev. B **18**, 4064 (1978).

41. M. Yokota and O. Tanimoto, J. Phys. Soc. Japan **22**, 779 (1967).

42. H. C. Chow and R. C. Powell, Phys. Rev. B **21**, 3785 (1980).

43. A. E. Siegman, **Lasers** (University Science Books, Mill Valley, Ca., 1986).

44. A. Yariv, **Quantum Electronics 3ed** (John Wiley, New York, 1989).

45. M. G. Jani, R. R. Reeves, R. C. Powell, G. J Quarles, and L. Esterowitz, J. Opt. Soc. Am. B **8**, 741 (1991).

46. L. F. Johnson, J. E. Guesic, and L. G Van Uitert, Appl. Phys. Letters **7**, 127 (1965).

47. L. F. Johnson, J. E. Guesic, and L. G. Van Uitert, Appl. Phys. Letters **8**, 200 (1966).

48. G. J. Quarles, A. Rosenbaum, C. L. Marquardt, and L. Esterowitz, Appl. Phys. Letters **55**, 1062 (1989).

49. T. Y Fan, G, Huber, R. L. Byer, and P. Mitzerlich, Optics Letters **12**, 678 (1987).

50. J. C. Tyminski, D. M. Franich, and M. Kokta, J. Appl. Phys. **65**, (1989).

51. B. M. Antipenko, V. A. Buchenkov, A. S. Glebov,T. I. Kiseleva, A. A. Nikitichev, and V. A. Pismennyi, Opt. Spectrosc. (USSR) **64**, 772 (1988).

52. T. Y. Fan, G. Huber, R. L. Byer, and P. Mitzerlich, IEEE J. Quantum Electron. **JQE-24**, 924 (1988).

53. G. Huber and P. Mitzerlich, J. Luminescence **40-41**, 509 (1988).

54. K. Y. Kim, Y. S. Choi, R. V. Hess, C. H. Blair, P. Brockman, N. P. Barnes, G. W. Henderson, and M. Kokta, in **Digest of Conference on Advanced Solid State Lasers** (Optical Society of America , Washington, D.C. , 1990), paper WB3.

55. T. Becker, R. Clausen, G. Huber, E. W. Duczyski, and P. Mitzerlich, in **Proceedings of Tunable Solid State Lasers Conference 5** (Optical Society of America, Washington, D.C., 1989), p. 150.

56. G. Armagan, A. M. Buoncristiani, and B. Di Bartolo, J. Luminescence **48-49**, 171 (1991).

57. G. Armagan, A. M. Buoncristiani, and B. Di Bartolo, Opt. Mater. **1**, 11 (1991)

58. T. Becker and G. Huber, **Proc. of the Conf. on Lasers and Electro-optics** (Optical Society of America, Washington, D.C., 1991), paper CTuO3.

59. V. A. French and R. C. Powell, Optics Letters **16**, 666 (1991).

60. V. A. French, R. R. Petrin, R. C. Powell, and M. Kokta, Phys. Rev. B **46**, 8018 (1992).

61. S. A. Payne, L. L. Chase, L. K. Smith, W. L. Kway, and W. F. Krupke, to be published.

62. J. B. Gruber, M. E. Hills, R. M. Macfarlane, C. A. Morrison, G. A. Turner, G. J. Quarles, G. J. Kintz, and L. Esterowitz, Phys. Rev. B. **40**, 9464 (1989).

63. J. B. Gruber, M. E. Hills, M. D. Seltzer, S. B. Stevens, C. A. Morrison, G. A. Turner, and M. R. Kokta, J. Appl. Phys. **69**, 8183 (1991).

64. J. A. Caird, L. G. DeShazer, and J. Nella, IEEE J. Quantum Electron. **QE-11**, 874 (1975).

65. M. Kh. Ashurov, Yu. K. Voron'ko, E. V Zharikov, A. A. Kaminskii, V. V. Osiko, A. A. Sobol', M. I. Timoshechkin, V. A. Fedorov, and A. A. Shabaltai, Inorg. Mater. **15**, 979 (1979).

66. J. A. Caird, A. J. Ramponi, and P. R. Staver, J. Opt. Soc. Am. B **8**, 1391 (1991).

67. G. Kintz, I. D. Abella, and L. Esterowitz, **Proc. of the International Conference on Lasers, LASERS '87**, 398 (1987).

68. A. A. Nikitichev, Sov. J. Quantum Electron. **18**, 918 (1988).

69. S. R. Bowman, M. J. Winnings, R. C. Y. Auyeung, J. E. Tucker, S. K. Searles, and B. J. Feldman, IEEE J. Quantum Electron. **JQE-27**, 2142 (1991).

70. T.Y. Fan and R.L. Byer, IEEE J. Quantum Electron. **QE-24**, 895 (1988).

71. F. Hanson and D. Haddock, Apll. Optics **27**, 80 (1988).

72. D.P. Caffey, R.A. Utano, and T.H. Allik, Appl. Phys. Lett. **56**, 808 (1990).

73. R.A. Fields, M. Birnbaum, and C.L. Fincher, Appl. Phys. Lett. **51**, 1885 (1987).

74. T.H. Allik, M.J. Ferry, R.J. Reeves, R.C. Powell, W.W. Hovis, D.P. Caffey, R.A. Utano, L. Merkle, and C.F. Campana, J. Opt. Soc. Am. B. **7**, 1190 (1990).

75. M.J. Ferry, M. L.Kliewer, R.J. Reeves, R.C. Powell, and T.H. Allik, J. Appl. Phys. **68**, 6372 (1990).

76. T.Y. Fan and M.R. Kokta, J. Quantum Electron. **QE-25**, 1845 (1989).

77. M.L. Kliewer and R.C. Powell, IEEE J. Quantum Electron. **QE-27**, 850 (1989).

78. R. R. Petrin, M. L. Kliewer, J. T. Beasley, R. C. Powell, I. D. Aggarwal, and R. C. Ginther, IEEE J. Quantum Electron. **QE-27**, 1031 (1991).

79. B.R. Reddy and P. Venkateswarlu, J. Chem. Phys. **79**, 1519 (1983).

80. T.Y. Fan and R.L. Byer, J. Opt. Soc. Am. B **11**, 1519 (1986).

81. G.E. Venikuoas, G.J. Quarles, J.P. King, and R.C. Powell, Phys. Rev. B **30**, 2401 (1984).

82. J. A. Mares, B. Jacquier, C. Pedrini, and G. Boulon, Mat. Phys. Chem. **21**, 237 (1989).

83. M. Malinowski, B. Jacquier, M Bouazoui, M. F. Joubert, and C. Linares, Phys. Rev. B **41**, 31 (1990).

84. J. H. Schloss, L. L. Chase, and L. K. Smith, J. Lumin. **48-49**, 857 (1991).

85. D. Hua, Z. Song, S. Wang, and Z. Rong, J. Chem. Phys. **89**, 5398 (1988).

86. J. B. Gruber, M. E. hills, T. H. Allik, C. K. Jayasankar, J. R. Quagliano, and F. S. Richardson, Phys. Rev. B **41**, 7999 (1990).

87. J. B. Gruber, M. E. hills, C. A. Morrison, G. A. Turner, and M. R. Kokta, Phys. Rev. B **37**, 8564 (1988).

88. W.F. Krupke, J. Quantum Electron. **QE-7**, 153 (1971).

89. A.A. Kaminskii and L. Lui, Phys. Status Solidi A **26**, K21 (1974).

90. W.F. Krupke, M.D. Shinn, J.E. Marion, J.A. Caird, and S.E. Stockman, J. Opt. Soc. Am. B **3**, 102 (1986).

91. L.L. Chase (private communication).

92. J.D. Axe, J. Chem. Phys. **39**, 1154 (1963).

93. W.F. Krupke and J.B. Gruber, Phys. Rev. **139**, A2008 (1968).

94. Z. Song, D. Hua, S. Wang, and Y. Gui, J. Chem. Phys. **89**, 5404 (1988).

95. S.A. Pollack and M. Robinson, Electron. Lett. **24**, 320 (1988).

96. F. Auzel, D. Meichenin, and H. Poignant, Electron. Lett. **24**, 909 (1988).

97. M.C. Brierly and P.W. France, Electron. Lett. **24**, 815 (1987).

98. R.R. Petrin, R.J. Reeves, M.L. Kliewer, R.C. Powell, I.D. Aggarwal and R.C. Ginther, in **OSA Proceedings Vol. 6: Advanced Solid-State Lasers**, eds H . P. Jensssen and G. Dube, (Optical Society of America, Washington, D. C., 1990) p236.

99. J. Lucas, M. Chanthanasinh, and M. Poulain, J. Noncrys. Solids **27**, 273 (1978).

100. L.Wetenkamp, G. F. West, and H. Tobben, J. Non-Cryst. Sol. **140**, 35 (1992).

101. R. Reisfeld, M. Eyal, and C. K. Jorgensen, J. Less. Common Metals **126**, 187 (1986).

102. A. A. Tesar, J. Quant. Spectrosc. Radiat. Transfer **46**, 425 (1991).

103. R. Cases and M. A. Chamarro, J. Sol. St. Chem. **90**, 313 (1991).

104. M. J. Weber, J. Non-Cryst. Sol. **123**, 208 (1990).

105. S.E. Stokowski, R.A. Saroyan, and M.J. Weber, Pub. M-095, U.S. Dept. Of Energy, Lawrence Livermore National Lab. 1978.

106. T.M. Pollak, W.F. Wing, R.J. Grasso, E.P. Chicklis, and H.P. Jenssen, IEEE J. Quantum Electron. **QE-18**,159 (1982).

107. D. Findlay and R.A.Clay, Phys. Lett. **20**, 277 (1966).

108. A.W. Tucker, M. Birnbaum, C.L. Fincher, and J.W. Erler, J. Appl. Phys. **48**, 4907 (1977).

109. R. Beach, S. Weinzapfel, R. Staver, R. Solarz, M. Shinn, and W. Krupke, Opt. Lett. **14**, 856 (1989).

110. J.A. Caird, S.A. Payne, P.R. Staver, A.J.Ramponi, L.L.Chase, and W.F.Krupke, IEEE J. Quantum Electron. **QE-24**, 1077 (1988).

111. S.A. Payne, L.L. Chase, H.W. Newkirk, L.K. Smith, and W.F. Krupke, IEEE J. Quantum Electron. **QE-24**, 2243 (1988).

112. A. A. S. da Gama, G. F. de Sa, P. Porcher, and P. Caro, J. Chem. Phys. **75**, 2583 (1981).

113. D. C. Yeh, W. A. Sibley, and M. Suscavage, J. Appl. Phys. **63**, 266 (1987).

114. A.D. McAulay, *"Optical Computer Architectures"*, John Wiley & Sons, New York, 1991.

115. K.Hwang and F.A.Briggs, *"Computer Architecture and Parallel Processing"*, McGraw-Hill Book Company, New York, 1984.

116. M.S. Petrovic, A. Suchocki, R.C. Powell, G.C. Valley and G. Cantwell, *Phys. Rev. B*, **43**, 2228 (1991).

117. F. Zernike and J.E. Midwinter, *"Applied Nonlinear Optics"*, John Wiley & Sons, New York, 1973.

118. J.D. Jackson, *"Classical Electrodynamics"*, John Wiley & Sons, New York, 1975.

119. M. Born and E. Wolf, *"Principles of Optics"*, Pergamon Press, Oxford, 1980.

120. D. Marcuse, *"Light Transmission Optics"*, Van Nostrand Reinhold, New York, 1972.

121. P. Meystre, M. Sargent III, *"Elements of Quantum Optics"*, Springer-Verlag, New York, 1991.

122. Y.R. Shen, *"The Principles of Nonlinear Optics"*, John Wiley & Sons, New York, 1984.

123. C. Kittel, *"Introduction to Solid State Physics"*, John Wiley & Sons, New York, 1986.

124. H.J. Eichler, P. Gunter and D.W. Pohl, *"Laser-Induced Dynamic Gratings"*, Springer-Verlag, New York, 1986.

125. H. Kogelnik, *Bell Syst. Tech. J.*, **48** 2909.(1968).

126. P.N. Butcher and D. Cotter, *"The Elements of Nonlinear Optics"*, Cambridge University Press, New York, 1990.

127. H.S. Brandi and C.B. de Araujo, *J. Phys. C: Solid State Phys.*, **16**, 5929, (1983).

128. H.D. Jones and H.R. Reiss, *Phys. Rev. B*, **16**, 2466 (1977).

129. M. Sheik-Bahae, D.C. Hutchings, D.J. Hagan and E.W. Van Stryland, "Dispersion of Bound Electronic Refraction in Solids", *IEEE J. Quantum Electron*, **27**, 1296 (1991).

130. R. Shankar, *"Principles of Quantum Mechanics"*, Plenum Press, New York, 1988.

131. D.M. Valkov, *Z. Phys.*, **94**, 250 (1935).

132. R.K. Jain and M.B. Klein, in *"Optical Phase Conjugation"*, Academic Press, New York, 1983.

133. P. Gunter, J.P. Huignard, in *"Photorefractive materials and their applications; vol I"*, P. Gunter and J.P. Huignard, Eds., Springer-Verlag, Heidelberg, 1988.

134. R.C. Powell, S.A. Payne, L.L. Chase and G.D. Wilke, *Phys. Rev. B.*, **41**, 8593 (1990).

135. B. Taheri, A. Munoz F., W.D. St John, J.P. Wicksted and R.C. Powell, *J. Appl. Phys.*, **71**, 3693 (1992).

136. J.C. Phillips, *"Bonds and Bands in Semiconductors"*, Academic Press, New York, 1973.

137. J.K. Furdyna, *J. Appl. Phys.*, **64**, R29 (1988). See for example, *Semiconductors and Semimetals*, R.K. Willardson and A.C. Beer, Treatise Editors; J.K. Furdyna and J. Kossut, Volume Editors, Academic, Boston, 1988, vol. **25**.

138. D. Weaire, B.S. Wherrett, D.A.B. Miller, and S.D. Smith, *Opt. Lett.*, **4**, 331 (1974).

139. E.W. Van Stryland, H. Vanherzeele, M.A. Woodall, M.J. Soileau, A.L. Smirl, S. Guha and T.F. Boggess, *Optical Engineering*, **24**, 613 (1985).

140. W. Zawadzki, in *Handbook on Semiconductors, vol 1: Band Theory and Transport Properties*, T.S. Moss and W. Paul, Editors, (North Holland, Amsterdam, 1980).

141. K.W. Boer, *"Survey of Semiconductor Physics"*, Van Nostrand Reinhold, New York, 1990.

142. B. Taheri, A. Munoz F., R.C. Powell, J.J. Song, and J.K. Furdyna, *SPIE Proceedings*, **2229** (1994).

143. H.J. Eichler, F. Massmann, *J. Appl. Phys.*, **53**, 3237 (1982).

144. K. Jarasiunas and J. Gerritsen, *Appl. Phys. Lett.*, **33**, 190 (1978).

145. G. Le Saux and A. Brun, *IEEE J. Quantum Electron.*, **QE-23**, 1680 (1987).

146. D. C. Jones and L. Solymar, *Opt. Comm.*, **85**, 372 (1991).

147. J. M. C. Jonathan, G. Roosen, and Ph. Roussignal, *Opt. Lett.*, **13**, 224 (1988).

148. G. Le Saux, G. Roosen, and A. Brun, *Opt. Comm.*, **56**, 374 (1986).

149. J. P. Hermann, J. P. Herriau, and J. P. Huignard, *App. Opt.*, **20**, 2173 (1981).

150. J.-L. Ferrier, J. Gazengel, X. N. Phu, and G. Rivoire, *Opt. Comm.*, **58**, 343 (1986).

151. G. Le Saux, J. C. Launay, and A. Brun, *Opt. Comm.*, **57**, 166 (1986).

152. A. Smirl, K. Bohnert, G. C. Valley, R. A. Mullen, and T. Boggess, *J. Opt. Soc. Am.*, **6**, 606 (1989).

153. L. Lam, T. Y. Chang, J. Feinberg, and R. Hellwarth, *Opt. Lett.*, **6**, 475 (1981).

154. I. Biaggio, M. Zqonik, and P. Gunter, *Opt. Comm.*, **77**, 312 (1990).

155. C.-T. Chen, D. Kin, and D. von der Linde, *IEEE J. Quantum Electron.*, **QE-16**, 126 (1980).

156. R. J. Reeves, H. Liu, and R. C. Powell, to be published *Phy. Rev. B.*

157. I. Foldvari, B. Taheri, R. J. Reeves, and R. C. Powell, *Opt. Comm.*, **102**, 245 (1993).

158. J.P. Huignard and F.Micheron; *Appl. Phys. Lett.*, **29**, 591 (1976).

159. G.C. Valley, M.B. Klein, R.A. Mullen, D. Rytz and B. Wechsler; *Ann. Rev. Mater. Sci.*, **18**, 165 (1988).

160. L. Arizmendi, J.M. Cabrera and F. Agullo-Lopez; *internat. J. Optoelectr.*, **7**, 149 (1992).

161. S.L. Hou, R.B. Lauer and R.E. Aldrich; *J. Appl. Phys.*, **44**, 2652 (1973).

162. B.C. Grabmayer and R. Oberschmidt; *Phys. Stat. Sol. (a)*, **96**, 199 (1986).

163. R.Oberschmidt; *Phys. Stat. Sol. (a)*, **89**, 263 (1985).

164. W. Rechwald, K. Frick, G.K. Lang and E. Meier; *J. Appl. Phys.*, **47**, 1292 (1976).

165. M.T. Harris, J.J. Larkin and J.J. Martin; *Appl. Phys. Lett.*, **60**, 2162 (1992).

166. P.Gunter; *Phys. Reports*, **93**, 93 (1982).

167. I. Foldvari, L.E. Halliburton, G.J. Edwards and L.Otsi; *Sol. State. Commun.*, **77**, 181 (1991).

168. J.J. Martin, I. Foldvari and C.A. Hunt; *J. Appl. Phys.*, **70**, 7554 (1991).

169. J.M.C. Jonathan, G.Roosen and Ph. Roussignal; *Opt. Lett.*, **13**, 224 (1988).

170. G. Le Saux, G. Roosen and A.Brun; *Opt. Commun.*, **56**, 374 (1986).

171. A.L. Khromov, M.P. Petrov and A.A. Kamshilin; *Sov. Phys. Sol. State*, **36**, 278 (1990).

172. G. Pauliat and G. Roosen; *J. Opt. Soc. Amer. B*, **7**, 2259 (1990).

173. G. Le Saux and A. Brun; *IEEE J. Quant. Electr.*, **23**, 1680 (1987).

174. D.C. Jones and L. Solymar; *Opt. Commun.*, **85**, 372 (1991).

175. D. von der Linde, A.M. Glass and K.F. Rodgers; *Appl. Phys. Lett.*, **25**, 155 (1974).

176. D. von der Linde, A.M. Glass and K.F. Rodgers; *Appl. Phys. Lett.*, **26**, 22 (1975).

177. T.F. Bogges, J.O. White and G.C. Valley; *J. Opt. Soc. Amer. B*, **7**, (1990).

178. M.Sylla, D. Rouede, R. Chevallier, N.P. Xuan and G. Rivoire; "*Tech. Dig. Topical Meeting on Photorefractive materials, Effects, and Devices II.*" (Opt. Soc. Amer., Washington D.C., 1990) p. 193.

179. I. Foldvari, J.J. Martin, C.A. Hunt, R.C. Powell and R.J. Reeves; *J. Appl. Phys.*, **74**, 783(1993).

180. I. Foldvari, A. Peter, R. Voszka and L.A. Kappers, *J. Crystal Growth*, **100**, 75 (1990).

181. B. Frit and M. Jaymes, *Rev. Chim. Miner.*, **3**, 453 (1971).

182. L.A. Demina, B.A. Dolgikh, B.A. Popovkin and A.V. Novoselova, *Dokl. Akad. Nauk. SSSR Ser. Khim.*, **244**, 94 (1979).

183. V.P. Avramenko, A.Yu. Kudzin, S.P. Reprentcheva, L.Ya. Sadovskaya and G.H. Sokolyanskii, *Ferroelectr.*, **82**, 173 (1988).

184. V.V. Kucha, A.V. Khomich, V.B. Kravchenko and P.I. Perov, *Izv. Akad. Nauk. SSSR Ser. Neorg. Mater.*, **20**, 414 (1984).

185. V.P. Avramenko, L.Ya. Sadovskaya, G.Kh. Sokolyanskii and O.V. Aga-fonov, *Bull. Acad. Sci. SSR. Ser. Phys.*, **54**, 184 (1990).

186. A.A. Astafev, A.A. Abdullaev, O.I. Vorobeva, V.A. dolgikh, B.A. Popovkin, I.M. Silvestrova and E.M. Spiridonov, *Izv. Adak. Nauk. SSSR Neorg. Mater.*, **27**, 60 (1991).

187. G. Mandula, L. Kovacs, A. Peter and E. Hartmann, *Opt. Mater.*, **1**, 161 (1992).

188. I. Foldvari, A. Peter, L.A. Kappers, O.R. Gilliam and R. Capelletti, *J. Meter. Sci.*, **27**, 750 (1992).

189. I. Foldvari, M.P. Scripsick, L.E. Halliborton and A. Peter, *Phys. Lett. A*, **154**, 84 (1991).

190. I. Foldvari, H. Liu, R.C. Powell and A. Peter, *J. Appl. Phys.*, **71**, 5465 (1992).

191. I. Foldvari, H. Liu and R. C. Powell, *SPIE Proc.*, **1626**, 9 (1992).

192. I. Foldvari, R.C. Powell, H. Liu and A. Peter, *Opt. Mater.*, **2**, 175 (1993).

193. M. D. Ewbank, R. R. Neurgaonkar, W. K. Cory, and J. Feinberg, *J. Appl. Phys.*, **62**, 374 (1987).

194. D. Rytz, B. A. Wechsler, R. N. Schwartz, C. C. Nelson, C. D. Brandle, A. J. Valentino, and G. W. Berkstresser, *J. Appl. Phys.*, **66**, 1920 (1989).

195. G. Salamo, M. J. Miller, W. W. Clark III, G. L. Wood, and E. J. Sharp, *Opt. Commun.* **59**, 417 (1986).

196. D. Mercurio, M. El Farissi, B. Frit, and P. Goursat, *Mater. Chem. Phys.*, **9**, 467 (1983).

197. H. Liu, and R.C. Powell, *J. Appl. Phys.*, **70**, 20 (1991).

198. G. L.Wood, W. W. Clark III, M. J. Miller, E. J. Sharp, G. Salamo, and R. R. Neurgaonkar, *IEEE J. Quantum Electron.*, **QE-22**, 2126 (1987).

199. J. B. Thaxter and M. Kestigian, *Appl. Opt.*, **13**, 913 (1974).

200. T. J. Hall, R. Jaura, L. M. Connors, and P. D. Foote, *Prog. Quant. Electr.*, **10**, 77 (1985).

201. A. L. Smirl, G.C. Valley, R. A. Mullen, K. Bohnert, G.D. Mire and T.F. Boggess, *Opt. Lett.*, **7**, 501 (1987).

202. R.J. Reeves, M.G. Jani, R.C. Powell and G.J. Mizell, *J. Luminesc.*, **45**, 419 (1990).

203. R.J. Reeves, M.G. Jani, B. Jassemnejad, R.C. Powell, G.J. Mizell and W. Fay, *Phys. Rev. B,* **43**, 71 (1991).

204. I. Biaggio, M. Zgonik and P. Gunter, *Opt. Commun.,* **77**, 312 (1990).

205. H. Liu, R.C. Powell and L.A. Boatner, *J. Appl. Phys.,* **70**, 20 (1991).

206. H. Liu, R.C. Powell and L.A. Boatner, *Phys. Rev. B,* **44**, 2461 (1991).

207. J.M.C. Jonathan, G. Roosen and Ph. Roussignol, *Optics Lett.,* **13**, 224 (1988).

208. I. Foldvari, B. Taheri, R.J. Reeves and R.C. Powell, *Opt. Commun.,* **102**, 245 (1993).

209. J.L. Ferrier, J. Gazengel, X.N. Phu and G. Rivoire, *Optics Commun.,* **58**, 343 (1986).

210. G. Lesaux, G. Roosen and A. Brun, *Optics Commun.,* **56**, 374 (1986).

211. G.C. Valley, *IEEE J. Quant. Electr.,* **QE-19**, 1637 (1983).

212. C. Medrano, E. Voit, P. Armhein and P. Gunter, *J. Appl. Phys.,* **64**, 4668 (1988).

213. R. Orlowski and E. Kratzig, *Solid State Commun.,* **27**, 1351 (1978).

214. F.M. Durville, E.G. Behrens, and R.C. Powell, *Phys. Rev. B,* **34**, 4213 (1986).

215. F.M. Durville, E.G. Behrens, and R.C. Powell, *Phys. Rev. B,* **35**, 4109 (1987).

216. E.G. Behrens, F.M. Durville, and R.C. Powell, *Opt. Lett.,* **11**, 653 (1986).

217. E.G. Behrens, F.M. Durville, and R.C. Powell, *Phys. Rev. B,* **39**, 6076 (1989).

218. E. G. Behrens, R.C. Powell, and D. H. Blackburn, *Appl. Opt.,* **29**, 1619 (1990).

219. E. G. Behrens, R.C. Powell, and D. H. Blackburn, *J. Opt. Soc. Am. B,* **7**, 1437 (1990).

220. V.A. French, R.C. Powell, D.H. Blackburn, and D.C. Cranmer, *J. Appl. Phys.,* **69**, 913 (1991).

221. R. Reisfeld, A. Honigbaum, and G. Michaeli, *Israel J. Chem.,* **7**, 613 (1969).

222. J.T. Fournier and R.H. Bartram, *J. Phys. Chem. solilds,* **31**, 2615 (1970).

223. R. Reisfeld, J. Hormodaly, and B. Barnett, *Chem. Phys. Lett.*, **17**, 248 (1972).

224. R. Reisfeld, *Structure and Bonding*, **Vol. 13**, 53 (1972).

225. R.A. Velapoldi, R. Reisfeld, and L. Boehm, *Phys. Chem. Glasses*, **14**, 101 (1973).

226. K.O. Hill, Y. Fujii, D.C. Johnson, and B.S. Kawasaki, *Appl. Phys. Lett.*, **32**, 647 (1978).

227. R. Reisfeld and Y. Eckstein, *J. Solid State Chem.*, **5**, 174 (1972).

228. J. Krogh-Moe, *Phys. Chem. Glasses*, **1**, 26 (1960).

229. *Handbook of Chemistry and Physics*, 70th ed. , CRC, Cleveland, 1990.

230. M.K. Murthy and B. Scroggie, *Phys. Chem. Glasses,* **7**, 68 (1966).

231. R. Reisfeld and N. Lieblich, *J. Phys. Chem. Solids*, **34**, 1467 (1973).

232. L. Ya Mazelev, *"Borate Glasses"* (Translated from Russian by Consultant Bureau, New York, 1960).

233. D.W. Moore and D.E. Day, *Phys. Chem. Glasses*, **12**, 75 (1971).

234. W. Vogel, *"Chemistry of Glass"*, The American Ceramic Society, columbus, 1985.

235. A. Paul, *"Chemistry of Glasses"*, Chapman and Hall Ltd., London, 1982.

236. P. Beekenkanp, *Phys. Chem. Glasses*, **9**, 14 (1968).

237. H.M. Heaton and H. Moore, *J. Soc. Glass Tech.*, **41**, 3 (1957).

238. N. Itoh, B.S.H. Boyce, and R. Smoluchowsky, *Phys. Rev.*, **137**, A1010 (1965).

239. S.N. Alekseichyk, Yu. E. Sverchkov, and S.E. Sverchkov, *Phys. Chem. Glasses*, (to be published).

240. S.A. Brawer and M.J. Weber, *J. Chem. Phys.*, **75**, 3522 (1981).

241. J. Felsche, *J. Less-Common Metals*, **21**, 1 (1970).

242. M.M. Broer, A.J. Bruce, and W.H. Goodkiewicz, presentation at the '8th International Conference on Dynamical Processes in Excited States of Solids,' Leiden, The Netherlands, August 1991 (unpublished).

243. J. Felsche, *Structure and Bonding*, **Vol. 13**, 99 (1972).

PART C

PUBLICATIONS

SECTION X

PUBLICATIONS

"Resonant Non-phase-matched SHG, Nonlinear Absorption and Nonlinear Refraction in CdMnSe and CdMnTe",B.Taheri, A. Munoz F., A.Hamad, J.P. Wicksted, R.C. Powell, J.K.Furdyna,*To be Submitted.*

"Carrier Transport and Recombination Dynamics in wide bandgap Dilute Magnetic Semiconductors", B.Taheri, B.Jassemnejad, R.C. Powell, J.K.Furdyna, *To be Submitted.*

"Nonlinear Absorption of Laser Light in $Bi_{12}GeO_{20}$ Single Crystals" B.Taheri, S.A.Holmstrom, R.C.Powell, J.J. Song, I.Foldvari, A.Peter, Optical Materials,**3**,(1994).

"Nonlinear Optical Responses of Strontium Barium Niobate", S.A.Holstrom, B.Taheri, R.J.Reeves, R.C.Powell, E.J.Sharp, R.R.Neurgoankar, *To be Published* in Opt. Communication.

"Nonlinear Optical and Transport Properties of CdMnSe and CdMnTe", B.Taheri, A.Munoz F., R.C.Powell, J.J.Song, J.K.Furdyna, Proc. SPIE, **2229** (1994).

"Nonlinear Absorption of Laser Light in Bi_2TeO_5 Single Crystals", I.Foldvri, B. Taheri, R.J. Reeves, R.C. Powell, Optics Communication **102**(1993)245-250.

"The Dependence of Laser-Induced Refractive Index Changes in Glass on the Chemical Composition", A.Munoz F., F.J.Reeves, B.Taheri, R.C.Powell, D.H.Blackburn, D.C.Cranmer, J. Chem. Phys. **98**(1993)6083-6091.

Roger R. Petrin, Michael L. Kliewer, John T. Beasley, Richard C. Powell, Ishwar D. Aggarwal, and Robert C. Ginther, "Spectroscopy and Laser Operation of Nd:ZBAN Glass", IEEE J.Quant. Electron. **OE-27**, 1031 (1991).

Roger R. Petrin, Mahendra G. Jani, and Richard C. Powell, "Spectral dynamics of laser-pumped $Y_3Al_5O_{12}$:Tm,Ho lasers", Optical Materials **1**,111 (1992).

Roger R. Petrin, Roger J. Reeves, Michael L. Kliewer, Richard C. Powell, Ishwar d. Aggarwal, and Robert C. Ginther, "Laser-Pumped Laser Properties of Nd^{3+} in Bulk ZBAN Glass, in *OSA Proceedings Vol.6: Advanced Solid-State Lasers*, edited by H.P. Jensen and G. Dube (Optical Society of America, Washington D.C., 1990), 236. (results presented at Advanced Solid State Lasers Conference, Salt Lake City, UT 1990).

Roger R. Petrin, Richard C. Powell, Mahendra G. Jani, Milan Kokta, and I.D. Aggarwal, "Comparison of Laser-Pumped Tm,Ho Laser Systems", in *OSA proceedings Vol. 13: Advanced Solid-State Lasers*, edited by L.L. Chase an A.A. Pinto (Optional Society of America, Washington

D.C. 1992), 139. (results presented at Advanced Solid State Lasers Conference, Santa Fe, NM, 1992).

Valentina A. French, Roger R. Petrin, and Richard C. Powell, "Energy Transfer Processes in Tm, Ho:YAG", Physical Review B **46**, 8018 (1992).

Mahendra G. Jani, James T. Murray, Roger R. Petrin, Richard C. Powell, D.N. Loiacono, and G. M. Loiacono, "Pump wavelength tuning of optical parametric oscillations and frequency mixing in KTiOAsO4", Appl. Phys. Lett.**60**, 2327 (1992).

SECTION XI

THESIS LIST

1. R.R. Petrin, Doctor of Philosophy, 1993.

2. V.A. French, Doctor of Philosophy, 1993.

3. B. Taheri, Doctor of Philosophy, 1994.

4. J.M. Murray, Master of Science, 1993.

5. S.A. Holmstrom, Master of Science, 1994.